

https://dspace.org/

A Novel Multi-Component 3D-Printed Scaffold for Targeted Bone Tuberculosis Therapy,

Mphaphuli, Mashudu Theodore

2025
University of the Witwatersrand, Johannesburg
https://hdl.handle.net/10539/49997

Mphaphuli, Mashudu Theodore. (2025). A Novel Multi-Component 3D-Printed Scaffold for Targeted Bone Tuberculosis Therapy, [PhD thesis, University of the Witwatersrand, Johannesburg]. WIReDSpace. https://hdl.handle.net/10539/49997

Downloaded from a DSpace repository. https://dspace.org/

A NOVEL MULTI-COMPONENT 3D-PRINTED SCAFFOLD FOR TARGETED BONE TUBERCULOSIS THERAPY

MASHUDU THEODORE MPHAPHULI

A thesis submitted to the Faculty of Health Sciences, University of the Witwatersrand in fulfilment of the requirements for the degree of Doctor of Philosophy

Supervisor:

Professor Yahya Essop Choonara

University of the Witwatersrand, Department of Pharmacy and Pharmacology, Johannesburg, South Africa

Co-Supervisors:

Professor Pradeep Kumar

University of the Witwatersrand, Department of Pharmacy and Pharmacology,

Johannesburg, South Africa

Dr. Mduduzi Sithole

University of the Witwatersrand, Department of Pharmacy and Pharmacology,

Johannesburg, South Africa

Johannesburg

2025

DECLARATION

I, Mphaphuli Theodore Mashudu, declare that this thesis is my work. It has been submitted for the degree of Doctor of Philosophy in the Faculty of Health Sciences at the University of the Witwatersrand, Johannesburg. It has not been submitted before for any degree or examination at this or any other University.



31st July 2025

PUBLICATIONS

1. Multi-purpose prototypes for extrapulmonary *Mycobacterium tuberculosis* targeting: A regenerative medicine perspective: Mashudu T. Mphaphuli, Mduduzi. Sithole, Pradeep Kumar, Pierre Kondiah, Mostafa Mabrouk, Yahya E. Choonara, Journal of Drug Delivery Science and Technology, 89, 105039, 2023.
2. Shaimaa ElShebiney, Sara A. M. El-Sayed, Mduduzi N. Sithole, Mashudu T. Mphaphuli, Hanan H. Beherei, Pradeep Kumar, Fariborz Sharifianjazi, Yahya E. Choonara*, and Mostafa Mabrouk. Innovative 3D Bioprinting: Alginate-MgP Scaffolds for Superior Regeneration of Calvarial Bone Defects in Rats. Submitted to International Journal of Biological Macromolecules, February 2025.

RESEARCH OUTPUTS AT CONFERENCE PROCEEDINGS

1. Mphaphuli, M.T., Sithole, M.N., Kumar, P., Kondiah, P.P., Mabrouk, M. and Choonara, Y.E. A Novel 3D Printed Multi-Component Scaffold for Targeted Spinal Tuberculosis Therapy **(Poster Presentation)**. Microphysiological Systems World Summit, Berlin, Germany, 26-30 JUNE 2023.

2. Mphaphuli, M.T., Sithole, M.N., Kumar, P., Kondiah, P.P., Mabrouk, M. and Choonara, Y.E. An advanced *in-vitro*–engineered, multi-component 3D-printed scaffold for targeted bone tuberculosis therapy. **(Oral Presentation**). 82nd FIP World Congress of Pharmacy and Pharmaceutical Sciences, Cape Town, South Africa, 1–4 September 2024.

ABSTRACT

Delivering therapeutic agents for the effective treatment of bone tuberculosis (TB) is significantly challenged by inadequate drug penetration into the infected skeletal tissues and limited regeneration of damaged bone. Traditional systemic drug administration often fails to achieve desired therapeutic concentrations locally, leading to increased risk of drug resistance, treatment failure, and systemic toxicity. The aim of this study was to develop a novel, multi-component 3D-printed scaffold incorporating bedaquiline (BQ)-loaded poly(lactic-co-glycolic acid) (PLGA) nanoparticles for localized, sustained release and simultaneous bone regeneration in the targeted management of bone TB. The BQ-loaded PLGA nanoparticles were synthesized using a solvent evaporation technique and optimized through a Box–Behnken design (BBD), focusing on critical quality attributes (CQAs). The optimized nanoparticles exhibited an average particle size of approximately 180 nm, a polydispersity index of less than 0.2, and an encapsulation efficiency (EE) of 78 ± 3%. *In-vitro* drug release assays demonstrated controlled and sustained release kinetics, achieving approximately 85% cumulative drug release over 21 days. The multi-component scaffold was fabricated using advanced 3D printing technology, integrating natural, synthetic, bioactive, and metallic biomaterials, specifically polycaprolactone (PCL), sodium alginate (NaAlg), bioactive glass (BG), and titanium (Ti). The scaffold exhibited a porosity of nearly 70% and demonstrated optimal mechanical properties with a compressive strength around 3.5 MPa. Comprehensive physicochemical, morphological, and thermal characterizations were conducted using Fourier Transform Infrared Spectroscopy (FTIR), X-ray Diffraction (XRD), Differential Scanning Calorimetry (DSC), Thermogravimetric Analysis (TGA), Scanning Electron Microscopy (SEM), and Transmission Electron Microscopy (TEM), confirming the scaffold's desirable structural integrity, thermal stability, and morphological properties. Cytotoxicity assessments performed using the MG-63 osteosarcoma cell line indicated high cell viability exceeding 85% after 72 hours, confirming excellent biocompatibility and suitability for bone tissue engineering applications. An *in vivo* evaluation in a New Zealand White rabbit femoral defect model provided further evidence of therapeutic efficacy, with histomorphometry analyses revealing bone regeneration at defect sites treated with the scaffold, compared to regeneration in untreated control sites after 4 weeks. Additionally, mechanical testing supported these findings, showing significantly enhanced structural integrity and load-bearing capabilities at the treated sites. The results of this comprehensive study demonstrate that the developed 3D-printed scaffold loaded with BQ-encapsulated nanoparticles effectively addresses the limitations associated with conventional systemic bone TB therapies. The scaffold provides sustained localized drug delivery, reduces systemic side effects, and significantly enhances bone tissue regeneration. This innovative platform holds promise for clinical translation, potentially revolutionizing the management and treatment of bone tuberculosis and similar skeletal conditions requiring targeted therapeutic intervention and robust regenerative support.

ACKNOWLEDGMENTS

I would like to begin by thanking the Lord Jesus Christ for being my anchor and source of great strength throughout this journey. His guidance and unfailing love have sustained me during the most challenging moments of my PhD studies.

I am profoundly thankful to my supervisor, Prof. Choonara YE, for being fundamental in the conceptualization of my project. He enlightened me that this project is not only for the corridors of WADDP but is a life-changing endeavour that demands thoroughness and passion. He also introduced me to other opportunities that helped me become a better scientist.

I am equally grateful to my co-supervisor, Prof. Kumar P, who was instrumental in the conceptualization of my research. He taught me how to become an exemplary scientist and think critically. I will always remember his motivating words, "Just start," which inspired me to embark on this journey and see it through to its successful completion.

I am forever indebted to Dr. Sithole M, who has been an angel in my life. I thank God for his contribution not only to my project but also to my personal growth. He taught me to take risks and never give up. His guidance and demonstration of hard work have left an indelible mark on my journey.

I am deeply thankful to my parents, Mr. Mphaphuli G and Mrs. Ndleve RG, for their unwavering support and love. I especially wish to acknowledge Mrs. Ndleve R for being a constant source of strength, always praying for me, introducing me to the pharmacy world, and being an exceptional mom. I also extend my gratitude to my siblings, Mphaphuli L, Mphaphuli M, and Mphaphuli V, for their continuous encouragement.

My sincere appreciation goes to everyone at the WADDP. I am especially grateful to my colleagues who became like family, namely Sikhosana N, Abdelgader A, Khoza L, Motaung A, and Varughese T, for their friendship and support. I also wish to acknowledge Dr. Mndlovu H and the entire staff at WADDP for their invaluable assistance in running the laboratories; their dedication and expertise were indispensable throughout my research endeavor. I would also like to extend my gratitude to the administrative team, including Sekgotho T and Damane N, as well as to the custodial staff at the lab, whose care and diligence made this journey seamless.

I extend my thanks to Dr Nxumalo S, Ms Matjila L, Mr Madavhu M, Ms Mathapo C, Ms Rammekwa A, and Mr Mbodi of the Wits Research Animal Facility (WRAF) for their exceptional support during the animal experimentation phase of my study. A special thank you also goes to the surgeon, Prof. Erlwanger K, whose expertise contributed greatly to the success of my project.

I am forever grateful to my pastor, Bishop AH Nenngwekhulu, whose teachings, guidance, and fatherly care kept me going in times of need. I also wish to thank the entire Christian Worship Centre (CWC) family, especially those from Johannesburg, for their continual support.

I would also like to acknowledge and greatly appreciate the financial assistance provided by the National Research Foundation (NRF) of South Africa and the University of the Witwatersrand, which made this research possible.

Finally, I thank all my friends and relatives who have supported me throughout this journey. Your encouragement and belief in me have been a constant source of inspiration.

Grace to you all

Mashudu Theodore Mphaphuli

DEDICATION

I dedicate this thesis to my maternal grandmother,

***Meriam Khubani Ndleve**,*

whose unwavering love, wisdom, and inspiration have profoundly influenced my life and academic journey.

ANIMAL ETHICS DECLARATION

I, Mashudu Theodore Mphaphuli confirm that the study entitled "*In vivo* evaluation of 3D printed multi-component scaffolds incorporated with growth factor and bedaquiline nanoparticles for bone regeneration and drug distribution in young New Zealand rabbits." received approval from the Animal Ethics Committee of the University of the Witwatersrand with ethics clearance number 23/09/004C (see Appendix B)

TABLE OF CONTENTS

DECLARATION i

PUBLICATIONS ii

RESEARCH OUTPUTS AT CONFERENCE PROCEEDINGS iii

ABSTRACT iv

ACKNOWLEDGEMENTS v

DEDICATIONS vii

ANIMAL ETHICS DECLARATION viii

TABLE OF CONTENTS ix

APPENDICES xvi

LIST OF FIGURES xvii

LIST OF TABLES xxv

LIST OF EQUATIONS xxvii

LIST OF ABBREVIATIONS xxviii

TABLE OF CONTENTS

Chapter 1

INTRODUCTION

1.1. Background of this study 1

1.2. Rationale and Motivation for this study 3

1.3. Aim and Objectives 5

1.4. Novelty of the Study 7

1.5. Overview of this Thesis 7

1.6. References 10

Chapter 2

MULTI-PURPOSE PROTOTYPES FOR EXTRAPULMONARY MYCOBACTERIUM TUBERCULOSIS TARGETING: A REGENERATIVE MEDICINE PERSPECTIVE

2.1. Introduction 15

2.2. *Mycobacterium tuberculosis* journey from pulmonary TB to extrapulmonary TB 20

2.3. Influence of affected tissue micro-environment on the performance of drug delivery system 24

2.4. The role of targeted therapy (TT) in treating *Mycobacterium* tuberculosis 27

2.4.1. Overview of bone-targeted therapies 29

2.4.2. Nanotechnology-based approach in targeted therapy 32

2.4.2.1. Organic nanoparticles 34

2.4.2.2. Inorganic nanoparticles 46

2.5. Design of a multi-purpose novel platform 48

2.5.1. The role of scaffolds in bone tissue engineering 50

2.5.1.1. Individual component and combined component biomaterials 51

2.5.2. Pros and Cons of 3D-printed scaffolds embedded with conventional drug delivery systems. 54

2.5.3. Polymeric Nanoparticles and 3D Printed Scaffolds 56

2.5.4. Lipidic nanoparticles and 3D printed scaffolds 59

2.5.5. Metallic nanoparticles and 3D printed scaffold 60

2.5.6. Mesoporous silica (MSN)and mesoporous bioactive glass (MBG) nanoparticles and 3D printed scaffold. 61

2.6. Concluding Remarks 63

2.7. References 65

Chapter 3

DEVELOPMENT AND OPTIMIZATION OF BEDAQUILINE-LOADED PLGA NANOPARTICLE FOR POTENTIAL TARGETED BONE DELIVERY

3.1. Introduction 86

3.2. Materials and Methods 89

3.2.1. Materials 89

3.2.2. Development and Optimization of PLGA BQ-loaded Nanoparticles 90

3.2.3. Fabrication of optimized BQ-loaded PLGA nanoparticles 91

3.2.4. Characterization of the Optimized BQ-loaded PLGA nanoparticles 92

3.2.4.1. Determination of particle size 92

3.2.4.2. Determination of particle surface morphology 92

3.2.4.3. Analysis of chemical integrity using FTIR spectroscopy analysis 92

3.2.4.4. Analysis of the crystallographic structure 93

3.2.4.5. Analysis of thermal behaviour using differential scanning calorimetry (DSC) 93

3.2.4.6. Analysis of thermal stability assessment using thermogravimetric analysis (TGA) 93

3.2.4.7. Determination of BQ content in the PLGA nanoparticles 94

3.2.4.8. Stability studies 94

3.2.4.9. Evaluation of In vitro release of BQ from the PLGA nanoparticles 94

3.2.4.10. In vitro assays for Cytotoxicity studies of PLGA nanoparticles 95

3.3. Results and Discussion 96

3.3.1. Statistical Optimization 96

3.3.1.1. Evaluation of model adequacy and ANOVA for particle size (Y_1) 97

3.3.1.2. Evaluation of model adequacy and ANOVA for polydispersity index (Y_2) 102

3.3.1.3. Evaluation of model adequacy and ANOVA for drug loading (%) (Y_3) 104

3.3.1.4. Evaluation of model adequacy and ANOVA for entrapment efficiency (Y_4) 108

3.3.1.5. Formulation Optimization 112

3.3.2. Characterization of optimized BQ-loaded PLGA nanoparticles 113

3.3.2.1. Assessment of BDQ-loaded PLGA nanoparticles in terms of particle size, PDI, and morphology 113

3.3.2.2. Determination of structural integrity of the optimized BQ-loaded PLGA nanoparticles 114

3.3.2.3. Assessment of the crystalline structural properties of optimized BQ-loaded PLGA nanoparticles 116

3.3.2.4. Evaluation of thermal behaviour using differential scanning calorimetry (DSC) of optimized BQ-loaded PLGA nanoparticles 118

3.3.2.5. Assessment of the thermal stability properties of optimized BQ-loaded PLGA nanoparticles release from the optimized PLGA nanoparticles 120

3.3.2.6. Evaluation of BQ entrapment efficiency, drug loading, and *In-vitro* release from optimized BQ-loaded PLGA nanoparticles 121

3.3.2.7. Assessment of long-term stability of optimized BQ-loaded PLGA nanoparticles 124

3.3.2.8. Evaluation of cytotoxicity of the optimized BQ-loaded PLGA nanoparticles on MG-63 cell line 126

3.4. Concluding Remarks 128

3.5. References 130

Chapter 4

DEVELOPMENT, AND *IN-VITRO*, CHARACTERIZATION OF THE NOVEL MULTI-COMPONENT 3D-PRINTED SCAFFOLD EMBEDDED WITH BQ-LOADED PLGA NANOPARTICLES FOR BONE TB THERAPY

4.1. Introduction 138

4.2. Materials and Methods 140

4.2.1. Materials 140

4.2.2. Fabrication of the novel multi-component 3D-printed scaffold 141

4.3. Characterisation Studies of the Loaded and Unloaded Novel Multi-component 3D-Printed Scaffold 142

4.3.1. Physicochemical properties of the novel multi-component 3D-printed scaffold 142

4.3.2. Thermal properties of the novel multi-component 3D-printed scaffold 143

4.3.3. Microstructure and morphology of the novel multi-component 3D-printed scaffold 143

4.3.4. Porosity and pore size distribution of the novel multi-component 3D-printed scaffold 143

4.3.5. Biomineralization of the novel multi-component 3D-printed scaffold 144

4.3.6. Swelling analysis of the novel multi-component 3D-printed scaffold 144

4.3.7. Biodegradation of the novel multi-component 3D-printed scaffold 144

4.3.8. Compressive strength analysis of the novel multi-component 3D-printed scaffold 145

4.3.9. Bedaquilline release from the novel multi-component 3D-printed scaffold 145

4.3.10. *In-vitro* Cytotoxicity analysis of the novel multi-component 3D-printed scaffold 146

4.3.11. Cell culture and experimental setup 146

4.3.11.1. Cell viability evaluation for the novel multi-component 3D-printed scaffold 146

4.3.12. Cell adhesion onto the novel multi-component 3D-printed scaffold 147

4.3.13. Statistical analysis 148

4.4. Results and Discussion 148

4.4.1. Chemical Integrity evaluation of the novel multi-component 3D-printed scaffold 148

4.4.2. Assessment of thermal stability and composition of the 3D-printed scaffold 152

4.4.3. Evaluation of microstructure, morphology, and porosity of the novel multi-component 3D-printed scaffold. 153

4.4.4. Evaluation of biomineralization of the Novel Multi-Component 3D-Printed Scaffold 157

4.4.5. Evaluation of biodegradation and swelling of the Novel Multi-Component 3D-printed Scaffold 160

4.4.6. Compressive strength of the novel multi-component 3D-printed scaffold. 162

4.4.7. *In-vitro* drug release of bedaquiline in the novel multi-component 3D-printed scaffold 164

4.4.8. *In-vitro* cell compatibility of loaded and unloaded novel multi-component 3D-printed scaffold 165

4.5. Concluding Remarks 166

4.6. References 168

Chapter 5

***IN-VIVO* EVALUATION OF THE NOVEL MULTI-COMPONENT 3D-PRINTED SCAFFOLD EMBEDDED WITH BQ-LOADED PLGA NANOPARTICLES FOR BONE TUBERCULOSIS THERAPY**

5.1. Introduction 176

5.2. Materials and Methods 177

5.2.1. Materials 177

5.2.2. Animal Welfare, Housing, and Habituation before Study Experiment 177

5.2.3. The novel multi-component 3D-printed Scaffolds Preparation Prior Implantation 179

5.2.4. Design and surgical procedure for the pilot Intervention 179

5.2.5. The design of the main study 180

5.2.5.1. Surgical procedure for the intervention 182

5.2.5.2. Post-operative Care of the New Zealand White Rabbits 183

5.2.5.3. Procedure for Euthanasia and Sample Collection 184

5.2.5.4. Mechanical Strength and Computed Tomography (CT) Assessment . 186
5.2.5.5. Evaluation of Micro-Computed Tomography scan of Rabbit femur 187
5.2.5.6. Sample Preparation for Histological Examination 187
5.2.5.7. Quantification of bedaquiline concentration in plasma using high-pressure liquid chromatography 188
5.3. Results and Discussion 188
5.3.1. Pilot Study Assessment 188
5.3.2. Clinical and Histological Analysis for main study 189
5.3.2.1. Clinical examination 189
5.3.2.2. Histological evaluation of right femur following various interventions .. 190
5.3.3. Assessment of mechanical strength 195
5.3.4. Assessment of micro-CT scans of right femur following various interventions 196
5.3.5. Concentration of Bedaquiline in the blood of the Rabbitt model 197
5.4. Concluding Remarks 198
5.5. References 200

Chapter 6

CONCLUSIONS AND RECOMMENDATIONS

6.1. Conclusion 202
6.2. Recommendations 203

Chapter 7

NOVARTIS NEXT GENERATION PROGRAM EXPERIENCE

7.1. Overview of the Program 205
7.2. Research Focus of Program 205
7.3. Achievements and Work Undertaken During the NGS Program Period 206
7.4. Highlights and Impact of the Work 206

APPENDICES

Appendix A:	Supplementary Material	205
Appendix B	Animal Ethics Clearance Certificate	208
Appendix C:	Publication	209
Appendix D:	Research Outputs	210

LIST OF FIGURES

Figure 1.1	A schematic representation of the design and application of the 3D-printed multi-component scaffold incorporating bedaquiline-loaded PLGA nanoparticles	6
Figure 2.1	Illustrates the different targets for each drug on the *Mycobacterium tuberculosis* structure	18
Figure 2.2	Pathway Mechanism from Pulmonary TB to EPTB	21
Figure 2.3	A general protocol for spinal TB	28
Figure 2.4	Demonstrates the process of natural bone healing following a fracture	29
Figure 2.5	Targeting systems that nanoparticles use for targeted therapy	32
Figure 2.6	Various forms of the most frequently utilized nanostructures as drug delivery systems	33
Figure 2.7	The plasma drug profile after a single nebulization of alginate nanoparticles loaded with antitubercular drugs and unbound drugs was evaluated in guinea pigs	35
Figure 2.8	The levels of antitubercular drugs in tissues on day 15 post aerosol administration of alginate nanoparticles in guinea pigs were determined. The data represent the mean ± standard deviation of six animals and includes RIF, INH, and PZA	35

Figure 2.9	depicts PLGA-PEG nanoparticles that are loaded with Clofazimine (CFZ) and functionalized with a transferrin receptor-binding peptide, intended for targeted drug delivery to the central nervous system in the treatment of multi-drug-resistant tuberculosis.	38
Figure 2.10	**(i–iii)** Time-dependent fluorescence imaging of PLGA–PEG–Asp3/FITC–PLGA–PEG–OMe (8/2) NP, **(iv–vi)** DAPI staining and **(vii–ix)** merge images, which transport into D1 living cells	40
Figure 2.11	**(A)** A graphical representation of the in vivo pharmacokinetic analysis. **(B)** An X-ray image showing the implantation of the MD probe in the joint cavity. **(C)** The stability of the in-vivo recovery of the MD probe. **(D)** The in-vivo profiles of the concentration-time of DINH in synovial fluid. **(E)** The ratios of C24h/C1h were obtained from **(D).**	43
Figure 2.12	Diagram demonstrating the features that a 3D scaffold made from biomaterials should possess	49
Figure 2.13	**(A)** Cell viability results, (B) SEM image depicting adhesion of scaffold to the rBMSCs cells, (**C, D, E**) inverted phase contrast microscope of the scaffold on the cells at 24hr, 48hr, and 72hr, respectively, (F) Drug release profile of the two anti-TB drugs from the β-TCP/PLGA microspheres scaffold	56

Figure 2.14	**.** The diagram depicts **(a)** the procedure involved in developing PLGA nanoparticles for BMP-2 delivery, and **(b)** The viability and cytotoxicity analysis conducted five days after seeding	57
Figure 2.15	Cumulative release **(a)** and release rate **(b)** curves of INH and RIF in SBF at 37 °C from scaffolds.	61
Figure 3.1	Schematic illustration of different nanoparticles and advantages of the nanoparticle systems	86
Figure 3.2	Schematic representation of the manufacturing process of BQ-loaded PLGA nanoparticles	96
Figure 3.3	**(a)** Normal plot of residuals depicting the impact of model terms on particle size, **(b)** Observed versus predicted response for particle size.	98
Figure 3.4	**(a)** 2D contour plot depicting the impact of X_1 and X_2 on particle size, **(b)** 3D response surface plot depicting the impact of X_1 and X_2 on the particle size of the BQ-loaded PLGA nanoparticles	100
Figure 3.5	**(a)** 2D contour plot depicting the impact of X_1 and X_3 on PDI, **(b)** 3D response surface plot depicting the impact of X_1 and X_3 on the PDI of the BQ-loaded PLGA nanoparticles	103
Figure 3.6	**(a)** Normal probability plot of residuals for DL, **(b)** plot of studentized residuals versus predicted responses for DL, **(c)** Box-cox plot for power transformation for DL	105

Figure 3.7	**(a)** 3D response surface plot showing the impact of X_1 and X_4 on DL(%), **(b)** 3D response surface plot depicting the impact of X_2 and X_4 on the DL(%) of the BQ-loaded PLGA nanoparticles	107
Figure 3.8	**(a)** Normal probability plot of residuals for EE, **(b)** Box-cox plot for power transformation for EE	109
Figure 3.9	**(a)** One-factor plot depicting the impact of X_4 on EE, **(b)** 2D contour plot depicting the impact of X_1 and X_4 on EE, **(c)** 3D response surface plot depicting the impact of X_1 and X_4 on the EE of the BQ-loaded PLGA nanoparticles	110
Figure 3.10.	A visualization of the morphological attributes of the optimized BQ-loaded PLGA nanoparticles, showing (**a**) average hydrodynamic particle size of 183.8±54.54 nm (PDI = 0.05 ± 0.02), (**b**) zeta potential of -5.5± 5.44 mV, and (**c**) SEM image showing overall morphology at 3 µg/ml scale (5.00 KX magnification), and **(d)** a higher magnification SEM image at 300 nm scale (50.00 KX magnification), showing a spherical nanoparticle morphology	113
Figure 3.11	FTIR spectra of the **(a)** PVA, **(b)** PLGA, **(c)** BQ, and **(d)** optimized lyophilized BQ-loaded PLGA nanoparticles.	115
Figure 3.12	XRD diffraction pattern of **the (a)** PVA, **(b)** PLGA, **(c)** BQ, and **(d)** optimized lyophilized BQ-loaded PLGA nanoparticles	117

Figure 3.13	DSC thermogram patterns of the **(a)** PVA, **(b)** PLGA, **(c)** BQ, and **(d)** optimized lyophilized BQ-loaded PLGA nanoparticles.	118
Figure 3.14	TGA thermogram patterns of the **(a)** PVA, **(b)** PLGA, **(c)** BQ, and **(d)** optimized lyophilized BQ-loaded PLGA nanoparticles	120
Figure 3.15	*In-vitro* BQ release profiles from the optimized PLGA nanoparticles at pH 7.4. Experiment data are presented as the mean ± SD, n = 3	122
Figure 3.16	Stability data of optimized BQ-loaded PLGA nanoparticles evaluating **(a)** particle size and PDI, **(b)** EE (%) and DL (%) at 25 ± 2 °C and 60 ± 5% relative humidity	124
Figure 3.17	Cell viability of MG-63 cell line treated with BQ-loaded PLGA nanoparticles and free BQ incubated at 37°C for 72 hours. Data presented as mean ± SD, n = 4 ($p<0.0001$)	125
Figure 4.1	Schematic and photographic depiction of the development of the novel multi-component 3D-printed scaffold	141
Figure 4.2	FTIR spectra of **(a)** native BGT 10%, **(b)** native polycaprolactone (PCL), **(c)** native polyvinyl alcohol (PVA), **(d)** native sodium alginate (NaAlg), **(e)** BQ-loaded PLGA nanoparticles **(f)** Unloaded 3D-printed scaffold and **(g)** Drug loaded 3D-printed scaffold	148
Figure 4.3	XRD spectra of **(a)** native BGT (10%) **(b)** native PVA, **(c)** native NaAlg**, (d)** unloaded novel multicomponent scaffold and **(e)**	149

	drug-loaded novel multicomponent scaffold	
Figure 4.4	TGA thermograms of **(a)** native BGT 10%, **(b)** native polycaprolactone (PCL), **(c)** native polyvinyl alcohol (PVA), **(d)** native sodium alginate (NaAlg), **(e)** Unloaded 3D-printed scaffold and **(f)** Drug loaded 3D-printed scaffold.	151
Figure 4.5	Visual and microscopic evaluation of the novel multi-component 3D-printed scaffold. **(a, b)** Macroscopic images showing the microstructure of the 3D-printed scaffold, highlighting its uniform grid-like pattern and structural integrity. **(c, d)** SEM images of the unloaded 3D-printed scaffold, displaying its porous architecture and surface morphology. **(e, f)** SEM images of the drug-loaded 3D-printed scaffold show spherical nanoparticulate structures distributed on the scaffold surface and within its internal pores, confirming successful nanoparticle incorporation.	155
Figure 4.6.	Structural and porosity evaluation of the novel multi-component 3D-printed scaffold. **(a)** SEM image showing the scaffold's macroporous architecture with pore sizes ranging from approximately 415.7 µm to 562.3 µm. **(b)** BET isotherm curve illustrating the scaffold's adsorption-desorption behavior, indicative of a mesoporous structure with a hysteresis loop, further supporting its suitability for controlled drug delivery and biomedical applications	156

Figure 4.7	Spectra of **(a)** FTIR and **(b)** XRD of the novel multi-component 3D-printed scaffolds before immersion in SBF (pH 7.4, 37°C) and after immersion for over 28 days	158
Figure 4.8	EDX of the novel multi-component 3D-printed scaffold **(a)** before immersion in SBF and **(b)** after immersion in SBF for 28 days. The presence of Ca and P can be attributed to the formation of apatite on the surfaces of the scaffolds	159
Figure 4.9	Degradation of novel multi-component 3D-printed scaffolds over 30 days	159
Figure 4.10	Swelling profiles of **(a)** unloaded novel multi-component 3D-printed scaffold and **(b**) drug-loaded novel multi-component 3D-printed scaffold measured over 30 days	161
Figure 4.11	Compressive strength (MPa) of various 3D-printed scaffolds	162
Figure 4.12.	*In-vitro* BQ release profile from the 3D-printed scaffold at pH 7.4. Experiment data are presented as the mean ± SD, n = 3	163
Figure 4.13	Assessment of osteoblast-like MG63 cell differentiation at ~90 confluence	164
Figure 4.14	**(a)** Viability of osteoblast-like MG63 cells, assessed using an MTT assay, in the presence of the optimal drug-free and drug-loaded 3D-printed scaffolds. **(b, c**) SEM images of the unloaded and loaded 3D-printed scaffolds, respectively, after 7 days of culture with osteoblast-like MG63 cells	165

Figure 5.1	Photographic representation of (a-b) housing of the New Zealand white Rabbits	177
Figure 5.2	Schematic showing the in-vivo studied model for the implanted scaffold	180
Figure 5.3	Surgical procedure demonstrating the creation of a critical-sized bone defect and scaffold implantation in Rabbits. **(a)** preparation of the rabbit pre-surgery, **(b-c)** creation of surgical defect before scaffold implantation with measurements to ensure defect dimension accuracy, **(d)** placement of 3D-printed scaffold into the defect, **(e-f)** surgical closure and suturing of the site post-implantation	182
Figure 5.4	Procedure for femoral bone extraction and sample preparation post-euthanasia: **(a)** isolated hind limb immediately post-euthanasia; **(b)** muscle tissue removal exposing femoral bone; **(c)** cleaned femur clearly showing the defect region; **(d)** femoral bone segment containing defect region; **(e)** extracted bone segment demonstrating intact and healthy bone marrow, and **(f)** samples stored in 10% buffered formalin awaiting histological analysis	184
Figure 5.5	**(a)** Rabbit femur specimen immediately after retrieval from storage**, (b)** clamping of the horizontally oriented femur in a vise under the textural analyzer, **(c)** positioning of the 5 mm diameter ball probe at the defect site, and **(d)**	186

	performing the indentation test to determine the bone's matrix hardness or indentation resistance	
Figure 5.6	Histological evaluation of femoral defect healing after 4 weeks post-implantation (H&E staining): **(a)** Scaffold loaded with BQ showing moderate bone regeneration and inflammatory response; **(b)** Scaffold loaded with BQ plus BMP illustrating similar regenerative activity and inflammation to the drug-only scaffold; **(c)** Drug-free scaffold exhibiting reduced bone formation activity; **(d)** Untreated defect (control) predominantly characterized by fibrous tissue and minimal bone regeneration.	188
Figure 5.7	Histological sections of rabbit femoral defects at Week 1, comparing **(a)** control defects, **(b)** defects treated with a 3D-printed scaffold only, and (**c)** defects treated with a 3D-printed scaffold loaded with BQ-loaded PLGA nanoparticles	190
Figure 5.8	Histological sections of rabbit femoral defects at Week 2, comparing **(a)** defects treated with a 3D-printed scaffold only **(b)** defects treated with a 3D-printed scaffold loaded with BQ-loaded PLGA nanoparticles, and **(c)** control defects.	191
Figure 5.9	Histological sections of rabbit femoral defects at Week 3, comparing **(a)** defects treated with a 3D-printed scaffold only **(b)** defects	192

	treated with a 3D-printed scaffold loaded with BQ-loaded PLGA nanoparticles, and **(c)** control defects	
Figure 5.10	Histological sections of rabbit femoral defects at Week 4, comparing **(a)** defects treated with a 3D-printed scaffold only **(b)** defects treated with a 3D-printed scaffold loaded with BQ-loaded PLGA nanoparticles, and **(c)** control defects	193
Figure 5.11	Analysis of indentation force of rabbit femoral defects over four weeks, comparing **(a)** control defects, **(b)** defects treated with a 3D-printed scaffold only, and **(c)** defects treated with a 3D-printed scaffold loaded with BQ-loaded PLGA nanoparticles	195
Figure 5.12	Micro-CT images of femoral **(a)** defect, **(b)** implantation of scaffold only, and **(c)** scaffold with BQ-loaded PLGA nanoparticles	196
Figure 5.13	Bedaquiline distribution with respect to weeks in blood	197

LIST OF TABLES

Table 2.1:	Different EPTB organ sites and their characteristics	22
Table 2.2:	How physiological changes caused by *Mycobacterium tuberculosis* affect drug properties and absorption	26
Table 2.3:	Advantages offered by targeted therapy in drug delivery	27
Table 2.4:	The study compared the pharmacokinetics of antitubercular drugs delivered in the form of alginate nanoparticles via nebulization to oral administration of unbound drugs in guinea pigs	34
Table 2.5:	Antimicrobial susceptibility test result	37
Table 2.6:	An overview of the anti-TB vesicular carriers that have been utilized	42
Table 2.7:	Summary of different individual-component biomaterials used for bone tissue scaffold	50
Table 2.8:	Highlights the various individual and multi-component biomaterials used in the development of 3D-printed scaffolds for bone tissue engineering (bone-TB).	52
Table 2.9:	Provides an overview of the different pros and cons associated with the utilization of 3D-printed scaffolds embedded with conventional drug delivery systems	54
Table 2.10:	Examples Lipid system that has been employed within scaffolds	59
Table 3.1:	BBD model for the effect of formulation composition on PLGA nanoparticles	90
Table 3.2:	Experimental design and characteristics of BQ-loaded PLGA nanoparticles	95
Table 3.3:	Model adequacy measures and values summary	96
Table 3.4:	Statistical measures of model adequacy	98
Table 3.5:	Model adequacy measures and values summary	101
Table 3.6:	ANOVA analysis model for PDI	101
Table 3.7:	ANOVA analysis model for DL(%)	104

Table 3.8:	ANOVA analysis model for EE	108
Table 3.9:	Optimized formulation variables and predicted response	111
Table 3.10:	Results BQ-loaded PLGA nanoparticles developed using the optimum process variables	111
Table 3.11:	Results of fitting in vitro data for BQ release from optimized BQ-loaded PLGA nanoparticles to various mathematical models.	122
Table 3.12:	IC50 values for the BQ-loaded PLGA nanoparticles and free BQ incubated. Data are presented as mean ± SD (n=4)	126
Table 4.1:	Parameters for the novel multi-component 3D-printed scaffold	141
Table 5.1:	Textural configurations for determining bone hardness	184

LIST OF EQUATIONS

Equation 3.1:	EE (%)	93
Equation 3.2:	DL (%)	93
Equation 3.3:	% Cell viability	95
Equation 3.4:	Particle size regression model	99
Equation 3.5:	PDI regression model	102
Equation 3.6:	EE regression model	106
Equation 3.7:	DL regression model	108
Equation 4.1:	Swelling ratio (%)	142
Equation 4.2:	Degradation rate (%)	143
Equation 4.3:	% Cell viability	145

LIST OF ABBREVIATIONS

AFB	Acid-Fast Bacilli
α-MEM	Alpha Minimum Essential Medium
ANOVA	Analysis of Variance
AuPd	Gold–Palladium
BCG	Bacille Calmette–Guérin
BBD	Box–Behnken Design
BQ	Bedaquiline
BG	Bioactive Glass
BTE	Bone Tissue Engineering
CD4	Cluster of Differentiation 4
CPPs	Critical Process Parameters
CQAs	Critical Quality Attributes
COVID-19	Coronavirus Disease 2019
CSF	Cerebrospinal Fluid
CT	Computed Tomography
DCM	Dichloromethane
DMSO	Dimethyl Sulfoxide
DL	Drug Loading
DSC	Differential Scanning Calorimetry
DoE	Design of Experiments
ECG	Electrocardiogram
EE	Encapsulation Efficiency

EPTB	Extrapulmonary Tuberculosis
FBS	Foetal Bovine Serum
FTIR	Fourier Transform Infrared Spectroscopy
GIT	Gastrointestinal Tract
HIV	Human Immunodeficiency Virus
HPLC	High-Performance Liquid Chromatography
HR	Isoniazid and Rifampicin
HRZE	Isoniazid, Rifampicin, Pyrazinamide, and Ethambutol
IGRAs	Interferon-Gamma Release Assays
INH	Isoniazid
MDR	Multidrug-Resistant Tuberculosis
MG-63	A human osteosarcoma cell line
Mtb	*Mycobacterium tuberculosis*
MRI	Magnetic Resonance Imaging
MWCO	Molecular Weight Cut-Off
NaAlg	Sodium Alginate
NZW	New Zealand White
o/w	Oil-in-Water
OP	Osteoporosis
PBS	Phosphate Buffered Saline
PCL	Polycaprolactone
PLGA	Poly(lactic-co-glycolic acid)

PDI	Polydispersity Index
PVA	Polyvinyl Alcohol
QbD	Quality by Design
RIF	Rifampicin
RPM	Revolutions Per Minute
RSM	Response Surface Methodology
S.D.	Standard Deviation
SEM	Scanning Electron Microscopy
SM	Streptomycin
TGA	Thermogravimetric Analysis
TSA	Tryptic Soy Agar
TST	Tuberculin Skin Test
TB	Tuberculosis
PTD	Pretomanid
UV	Ultraviolet
XDR	Extensively Drug-Resistant Tuberculosis
XRD	X-ray Diffraction
WHO	World Health Organization

CHAPTER 1

INTRODUCTION

1.1. Background of this study

According to the World Health Organization (WHO), tuberculosis (TB) is one of the leading causes of death globally, with an estimated 1.3 million TB-related deaths in 2023. Approximately 10.8 million people were infected with TB in 2023, including around 600,000 cases among individuals living with the human immunodeficiency virus (HIV) (Goletti et al., 2025; World Health Organization, 2024). The COVID-19 pandemic has further exacerbated the TB crisis by disrupting healthcare services, delaying diagnosis, and interrupting treatment regimens. Lockdowns, resource reallocation, and overwhelmed healthcare systems have led to decreased TB detection rates and increased transmission, contributing to worsened disease progression and higher mortality rates (Cioboata et al., 2023; Khoza et al., 2022; World Health Organization, 2024). TB is a well-known poverty-related disease that is frequently linked to socioeconomic status and is an ancient chronic infectious disease caused by bacillus *Mycobacterium tuberculosis* (Foster et al., 2015; Murdoch et al., 2021). The TB bacteria primarily infect the lungs, with secondary infections being to other parts of the body and this is known as extrapulmonary TB (EPTB) (Lee, 2015). EPTB is more common in HIV-positive patients, particularly those with low CD4 counts. EPTB sites include intestines, skeletal, spine, renal, kidneys, and brain (Kumar et al., 2010). These types of TB appear to be more common in young patients, women, and people of African or Asian ancestry (Forssbohm et al., 2007).

Extrapulmonary tuberculosis (EPTB) accounts for approximately 10–16% of all TB cases, with skeletal TB (STB) comprising around 10% of EPTB cases. Among these, spinal TB is the most prevalent form, representing nearly half of all skeletal EPTB cases (Baykan et al., 2022; Gopalaswamy et al., 2021). Other commonly affected sites include the hip, sacroiliac joints, knees, ribs, shoulders, ankles, elbows, and wrists (El Farhaoui et al., 2023; Leonard and Blumberg, 2017). Additionally, bone TB shows a higher predilection for long bones such as the femur, tibia, and humerus, where the rich vascular supply provides a favorable environment for *Mycobacterium tuberculosis*

bacilli to establish infection (Hopewell and Jasmer, 2004; Leonard and Blumberg, 2017). Tuberculosis osteomyelitis is caused by the reactivation of bacilli that were trapped in bone during the primary infection of *Mycobacterium tuberculosis* in the lungs (Pigrau-Serrallach, 2013).

Diagnosing bone TB is particularly challenging due to its slow progression and nonspecific symptoms, which often mimic other musculoskeletal disorders such as pyogenic osteomyelitis, metastatic bone disease, or inflammatory arthritis (Pigrau-Serrallach, 2013; Ye et al., 2016). Early detection is crucial to prevent severe complications like bone destruction, deformities, and neurological impairment, especially in cases of spinal TB (Garg and Somvanshi, 2011; Pandita et al., 2020). Clinical evaluation plays a key role in identifying patients with persistent bone pain, localized swelling, restricted mobility, weight loss, night sweats, and low-grade fever. In spinal TB, symptoms can progress to neurological deficits due to spinal cord compression, making early intervention essential (Hegde Amogh et al., 2016; Ye et al., 2016). Various imaging techniques assist in diagnosing bone TB. While X-rays are often used as an initial screening tool, they are less effective in detecting early-stage disease, as bone changes may only become visible in later stages. Magnetic Resonance Imaging (MRI) is considered the gold standard for detecting early bone and soft tissue involvement, particularly in spinal TB, while Computed Tomography (CT) scans provide detailed bone structural changes and are useful when MRI is unavailable. Additionally, bone scintigraphy, a nuclear imaging technique, can help identify TB lesions in multiple bone sites, offering a broader assessment of disease spread (Pineda et al., 2009; Rodriguez-Takeuchi et al., 2019). Moreover, laboratory tests like Erythrocyte Sedimentation Rate (ESR) and C-reactive protein (CRP) assist in detecting inflammation but lack TB specificity, while Tuberculin Skin Test (TST) and Interferon-Gamma Release Assays (IGRAs) indicate TB infection without distinguishing between latent and active disease (Lee, 2015; Rafaoui et al., 2023; Ye et al., 2023). More definitive diagnosis relies on molecular and microbiological tests, with Polymerase Chain Reaction (PCR) providing rapid Mycobacterium TB detection and bone biopsy and culture serving as the gold standard despite their long processing time (Lee, 2015; Pandey et al., 2009). Histopathological analysis can further confirm TB by identifying caseating granulomas (Pandey et al., 2009).

The treatment of bone TB follows a long-term multi-drug anti-TB regimen, similar to pulmonary TB but often requiring an extended duration due to the difficulty of drug penetration into bone tissue. The World Health Organization (WHO) recommends a treatment course lasting between 6 to 12 months, divided into two phases. The intensive phase, typically lasting two months, consists of four first-line anti-TB drugs: isoniazid, rifampicin, pyrazinamide, and ethambutol (HRZE). This is followed by a continuation phase of isoniazid and rifampicin (HR) for an additional four to ten months, depending on disease severity and treatment response (Garg and Goyal, 2020; Hegazy et al., 2021; Hua et al., 2022). In cases of severe or bone TB, therapy is often extended to nine months or longer to ensure complete eradication of the infection (Garg and Goyal, 2020; Pei et al., 2018).

Surgical intervention is required in severe cases of bone TB when there is significant bone damage, spinal instability, abscess formation, or neurological deficits. During surgery, the affected bone is removed, resulting in a defect (Mak and Cheung, 2013; Zhang et al., 2015). Autogenous bone grafts are considered the gold standard for bone restoration and regeneration in bone TB, although they come with several challenges (Pei et al., 2018; Tang et al., 2020). To address bone defects, bone tissue engineering (BTE) approaches, including the use of 3D scaffolds, are being explored (Alaribe et al., 2016; Bose et al., 2013). For a 3D scaffold to be suitable for bone regeneration, it must meet key criteria such as biocompatibility, optimal porosity, appropriate degradability, favourable composition, antibacterial properties, and mechanical strength (Alvarez and Nakajima, 2009; Baptista and Guedes, 2021; Jones et al., 2010; Chindamo et al., 2020). In this study, a novel 3D-printed multi-component scaffold is proposed for the targeted treatment of bone tuberculosis. This scaffold is designed for bone tissue engineering, aiming to repair bone defects caused by bone TB while enabling the localized release of anti-TB drugs to minimize the risk of drug resistance.

1.2. Rationale and Motivation for this study

Currently, there is no available product specifically designed to effectively treat bone defects resulting from bone TB in patients who have undergone surgery. Additionally, no localized sustained drug delivery system is currently in use for the treatment of bone TB. This study proposes the development of a novel 3D-printed multi-component

scaffold that aims to address the challenges associated with bone regeneration and the inadequate treatment of bone TB in post-surgical patients. The scaffold will be loaded with bedaquiline (BQ) encapsulated in polylactic-co-glycolic acid (PLGA) nanoparticles, enabling localized and sustained drug release.

BQ was chosen over conventional anti-TB drugs due to its unique mechanism of action, targeting mycobacterial ATP synthase, making it particularly effective against drug-resistant TB and persistent infections. Its strong intracellular penetration enhances efficacy in bone tissue, where conventional drugs have limited reach (De Matteis et al., 2018; Veziris et al., 2017). To further support this, De Vito et al. conducted a study on the impact of BQ on bone infections, demonstrating that treatment led to complete healing without severe adverse effects, reinforcing its potential as a superior therapeutic option for bone TB (De Vito et al., 2022). To optimize delivery, PLGA nanoparticles were selected for their biocompatibility, biodegradability, and ability to provide controlled, sustained drug release, ensuring continuous drug availability at the infection site while minimizing systemic side effects (Budhian et al., 2007; Makadia and Siegel, 2011). Additionally, Response Surface Methodology (RSM) will be employed to optimize the nanoparticle formulation, enhancing key critical parameters such as drug loading, and particle size. By incorporating bedaquiline-loaded PLGA nanoparticles into a 3D-printed scaffold, this approach not only addresses bone regeneration challenges but also provides a localized, sustained drug delivery system, ultimately improving treatment outcomes, reducing drug resistance, and enhancing patient compliance (Hua et al., 2022; Jones et al., 2010).

The use of 3D printing has emerged as a powerful technology in bone tissue engineering, offering precise control over scaffold architecture, porosity, and material composition to enhance bone regeneration (Bose et al., 2013). The ability to fabricate patient-specific scaffolds with tailored mechanical and biological properties makes 3D printing an ideal approach for addressing bone defects caused by surgical resection in bone TB (Zhu et al., 2015). This study integrates a combinatory biomaterial approach, utilizing polycaprolactone (PCL), sodium alginate (NaAlg), bioactive glass (BG), and titanium (Ti) to optimize scaffold performance. PCL, a biodegradable polymer, serves as the structural framework, providing mechanical stability and controlled degradation (Biswas et al., 2020; Gómez-Lizárraga et al., 2017). NaAlg, a naturally derived

biopolymer, enhances cell adhesion, proliferation, and bioactivity, further supporting bone regeneration (Farshidfar et al., 2023). BG has demonstrated excellent biocompatibility with bone tissue, promoting cell adhesion and proliferation, osteo-integration and mineralization, thus stimulating new bone formation at the defect site (Fernandes et al., 2018; Jones et al., 2010). Additionally, Ti is incorporated to improve mechanical strength, reducing the risk of implant failure (Smith et al., 2021; Zhao et al., 2020).

1.3. Aim and Objectives

The aim of this study was to develop a 3D-printed multi-component scaffold incorporating bedaquiline-loaded PLGA nanoparticles for the targeted treatment of bone TB-related defects. The scaffold utilizes a combination of natural, synthetic, metal, and bioactive biomaterials to provide optimal support for bone regeneration. Localized and sustained drug release is achieved through PLGA nanoparticles, reducing systemic side effects and minimizing drug resistance **(Figure 1.1)**. The specific objectives of this research are as follows:

1. Developed and optimized bedaquiline-loaded PLGA nanoparticles using a solvent evaporation method and Box-Behnken design to create a localized and sustained drug release system for targeted treatment of bone TB-related defects.

2. Characterized the physicochemical properties and evaluated the *in-vitro* cytotoxicity of the optimized bedaquiline-loaded PLGA nanoparticles using the MG-63 cell line to assess their potential for bone regeneration and therapeutic efficacy.

3. Integrated natural, synthetic, metal, and bioactive biomaterials into a suitable Ink for a 3D-printed scaffold to support bone regeneration, providing necessary osteo-integration, and mechanical strength.

4. Incorporated the bedaquiline-loaded PLGA nanoparticles into the optimized Ink for a 3D-printed multi-component scaffold for enhanced drug delivery and bone regeneration, ensuring a patient-specific, customizable solution.

5. Undertook physicochemical, physicomechanical, morphological, and thermal characterization studies on both the drug-free and bedaquiline-loaded 3D-printed multi-component scaffold to evaluate their properties for bone regeneration and drug delivery.

6. Conducted an *in vivo* study using New Zealand White (NZW) rabbit models to confirm the bone regeneration and drug delivery capabilities of the drug-free and bedaquiline-loaded 3D-printed multi-component scaffold.

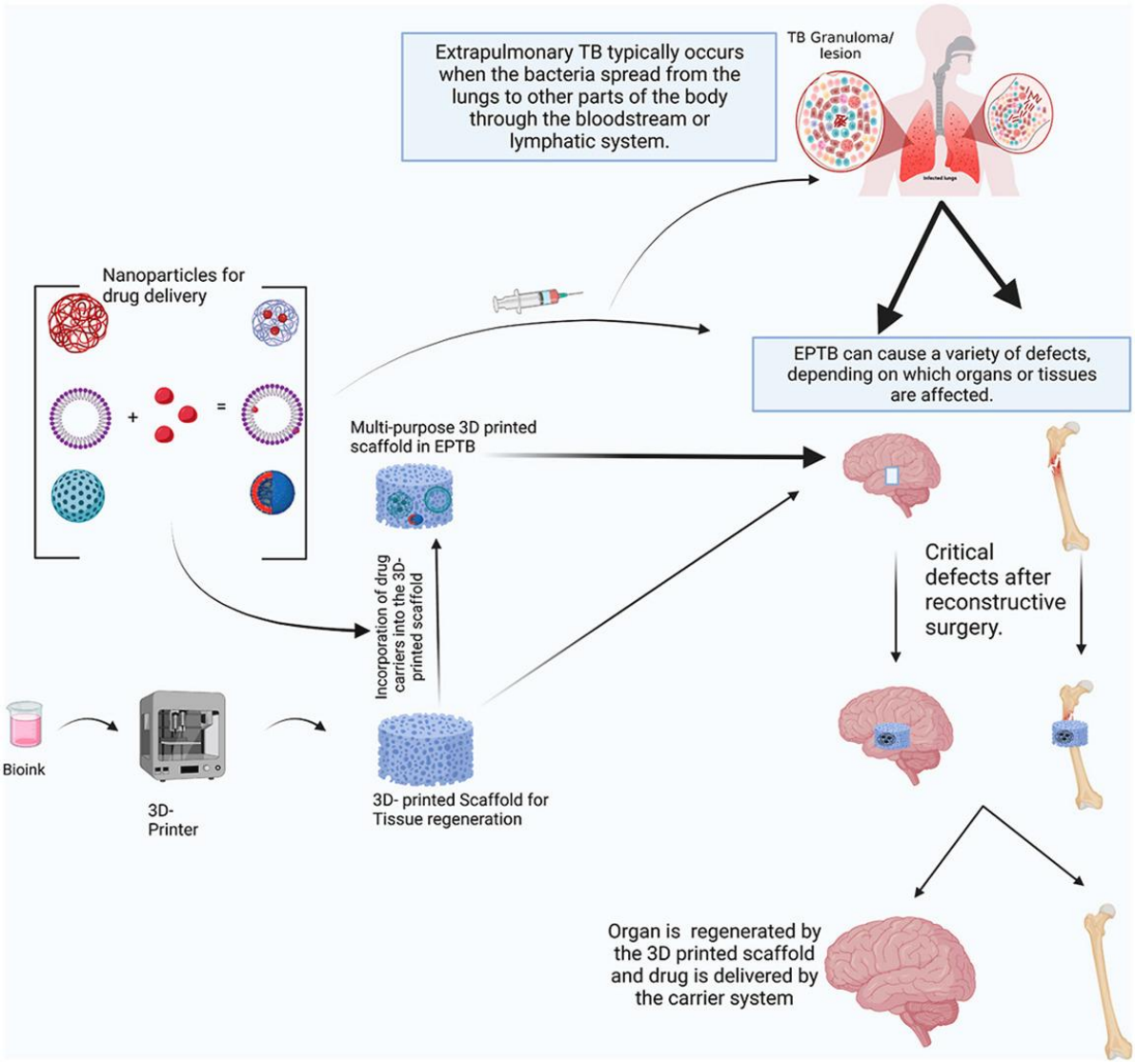


Figure 1.1: A schematic representation of the design and application of the 3D-printed multi-component scaffold incorporating bedaquiline-loaded polylactic-co-glycolic acid nanoparticles.

1.4. Novelty of the Study

1. This study is the first to propose a 3D-printed multi-component scaffold incorporating bedaquiline-loaded PLGA nanoparticles for the targeted treatment of bone TB-related defects, offering a localized and sustained drug release system to enhance therapeutic efficacy while minimizing systemic side effects.

2. The study is the first to establish the application of bedaquiline-loaded PLGA nanoparticles for targeted bone TB treatment, employing Box-Behnken Design (BBD) to optimize the formulation and improve drug loading, particle size, and encapsulation profile.

3. The study has shown that a novel 3D-printed multi-component scaffold incorporating bedaquiline-loaded PLGA nanoparticles enhances the bone regeneration activity and there is adequate release of drug *in vivo*.

1.5. Overview of this Thesis

The thesis is presented as multiple chapters, structured to provide a comprehensive understanding of the design, development, and optimization of a novel 3D-printed multi-component scaffold incorporating bedaquiline-loaded PLGA nanoparticles for targeted bone TB therapy.

Chapter 1 provides an introduction and background of the study, outlining the challenges associated with treating bone TB and the limitations of current treatment methods. It discusses the need for improved drug delivery systems and the potential of 3D-printed scaffolds for localized drug release and bone regeneration. The rationale, motivation, and objectives of the research are also presented in this chapter.

Chapter 2 presents a literature review, focusing on current strategies for treating bone TB, including drug delivery methods and tissue engineering approaches. It explores the potential of 3D printing technology for fabricating scaffolds with tailored properties and the use of nanoparticles for drug delivery. Additionally, the chapter discusses various biomaterials used in scaffold fabrication, with a focus on their roles in bone regeneration and drug release

Chapter 3 describes the synthesis of bedaquiline-loaded PLGA nanoparticles, including the optimization process using Response Surface Methodology (RSM) to ensure controlled and sustained drug release. The characterization of the nanoparticles in terms of physicochemical properties, drug loading efficiency, and *in-vitro* cytotoxicity using MG-63 cell lines is presented. The study also evaluates the nanoparticle's stability and its potential for localized drug delivery in bone TB therapy.

Chapter 4 details the design and development of the novel 3D-printed multi-component scaffold. This section covers the fabrication process, material selection, and integration of Bedaquiline-loaded PLGA nanoparticles into the scaffold. Comprehensive in vitro characterization studies, including physicochemical assessments, mechanical testing, and cell viability/proliferation assays, are presented to validate the scaffold's biocompatibility, osteoconductive, and sustained drug release profile. These findings provide the foundational evidence supporting the scaffold's potential for localized bone TB therapy.

Chapter 5 focuses on the in vivo performance of the optimized scaffold using a rabbit femoral defect model. Detailed surgical protocols, post-operative care, and experimental design are outlined, along with assessments of bone regeneration through histological analysis, micro-CT imaging, and mechanical strength testing. Pharmacokinetic studies further evaluate the sustained release of Bedaquiline and its systemic availability relative to therapeutic thresholds. This chapter demonstrates that the scaffold not only enhances bone repair compared to untreated defects but also achieves effective localized drug delivery, thereby underscoring its potential for clinical translation in the treatment of bone TB.

Chapter 6 summarizes the findings of the study, providing a comprehensive overview of both loaded and unloaded scaffold results. The study demonstrated that the novel multi-component 3D-printed scaffold, developed and characterized in Chapter 5, effectively promotes bone regeneration and supports sustained drug release. In vivo evaluations detailed in Chapter 6 confirmed that both the unloaded and BQ-loaded scaffold versions significantly enhance bone repair in a rabbit femoral defect model compared to untreated controls. These promising results underscore the scaffold's potential as a localized treatment for bone tuberculosis, addressing the challenges of

conventional systemic therapies. Based on these findings, recommendations for future research include further optimization of scaffold composition, extended in vivo studies to assess long-term efficacy and safety, and detailed mechanistic studies to better understand the interplay between scaffold-induced bone regeneration and localized drug delivery. Ultimately, the implications for clinical applications are significant, suggesting that this scaffold could be a transformative approach in the treatment of bone TB, paving the way for its translation into clinical practice with further refinement and validation.

Chapter 7 details my research experience at Novartis Pharma in Switzerland, where I was involved in developing thermosensitive drug delivery polymers for osteoarthritis treatment. I contributed to formulating and testing polymers designed for controlled and localized drug release, ensuring sustained delivery at the site of action. My role included characterizing the polymers' physicochemical properties and assessing their effectiveness *in-vitro*.

1.6. References

Alaribe, F.N., Manoto, S.L., Motaung, S.C.K.M., 2016. Scaffolds from biomaterials: advantages and limitations in bone and tissue engineering. Biologia (Bratisl.) 71, 353–366. https://doi.org/10.1515/biolog-2016-0056

Alvarez, K., Nakajima, H., 2009. Metallic scaffolds for bone regeneration. Materials 2, 790–832. https://doi.org/10.3390/ma2030790

Baptista, R., Guedes, M., 2021. Porosity and pore design influence on fatigue behavior of 3D printed scaffolds for trabecular bone replacement. J. Mech. Behav. Biomed. Mater. 117, 104378. https://doi.org/10.1016/j.jmbbm.2021.104378

Baykan, A.H., Sayiner, H.S., Aydin, E., Koc, M., Inan, I., Erturk, S.M., 2022. Extrapulmonary tuberculosıs: an old but resurgent problem. Insights Imaging 13, 39. https://doi.org/10.1186/s13244-022-01172-0

Biswas, M., Libera, J.A., Darling, S.B., Elam, J.W., 2020. Polycaprolactone: A promising addition to the sequential infiltration synthesis polymer family identified through in situ Infrared spectroscopy. ACS Appl. Polym. Mater. 2, 5501–5510. https://doi.org/10.1021/acsapm.0c00855

Bose, S., Vahabzadeh, S., Bandyopadhyay, A., 2013. Bone tissue engineering using 3D printing. Mater. Today 16, 496–504. https://doi.org/10.1016/j.mattod.2013.11.017

Budhian, A., Siegel, S.J., Winey, K.I., 2007. Haloperidol-loaded PLGA nanoparticles: Systematic study of particle size and drug content. Int. J. Pharm. 336, 367–375. https://doi.org/10.1016/j.ijpharm.2006.11.061

Cioboata, R., Biciusca, V., Olteanu, M., Vasile, C.M., 2023. COVID-19 and tuberculosis: unveiling the dual threat and shared solutions perspective. J. Clin. Med. 12, 4784. https://doi.org/10.3390/jcm12144784

De Matteis, L., Jary, D., Lucía, A., García-Embid, S., Serrano-Sevilla, I., Pérez, D., Ainsa, J.A., Navarro, F.P., M. de la Fuente, J., 2018. New active formulations against M. tuberculosis: Bedaquiline encapsulation in lipid nanoparticles and chitosan nanocapsules. Chem. Eng. J., Smart nanomaterials and nanostructures for diagnostic and therapy 340, 181–191. https://doi.org/10.1016/j.cej.2017.12.110

De Vito, A., Fiore, V., Urru, V., Bozzi, E., Geremia, N., Princic, E., Canu, D., Molicotti, P., Are, R., Babudieri, S., Madeddu, G., 2022. Use of bedaquiline in spinal osteomyelitis and soft tissue abscess caused by multidrug-resistant *Mycobacterium tuberculosis*: A case report. Braz. J. Infect. Dis. 26, 102701. https://doi.org/10.1016/j.bjid.2022.102701

El Farhaoui, A., Batou, Y., Benalia, K., Lachkar, A., abdeljaouad, N., Yacoubi, H., 2023. Tuberculosis of navicular bone: An exceptional localization of

osteoarticular tuberculosis. Radiol. Case Rep. 18, 1989–1992. https://doi.org/10.1016/j.radcr.2023.01.061

Farshidfar, N., Iravani, S., Varma, R.S., 2023. Alginate-based biomaterials in tissue engineering and regenerative medicine. Mar. Drugs 21, 189. https://doi.org/10.3390/md21030189

Fernandes, H.R., Gaddam, A., Rebelo, A., Brazete, D., Stan, G.E., Ferreira, J.M.F., 2018. Bioactive glasses and glass-ceramics for healthcare applications in bone regeneration and tissue engineering. Materials 11, 2530. https://doi.org/10.3390/ma11122530

Forssbohm, M., Zwahlen, M., Loddenkemper, R., Rieder, H.L., 2007. Demographic characteristics of patients with extrapulmonary tuberculosis in Germany. Eur. Respir. J. 31, 99–105. https://doi.org/10.1183/09031936.00020607

Foster, N., Vassall, A., Cleary, S., Cunnama, L., Churchyard, G., Sinanovic, E., 2015. The economic burden of TB diagnosis and treatment in South Africa. Soc. Sci. Med. 130, 42–50. https://doi.org/10.1016/j.socscimed.2015.01.046

Garg, D., Goyal, V., 2020. Spinal tuberculosis treatment: an enduring bone of contention. Ann. Indian Acad. Neurol. 23, 441–448. https://doi.org/10.4103/aian.AIAN_141_20

Garg, R.K., Somvanshi, D.S., 2011. Spinal tuberculosis: A review. J. Spinal Cord Med. 34, 440–454. https://doi.org/10.1179/2045772311Y.0000000023

Goletti, D., Meintjes, G., Andrade, B.B., Zumla, A., Lee, S.S., 2025. Insights from the 2024 WHO Global Tuberculosis Report – more comprehensive action, Innovation, and Investments required for achieving WHO End TB goals. Int. J. Infect. Dis. 150. https://doi.org/10.1016/j.ijid.2024.107325

Gómez-Lizárraga, K.K., Flores-Morales, C., Del Prado-Audelo, M.L., Álvarez-Pérez, M.A., Piña-Barba, M.C., Escobedo, C., 2017. Polycaprolactone- and polycaprolactone/ceramic-based 3D-bioplotted porous scaffolds for bone regeneration: A comparative study. Mater. Sci. Eng. C 79, 326–335. https://doi.org/10.1016/j.msec.2017.05.003

Gopalaswamy, R., Dusthackeer, V.N.A., Kannayan, S., Subbian, S., 2021. Extrapulmonary tuberculosis—an update on the diagnosis, treatment and drug resistance. J. Respir. 1, 141–164. https://doi.org/10.3390/jor1020015

Hegazy, W.A.H., Mamari, R.A., Almazroui, K., Habsi, A.A., Kamona, A., AlHarthi, H., Lawati, A.I.A., AlHusaini, A.H., 2021. Retrospective study of bone-TB in Oman: 2002–2019. J. Epidemiol. Glob. Health 11, 238–245. https://doi.org/10.2991/jegh.k.210420.002

Hegde Amogh, Jankharia Bhavin, Jankharia Bhavin, 2016. TB of the radial neck: A typical presentation in an atypical location. Pediatr. Infect. Dis. 8, 100–101. https://doi.org/10.1016/j.pid.2016.07.008

Hopewell, P.C., Jasmer, R.M., 2004. Overview of clinical tuberculosis, in: tuberculosis and the tubercle bacillus. John Wiley & Sons, Ltd, pp. 13–31. https://doi.org/10.1128/9781555817657.ch2

Hua, L., Qian, H., Lei, T., zhang, yu, Lei, P., Hu, Y., 2022. 3D-Printed porous tantalum coated with antitubercular drugs achieving antibacterial properties and good biocompatibility. Macromol.biosci 22. https://doi.org/10.1002/mabi.202100338

Jones, J.R., Lin, S., Yue, S., Lee, P.D., Hanna, J.V., Smith, M.E., Newport, R.J., 2010. Bioactive glass scaffolds for bone regeneration and their hierarchical characterisation. Proc. Inst. Mech. Eng. [H] 224, 1373–1387. https://doi.org/10.1243/09544119JEIM836

Khoza, L.J., Kumar, P., Dube, A., Demana, P.H., Choonara, Y.E., 2022. Insights into innovative therapeutics for drug-resistant tuberculosis: Host-directed therapy and autophagy inducing modified nanoparticles. Int. J. Pharm. 622, 121893. https://doi.org/10.1016/j.ijpharm.2022.121893

Kumar, S.V., Deka, M.K., Bagga, M., Kala, M.S., Gauthaman, K., 2010. A systematic review of different type of tuberculosis. Eur. Rev. Med. Pharmacol. Sci. 14, 831–843.

Lee, J.Y., 2015. Diagnosis and Treatment of Extrapulmonary Tuberculosis. Tuberc. Respir. Dis. 78, 47–55. https://doi.org/10.4046/trd.2015.78.2.47

Leonard, M., Blumberg, H., 2017. Musculoskeletal Tuberculosis. Microbiol. Spectr. 5, 5.2.28. https://doi.org/10.1128/microbiolspec.TNMI7-0046-2017

Mak, K.C., Cheung, K.M.C., 2013. Surgical treatment of acute TB spondylitis: indications and outcomes. Eur. Spine J. 22, 603–611. https://doi.org/10.1007/s00586-012-2455-0

Makadia, H.K., Siegel, S.J., 2011. Poly Lactic-co-Glycolic Acid (PLGA) as Biodegradable Controlled Drug Delivery Carrier. Polymers 3, 1377–1397. https://doi.org/10.3390/polym3031377

Murdoch, J., Curran, R., van Rensburg, A.J., Awotiwon, A., Dube, A., Bachmann, M., Petersen, I., Fairall, L., 2021. Identifying contextual determinants of problems in tuberculosis care provision in South Africa: a theory-generating case study. Infect. Dis. Poverty 10, 67. https://doi.org/10.1186/s40249-021-00840-5

Pandey, V., Chawla, K., Acharya, K., Rao, Sripathi, Rao, Sugandhi, 2009. The role of polymerase chain reaction in the management of osteoarticular tuberculosis. Int. Orthop. 33, 801–805. https://doi.org/10.1007/s00264-007-0485-8

Pandita, A., Madhuripan, N., Pandita, S., Hurtado, R.M., 2020. Challenges and controversies in the treatment of spinal tuberculosis. J. Clin. Tuberc. Mycobact. Dis. 19, 100151. https://doi.org/10.1016/j.jctube.2020.100151

Pei, P., Tian, Z., Zhu, Y., 2018. 3D printed mesoporous bioactive glass/metal-organic framework scaffolds with antitubercular drug delivery. Microporous Mesoporous Mater. 272, 24–30. https://doi.org/10.1016/j.micromeso.2018.06.012

Pigrau-Serrallach, C., 2013. Bone and joint tuberculosis. Eur. Spine J. 22, 556–566. https://doi.org/10.1007/s00586-012-2331-y

Pineda, C., Espinosa, R., Pena, A., 2009. Radiographic Imaging in Osteomyelitis: The Role of Plain Radiography, Computed Tomography, Ultrasonography, Magnetic Resonance Imaging, and Scintigraphy. Semin. Plast. Surg. 23, 80–89. https://doi.org/10.1055/s-0029-1214160

Rafaoui, A., Lamris, M.A., El Kassimi, C., Fnini, S., Rafai, M., 2023. Diagnosis and treatment of osteo-articular tuberculosis of the foot and ankle (a five-case series). Int. J. Surg. Case Rep. 111, 108739. https://doi.org/10.1016/j.ijscr.2023.108739

Rodriguez-Takeuchi, S.Y., Renjifo, M.E., Medina, F.J., 2019. Extrapulmonary Tuberculosis: Pathophysiology and Imaging Findings. RadioGraphics 39, 2023–2037. https://doi.org/10.1148/rg.2019190109

Smith, S., ElKashty, O., Tamimi, F., Tran, S.D., Cerruti, M., 2021. Titanium-Containing Silicate-Based Sol–Gel Bioactive Glass: Development, Characterization, and Applications. Langmuir 37, 14243–14253. https://doi.org/10.1021/acs.langmuir.1c01593

Tang, K., Li, J., Huang, T., Zhong, W., Luo, X., Quan, Z., 2020. Clinical efficacy of three types of autogenous bone grafts in treatment of single-segment thoracic tuberculosis: A retrospective cohort study. Int. J. Med. Sci. 17, 2844–2849. https://doi.org/10.7150/ijms.47309

Veziris, N., Bernard, C., Guglielmetti, L., Du, D.L., Marigot-Outtandy, D., Jaspard, M., Caumes, E., Lerat, I., Rioux, C., Yazdanpanah, Y., Tiotiu, A., Lemaitre, N., Brossier, F., Jarlier, V., Robert, J., Sougakoff, W., Aubry, A., 2017. Rapid emergence of *Mycobacterium tuberculosis* bedaquiline resistance: lessons to avoid repeating past errors. Eur. Respir. J. 49. https://doi.org/10.1183/13993003.01719-2016

World Health Organization, 2024. Global tuberculosis report 2024. Geneva.

Ye, M., Huang, J., Wang, J., Ren, J., Tu, J., You, W., Zhu, T., 2016. Multifocal musculoskeletal tuberculosis mimicking multiple bone metastases: a case report. BMC Infect. Dis. 16, 34. https://doi.org/10.1186/s12879-016-1376-7

Ye, Z., Zhu, J., Liu, C., Lu, Q., Wu, S., Zhou, C., Liang, T., Jiang, J., Li, H., Chen, T., Chen, J., Deng, G., Yao, Y., Liao, S., Yu, C., Sun, X., Chen, L., Guo, H., Chen, W., Jiang, W., Fan, B., Tao, X., Yang, Z., Gu, W., Wang, Y., Zhan, X., 2023. Difference between the blood samples of patients with bone and joint

tuberculosis and patients with tuberculosis studied using machine learning. Front. Surg. 9, 1031105. https://doi.org/10.3389/fsurg.2022.1031105

Zhang, H., Zeng, K., Yin, X., Huang, J., Tang, M., Guo, C., 2015. Debridement, internal fixation, and reconstruction using titanium mesh for the surgical treatment of thoracic and lumbar spinal tuberculosis via a posterior-only approach: a 4-year follow-up of 28 patients. J. Orthop. Surg. 10, 150. https://doi.org/10.1186/s13018-015-0292-7

Zhao, P., Liu, Y., Li, T., Zhou, Y., Leeflang, S., Chen, L., Wu, C., Zhou, J., Huan, Z., 2020. 3D printed titanium scaffolds with ordered TiO2 nanotubular surface and mesoporous bioactive glass for bone repair. Prog. Nat. Sci. Mater. Int. 30, 502–509. https://doi.org/10.1016/j.pnsc.2020.08.009

Zhu, M., Li, K., Zhu, Y., Zhang, J., Ye, X., 2015. 3D-printed hierarchical scaffold for localized isoniazid/rifampin drug delivery and osteoarticular tuberculosis therapy. Acta Biomater. 16, 145–155. https://doi.org/10.1016/j.actbio.2015.01.034

CHAPTER 2

MULTI-PURPOSE PROTOTYPES FOR EXTRAPULMONARY *MYCOBACTERIUM TUBERCULOSIS* TARGETING: A REGENERATIVE MEDICINE PERSPECTIVE

(PUBLISHED 2023)

Published in Journal of Drug Delivery Science and Technology
Mphaphuli, M.T., Sithole, M.N., Kumar, P., Kondiah, P.P., Mabrouk, M. and Choonara, Y.E., 2023. Multi-purpose prototypes for extrapulmonary *Mycobacterium tuberculosis* targeting: A regenerative medicine perspective. Journal of Drug Delivery Science and Technology, 89, p.105039.

2.1. Introduction

Tuberculosis (TB) is an ancient infectious disease caused by bacterium called *Mycobacterium tuberculosis (Mycobacterium tuberculosis*), which is an intracellular acid-fast bacillus that has developed mechanisms to circumvent macrophages (Grotz et al., 2018; Smith, 2003). This bacterium is an actinomycetales bacteria of the *Mycobacteriacea* family and *Mycobacterium* genus (Gagneux, 2018; Smith, 2003). Humans are the primary host of *Mycobacterium tuberculosis,* and TB is primarily a human disease. Generally, the *Mycobacterium tuberculosis* bacterium that targets the lungs becomes airborne *Mycobacterium tuberculosis* bacteria. These airborne particles are infectious droplet nuclei ranging from 1 to 5 μm in diameter (Khoza et al., 2022; Sia and Rengarajan, 2019; Smith, 2003). It has been reported in the literature that the latent tuberculosis infection (LTBI), which is a condition caused by the bacterium *Mycobacterium tuberculosis,* has infected approximately one-third of the world population. The LTBI does not show any immediate symptoms, and it does not spread to others (Houben and Dodd, 2016). Although the LTBI is dormant in a person, however, the bacteria remain alive in the body and can reactivate at a later stage, leading to active tuberculosis if left untreated. Reactivation occurs in the context of an impaired immune system. Therefore, patients with poor immunity or diseases that impair immunity, such as an HIV-infected person or a person with type 2 diabetes (T2DM), are more prone to active TB infection (Gagneux, 2018; Lee, 2016; Smith, 2003).

Consequently, the World Health Organization (WHO) predicted that more than 2 million people would die from TB-related causes globally in 2020, making TB one of the most common causes of death globally, and the second most lethal infectious disease after COVID-19 (Bhargava and Shewade, 2020; Tadolini et al., 2020). The emergence of COVID-19 has affected various sectors of the economy worldwide, especially the

health sector. Migliori et al. (2021) conducted an investigational study to evaluate the effect of the COVID-19 pandemic on TB and established that years of progress in providing critical TB services and reducing the TB disease burden had been halted by the COVID-19 pandemic (Migliori et al., 2021; World Health Organization, 2021a). According to the global tuberculosis report published by WHO, TB affects both developed and developing countries; however, it is more prevalent in developing countries since approximately 58% of new TB cases worldwide can be accounted for by the following countries: India, China, Indonesia, the Philippines, Pakistan, Nigeria, Bangladesh, and South Africa (World Health Organization, 2021b).

The bacterium primarily infects the lungs (pulmonary TB), with secondary infections occurring in other parts of the body, and this is known as extrapulmonary TB (EPTB) (Khoza et al., 2022; Kumar et al., 2010). EPTB is estimated to account for 15–25% of all TB cases and is more common in children than adults and HIV-positive patients, particularly those with low CD4 counts (Haulman et al., 2008; Kaba et al., 2019; Pang et al., 2019; Shafer et al., 1991; Sharma et al., 2021). According to researchers, EPTB can stem from either the initial point of infection or a secondary location that may happen due to the spread of bacteria through the bloodstream or lymphatic system, activation of latent tuberculosis (LTB), consumption of contaminated sputum, or the local spread from neighbouring organs (Gopalaswamy et al., 2021). Henceforth, for people with HIV, the risk of developing EPTB is more than 50% (Hegazy et al., 2021). Nearly any body organ can develop EPTB, but commonly infected organs include the urogenital tract, meninges, lymph nodes, pleura, gastrointestinal system, central nervous system (CNS), and bone**s** (Baykan et al., 2022; Gopalaswamy et al., 2021).

EPTB is more challenging to diagnose than pulmonary TB and obtaining tissue or fluid samples necessitates invasive procedures. EPTB is found in hard-to-reach areas of the body, like the liver, which is in the middle of the abdomen and cannot be easily touched or examined. The symptoms and indicators are usually particular to the affected organ system (Lee, 2015; Purohit and Mustafa, 2015). Furthermore, clinical manifestations are frequently nonspecific and subtle, and diagnosis can take years (Lee, 2015). A diagnostic test for EPTB should ideally be precise, rapid, simple to implement, reliable, and cost-effective (Gopalaswamy et al., 2021; Purohit and Mustafa, 2015).

The treatment protocol for EPTB involves medical chemotherapy (drugs) and surgical intervention where necessary (Yang and Liu, 2013). The chemotherapy used for EPTB are the same as for PTB, and the treatment regimen is differentiated into two phases: the intensive phase, and the continuation phase. The intensive phase consists of the following drugs: Isoniazid (INH), Rifampicin (RIF), Pyrazinamide (PZA), Streptomycin (SM), and Ethambutol (EMB) (Baykan et al., 2022; Hegazy et al., 2021; Lee, 2015), while the continuation phase consist of RIF and INH (Chakaya et al., 2021; Lee, 2015). The intensive phase reduces bacillary load by killing approximately 95% of microorganisms, whereas the continuation phase focuses on eliminating semi-dormant organisms and preventing the development of drug resistance (Chakaya et al., 2021; Chou Tseng, 2014). The difference between PTB and EPTB treatment is on the duration of treatment; henceforth, the proposed treatment regimen for EPTB is as follows: six- to nine-month regimen (two months of INH, RIF, PZA, and EMB, followed by four to seven months of INH and RIF) is advised as initial therapy for all forms of EPTB (Chou Tseng, 2014; Gopalaswamy et al., 2021; Purohit and Mustafa, 2015). Different health organizations in different countries suggested that patients with CNS-TB, including meningitis, get treatment for at least nine to twelve months (Chen et al., 2020). Patients with bone TB that manifest delayed therapeutic response or antibiotic resistance may also require extended therapy. Furthermore, adjunctive corticosteroids may be beneficial for patients with TB meningitis or TB pericarditis (Chen et al., 2020; Isiguzo et al., 2020). The mechanism of action of these drugs against *Mycobacterium tuberculosis,* targets different sites of the bacteria, and **Figure. 2.1** illustrates what the drugs targets in the *Mycobacterium tuberculosis* bacterium structure (Jain et al., 2018; Palomino and Martin, 2014).

The long duration treatment in EPTB had a devastating impact on treatment outcomes, since the drugs do not last long enough to have the desired effect against *Mycobacterium tuberculosis*, and they can also cause severe toxic effects (Gopalaswamy et al., 2021; Hegazy et al., 2021; Jain et al., 2018). Hence long duration treatment in EPTB can lead to low patient adherence, leading to patients developing multidrug-resistant TB (MDR TB) (resistance to the chemotherapeutic drugs INH and RIF). At the same time, extensively drug-resistant TB (XDR TB), defined as MDR with additional resistance to any fluoroquinolone and second-line injectable drug, may also be developed (Alam et al., 2015; Seung et al., 2015). Although researchers are developing new drugs to aid in the treatment of *Mycobacterium tuberculosis* bacterium,

such as bedaquilline (BDQ), delamanid and pretomanid. However, developing new drugs is a process that often takes a long duration to be approved or to get into the market (D'Ambrosio et al., 2015; De Matteis et al., 2018).

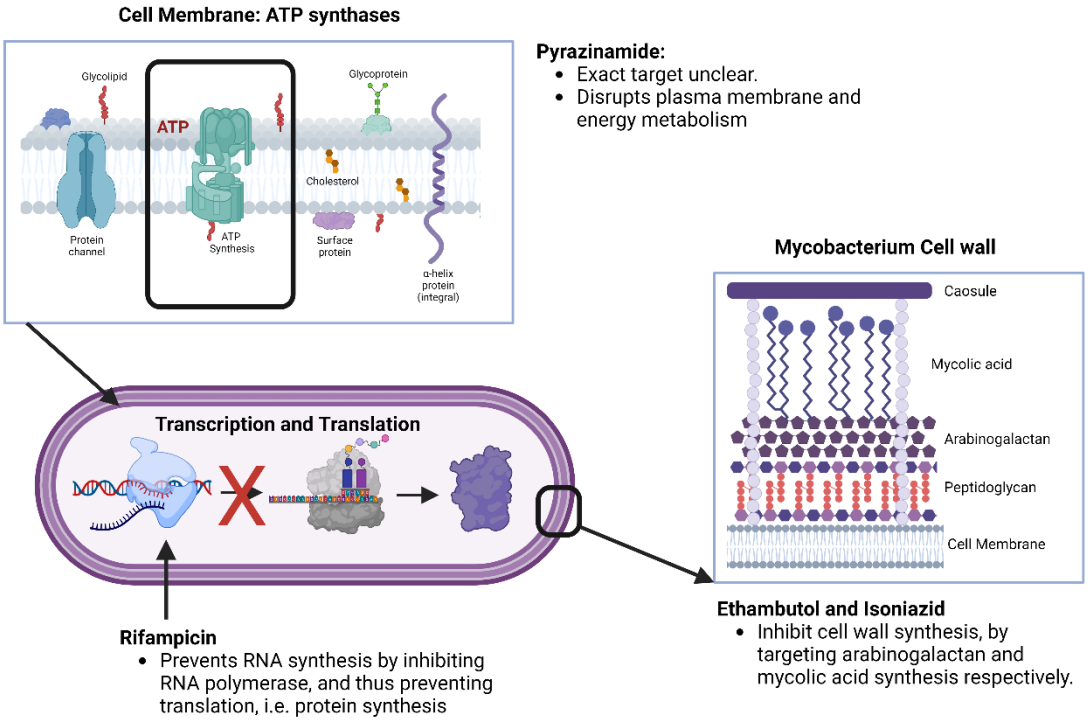


Figure 2.1: illustrates the different targets for each drug on the M. tuberculosis (Mtb) structure.

Current research in many disciplines focused on the development of innovative solutions that address the constraints and difficulties faced by drug-resistant tuberculosis, including drug target treatment, which incorporates host-directed therapy (HDT) (Khoza et al., 2022). HDT refers to the use of small molecules or biologics that (a) interfere with host pathways manipulated by the pathogen to persist or replicate in host tissues; (b) boost the host immune defense against the pathogen; (c) target pathways that may contribute to disease or immunopathology, as classically emphasized by hyper-inflammation; and (d) modulate host factors at the local level that a pathogen uses to cause disease (Kaufmann et al., 2018; Kolloli and Subbian, 2017). HDTs aimed at assisting the host immune system in controlling bacterial multiplication and tissue damage (Kaufmann et al., 2018). The use of HDT compounds in combination with traditional therapy for the treatment of *Mycobacterium tuberculosis* infections has been extensively reported, and these compounds target host pathways that include autophagy, cholesterol, eicosanoids, and granuloma (Kolloli and Subbian,

2017). However, a limitation of HDT compounds is that the compounds are mostly repurposed drugs such as aspirin, statins, vitamin D3, and metformin (Khoza et al., 2022). The drugs already have a presence in the drug market and have their side effect profile. In addition, they are not selective to a specific pathway, however, may act systematically in the body (Ahmed et al., 2020). Another current approach in reducing resistance and side effects associated with traditional drugs is the use of nanotechnology to encapsulate the drugs for the improvement of their therapeutical outcome. The development of nanocarriers has been established to have targeted drug release, which may be advantageous because they can achieve high drug concentration at the targeted sites while having low drug concentration throughout the body, reducing resistance and toxic side effects dramatically (Baranyai et al., 2021; Grotz et al., 2018).

Patients may urgently require surgery in some EPTB sites, such as bone TB, gastrointestinal TB, CNS TB, and female genital TB when complications arise. This includes failure to respond to current treatment and delayed diagnosis (Alam et al., 2015; Al-Zanbagi and Shariff, 2021; Rock et al., 2008). After lesion debridement, autogenous bone grafts and biomaterials such as titanium mesh cages, steel, and carbon fiber are the gold standards for bone restoration and regeneration in bone TB (Hegazy et al., 2021; Pigrau-Serrallach and Rodríguez-Pardo, 2013; Rajasekaran et al., 2014). The primary use of titanium mesh in bone TB surgery has resulted in successful bony defect restoration and treatment of kyphosis abnormalities (Yin et al., 2017; Zeng et al., 2020; Zhang et al., 2015). However, the gold standards are associated with a slew of drawbacks, that include restricted donor sites and potential harvesting morbidity for autogenous bone grafts (Jensen et al., 2016; Suleman et al., 2021). Furthermore, the host organism can easily absorb a small amount of autogenous bone. In addition, the commonly used biomaterials have been established to lack osteoconductive and osteoinductive properties (Dong et al., 2014; Tang et al., 2020a). Henceforth, there is a need for the development of an alternative system, that can address the above shortfalls.

Alternatively, the use of bone tissue engineering (BTE) to overcome bone defects is being employed, and the development of an implantable scaffold to initiate bone regeneration for bone TB is of great need according to orthopedic experts, as the platform will be able to ensure bone regeneration (Zhu et al., 2015). Advances in BTE have resulted in the use of 3D printing technologies to improve the prospects of

significant bone deformities (Haleem et al., 2020). 3D printing techniques uses the existing biodegradable biomaterials to construct new scaffolds with improved mechanical characteristics for load-bearing applications (Arefin et al., 2021; Haleem et al., 2020; Nikolova and Chavali, 2019). 3D printing technologies provides mold-free manufacture of patient-specific bone replacements with complex topologies directly from biomaterials and accurate macro- and micro-scale structure designs that give optimum *in vivo* responses, such as increased bone regeneration (Gu et al., 2020).

This review explores the use of different technologies, such as nanotechnology and 3D-printing amongst others, to address targeted therapy against *Mycobacterium tuberculosis* in the context of drug delivery. Furthermore, in the case of bone TB, where surgery is required, this review will also address the potential use of a multi-purpose targeted therapy platform such as combined/merged effort of 3D-printed biomaterial scaffolds and nanotechnology systems loaded with anti-TB drugs. Likewise, to substantiate the use of these platforms, the influence of physiological changes on these platforms for targeted therapy and tissue regeneration.

2.2. *Mycobacterium tuberculosis* journey from pulmonary TB to extrapulmonary TB

The characteristics of different organ sites affected by extrapulmonary tuberculosis (EPTB) are summarized in **Table 2.1.** However, **Figure. 2.2**, represents the general infection pathway of TB to an individual, where the *Mycobacterium tuberculosis* bacteria travel to the lungs through air droplets, and the droplets emanate from an individual with PTB. The droplets must implant in the lung's alveoli before being ingested by nonimmune alveolar macrophages to cause infection. Furthermore, bacteria that survive the initial attack multiply within the macrophage. The proliferation of bacteria results in the death of macrophages and the release of chemokines that draw in other immune cells such as macrophages, natural killer cells, and T lymphocytes. The bacterium then spreads locally before being transported via the lymphatic system to the hilar lymph nodes and disseminating throughout the body, leading to multiple sites infection. Although high-oxygen-saturated areas such as the top of the lungs, kidneys, bones, and brain are more susceptible, however any tissue or organ can be affected (Baykan et al., 2022; Houston and Macallan, 2014; Lee, 2015, 2016; Sharma et al., 2021).

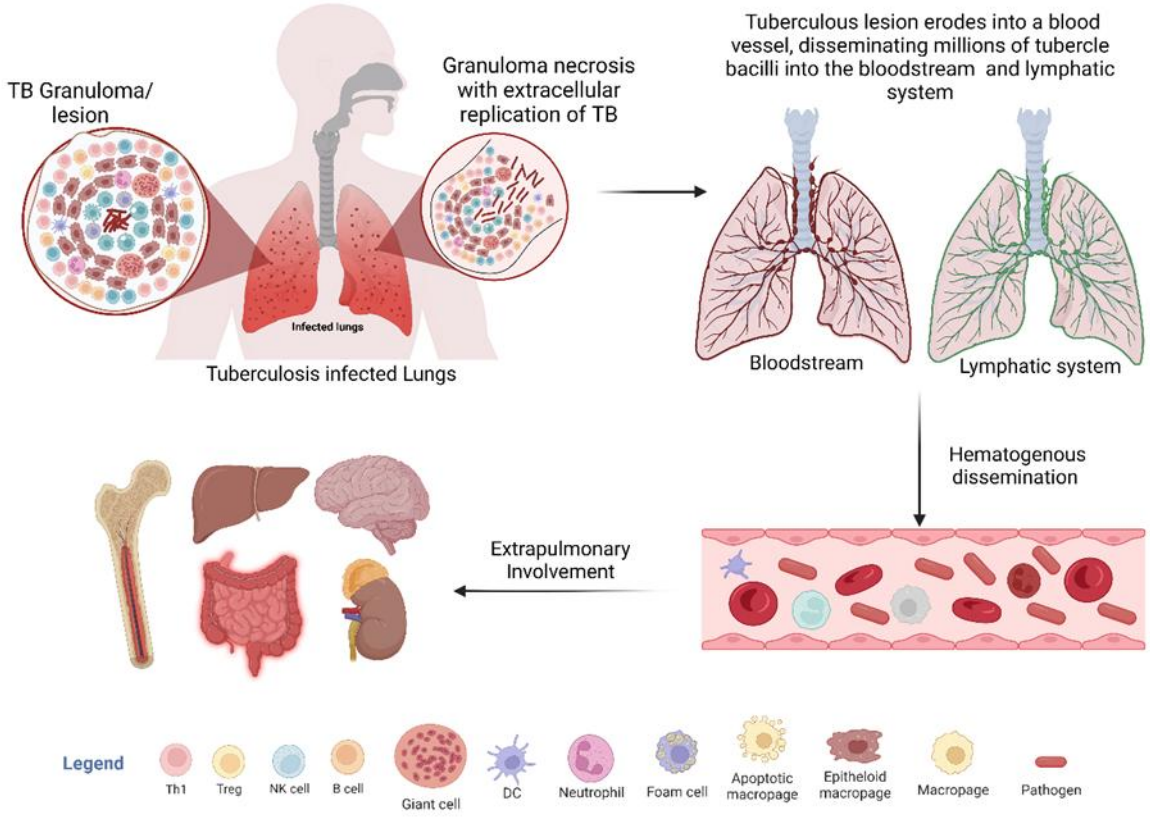


Figure 2.2: Pathway mechanism from Pulmonary TB to EPTB.

Table 2.1: Different EPTB organ sites and their characteristics.

Most common EPTB infection organs	Pathophysiology	Diagnostic Test	Prevalence of specific EPTB	Common clinical manifestation	References
Spine	Inflammation of the spinal cord and nerve roots results from a massive granulomatous exudate that fills the subarachnoid space. Exudate causes adhesions and fibrosis in chronic situations. Vasculitis can also damage the spine, resulting in isolated segmental infarcts and edema of the spinal cord.	Positive skin test, Biopsy, PCR, Computed tomography (CT), magnetic resonance imaging (MRI)	40-50%	Back pain, spinal tenderness, paraplegia, and spinal deformities	(Garg and Somvanshi, 2011; Hegazy et al., 2021; Rajasekaran et al., 2018; Rodriguez-Takeuchi et al., 2019)
Central nervous system (CNS)	CNS TB is initiated by small tuberculous foci in the brain, spinal cord, or meninges. The location and control of these foci determine the type of CNS TB. Tuberculous meningitis is the most common type, while tubercular encephalitis, tuberculoma, and brain abscess are less common.	Cerebrospinal Fluid Examination (CSF), Smear Examination and Culture, Adenosine Deaminase, PCR, GeneXpert MTB/RIF Ultra, enzyme-linked immunospot (ELISPOT), QuantiFERON Gold, proteomics	5-10 %	Fever, headache, and meningismus with focal neurological deficits, behavioral changes, and alterations in consciousness	(Rock et al., 2008; Sharma et al., 2021)
Genitourinary	Bacteria disseminate through the blood to the kidneys, settling in periglomerular capillaries and forming latent granulomas.	acid-fast bacilli (AFB), Nucleic Acid Amplification Tests, Whole-Genome Sequencing (WGS), CT, MRI, ultrasonography (US), Plain abdomen, chest X-rays, and Hysterosalpingography (HSG)	5.3%	dysuria, haematuria, abdominal or flank pain Fever, weight loss, and night sweats	(Horne and Misch, 2017; Jones-Lopez and Ellner, 2011; Mantica et al., 2021)

PERICARDITIS	Retrograde lymphatic spread from peritracheal, peribronchial, or mediastinal lymph nodes or hematogenous dissemination from original TB may cause pericardial involvement.	ECG, CT, MRI,	1%	chest pain, dyspnea, and ankle edema. Cardiomegaly, tachycardia, fever, pericardial rub, pulsus paradoxus, or distended neck veins	(Isiguzo et al., 2020; Mayosi et al., 2005)
Gastrointestinal (GIT)	Infection to this site can occur in different ways: 1) Hematogenous spread from a distant focus; 2) Spread of lymph through diseased node; 3) Extension directly from a nearby site.	CT, US, Colonoscopy, and AFB smear	13%	abdominal pain, weight loss, anemia, and fever with night sweats	(Al-Zanbagi and Shariff, 2021; “Gastrointestinal Tuberculosis Imaging,” 2019)
Knee & hip	Joint tuberculosis commonly results from osteomyelitis or hematogenous dissemination. The bacteria cause synovial inflammation, leading to bone erosion.	CT, MRI, AFB smear, Tuberculin Skin Test, Synovial Fluid Examination, Interferon Gamma Release Assays (IGRAs), PCR	10-11%	Local pain, swelling, immobility, painless. cold abscess, fever, weight loss, and night sweat	(Chou Tseng, 2014; Malaviya and Kotwal, 2003; Pigrau-Serrallach and Rodríguez-Pardo, 2013)

2.3. Influence of affected tissue micro-environment on the performance of drug delivery system

The survival of the *Mycobacterium tuberculosis* in the human host has been well-researched over the years (Cook et al., 2009; Ehrt and Schnappinger, 2009; Meena and Rajni, 2010; Schaible et al., n.d.; Sia and Rengarajan, 2019; Sundaramurthy et al., 2017; Warner and Mizrahi, 2007). The adaptation of this bacterium involves a plethora of mechanisms, such as (a) the maturation of the macrophage phagosomal system, (b) granuloma and caseation adaptation, (c) preventing of phagosomal acidification, (d) induction of phagosome- lysosome fusion, and (e) resistance to acidic stress and reaction to oxidative stress (Devarajan et al., 2015; Ehrt and Schnappinger, 2009; Garg et al., 2009; Schaible et al., n.d.). The current first and second-line therapeutics against *Mycobacterium tuberculosis* can only be effective if we understand how the bacterium changes the microenvironment of the affected tissues and evades the immune system, thus remaining dormant for long periods (Cook et al., 2009; Tanner et al., 2018). These factors often result in decreased drug absorption and the accumulation of mutations within the bacteria that contribute to the formation of drug-resistant strains. As previously stated, *Mycobacterium tuberculosis* initially targets the lungs due to the high oxygen content. In addition to the increased oxygen content, the mucosa in the respiratory tract has a temperature range of 30°C to 36.6°C, which is close to body temperature and has a pH between 3.5 & 5.5 which provides optimal growth conditions for *Mycobacterium tuberculosis* (Doig et al., 2002; Piddington et al., 2000; Wadowsky et al., 1985). The pH of the lung alveoli microenvironment is relatively higher than that of the upper respiratory tract, which further contributes towards ideal conditions for *Mycobacterium tuberculosis* growth (Maphasa et al., 2021).

In the case of EPTB, depending on the microenvironment, the oxygen level is typically low, the pH is usually acidic, and the temperature corresponds to the body temperature (Smith, 2003). This leads to minimal bacterium growth, hence the low percentage rates of cases of EPTB compared to the pulmonary TB. However, a question may arise as to how these tissues get infected if their microenvironment is not suitable for the optimal growth of the bacterium. For example, in the case of bone TB, the bacterium's preference is the spine and large joints, which can be explained by the rich vascular supply of the vertebrae and long bone growth plates (Rajasekaran et al., 2014; Rodriguez-Takeuchi et al., 2019). In the case of other extremities, such as the brain, the dependent factor is the blood-brain barrier (BBB) which, like in bone TB, is highly

vascularized, allowing the bacterium to migrate through the BBB (Beres and Meltzer, 1938; Davis et al., 2019; Manyelo et al., 2021).

The presence of *Mycobacterium tuberculosis* into a particular tissue/organ result in changes in the physiological microenvironment of that tissue/organ, and this may affect the physicochemical properties of the used drug(s), leading to unsatisfactory absorption, release, distribution of the drug(s) and platform degradation (Smith, 2003; Tanner et al., 2018; Wang et al., 2017). Therefore, the physicochemical properties of anti-TB drugs can be affected by the TB microenvironment, such as pH variations, granuloma formation, caseum presence, drug metabolism by *Mycobacterium tuberculosis*, cellular uptake, and protein binding. Hence, the understanding of these influences is critical for the optimization of drug design/delivery and the improvement of treatment outcomes in TB patients (Fullam and J. Young, 2021; Sarathy and Dartois, 2020). The essential drug(s) physicochemical properties that may affect the factors mentioned above include hydrophobicity, molecular weight, surface charge, and ionization (Malan and Chetty, 2002; Piccaro et al., 2015; Tanner et al., 2018). Hydrophilic anti-TB drugs show higher absorption through the gastrointestinal (GIT) mucosa compared to lipophilic (log P>2) drugs (Iacobino et al., 2016). Furthermore, high molecular-weight lipophilic therapeutic agents are less likely to be absorbed orally than low molecular weight lipophilic therapeutic agents (Vélez et al., 2022). Due to the inability of essential compounds to be ionized in a primary media, weak bases are absorbed more rapidly from the intestine (Caldwell et al., 1995). Similarly, a weak acid is rapidly taken up from the gastrointestinal tract (Hua, 2019; Manallack et al., 2013), and the *Mycobacterium tuberculosis* bacterium is highly susceptible to weakly acid drugs such as PZA (Siew et al., 2012). Nonetheless, the GIT pH can directly influence the ionization of the drug and, consequently, the drug solubility and absorption (Abuhelwa et al., 2017; Akula and P. K., 2018; Caldwell et al., 1995). The influence of the physicochemical properties differs from tissue to tissue, as the above case focused on just the GIT mucosa. However, the effects are different if we examine other tissues, such as the brain and bone. For example, for the brain, low molecular weight and hydrophobic/lipophilic drugs are easily absorbed through the BBB as they cross through a transmembrane diffusion (Banks, 2009). This is a challenge in treating EPTB after GIT absorption; the drug still needs to go to the target site and be absorbed, leading to a long-term therapeutic effect (Baykan et al., 2022; Gopalaswamy et al.,

2021; Houston and Macallan, 2014). Therefore, target therapy in TB is an excellent need, especially in EPTB.

In addition, the properties of the excipients and delivery platform can significantly alter the absorption of the drug (Hua, 2019; Stillhart et al., 2020). The desired therapeutic effect could be accomplished with an appropriately designed delivery method. The hydrophilic-lipophilic balance and absorption can be controlled through correct excipient selection and dosage form design, making the drug's pKa more critical than its molecular weight for creating formulations with the necessary characteristics (Alqahtani et al., 2021; Caldwell et al., 1995; Hua, 2019). However, the dynamic changes in the specific tissue environment can limit the physicochemical qualities of the drug; therefore, it is essential to examine the physiological parameters before developing the delivery system (Malan and Chetty, 2002). **Table 2.2** highlights how the changes in the physiological microenvironment caused by the infection of *Mycobacterium tuberculosis* affect the absorption of the first-line anti-TB drugs in EPTB.

Table 2.2: How physiological changes caused by *Mycobacterium tuberculosis* affect drug properties and absorption.

Anti-TB drugs	**Effect of change in the pH and temperature in the absorption of each drug and activity against *Mycobacterium tuberculosis***		**Reference**
	pH	Temperature	
Rifampicin (RIF)	In an acidic pH environment, when in combination with INH, RIF is hydrolyzed to 3-formyl rifamycin (3-FRSV), which is poorly absorbed.	-	(Alves et al., 2010; Freire et al., 2014; Sankar et al., 2003)
Isoniazid	The stability of the drug is not affected in either acidic or basic pH, however, in acidic pH the drug has low permeability	-	(Coleman et al., 2011; Klein et al., 2016)
Pyrazinamide	The drug is active against *Mycobacterium tuberculosis* only at a slightly acidic pH.	An increase in temperature enhances the solubility and thus absorption of the drug is increased	(Jia et al., 2020; Zhang et al., 2003)
Ethambutol	Ethambutol's growth-inhibiting effect is greatest near neutral pH, where it exists primarily as a monohydrochloride and binds poorly.	-	(Beggs and Andrews, 1974)

Streptomycin	Streptomycin is stable within a pH range of 2 to 9 but deteriorates in highly acidic or basic conditions.	-	(Ujváry, 2001)

2.4. The role of targeted therapy (TT) in treating *Mycobacterium tuberculosis*

Despite the availability of potent anti-TB drugs, therapeutically appropriate dosages are limited by toxic side effects in regions other than the infected site (Seung et al., 2015). In addition, drug resistance develops when the bacterium is treated with subtherapeutic levels of the drug. Henceforth, constructing a system that enables the distribution of high concentrations of anti-TB drugs to locations where bacteria proliferate would simplify the administration of sterilizing dosages to sites of infection and decrease the formation of drug resistance (Seung et al., 2015; Tewabe et al., 2021). TT is a new research field that researchers have also explored for *Mycobacterium tuberculosis* and, more specifically, EPTB, since the uniqueness of this type of disease is that the treatment involves not only chemotherapy but surgery, which speaks to regenerative medicine. The advantages of TT in the drug delivery community have been extensively researched, and some of them are depicted in **Table 2.3**. Strategies to achieve TT for *Mycobacterium tuberculosis* in EPTB include using different technologies, either in combination or individually, such as nanotechnology and/ or scaffolds. However, each TT technology may vary due to the vastly different characteristics of the tissues involved/ affected by EPTB. For this review, CNS and Bone TB will be considered the most prevalent EPTB sites.

Table 2.3: Advantages offered by targeted therapy in drug delivery.

- Incorporating drugs that are hydrophilic and hydrophobic simultaneously is a possibility.
- In cases where tissue loss has occurred due to the progression of the bacterium, a single platform that speaks to both regeneration of tissue and delivery of the drugs can be implemented
- The delivery of drugs near their target sites of action and the minimization of unwanted side effects at other body locations.
- The enhanced sustained release mechanism provides improved patient adherence.
- Contrary to injectable medication delivery methods, implanted devices may be removed immediately in the event of severe allergies or adverse reactions to previously delivered pharmaceuticals.
- Less drug is needed to address the illness condition, hence lowering potential adverse effects, and improving therapy effectiveness.

- These TT platforms can circumvent systemic creation, resulting in higher drug concentrations at the target site than could be attained through systemic administration.

The CNS consists of two types of organs: the brain and the spinal cord; but, CNS TB has been reported only for the brain (Rock et al., 2008). Henceforth, two kinds of brain TB occur, which is meningitis and intracranial tuberculomas (Chatterjee, 2011; Rock et al., 2008). Bone TB is the third most frequently occurring EPTB, and it appears to be on the rise and is an area with limited research. However, it accounts for 40-50% of all EPTB cases, resulting in a global prevalence estimate of 19–38 million cases (Alene et al., 2021; Haulman et al., 2008; Huang et al., 2015; Malaviya and Kotwal, 2003; Pigrau-Serrallach and Rodríguez-Pardo, 2013). As shown in **Table 1**, spinal TB is the most prevalent bone TB, contributing to over 50% of all bone TB cases, and features of spinal TB have long been reported in Egyptian mummies dating back to 9000 years (Alam et al., 2015; Garg and Goyal, 2020; Hegazy et al., 2021; Rodriguez-Takeuchi et al., 2019). The dorsal and lumbar spine sections are the most afflicted, whereas the sacral and cervical vertebrae are the least affected. TB can also affect the dorsal and sacroiliac joints (Hegazy et al., 2021; Zhan et al., 2022). The need for surgical therapy in TB patients has substantially diminished since the development of potent chemotherapeutic drugs.

Nonetheless, surgery is frequently required to treat spinal TB with anti-TB drugs and supportive management (Garg and Somvanshi, 2011; Tuli, 1975). The spine is the highest site of bone TB, with over 50-60% of bone TB states from the spine (Hegazy et al., 2021). Henceforth, much of the treatment in this section will focus on spinal TB. The need for surgery in spinal TB is guided by if the patient has no sign of increasing neurological recovery and if, during treatment, neurological problems arise (Rasouli et al., 2012). **Figure.2.3** depicts a general treatment protocol for patients requiring surgery for spinal TB.

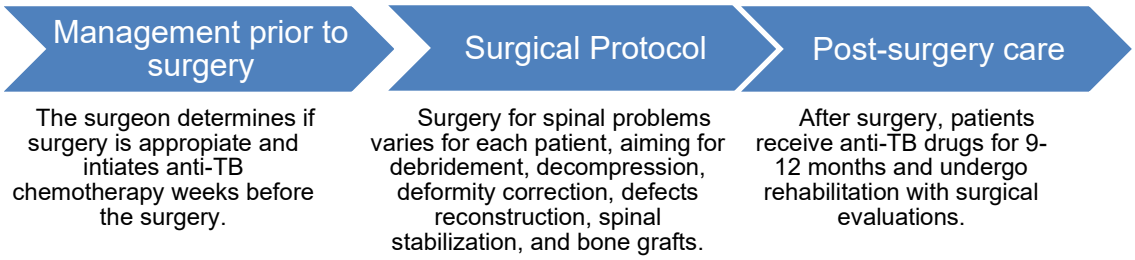


Figure 2.3: A general protocol for spinal TB.

Bone grafts are essential surgical treatments for spinal TB because they can restore spinal stability and maintain alignment. Currently, surgeons have been utilizing autogenous bone grafts (autografts) and allogeneic bank bone (allografts) for bone regeneration after surgery (Tang et al., 2020b). However, there remain concerns, such as disease transmission, immunogenicity, and sufficient donor tissue availability when used (Marrale et al., 2007). Hence, researchers and orthopedics' have started looking at alternative treatments for bone TB, and currently, TT in bone tissue engineering (BTE) is hoped to be the therapy of choice in the future, as it will likely alleviate many of the drawbacks of the existing treatments (Dong et al., 2014; Garg and Goyal, 2020; Huang et al., 2015).

2.4.1. Overview of bone-targeted therapies

Bone regeneration mechanism of action has been thoroughly investigated over the years and involves intricate mechanisms to repair damaged bone tissue. Inflammation triggers cell recruitment and clears debris, while blood vessels provide nutrients (Chindamo et al., 2020; V. K. et al., 2022). Mesenchymal stem cells differentiate into osteoblasts, forming a mineralized scaffold. Growth factors regulate cell behavior, and osteoclasts remodel the tissue, restoring bone structure and function (V. K. et al., 2022). **Figure. 2.4** illustrates how natural bone healing occurs after a fracture.

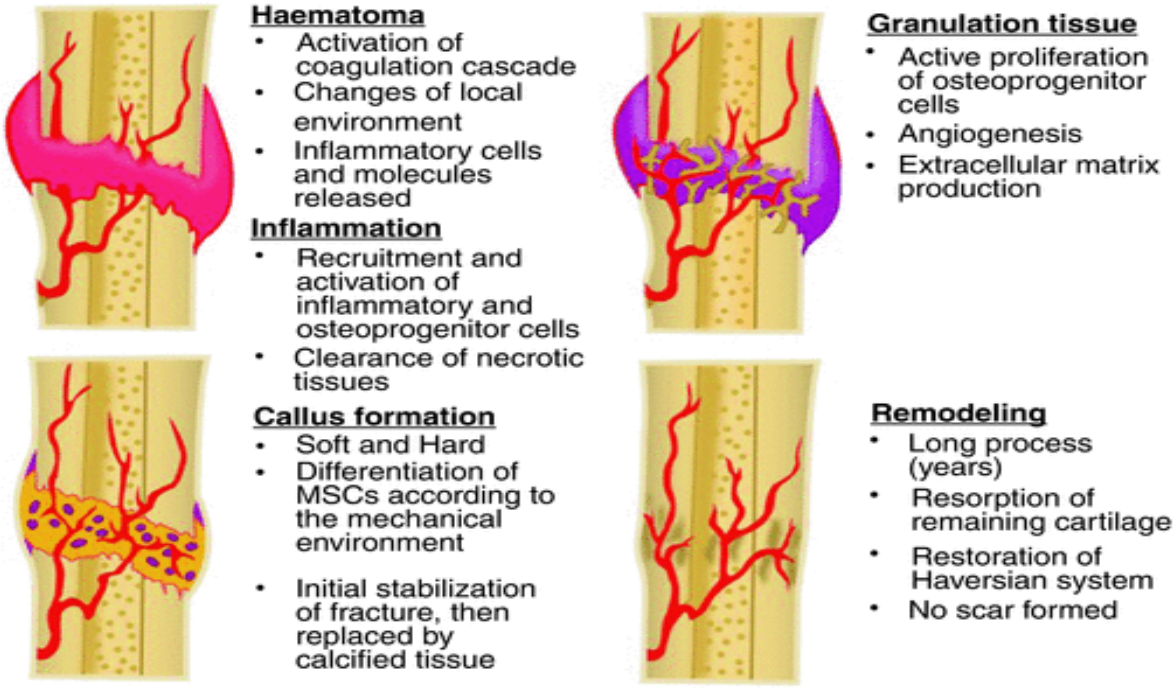


Figure 2.4: Demonstrates the process of natural bone healing following a fracture. (Reprinted from Pountos et al, 2021 with permission).

Bone diseases, such as osteoporosis (OP), Paget's disease, osteoarthritis (OA), osteosarcoma (OS), and osteomyelitis, pose significant public health challenges. These conditions disrupt the normal functioning of the skeletal system, leading to substantial patient distress and impeding their ability to live a normal life. Moreover, they impose a considerable burden on healthcare systems due to the increased demand for medical care and resources required for the diagnosis, treatment, and management of these diseases. As a result, addressing bone diseases is crucial for both individual well-being and the overall healthcare system. Bone targeting therapies have been researched for the past two decades with the main objective being to employ distinctive components that are composed of hydroxyapatite component found in bone. Here is an overview of some commonly used bone-targeted therapies:

- Bisphosphonates: Bisphosphonates are a class of drugs that inhibit bone breakdown by targeting osteoclasts, the cells responsible for bone resorption. These drugs help prevent bone loss and reduce the risk of fractures in conditions like osteoporosis and bone metastases (Farrell et al., 2018).

- Denosumab: Denosumab is a monoclonal antibody that works by inhibiting the formation and activity of osteoclasts. It is used to treat osteoporosis and bone

metastases, reducing the risk of fractures and skeletal-related events (Chang et al., 2018).

- Hormone Replacement Therapy (HRT): Hormone replacement therapy, typically involving estrogen or a combination of estrogen and progesterone, is used to manage osteoporosis in postmenopausal women. HRT helps maintain bone density and reduces the risk of fractures (Gambacciani and Levancini, 2014).

- Selective Estrogen Receptor Modulators (SERMs): SERMs, such as raloxifene, act as estrogen agonists or antagonists in different tissues. They are prescribed to postmenopausal women with osteoporosis to increase bone density and reduce fracture risk (Falsetti et al., 2022).

- Calcitonin: Calcitonin is a hormone that inhibits bone resorption. It can be administered as a nasal spray or injection to treat osteoporosis and reduce pain in bone metastases (Ukon et al., 2019).

- Targeted Therapies for Bone Metastases: In cases of cancer that have spread to the bones (bone metastases), targeted therapies can be used to inhibit the growth of cancer cells and reduce bone-related complications. Examples include inhibitors of the RANK/RANKL pathway (e.g., denosumab) and tyrosine kinase inhibitors (e.g., sorafenib) (Sousa and Clézardin, 2018).

- Radiopharmaceuticals: Radiopharmaceuticals, such as radium-223, deliver radiation directly to bone metastases, targeting cancer cells and reducing pain and skeletal-related events (Ryan et al., 2014).

It's important to note that the choice of bone-targeted therapy depends on the specific condition, disease stage, patient characteristics, and other individual factors. The treatment plan is typically determined by healthcare professionals based on a thorough assessment and consideration of the benefits and risks of each therapy (Zhong and Li, 2021). As all these bone targeting therapies are promising, however, some disadvantages have to be considered, such as potential side effects, limited efficacy, long-term challenges, cost of these therapies, potential interactions with other drugs, and individual variability (Lu et al., 2020; Zhong and Li, 2021). Researchers have suggested that this challenge can be mitigated by the use of nanotechnology drug delivery systems, which will be discussed in section 2.4.2.

2.4.2. Nanotechnology-based approach in targeted therapy

In most pathological conditions, the current therapeutic agents require an efficient and effective delivery method that can traverse biological barriers while minimizing harm to the host. Nanotechnology has dramatically changed treatment tactics for treating lethal infections using functionalized biocompatible nanocarriers that can transport the load correctly at the targeted spot without any substantial harmful effect on the host. Nanoparticle technology has enhanced drug retention and release effectiveness, most uses biodegradable materials, and reduced cytotoxicity and adverse effects. In most instances, the surface of the nanoparticles is tunable with ligands, enabling the integrated therapies to target cells and organs (Patra et al., 2018). The two categories of nanotechnology TT (NTT) are passive and active drug targeting (Baranyai et al., 2021; Devarajan et al., 2015; Zhang and Zhang, 2005). A significant difference between the two types of drug targets is that passive targeting is based on the size, shape, and surface charge of the nanoparticles, while active targeting is more established for nanoparticles that have been functionalized to facilitate binding to a specific tissue (Baranyai et al., 2021; Patra et al., 2018; Singh and Lillard, 2009). **Figure. 2.5** illustrates the mechanisms of nanoparticles' two different targeting systems (Mazlan et al., 2021).

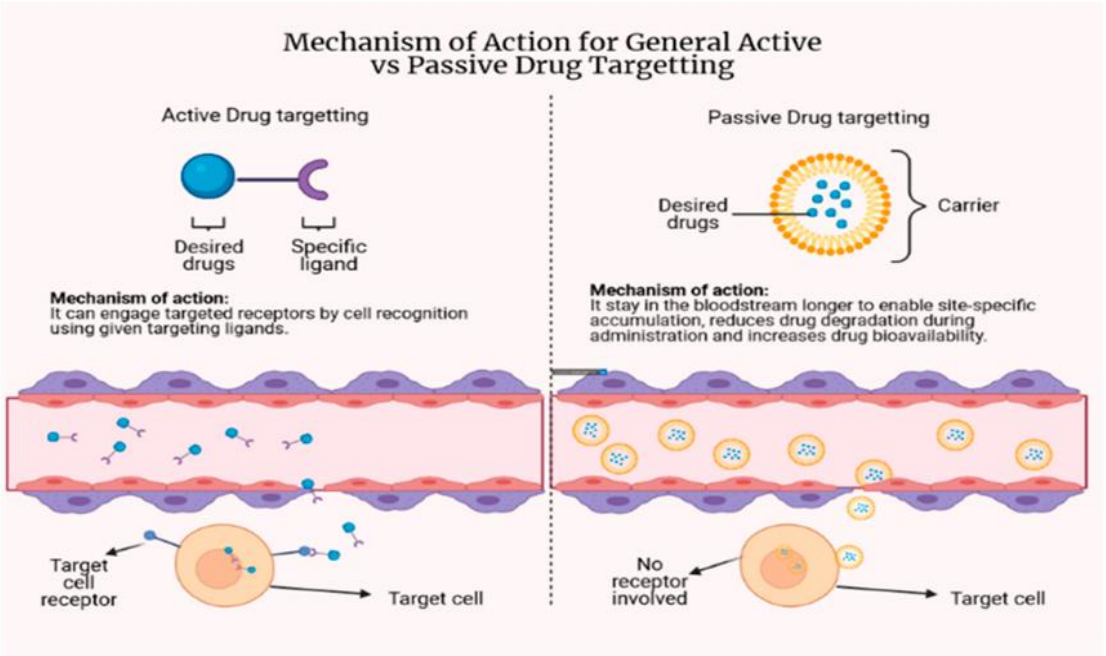


Figure 2.5: Targeting systems that nanoparticles use for targeted therapy (Mazlan et al., 2021) (Reprinted from Mazlan et al, 2021 with permission).

Given the challenges of effectively diagnosing and treating *Mycobacterium tuberculosis*, nanotechnology may provide an alternative avenue to supplement traditional therapeutic approaches (Grotz et al., 2018; Kerry et al., 2018). Typically, drug delivery vehicles can be classified into two broad categories: organic carriers and inorganic carriers (**Figure. 2.6**). Some of these nanotechnology-based drug delivery systems have been documented for treatment against *Mycobacterium tuberculosis* and are classified into several categories based on their composition (Bai et al., 2018; Baranyai et al., 2021; Grotz et al., 2018; Khiev et al., 2021; Tazhbayev et al., 2021; Wagner et al., 2006; Zhang and Zhang, 2005). Although most published research on the nanoparticles currently speaks to PTB and not EPTB, it is crucial to comprehend the mechanisms underlying these two disease conditions. The key distinction between the two forms of TB is the site of the disease, but as previously noted, most extra-pulmonary TB cases arise from pulmonary TB. As such, the nanotechnology platforms developed for PTB can be utilized as they are or modified for EPTB treatment and diagnosis. As only a few nanotechnology formulations have been reported specific for EPTB. These TT nano preparations have been developed for different organs such as the brain, bones, and liver. Thus, some of these technologies have been implemented, and some have the potential to be implemented into different types of EPTB, namely, CNS, bone, and GIT.

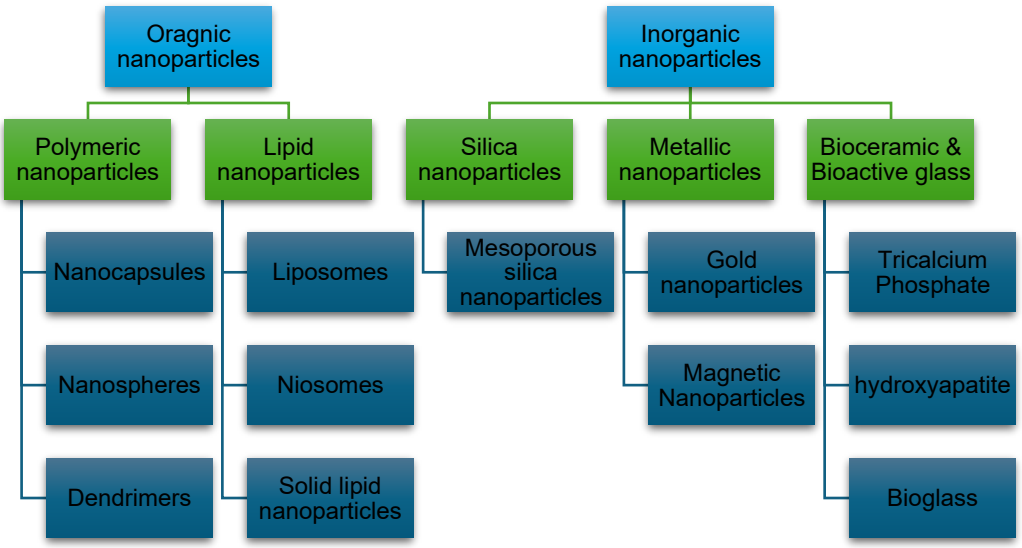


Figure 2.6: Various forms of the most frequently utilized nanostructures as drug delivery systems (Baranyai et al., 2021).

2.4.2.1. Organic nanoparticles

2.4.2.1.1. Polymeric nanoparticles

In recent years, polymeric nanoparticles gained significant attention owing to their qualities deriving from their small size (Begines et al., 2020). The benefits of using polymeric nanoparticles as drug delivery vehicles include their ability to provide sustained release, protect drugs and other biologically active compounds from the surroundings, and enhance bioavailability and therapeutic efficacy (Begines et al., 2020; Patra et al., 2018). Furthermore, different types of polymeric nanoparticles exist, which are nanocapsules (reservoir system) and nanospheres (matrix system), polymersomes, polymeric micelles, and dendrimers (Begines et al., 2020; Pandey and Khuller, 2004). Various authors have reported on different nanoparticle preparation methods, including polymerization, nanoprecipitation, solvent evaporation, ionotropic gelation, and emulsification (Begines et al., 2020).

Polymeric nanoparticles that have been explored in the treatment of TB use two types of polymers, which can either be natural or synthetic polymers or a combination (Begines et al., 2020; Iyisan and Landfester, 2019; Mazlan et al., 2021). The utilization of natural polymers as responsive drug carriers against *Mycobacterium tuberculosis* is widespread due to their biocompatibility, low toxicity, and abundance of functional groups (Kerry et al., 2018; Zielińska et al., 2020). By modifying their surface features, these polymers can be made specific to a target. Several natural polymers, such as alginate, chitosan, guar gum, gelatin, and albumin, have been utilized for encapsulating anti-TB drugs (Ahmad et al., 2007; Ghosh et al., 2022; Kerry et al., 2018; Viswanathan et al., 2018).

Zahoor et al., (2005) developed an aerosolized *Mycobacterium tuberculosis*-targeted alginate polymeric nanosystem encapsulating INH, RIF, and PZA that enhanced the bioavailability of all drugs encapsulated in the nanosystem compared with oral-free medications (**Table 2.4**) (Zahoor et al., 2005). The system further showed it was effective against *Mycobacterium tuberculosis* in guinea pigs in a maximum of 15 days after nebulization, all drugs were found in organs (lungs, liver, and spleen) at concentrations higher than the minimum inhibitory concentration (MIC), whereas free drugs remained in the body until day 1 (**Figure. 2.7 & 2.8**) (Zahoor et al., 2005). The research also disclosed that the therapeutic efficacy of three doses of the drug-loaded alginate nanoparticles delivered via nebulization at 15-day intervals was comparable

to the effectiveness of 45 daily doses of the unbound drugs taken orally (Zahoor et al., 2005). A similar study by the same group confirmed that in mice infected with TB, *Mycobacterium tuberculosis* H37Rv strain, administering three oral doses of the formulation 15 days apart resulted in total *Mycobacterium tuberculosis* clearance from the organs (Ahmad et al., 2006). The study compared the above formulation to administering 45 traditional doses of orally given free drugs. Additionally, the results showed that the nanosystem created was non-toxic, making it imperative to further investigate the feasibility of using inhalable alginate nanoparticles as a suitable vehicle for the controlled delivery of anti-TB drugs (Ahmad et al., 2006).

Table 2.4: The study compared the pharmacokinetics of antitubercular drugs delivered in the form of alginate nanoparticles via nebulization to oral administration of unbound drugs in guinea pigs. (Reprinted from Zahoor et al., 2005, with permission).

Group	C_{max} (µg/mL)	T_{max} (h)	K_{el}	$T_{1/2}$ (h)	$AUC_{0-\infty}$ (µg.h/mL)	Relative Bioavailability
Oral free drugs						
RIF	0.8 ± 0.18	1	-0.15 ± 0.0	4.5 ± 0.53	8.37 ± 1.10	1.00
INH	2.5 ± 0.13	1	-0.21 ± 0.01	3.1 ± 0.53	10.93 ± 1.90	1.00
PZA	22.0 ± 1.63	0.5	-0.1 ± 0.01	6.5 ± 1.43	185 ± 10.00	1.00
Aerosol alginate nanoparticles						
RIF	1.12 ± 0.02	96	-0.158 ± 0.01	4.39 ± 0.06	138.46 ± 5.32	16.54
INH	4.90 ± 0.3	168	-0.59 ± 0.01	1.17 ± 0.3	521.45 ± 32.4	47.71
PZA	35.00 ± 1.1	144	-4.41 ± 0.09	0.16 ± 0.02	7776.00 ± 50.34	42.02

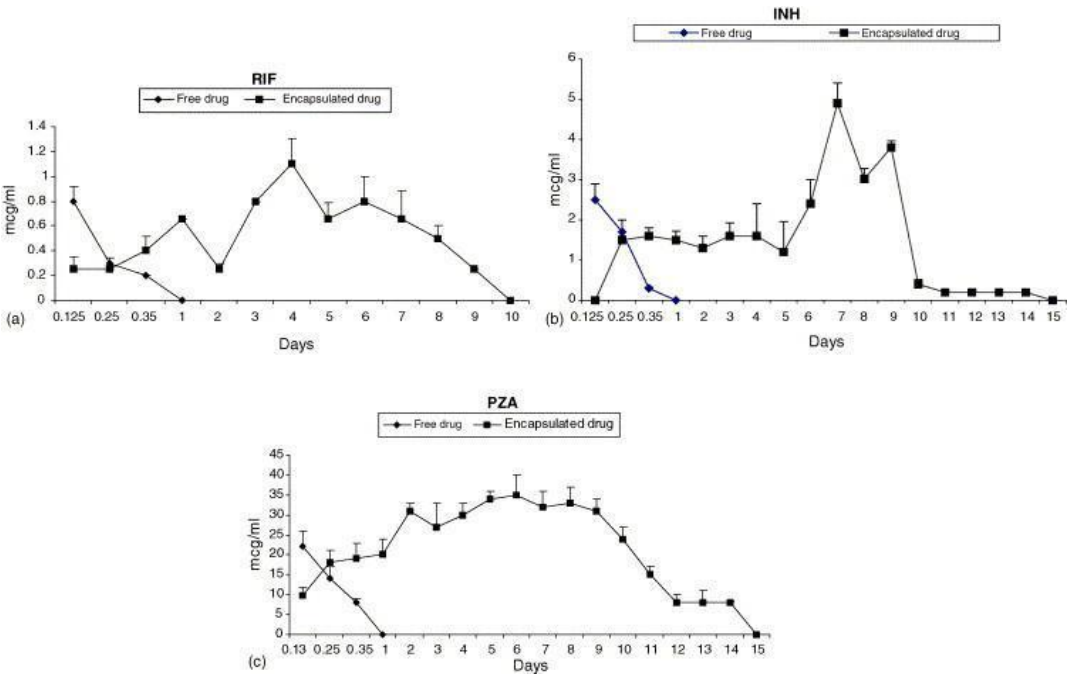


Figure 2.7: The plasma drug profile after a single nebulization of alginate nanoparticles loaded with antitubercular drugs and unbound drugs was evaluated in guinea pigs. (Reprinted from Zahoor et al., 2005, with permission).

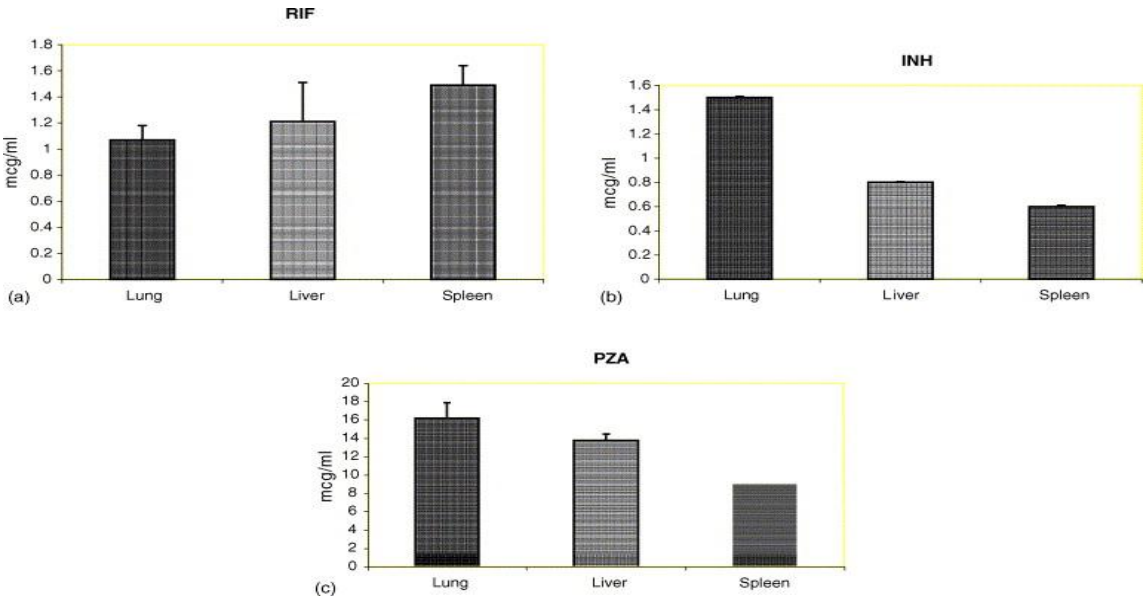


Figure 2.8: The levels of antitubercular drugs in tissues on day 15 post aerosol administration of alginate nanoparticles in guinea pigs were determined. The data represent the mean ± standard deviation of six animals and includes RIF, INH, and PZA. (Reprinted from Zahoor et al., 2005, with permission).

In these two similar studies (Ahmad et al., 2006; Zahoor et al., 2005), the author designed the same drug delivery system in order to address the hard-to-treat infectious bacteria *Mycobacterium tuberculosis* using polymeric nanoparticles. The significant difference was the quantity of the first-line drugs that the system can deliver. The polymeric nanoparticles were produced by employing a well-established modified

cation-induced controlled gelification of the alginate gel technique. In both studies, the author showed the effectiveness of the designed nanosystem intended for treatment against *Mycobacterium tuberculosis* by applying the necessary physicochemical characterization of nanoparticles, aerodynamic characterization, and *in vivo* characterization in different animal models. Furthermore, the *in vivo* characterization involved drug deposition studies, experimental infection & chemotherapy, and biochemical hepatotoxicity. The outcomes from these studies are significant for further examination of polymeric nanomaterials against *Mycobacterium tuberculosis.* Nevertheless, these natural polymers face some limitations, that's includes inconsistent structure between batches and the potential for human allergies (Daemi and Barikani, 2012; Iyisan and Landfester, 2019).

One of the most commonly used synthetic polymers in the pharmaceutical industry is poly lactic-co-glycolic acid (PLGA), especially in the development of polymeric nanoparticles for anti-TB drug delivery (Essa et al., 2020; Zielińska et al., 2020). PLGA has a long history of use in sustained-release drug delivery and tissue engineering and has received approval for human use from the Food and Drug Administration (Essa et al., 2020; Kalluru et al., 2013; Makadia and Siegel, 2011). Hakkimane et al., (2018) formulated PLGA polymeric nanoparticles through solvent evaporation (Hakkimane et al., 2018). The polymeric nanoparticles were developed for targeted delivery of RIF and a modified INH called IH2 for the treatment against *Mycobacterium tuberculosis*. INH was changed to IH2 since it has the same therapeutic effect but is more stable and increases the drug incorporated into PLGA nanoparticles relative to INH. The group conducted *in-vitro* studies and tested antimycobacterial susceptibility against *the Mycobacterium tuberculosis* H37Rv strain. The results showed that owing to the hydrophobicity of IH2, PLGA polymer nanoparticles encapsulated a greater quantity of drug by up to 15 folds compared to INH. In addition, RIF-loaded PLGA polymeric nanoparticles inhibited the development of the H37Rv strain to a lower concentration, 0.7 g/mL, than the minimum inhibitory concentration (MIC) level of RIF (1 g/mL) (Hakkimane et al., 2018). The overall results suggested that the drug-targeted polymeric nanoparticles, encapsulated with RIF and IH2, demonstrate a higher efficacy in eliminating the H37Rv strain of *Mycobacterium tuberculosis* (**Table 2.5**). The targeting mechanism for this system can be elucidated as being passive, as both drugs were sustained and released for 30 days, and the stability of the drugs was enhanced (Hakkimane et al., 2018).

Table 2.5: Antimicrobial susceptibility test result. (Reprinted from Hakkimane et al, International Journal of Nanomedicine 2018:13 4303-4318. Originally published by and used with permission from Dove Medical Press Ltd).

Tube position	Growth unit	Status	Drug concentration (mg/ml)	Samples
B/M15	400	Control	-	Growth control
B/M17	0	Sensitive	1.0	Free RIF
B/M16	400	Resistant	-	Formulation without drug
B/M18	0	Sensitive	1.0	Formulation with RIF
B/M04	400	Resistant	0.70	Free RIF
B/N09	0	Sensitive	0.70	Formulation with RIF
B/J14	0	Sensitive	0.1	Free INH
B/J12	0	Sensitive	0.16	Free IH2
B/J14	0	Sensitive	0.16	Formulation with IH2

In the ploy to develop new therapeutic techniques to reduce the occurrence of *Mycobacterium tuberculosis* resistance, Lemmer et al., (2015) investigated mycolic acids as a potential mycobacterial ligand for drug targeting utilizing INH PLGA nanoparticles (Lemmer et al., 2015). The production of nanoparticles involved the use of a double emulsion solvent evaporation technique. The incorporation of mycolic acid into the nanoparticles was verified using the Enzyme-linked immunosorbent assay (ELISA) (Lemmer et al., 2015). The findings indicated that macrophages infected with mycobacteria had a considerable increase in the uptake of nanoparticles coated with mycolic acid. As a result, the use of mycolic acid as a targeting ligand for various nanoformulations may be worth exploring as a means to effectively treat TB (Lemmer et al., 2015).

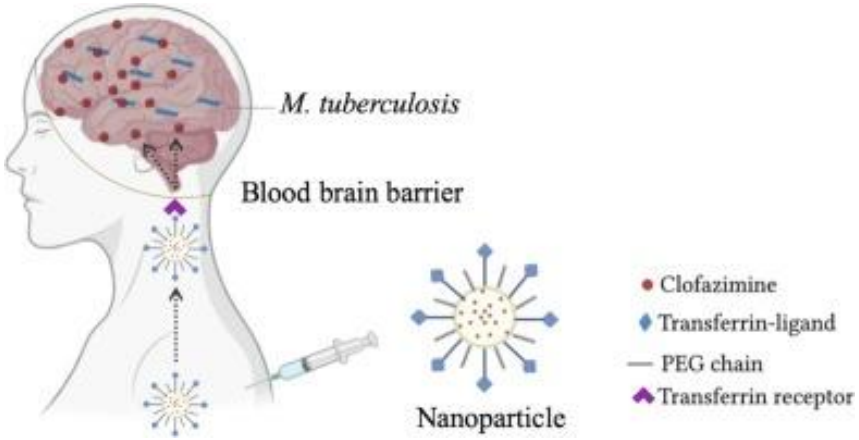


Figure 2.9: depicts PLGA-PEG nanoparticles that are loaded with Clofazimine (CFZ) and functionalized with a transferrin receptor-binding peptide, intended for targeted drug delivery to the central nervous system in the treatment of multi-drug-resistant tuberculosis. (Reprinted from De Castro et al., 2021, with permission).

To address the role of polymeric nanoparticles for TT in EPTB. De Castro et al. (2021) aimed to develop a new approach for treating CNS-TB by creating intravenous PLGA-PEG nanoparticles loaded with Clofazimine (CLZ) and functionalized (**Figure 2.9**) (de Castro et al., 2021). The reason for this study was because CLZ, though being a strong anti-MDR drug, has low and inconsistent bioavailability, high plasma protein binding, and build-up in fatty tissue after oral administration, hindering its therapeutic efficacy, due to its limited water solubility and high lipophilicity. The study demonstrated that the PLGA-PEG nanoparticles with functionalization are a potential method for delivering CFZ, as indicated by the low binding to plasma proteins, selective distribution, and precise delivery to the brain tissue. However, further *in vivo* studies are required to validate these findings (de Castro et al., 2021).

In a study relating to central nervous system tuberculosis (CNS-TB), Pandey et al. (2006) developed a poly(lactic-co-glycolic acid) (PLGA) nanosystem for the co-delivery of rifampin, isoniazid, pyrazinamide, and ethambutol through oral administration (Pandey and Khuller, 2006). The author conducted pharmacokinetic and chemotherapeutic evaluations, which demonstrated that a single oral dose of the nanosystem could maintain drug levels in mice for 5 to 8 days in plasma and 9 days in the brain, compared to the free drugs (Pandey and Khuller, 2006). The results showed improved pharmacokinetic measures such as mean residence time and relative bioavailability and enhanced pharmacodynamic measures such as the area under the curve to the minimal inhibitory concentration (AUC/MIC) and time to sustained MIC

values in plasma. In *Mycobacterium tuberculosis* H37Rv-infected mice, five oral doses of the nanoparticle formulation every ten days led to undetectable bacilli in the meninges, as determined by colony-forming units and histology. Thus, the PLGA polymeric nanoparticle formulation is a promising alternative therapy for CNS-TB that should be further investigated for intravenous or oral administration.

Although, to date, no PLGA nanoparticles have been synthesized targeting *Mycobacterium tuberculosis* in the bone. However, the potential of using PLGA nanoparticles in bone drug delivery has been explored in other bone conditions. A study by Fu et al. (2014) where the author successfully designed and synthesized nanoparticles containing PLGA–PEG (poly(lactic-co-glycolic acid)–polyethylene glycol) diblock copolymers and bone-targeting moieties based on aspartic acid, (Asp)n that target bone tissue (Fu et al., 2014). The authigenic of the polymeric nanoparticles was evaluated by conducting different characterizations such as ^{1}H NMR, FTIR, and size characteristics. Additionally, to evaluate the ability of the nanoparticles to target bone, both *in-vitro*, hydroxyapatite affinity tests, and *in vivo*, fluorescence imaging was performed using zebrafish and rats (Fu et al., 2014). The results showed that the dendritic Asp3 moiety of the PLGA–PEG–Asp3 nanoparticles showed the best apatite mineral ability (Fu et al., 2014). In addition, following injection with PLGA–PEG–Asp3 nanoparticles, the intraosseous fluorescence signal was delivered to be more intense than after treatment with other PLGA–PEG-based NP that lacks a dendritic Asp3 moiety (**Figure 2.10**). The Figure demonstrates the results of the treatment of the D1 bone marrow stem cell line with hybrid nanoparticles. The data indicate that the hybrid nanoparticles, which were labelled with FITC, were taken up by the cells in a time-dependent manner and accumulated in a perinuclear pattern as evidenced by the co-staining with DAPI and FITC. Furthermore, the majority of the hybrid nanoparticles were internalized through endocytosis and did not reside in the plasma membrane. The study yielded that the nanoparticles containing an Asp3 moiety significantly influenced the endocytosis, intracellular route, and cellular response to the nanoparticles in D1 cells. Moreover, the coupling of PLGA with PEG–(Asp)3 does not affect its biocompatibility. The author further suggested that these nanoparticles may serve as a delivery mechanism for lipophilic drugs, necessitating more research into treating bone diseases (Fu et al., 2014).

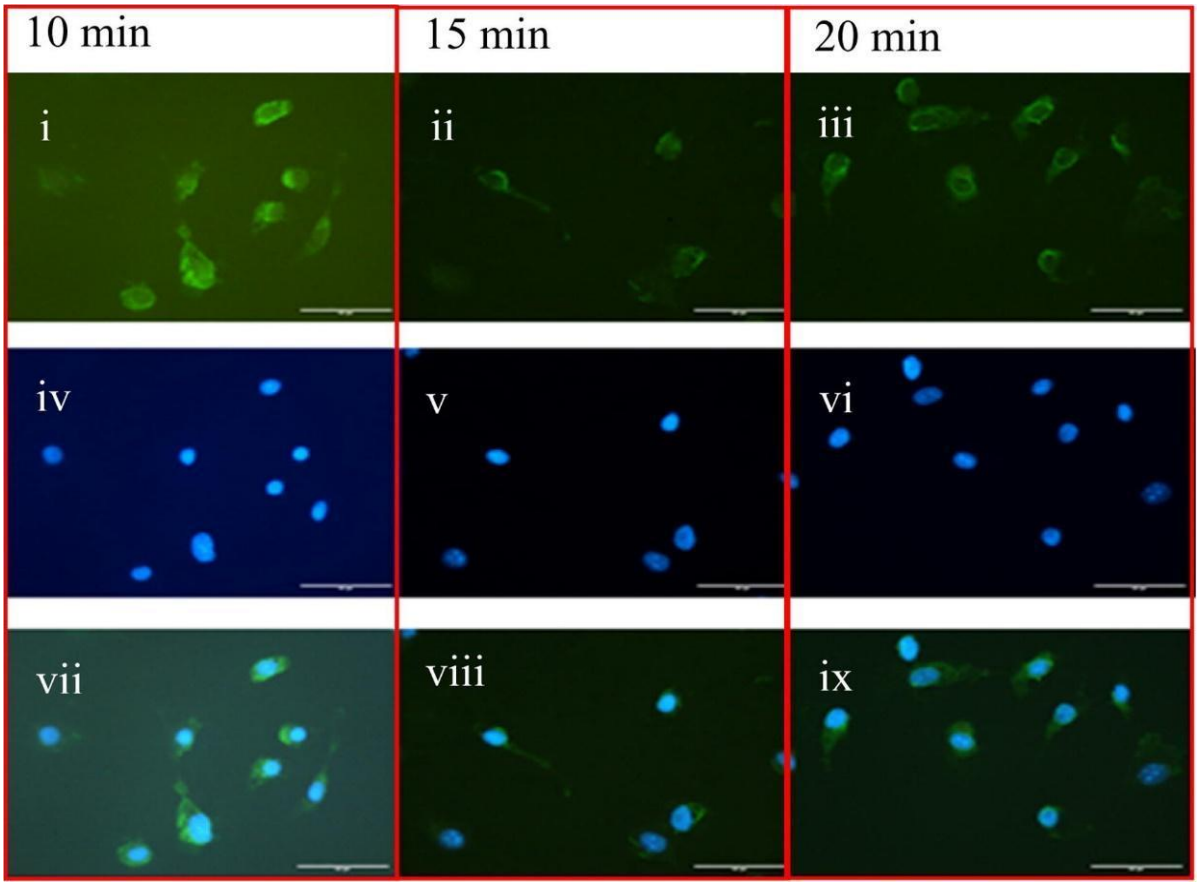


Figure 2.10: (i–iii) Time-dependent fluorescence imaging of PLGA–PEG–Asp3/FITC–PLGA–PEG–OMe (8/2) NP, (iv–vi) DAPI staining and (vii–ix) merge images, which transport into D1 living cells. (Reprinted from Yin-Chih Fu et al., 2014, with permission).

2.4.2.1.2. Vesicular-based nanoparticles: liposomes and niosomes

In the field of drug delivery, liposomes and niosomes are the most widely used vesicular-based systems (Kumar and Rajeshwarrao, 2011). These systems are made up of a phospholipid bilayer that encloses an aqueous compartment. Both platforms have received extensive research, making them viable drug delivery options for a variety of diseases, including tuberculosis, due to their ability to encapsulate both hydrophilic and hydrophobic drugs (Bartelds et al., 2018; Judson et al., 2001; Pinheiro et al., 2011). The first commercially available liposome formulation was Doxil® doxorubicin, a PEGylated liposome containing doxorubicin, which was introduced in 1995 (Lao et al., 2013). The use of polyethylene glycol increases the lifespan of doxorubicin. The difference between niosomes and liposomes lies in the composition of their surfactant bilayer, with the former having hydrophilic ends that are exposed to the aqueous phase on both the exterior and interior of the vesicle and hydrophobic chains facing each other inside the bilayer (Bartelds et al., 2018; Kazi et al., 2010;

Kumar and Rajeshwarrao, 2011). However, the use of liposomes as a means of delivering drugs parenterally, specifically for the selective administration of anti-cancer, antibiotic, and antifungal medications, has been extensively researched for many years (Pinheiro et al., 2011; Sercombe et al., 2015). However, due to drug-carrier complex changes, liposome systems cannot be replicated and have low stability during storage (Kazi et al., 2010; Sercombe et al., 2015). The niosomal drug delivery system holds great potential as a targeted drug carrier, with its ability to transport medications in a controlled and sustained manner leading to improved bioavailability and prolonged therapeutic effects. These benefits have made niosomes a popular choice in many applications and treatments.(Bartelds et al., 2018; Kazi et al., 2010; Kulkarni et al., 2019; Nasr et al., 2008).

Niosomes have been utilized for oral delivery of anti-TB drugs such as RIF, INH, PZA, and EMB (**Table 6**). For example, El-Ridy et al. (2015) demonstrated sustained release of EMB from the span 60 niosomes membrane (El-Ridy et al., 2015). The results of the study demonstrated that the use of a niosomal formulation improved drug retention in the lungs of mice, resulting in a decrease in the weight of the lung tissue at the root, a reduction in the number of bacteria present in lung samples, and an improvement in the pathological effects on the lungs, livers, and spleens of guinea pigs (El-Ridy et al., 2015). El-Ridy et al. (2011) evaluated the bactericidal effects of PZA-loaded niosomes against H37Rv (El-Ridy et al., 2011). The formulations were prepared through the Vortex dispersion technique, and the effect of different Span's with cholesterol concerning the entrapment of the drug was evaluated (El-Ridy et al., 2011). In addition, the charge of the niosomes was also investigated by the use of diacetyl phosphate and stearyl amine. The study revealed that Span 60 and negatively charged niosomes resulted in the maximum percentage of PZA encapsulation. In addition, the niosome formulation was found to be more effective than free PZA in terms of reducing bacterial growth and promoting the extended release of PZA, which requires a reduced dosage, shorter therapy duration, and improved patient adherence (El-Ridy et al., 2011).

Table 2.6: An overview of the anti-TB vesicular carriers that have been utilized.

Anti-TB drug	vesicular systems	Technique of preparation	In vivo model	Outcomes observed or outcomes	Ref
Rifabutin (RFB)	Liposomes	Remote loading	Mice	Loaded RFB showed greater therapeutic activity in the spleen and liver. Suggesting the suitability of formulation to manage EPTB in patients.	(Gaspar et al., 2008)
RIF	Liposomes	Remote loading	Mice	High antimicrobial activity of RIF when compared to free drug	(Agarwal et al., 1994)
EMB	Niosomes	Thin film hydration	guinea pigs	. Improved efficacy and safety were observed compared to the unbound drug.	(El-Ridy et al., 2015)
RIF, INH, PZA	Niosomes	Sonication	-	The loading efficiency for all drugs was high, and sustained release was achieved for hydrophilic drugs. The release profile of RIF was deemed acceptable.	(Mehta and Jindal, 2013)
Ethionamide and D-cycloserine	Niosomes	Ethanol injection	-	The formulation inhibited bacteria more than free drugs	(Kulkarni et al., 2019)
RIF, INH, PZA	Liposomes	Thin film hydration	Rats	The efficacy of INH/RIF/PZA was enhanced both in vitro and in vivo, as compared to the individual drugs in their unbound form.	(Bhardwaj et al., 2013)
RIF, INH, PZA	Nanoliposomes	reverse-phase evaporation	-	demonstrated negligible cytotoxicity and influenced THP-1-derived macrophage viability.	(Yang et al., 2022)

Although only a few studies focused on using these vesicular-based drug systems, have been reported for EPTB, most especially CNS, and bone-TB. However, using these drug delivery systems is of great potential for targeted therapy (Pinheiro et al., 2011). The lipid bilayer of liposomes and niosomes mimics the structure of cell membranes, enabling them to easily fuse with the target microbe's plasma membrane

and deliver drugs. Niosomes can also be employed for prolonged drug delivery, which reduces drug consumption and adverse effects by boosting their bioavailability (Bartelds et al., 2018; Chen et al., 2020; Kazi et al., 2010). Liu et al. (2019) created a self-healing and temperature-responsive hydrogel-based liposomal system that contained a modified form of isoniazid called N′-Dodecanoylisonicotinohydrazide (DINH) for treating bone TB (Liu et al., 2019). The technique employed for the development of liposomes is thin-film hydration, and the produced liposome was integrated into the PLGA-PEG copolymer hydrogel matrix (Liu et al., 2019). *In-vitro*, the system exhibited extended drug release capabilities, while microdialysis (MD) and optical imaging indicated *in vivo* sustained drug release (**Figure.2.11**), illustrating the practical benefits afforded by liposomes (Liu et al., 2019).

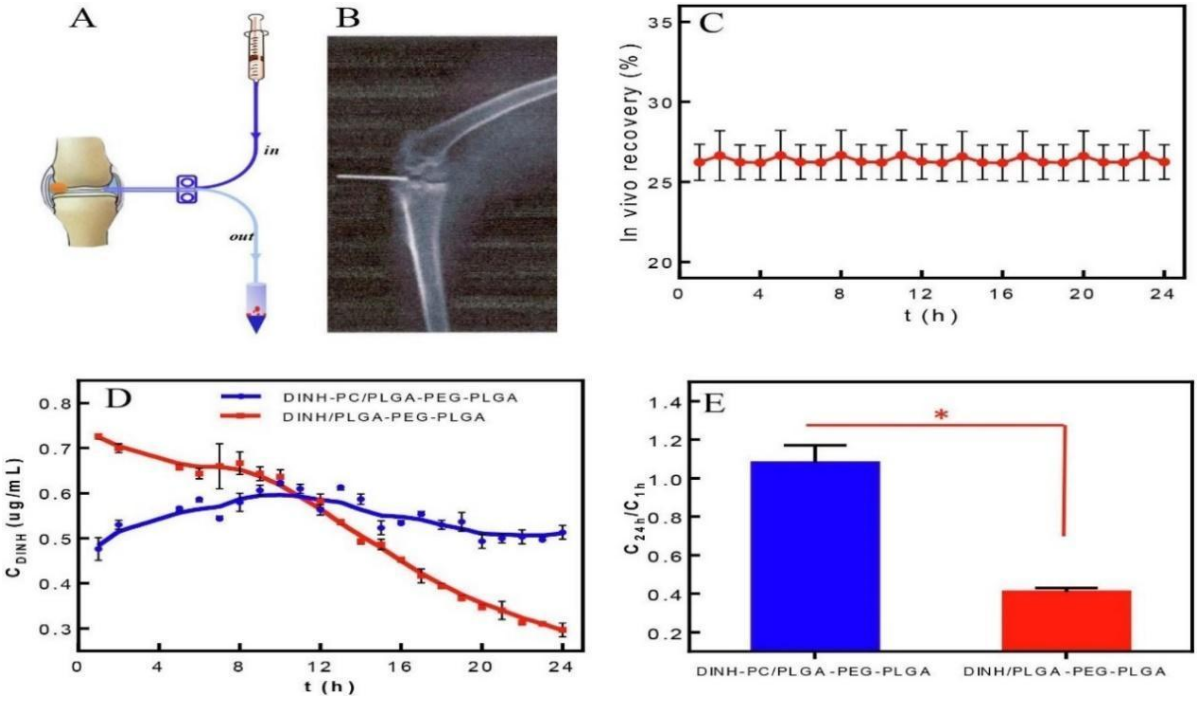


Figure 2.11: (A) A graphical representation of the in vivo pharmacokinetic analysis. (B) An X-ray image showing the implantation of the MD probe in the joint cavity. (C) The stability of the in-vivo recovery of the MD probe. (D) The in-vivo profiles of the concentration-time of DINH in synovial fluid. (E) The ratios of C24h/C1h were obtained from (D). (Reprinted from Liu et al., 2019, with permission).

A recent study by Yang et al., (2022), explored the use of a positively charged liposome system to treat spinal TB caused by *Mycobacterium tuberculosis* (Yang et al., 2022). The aim was to improve the efficacy of anti-TB treatments and reduce the release of transforming growth factor (TGF-1) in macrophages to promote *Mycobacterium tuberculosis* clearance by encapsulating anti-TB drugs and short interfering RNA

(siRNA) to downregulate TGF-β1 in human macrophages (Yang et al., 2022). However, the study had limitations, including a lack of antimicrobial susceptibility testing and *in vivo* studies to support the findings.

2.4.2.1.3. Solid lipid nanoparticles-based drug delivery system

In recent years, the creation of drug delivery methods such as solid lipid nanoparticles (SLNs) has led to significant progress in the treatment of various diseases (Khatak et al., 2020; Paliwal et al., 2020). SLNs are a type of colloidal drug delivery system that can incorporate both hydrophilic and lipophilic drugs within their solid hydrophobic lipid core. They are gaining popularity as a possible alternative to polymeric nanoparticles and vesicular drug delivery systems as carriers for drugs (Geszke-Moritz and Moritz, 2016; Khatak et al., 2020; Mehnert and Mäder, 2012). Henceforth, SLNs offer a longer/higher stability, increased encapsulation efficiency, and need little quantity of organic solvents in comparison to the two other drug delivery systems (Khoza et al., 2022). Furthermore, the use of SLNs for targeted drug delivery has been reported for different routes of administration, which include oral (Bhalekar et al., 2017), parenteral (Yang et al., 1999), rectal (Sznitowska et al., 2001), ophthalmic (Singh et al., 2019), and topical (Bhalekar et al., 2017).

Singh et al., (2019) synthesized a targeted SLN strategy against *Mycobacterium tuberculosis* infection of an EPTB origin which is ocular (Singh et al., 2019). The justification for the design of such a system emanated from the challenges that the eye presents in drug delivery, such as highly impenetrable eye milieu, immediate washout by tears, drainage via the nasolacrimal duct, and ineffective absorption. Hence, it was necessary to evaluate the suitability to deliver INH into the eye following topical application as drops (Singh et al., 2019). The formulation exhibited prolonged release, increased corneal permeability, considerable *in-vitro* and *in vivo* absorption of fluorescein-labeled SLNs, and a 4.2-fold ocular bioavailability (Singh et al., 2019). Compared to the free drug value, the reduced MIC value of the INH-SLNs suggested increased Mycobacterial absorption and intracellular retention, making the system potentially an anti-TB drug nanocarrier.

In another work, Bhandari et al., (2013) developed orally administered SLNs loaded with INH to improve the limitations related to INH and enhance its oral bioavailability (Bhandari and Kaur, 2013) The author conducted pharmacokinetic, tissue distribution, and relative bioavailability studies in rat models to achieve this. The release profile of

the formulation showed a burst release in the initial hour and a slow release post the first hour up to 24 hours. Moreover, the *in vivo* experiments showed that the bioavailability of INH in plasma and brain significantly increased when isoniazid was administered as solid lipid nanoparticles (SLNs) compared to the free drug solution at the same dose (Bhandari and Kaur, 2013). SLNs are an excellent carrier to deliver drugs, more specifically anti-TB drugs, as improved relative availability of drugs can be achieved in different organs.

To the best of our knowledge, the literature has not yet reported any SLN system for CNS-TB and bone-TB. However, due to favorable observed outcomes of SLNs for targeted delivery of drugs for other CNS and bone conditions, this nanosystem can be investigated further for potential use in CNS-TB and Bone-TB targeted drug delivery. A study by Kakkar et al., (2011) demonstrated that curcumin-loaded SLNs (C-SLNs) provided enhanced bioavailability and permeability in mice brains for the cure of Alzheimer's disease (Kakkar and Kaur, 2011). The research highlights the potential of solid lipid nanoparticles (SLN) to enhance the ability of drugs to penetrate the blood-brain barrier and suggests that it is a hopeful drug-targeting approach for treating central nervous system disorders.

2.4.2.2. Inorganic nanoparticles

The study of nanoparticles has reached a thrilling new stage with the discovery of inorganic nanoparticles. They have exceptional physical and chemical properties and offer numerous potential applications in the biomedical, physical, and pharmaceutical fields. The use of inorganic nanoparticles also has the advantage of their smaller size, which makes it easier to administer drugs, as they can cross cell barriers that traditional drugs cannot, such as the blood-brain barrier. The study of inorganic materials loaded with drugs or not for treating various diseases through tissue targeting has been documented.

2.4.2.2.1. Metallic nanoparticles

Metal nanoparticles are nanoscale particles of pure metals (e.g., gold, platinum, silver, titanium, zinc, cerium, iron, and thallium), bimetallic (FePt), and metal oxides (Ceo_2, and SiO_2) (Mody et al., 2010; Yaqoob et al., 2020). In recent years, there has been a significant increase in the use of metallic nanoparticles as carriers for delivering drugs to treat various illnesses (Yaqoob et al., 2020). These nanoparticles can enter

biological or physiological membranes that are usually impermeable to macromolecules due to their tiny size (Singh et al., 2016).

As previously stated, the diagnosis of *Mycobacterium tuberculosis*, especially in the EPTB context, has been poor and yields the progression of the disease. Hussain et al., (2013) developed unmodified gold (Au) nanoparticles to detect different types of *Mycobacterium tuberculosis* strains directly and rapidly. The findings indicated that the prototypes produced are uncomplicated, responsive, and quick, and can serve as an alternative to PCR-based detection methods (Hussain et al., 2013). Furthermore, the treatment against *Mycobacterium tuberculosis* with metallic nanoparticles free of the drug has been extensively reported, especially with silver (Ag), zinc, and Au metals individually and combined. Furthermore, Ag nanoparticles are the most favourable metal in treating *Mycobacterium tuberculosis* due to their antimycobacterial potency. However, this system has shown low selectivity to *Mycobacterium tuberculosis* in comparison to the individual use of drugs. Thus, Singh et al., (2016) exhibited that combining Au and Ag nanoparticles may yield greater efficiency, specificity, and selectivity to kill *Mycobacterium tuberculosis* (Singh et al., 2016). In addition, Au nanoparticles have beneficial impacts on the development of bone.

Iron oxide nanoparticles have been the subject of investigation as another type of metallic nanoparticle due to their exceptional characteristics, including superparamagnetism, high surface-to-volume ratio, substantial surface area, and straightforward separation process (Jabbar et al., 2022; Padwal et al., 2015). They have also been studied for their potential use in delivering anti-tuberculosis medications, including for the treatment of EPTB (Lee et al., 2012, p.; Miranda et al., 2018).

2.4.2.2.2. Mesoporous silica nanoparticles

Compared to other inorganic nanoparticles, MSNs have adequate biocompatibility and highly organized and stable porous networks into which large amounts of the drug may be loaded (Bharti et al., 2015). In addition, the size, shape, and pore characteristics of MSNs may be significantly manipulated during synthesis processes, producing numerous nanoparticle formulations from the same composite materials (Bharti et al., 2015; Sun et al., 2021; Yu et al., 2018). MSNs are frequently capped with a gatekeeper that inhibits sudden and unexpected drug release, allowing for regulated drug release (Bharti et al., 2015; Karimi et al., 2016).

MSNs have been investigated extensively as possible drug delivery vehicles. Concerning treatment against *Mycobacterium tuberculosis,* Clemens et al. (2012) developed INH and RIF-loaded MSNs by designing two different MSNs formulations for each anti-TB drug (Clemens et al., 2012). The two different formulations include (F1) MSNs modified through functionalization with a cationic polyethyleneimine (PEI) polymer to increase cellular absorption and lysosomal release while still allowing the porous interior to be used for drug binding and delivery and (F2) MSNs modified with pH-operated beta-cyclodextrin nano valves. The results demonstrate that F1 exhibited a much higher loading of RIF compared to uncoated MSN and significantly higher effectiveness against macrophages infected with *Mycobacterium tuberculosis*. In addition, F2 demonstrated higher effectiveness at killing *Mycobacterium tuberculosis* inside macrophages than an equal quantity of free drug (Clemens et al., 2012).

The limited biodegradability of MSNs is one of their disadvantages (Pohaku Mitchell et al., 2012; Yu et al., 2018). A recommended approach for adjusting the biodegradability of MSNs is to dope them with metal cations, such as gold, calcium, iron, and manganese (Pohaku Mitchell et al., 2012). In a recent study, Sun et al. (2021) produced a gold-loaded MSN for the treatment and diagnosis of *Mycobacterium tuberculosis* (Sun et al., 2021). The *in-vitro* antimicrobial test revealed that the formulation maintained substantially reduced MIC values and could efficiently destroy *Mycobacterium tuberculosis* (Sun et al., 2021).

2.5. Design of a multi-purpose novel platform

As previously mentioned, *Mycobacterium tuberculosis* effective treatment in the context of EPTB does not only require drug therapy; however, surgery may be necessary for some affected organs such as the bone. Surgery procedures involve the loss of a specific portion of the tissue, which induces a defect in that tissue (Hegazy et al., 2021; Rajasekaran et al., 2014). Thus, any missing piece of tissue due to surgery must be replaced with a proper functional alternative, and this speaks to tissue engineering (TE) in regenerative medicine (Chan and Leong, 2008; O'Brien, 2011). Therefore, providing a TT multi-purpose platform will ensure drug delivery and TE to achieve the optimum therapeutic outcome (Baptista and Guedes, 2021).

Bone is a complex and dynamic tissue capable of performing various functions, and responding to various metabolic, physical, and endocrine stimuli (Chindamo et al., 2020). Bone consists of different structures, and the functions vary from mobility to

protection of essential organs. This tissue may also vary in mechanical strength and modulus, for example, cortical bone has a higher Young's modulus and compressive strength (Blumer, 2021; Chindamo et al., 2020; Morgan et al., 2018). Cortical bone is 30–211 MPa strong and 16–20 GPa elastic. Cancellous bone is 51–193 MPa strong and 4.6–15 GPa flexible. Despite the complexity of its features and shapes, its tiny hierarchical design is relatively straightforward (Morgan et al., 2018). The extracellular matrix (ECM) of bone is composed of a non-mineralized organic component, type-1 collagen, and a mineralized inorganic component. The nanocomposite structure, which is comprised of rigid and flexible collagen fibers supported by hydroxyapatite crystals, plays a crucial role in providing the necessary compressive strength and high resistance to fracture that is essential for bone tissue (Chindamo et al., 2020; Lin et al., 2020).

The individual use of NTT systems, as described in section 4, has been explored in TE, and their fundamental role is to facilitate tissue growth. However, certain limitations with most of the NTT platforms, especially in bone diseases, have hindered the success of these systems in achieving acceptable BTE. Limitations of the singular system include that most of these systems are designed for either oral or parenteral administration, making it challenging to target a specific organ (Suleman et al., 2021). For example, physical support is required in bone regeneration after losing bone tissue; these systems don't provide for that. Therefore, the development of multi-purpose targeted therapy (MPTT) is another approach that is being actively researched by orthopedics in infectious diseases that affect the skeletal system, such as spinal-TB, to provide delivery of different compounds for treatment against *Mycobacterium tuberculosis* whiles providing regenerative properties and support to the bone. In addition, the use of MPTT therapies would have a positive impact on patients with EPTB by shortening the duration of treatment and thus decreasing the occurrence of side effects and enhancing patient compliance. In general, MPTT is a treatment in which drugs or other substances are explicitly delivered to the targeted body's organ, cellular and subcellular level (Devarajan et al., 2015; Ji et al., 2012; Majeed et al., 2021; Tewabe et al., 2021, 2021).

There has been a growing interest in BTE, which includes restoring damaged tissue structure or function with live cells (Preethi Soundarya et al., 2018). BTE employs scaffolds to provide regenerative properties and support the dramatic bone structure. Although some may define scaffolds as MPTT platforms, the challenge is that scaffolds

have been shown to have poor and erratic behavior as carriers of either drugs or other compounds, such as growth factors (Alvarez and Nakajima, 2009; Baptista and Guedes, 2021). Therefore, it would be beneficial to combine nanoparticles with scaffolds for the sole reason of MPTT.

2.5.1. The role of scaffolds in bone tissue engineering

A scaffold can be described as an engineered support structure that promotes the growth of three-dimensional (3D) tissue. Furthermore, these structures are not intended to be permanent implants and should facilitate the replacement of the scaffold material by host cells through the deposition of extracellular matrix (ECM) (Preethi Soundarya et al., 2018; Webber et al., 2015). For a scaffold to be approved for bone regeneration, it must fulfil specific acceptance criteria, as illustrated in **Figure 2.12** (Chan and Leong, 2008; Garg et al., 2012; O'Brien, 2011). Therefore, scaffolds are fabricated using biomaterials to achieve the desired properties discussed. Biomaterials are substances that have an interaction with biological systems, and this topic will be covered in this review section.

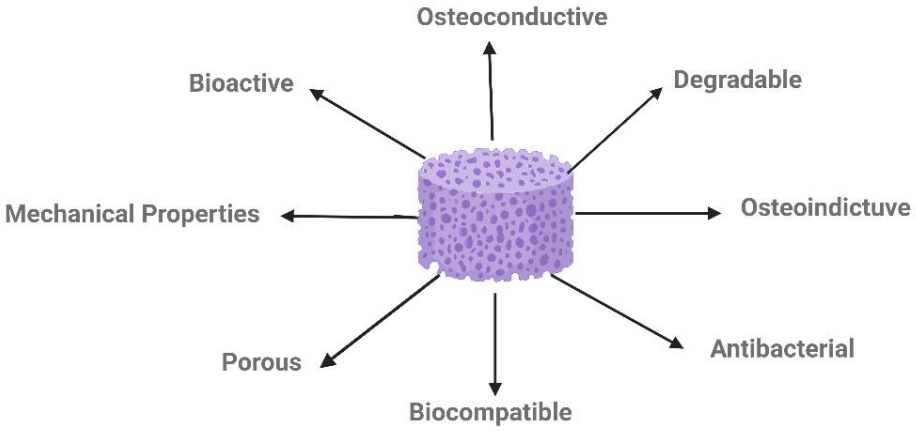


Figure 2.12: Diagram demonstrating the features that a 3D scaffold made from biomaterials should possess (Chan and Leong, 2008; Garg et al., 2012; O'Brien, 2011).

Novel biomaterials are available in various forms, including biopolymers, bioceramics, and biodegradable metals. **Table 2.7** depicts each of these biomaterial's advantages and limitations. Most of these biomaterials must be engineered to provide biocompatible and mechanical qualities for medicinal uses (Nikolova and Chavali, 2019). A range of established methods for fabricating scaffolds composed of

biomaterials using 3D printing has been developed and put into practice, including selective laser sintering (SLS), stereolithography (SLA), inkjet 3D printing, and fused deposition modelling (Williams et al., 2005). All these 3D printing technologies involve layer-by-layer material patterning to create the desired structure/object. 3D printing enables exact control over the scaffold's form, pore size, and interconnectivity and reduces production time. In addition, 3D printing is the preferred approach for fabricating 3D biomaterial scaffolds for BTE in regenerative medicine.

Table 2.7: Summary of different individual-component biomaterials used for bone tissue scaffold (Nikolova and Chavali, 2019; O'Brien, 2011).

Biomaterial	Examples	Advantages	Limitations	Application
Natural polymers	Alginate, chitosan, silk, gelatin, and DNA	- Superior biocompatibility - Natural remodeling - Easily recognized by cells and better adhesion	- Its mechanical qualities are inadequate for load bearing. - Rapid degradation rate	-Hard and soft tissue. -Gene therapy
Synthetic polymers	Polycaprolactone, Poly-l-lactic acid, PLGA, polyglycolic acid	- High mechanical strength - Can be altered variously	- Slow degradation rate - Inadequate cell affinity	Tissue engineering scaffolds
Bioceramics	porous bioglass, calcium silicate, calcium sulphate	-Good Bioactivity - Good biocompatibility - Osteoconductive	- Brittle - High stiffness - low flexibility	- Replacement of hard tissue - Orthodontic use
Metals	TiO2, Ti–6Al–4V, stainless steel	- High mechanical strength - Easy to produce and sterilize	-Corrosive	- Orthopaedic Implants - screws, pins, and plates

2.5.1.1. Individual component and combined component biomaterials

Biomaterials, as mentioned above, play a massive role in developing 3D-printed biomaterial scaffolds (Nikolova and Chavali, 2019). These biomaterials may be employed individually or in combination. The current challenges in developing 3D-printed scaffolds for bone tissue engineering include the limited mechanical strength

and cellular compatibility of available biomaterials and the limited selection of printable biomaterials (O'Brien, 2011; Preethi Soundarya et al., 2018). Thus, individual-component biomaterials have limited qualities, hence, their printability and properties must be adjusted to completely reproduce the properties of the tissue under study using 3D printing technical approaches (Chindamo et al., 2020; Garg et al., 2012; Preethi Soundarya et al., 2018).

To overcome challenges with individual-component biomaterials, adequate research has shown and proved that the blending two or more biomaterials to create composite (hybrid) multi-biomaterial 3D scaffolds, the biomaterial qualities may be enhanced, benefiting from the merged properties of the two or more biomaterial of interest (Mahdy et al., 2021; O'Brien, 2011). For example, combining natural + synthetic polymers + bioactive glass in producing a 3D biomaterial scaffold has shown promising results for BTE, as the bioactive components (such as bioceramics) improve osteogenesis, bioactivity, and mechanical strength (Daskalakis et al., 2022; Yao et al., 2014). In addition, the physical/chemical bonding of bioceramics into polymeric/biomaterial scaffolds may alleviate the mechanical property limits of pure biomaterials or individual-component biomaterials. Most bioceramics are mixed with polymers to improve their printability (Alaribe et al., 2016; Nikolova and Chavali, 2019; O'Brien, 2011). The choice of appropriate biomaterial/s for scaffold development depends on the tissue needs that one is targeting (Chan and Leong, 2008).

Ongoing investigations are underway to explore the utilization of 3D-printed scaffolds made from biomaterials for bone-TB therapy. Table 8 presents an overview of the various individual and multi-component biomaterials utilized in these scaffolds. These biomaterials offer unique advantages, such as enhanced bioactivity, controlled drug release, and improved mechanical strength, enabling the development of advanced scaffolds for bone-TB therapy (Alaribe et al., 2016; Dong et al., 2014; Zhu et al., 2015). Their incorporation into 3D-printing technology holds tremendous potential for transforming the field of bone-TB treatment, opening doors to personalized and effective therapeutic approaches (Pei et al., 2018a; Yuan et al., 2015; Zhu et al., 2015). Further research and development efforts are warranted to optimize scaffold design and fully harness their clinical potential in addressing the complex challenges associated with bone-TB management.

Recent studies have aimed at creating new biomaterial scaffolds for delivering therapeutic agents such as proteins and drugs, and it is important to secure these molecules to the platform for efficient loading. Bone Morphogenic Protein-2 (BMP-2) and Vascular Endothelial Growth Factor (VEGF) are examples of proteins introduced to scaffolds. The interaction between biomaterials and cells is crucial for cell survival, growth, and differentiation, so the features of biomaterials such as surface chemistry, charge, roughness, reactivity, hydrophilicity, and stiffness must be considered.

Table 2.8: Highlights the different individual/multi-component biomaterials utilized in the development of 3D-printed scaffolds explored in bone-TB.

Biomaterial/s	Type of material/s	Benefits	Limitations	References
Tantalum	Metal	Achieved Antibacterial Properties and Good Biocompatibility	The scaffold exhibited mild cytotoxicity during the early stages of implantation.	(Hua et al., 2022)
PHBHHx/ MBG-COOH	Natural polymer/ bioceramic	Scaffolds exhibit prolonged drug release compared to commercial scaffolds. Drugs maintain high concentrations in peripheral tissues but low levels in the bloodstream.	The study didn't include biodegradability and porosity studies	(Zhu et al., 2015)
Polycaprolactone (PCL)	Synthetic polymer	No cytotoxic effect from the scaffold and easy printability.	Erratic drug release and low drug entrapment. Limited bioactivity. Additionally, the study didn't conduct any *in vivo* studies to show the release profile of the drug.	(Lee et al., 2020)
β-tricalcium phosphate/PLGA	Bioceramic/synthetic polymer	The bone scaffold displayed strong compression resistance and high porosity. *In vivo*, it achieved a stable 90-day drug release, effectively eliminating tuberculosis bacteria and promoting bone regeneration.	This study was unable to achieve precise control over the drug release from the microspheres.	(Yuan et al., 2015)

		Promising for future bone-TB treatment.		
MBG/FE	Bioceramic/metal	Excellent sustained release of anti-Tb drugs, with enhanced mechanical strength. Good bioactivity and pH control	Lack of *in vivo* studies for correlation.	(Pei et al., 2018a)
Polylactide Acid	Synthetic Polymer	Excellent biodegradability profile of the scaffold	Limited *in-vitro* and *in vivo* studies	(Wardhani et al., 2019)

2.5.1.2. Combined efforts of nanoplatforms and scaffolds

Over the past few years, many 3D-printed biomaterial scaffolds have been studied for BTE applications. In addition, the developed biomaterials scaffold platforms also possess qualities for targeted/localized drug delivery interventions for bone tissue (Pei et al., 2018a; Zhu et al., 2015). However, these platforms have been proven to have poor drug delivery characteristics, which results in poor therapeutic outcomes, especially in infectious bone diseases such as spinal TB. The use of nanoparticles offers a consistent and gradual release of the substance, resulting in a high concentration at the site of action for maximum therapeutic effect. Applying suitable biomaterials in combination with nanoparticles in bone disease, including spinal TB, has proved to possess great potential for enhanced bone regeneration and targeted drug delivery interventions

2.5.2. Pros and Cons of 3D-printed scaffolds embedded with conventional drug delivery systems.

The current advancements in the field of 3D-printing of scaffolds incorporated with drug delivery systems exemplify the continuous efforts being made toward personalized medicine, which is required in several applications (Hua et al., 2022; Suleman et al., 2021; Zhu et al., 2015). These scaffolds, developed using advanced additive manufacturing techniques, offer a unique approach to delivering drugs in the field of TE and regenerative medicine. However, they also present certain challenges that need to be considered for their effective implementation. **Table 2.9** presents the various pros and cons to consider with 3D-printed scaffolds embedded with conventional drug delivery systems.

Table 2.9: Provides an overview of the different pros and cons associated with the utilization of 3D-printed scaffolds embedded with conventional drug delivery systems (Domsta and Seidlitz, 2021).

Pros	Cons
● By integrating these conventional drug delivery systems into the 3D-printed scaffolds, precise and targeted drug release can be achieved. This allows for localized delivery of drugs directly to the tissue site of interest, enhancing therapeutic effectiveness while minimizing systemic side effects.	● Designing multi-functional 3D-printed scaffolds incorporating organic and inorganic drug delivery systems can be a complex process. Achieving the desired scaffold architecture, porosity, and drug loading capacity while ensuring structural integrity and biocompatibility requires careful consideration and optimization.
● The combination of 3D-printed scaffolds and conventional drug delivery systems promotes tissue regeneration by providing a supportive structure for cell growth while simultaneously delivering therapeutic agents. This synergy accelerates the healing process and improves the overall quality of tissue repair.	● The compatibility between the drug, scaffold material, and drug delivery system is critical for successful implementation. Certain drugs may have limited compatibility with the utilized biomaterials or drug delivery system, posing challenges in achieving effective drug release and maintaining therapeutic efficacy.
● These scaffolds enable precise control over the release kinetics of drugs. Different drug release profiles can be achieved by modifying the scaffold's design, composition, or the drug encapsulation method, allowing for tailored release patterns based on specific treatment requirements.	● Understanding the long-term performance and degradation of these multi-functional scaffolds is crucial. Factors such as scaffold degradation rates, drug stability over time, and maintaining controlled release profiles need to be thoroughly evaluated to ensure sustained therapeutic effects and avoid potential complications.
● 3D-printing technology allows for the fabrication of scaffolds with patient-specific designs and dimensions. This customization enables the development of personalized treatments where the scaffold, along with the embedded drug delivery system, can be tailored to meet the unique needs of each patient.	● Regulatory approval for these scaffolds may involve additional scrutiny due to the combination of medical devices and pharmaceuticals. Navigating the regulatory landscape and demonstrating safety, efficacy, and quality assurance may pose challenges for manufacturers seeking market authorization.

These multi-functional scaffolds offer several advantages, including targeted drug delivery, enhanced tissue regeneration, controlled release profiles, and customization for patient-specific treatments. However, challenges related to scaffold design complexity, compatibility issues, long-term performance, and regulatory considerations need to be addressed to ensure their successful integration into clinical practice. Continued research, collaboration between different disciplines, and regulatory

guidance are essential for harnessing the full potential of this innovation technology in TE and regenerative medicine. In this review, potential 3D printed scaffolds employed for the intention of MPTT in bone tissue and their application in bone-TB and other similar bone infections are discussed in detail.

2.5.3. Polymeric Nanoparticles and 3D Printed Scaffolds

Polymeric nanoparticles have been demonstrated to be highly effective carriers of various substances, such as drugs and growth factors. Furthermore, novel and innovative research on incorporating these nanoparticles in 3D-printed scaffolds for other tissues, including bone tissue, has been ongoing. The proof-of-concept study by Yuan et al. (2015) explored the use of 3D printing technology embedding PPLGA-composed microspheres loaded with anti-TB drugs for bone-TB, RIF, and INH. The study evaluated the *in vivo* performance of these structures, including mechanical studies, osteogenesis, cell viability, and migration using Wistar rat models. To assess the cell viability, the study utilized rBMSCs cells and these were analysed through MTT assays. The results showed that the scaffold was not toxic to the mentioned cells (**Figure. 13**). The PLGA microspheres containing the two drugs were synthesized through solvent evaporation method, respectively, and incorporated into the β-tricalcium phosphate scaffold by employing the centrifugation method. During *in-vitro* testing (**Figure. 2.13**), it was observed that the PLGA microspheres formulations embedded in the scaffold had an erratic release profile in the first 10 days of testing and then stabilized until day 90 (Yuan et al., 2015). The erratic release behaviour is not desirable in TT and is suggested to be caused by the method employed to incorporate the microspheres into the scaffold. Additionally, the loading capacity of the microspheres was relatively low, and this improved with an increase in concentrations of the PLGA solution.

A

Group	OD value			ALP (U/100ML)
	24h	48h	72h	
Control	0.44 ±0.01	0.45 ±0.05	0.46 ±0.03	14.33 ±0.14
Experimental	0.41 ±0.03	0,43 ±0.03	0.44 ±0.02	6.34 ±0.34
RGB%	107	104	104	
Cytotoxicity	0	0	0	

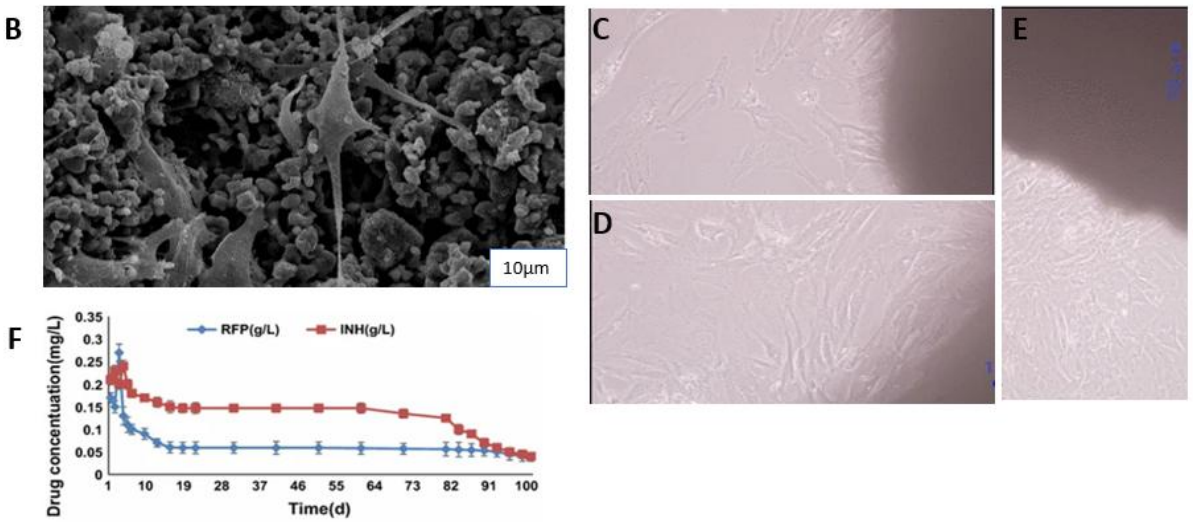


Figure 2.13: (a) Cell viability results, **(b)** SEM image depicting adhesion of scaffold to the rBMSCs cells, (**c, d, e**) inverted phase contrast microscope of the scaffold on the cells at 24hr, 48hr, and 72hr, respectively, **(f)** Drug release profile of the two anti-TB drugs from the β-TCP/PLGA microspheres scaffold (Reprinted from Jing Yuan et al., 2015 with permission).

Kim et al. (2018) developed a 3D-printed hydroxyapatite scaffold that incorporated PLGA nanoparticles filled with BMP-2 for the treatment of bone defects (Kim et al., 2018). A four-step process was undertaken to achieve the desired 3D-printed scaffold (**Figure. 2.14A**). The scaffold composition consisted of a bioceramic (hydroxyapatite) reinforced by synthetic polymer (PCL) to assist with mechanical strength. On the other hand, the polymeric nanoparticle consisting of BMP-2 encapsulated in PLGA polymer was synthesized via a double emulsion-solvent evaporation technique. Furthermore, the nanoparticles were incorporated into the scaffold by coating the surface of the platform with PCL with the PLGA nanoparticles. The described process produced a 3D-printed scaffold with increased compressive strength and bestowed the scaffold with a BMP-2 releasing function. This study utilized Human bone marrow-derived mesenchymal stem cells (hMSCs) to assess the cellular toxicity of the 3D-printed scaffolds. The PCL_BMP-2/NPs scaffold exhibited excellent cellular cytocompatibility, demonstrating its optimal compatibility with cells (Figure. 14B). The fluorescence

images of live and dead cells revealed high cell viability on the scaffolds, indicating that the majority of hMSCs remained viable. Additionally, no cytotoxic effects were observed in the study. In a rabbit calvarial defect model, the PCL BMP-2/NPs scaffolds that were constructed showed minimal toxicity, and improved bone regeneration. The release profile of the BMP-2 in the nanoparticles alone showed a burst release profile, and this is not a desired quality in BTE as a slow, sustained release is required as the implant will be in the bone for a specific period. This was achieved when the PLGA nanoparticles were coated on the scaffold, which was attributed to the mixture of the PCL with the nanoparticle.

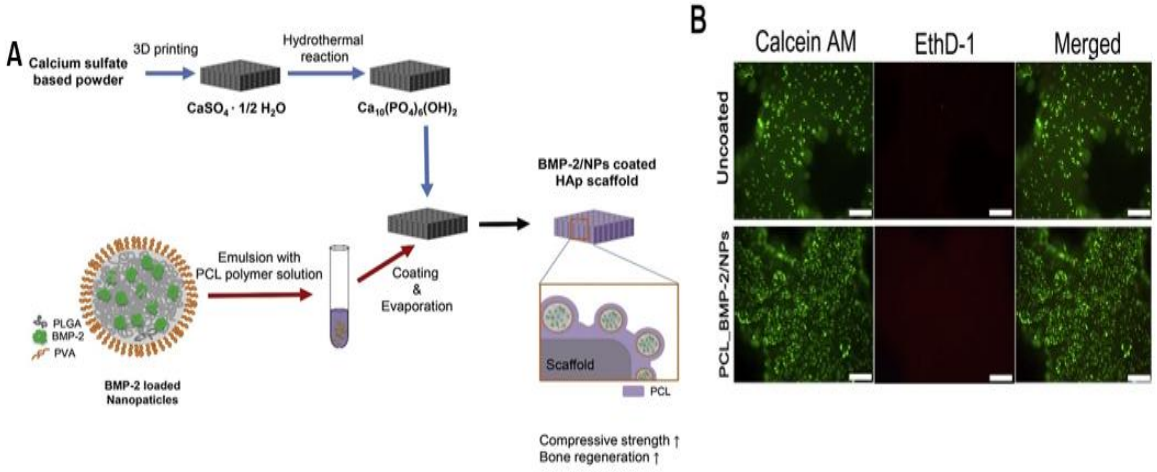


Figure 2.14: The diagram depicts **(a)** the procedure involved in developing PLGA nanoparticles for BMP-2 delivery, and **(b)** The viability and cytotoxicity analysis conducted five days after seeding. (Reprinted from Beom-Su Kim et al., 2018 with permission).

The use of PLGA has also been applied in developing not only nanoparticles but also microspheres that can be integrated into 3D-printed scaffolds. Zhou et al. (2018) developed a PCL/Polydopamine (PDA) 3D-printed scaffold for a bone infection (Zhou et al., 2018). The platform was loaded with vancomycin-containing PLGA microcarriers. Vancomycin was incorporated into PLGA microspheres to ensure its sustained release. The microspheres were synthesized through the double-emulsion solvent evaporation process, while the scaffold was produced using a 3D printer that employs the fused deposition technique. The adsorption process achieved the incorporation of the microsphere into the surface of the platform. The study exhibited that immediate burst release of vancomycin from a scaffold-free of microspheres

occurs, with the most significant release happening within 3–5 days. However, a slow and sustained release was reported with the incorporation of the drug into the microsphere and into the scaffold (Zhou et al., 2018). *In vivo,* studies are needed to ensure this claim's credibility and proof of concept.

To the best of the author's knowledge, no studies have reported the use of an MPTT platform that incorporates polymeric nanoparticles into the surface of a 3D-printed scaffold for the treatment of bone TB. However, the exploration of such MPTT platforms for bone-TB is necessary since polymeric nanoparticles have been demonstrated to have the capacity to contain anti-TB drugs. Furthermore, bone proteins may also be encapsulated into the polymeric nanoparticles to ensure a biomimetic environment, as research has shown that they can be encapsulated into the polymeric nanoparticles, especially PLGA. It is clear from the perspective of biomaterials that various biomaterials can be combined effectively with polymeric nanoparticles.

2.5.4. Lipidic nanoparticles and 3D printed scaffolds

The efficacy of using lipids as a drug delivery mechanism has been proven, particularly against *Mycobacterium tuberculosis*, as described in *sections 4.1.1.2* & 4.1.1.3. Lipid systems are excellent carriers for hydrophobic drugs. Hence, hydrophobic anti-TB drugs such as RIF and BDQ may be great candidates to be encapsulated by lipid systems. Liposomes have been employed as a drug carrier in 3D-printed scaffolds for bone tissue application. For example, Sarkar et al. (2019) fabricated a 3D-printed calcium phosphate (CaP) scaffold incorporated with liposomes filled with curcumin for the cure of bone cancer (Sarkar and Bose, 2019). The liposomes were fabricated through a technique referred to as thin-film hydration, which is wildly used and ensures high encapsulation. The alteration of the different liposome formulation parameters achieved a 68% encapsulation efficiency. Interestingly, the liposomal-loaded curcumin produced using 3D printing showed remarkable cellular toxicity against osteosarcoma cells grown in the laboratory, while promoting the survival and growth of osteoblasts (Sarkar and Bose, 2019). This study implies that liposome systems can be effectively combined with bioceramic biomaterials. **Table 2.10** shows lipid systems used with other biomaterials in BTE.

Table 2.10: Examples Lipid system that has been employed within scaffolds.

Biomaterial/s utilized for scaffold	Lipidic system	Drug encapsulated	Key findings	References
Polycaprolactone (PCL)	Nano-liposome	Asprin	Aspirin can be enclosed within nanoliposomes and stimulate osteogenesis and the modulation of the immune system in human mesenchymal stem cells (hMSCs).	(Li et al., 2019)
gelatin methacrylate	Solid lipid nanoparticles	Resveratrol	Studies both in the laboratory and in living organisms demonstrate that the various SLNs/GelMA scaffolds enhance the osteogenic differentiation of BMSCs through an optimal, gradual release of the drug.	(Wei et al., 2021)
Calcium Phosphate	Liposomes	Curcumin	Not only did his bifunctional scaffold support the development of bone cells, but it exhibited anti-cancer characteristics.	(Sarkar and Bose, 2019)

Furthermore, just like the polymeric nanosystem, no application of any of this lipid system incorporated in a 3D printed scaffold for bone-TB has been documented or reported as per the publication of this work. However, this proof-of-concept may be investigated for application in bone TB as lipidic systems have been explored for this disease, and BTE is also ongoing research for bone TB.

2.5.5. Metallic nanoparticles and 3D printed scaffold.

Among the various metallic nanoparticles, the most beneficial and positive-yielding nanoparticles in the treatment against *Mycobacterium tuberculosis* are Au and Ag nanoparticles due to their antibacterial properties. Therefore, the Au and Ag nanoparticles can be employed either alone or as carriers of anti-TB drugs onto a 3D-printed scaffold for bone TB. Various studies have been conducted where these

metallic nanoparticles have been incorporated into 3D-printed scaffolds for enhanced bone regrowth and drug delivery properties.

To stimulate osteogenic differentiation, Au nanoparticles were integrated into PCL 3D-printed scaffold coated with PDA (Jin Lee et al., 2018). Studies have been conducted for decades to examine the use of Au nanoparticles as carriers for drug agents due to their unique characteristics, such as their ability to be multi-functionalized, large surface area to volume ratio, increased permeability, high stability, ease of production, and flexible surface chemistry (Singh et al., 2016). The Au nanoparticles are exogenous inducers of reactive oxygen species (ROS). After being exposed to gold nanoparticles, the targeted organ cells go through the process of apoptosis because they cannot tolerate the oxidative stress caused by the excessive creation of ROS (Enea et al., 2020; Li et al., 2020; Sun et al., 2018). It is essential to keep in mind that the cellular response to Au nanoparticles varies significantly across cell lines (Sun et al., 2018). Fan et al., (2011) tested Au nanoparticles of three sizes: Au nanoparticles-S, Au nanoparticles-M, and Au nanoparticles-L on hMSCs (Fan et al., 2011). Au nanoparticles-S demonstrated the maximum toxicity of the three nanoparticle types, whereas Au nanoparticles-M triggered necrosis and killed hMSCs. Less toxic to cells, Au nanoparticles-L reduced osteogenic and adipogenic development (Fan et al., 2011). Concerns have been expressed about using Au nanoparticles as a long-term cell tracer. Safely using gold nanoparticles requires further investigation.

Furthermore, Ag nanoparticles are being studied for their physical, chemical, and biological characteristics (Bhagyaraj and Krupa, 2020; Sharma et al., 2012). The studies have demonstrated the integration of Ag nanoparticles into 3D printed β-TCP scaffolds in the form of Ag-GO nanocomposites, resulting in scaffolds with both osteogenic and antibacterial properties (Zhang et al., 2017). Ag nanoparticles may trigger apoptosis in disease-targeted organ cells by generating ROS, which causes mitochondrial malfunction (Dey et al., 2022). To further reinforce the properties of Ag nanoparticles, the combination of Ag and Au nanoparticles may be beneficial in developing a more effective system (Singh et al., 2016).

2.5.6. Mesoporous silica (MSN)and mesoporous bioactive glass (MBG) nanoparticles and 3D printed scaffold.

MSNs have been utilized in drug delivery due to its extensive nanopore structure. MSNs materials may provide a more practical choice for controlled and localized anti-

TB drug delivery without causing significant decreases in pH (Clemens et al., 2012; Yu et al., 2018). Furthermore, to achieve MPTT, these systems have been incorporated into the 3D printed scaffolds for bone purposes, specifically bone-TB. Zhu et al., (2011) developed a multi-component, anti-TB-loaded, multi-facet 3D printed scaffold for bone-TB (Zhu et al., 2011). The MPTT platform was composed of an MSNs porous β-TCP scaffold and then coated with bioactive glass to enhance slow, sustained release. The results of both *in-vitro* and *in vivo* release assays showed a prolonged pattern of co-release for both RIF and INH from the platform. The drug concentrations remained above their effective values for killing *Mycobacterium tuberculosis* for a period of up to 40 days. (**Figure 2.15**) (Zhu et al., 2011). The prolonged, controlled release of anti-TB drugs in the scaffold is advantageous in bone TB, as it will provide sufficient drug levels for multi-drug treatment post-surgery, effectively eliminating bacteria. This study didn't adequately show the effect of the 3D-printed scaffold in enhancing bone regeneration. Therefore, future studies can focus on *in vivo* for both enhanced bone regeneration and drug delivery systems.

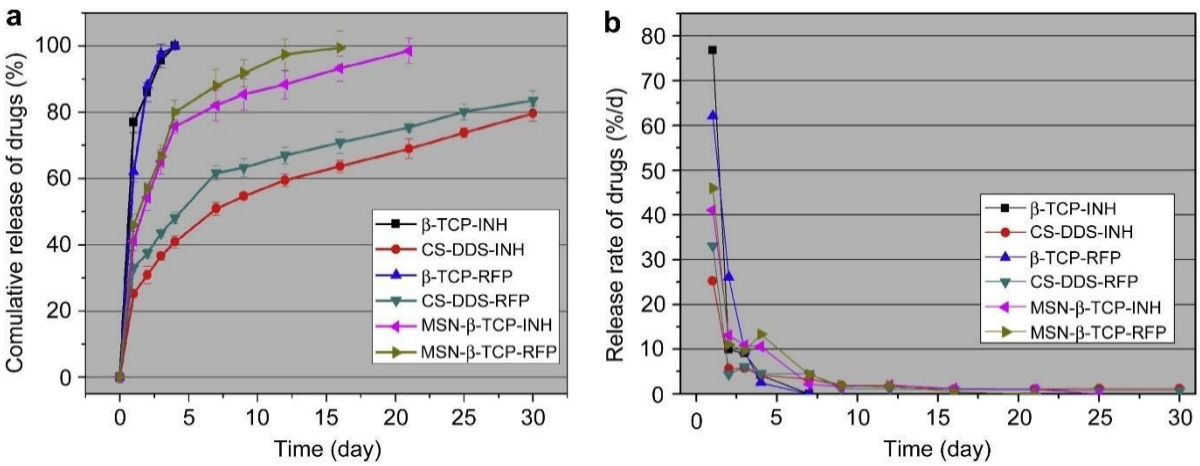


Figure 2.15: Cumulative release **(a)** and release rate **(b)** curves of INH and RIF in SBF at 37 °C from scaffolds. (Reprinted from Zhu et al., 2011 with permission).

However, combined MSN and dense calcium phosphate bioceramics have limited solubility, which hinders osteogenesis. Thus, researchers have suggested replacing the MSN with MBG (Zhu et al., 2015). Bioactive glasses (BG) are solid, nonporous, and hard bioceramics made up of silicon dioxide (or silicate) as the major component and three other essential components: sodium dioxide, calcium oxide, and phosphorus (Kaur et al., 2014). These components can be modified to create various types of bioactive glass. Literature has shown that BG's used for bone regeneration have unique characteristics, including biocompatibility, excellent osteoconductive, and

osteoinductive properties (Cao and Hench, 1996; Jones et al., 2010; Kaur et al., 2014). BG platforms can release ions when in contact with deformed bone, forming a hydroxyapatite-like (HA) layer, facilitating the interaction between the two platforms (Faure et al., 2015; Fernandes et al., 2018; Karadjian et al., 2019; Kaur et al., 2014). In addition, BG platforms have been established as capable of loading and releasing drugs, but their uneven distribution of micropores results in limited drug loading capacity. To address this issue, researchers have suggested using mesoporous bioactive glass (MBG) to enhance drug loading efficiency (Gómez-Cerezo et al., 2021; Wu and Chang, 2012). The M-BGs contain organized mesopores, and tunable pores, and have a high surface area, making them an excellent drug and bioactive factor-controlled release carrier (Vallet-Regi and Salinas, 2021; Wu and Chang, 2012)

Min et al., (2015) fabricated a dual function 3D printed scaffold for bone TB where INH and RIF were impregnated into functionalized MBG and MSN respectively (Zhu et al., 2015). The formation of the bio-ink for 3D printing consisted of the functionalized MBG and MSN with the drug and bonded with 3-hydroxybutyrate-co-3-hydroxyhexanoate (PHBHHx). The *In-vitro* or *in vivo* results indicated that the composite scaffolds released drugs more slowly when compared to commercialized MSN and calcium phosphate scaffolds. These findings are desired as the long-term sustained release of anti-TB drugs needs to be achieved to be able to kill *Mycobacterium tuberculosis* effectively (Zhu et al., 2015). Pei et al. (2018) conducted a study that looked into utilizing a blend of PCL, MBG, and Metal-Organic Frameworks (MOF) to create a 3D-printable scaffold for bone-TB (Pei et al., 2018b). The study utilized INH as the model drug and incorporated it into the MBG using a wetness impregnation method. The MPTT scaffold demonstrated remarkable mechanical stability, primarily due to the presence of MOF in the scaffold structure (Pei et al., 2018b). Furthermore, cell work and *in-vitro* results showed enhanced bioactivity and good scaffold biocompatibility. *In-vitro*, release of the INH from the platform exhibited a sustained drug release behavior (Pei et al., 2018b).

2.6. Concluding Remarks

Significant research data and reports is evaluating the use of nanotechnology-targeted therapy for anti-TB drugs for pulmonary and extrapulmonary TB against *Mycobacterium tuberculosis*. However, there have been limited advances in the development of a multi-purpose system that will address the enhancement of

regeneration medicine and drug delivery in EPTB cases. Bone-TB is the highest form of EPTB, and the treatment protocol necessitates drug therapy and surgical intervention where necessary, especially for bone-TB application.

3D printing technology has lifted many constraints in the production of 3D biomaterial scaffolds for tissue engineering. However, due to the nature of some biomaterials, poor release profile of the drugs/proteins loaded into the 3D-printed scaffold has been reported. Hence, the use of two or more biomaterial to benefit from the combined properties of the different hybrid/merged biomaterials is preferred in 3D printing technology (e.g., 3D-printed biomaterials scaffolds), to attempt to meet the appropriate properties of the tissue of interest, e.g., bone tissue mechanical strength amongst others. The biomaterials for 3D-printed scaffolds can address the regeneration and drug delivery issues. Therefore, a multi-purpose targeted therapy platform comprised of a 3D-printed scaffold integrated with nanoparticles for enhanced bone regeneration and drug delivery is imperative in bone-TB treatment. The combinatory platform's design and development require a thorough investigation into the suitable nanoparticle to be utilized, appropriate biomaterial for 3D printing of scaffold, and an excellent method to combine the two systems.

In conclusion, the mechanical killing of *Mycobacterium tuberculosis* by drugs alone is insufficient in EPTB, such as bone-TB. Nanomedicine has been leading in the new research as a technique used to provide appropriate low doses of drugs to kill the bacterium, while limiting systemic side effects. The development of a multi-functional targeted therapy for bone TB, which utilizes 3D-printed scaffolds blended with biomaterials to promote bone regrowth and integrated with nanoparticles for drug delivery, will greatly enhance the effectiveness of targeted therapy against *Mycobacterium tuberculosis*.

2.7. References

Abuhelwa, A.Y., Williams, D.B., Upton, R.N., Foster, D.J.R., 2017. Food, gastrointestinal pH, and models of oral drug absorption. Eur. J. Pharm. Biopharm. 112, 234–248. https://doi.org/10.1016/j.ejpb.2016.11.034

Agarwal, A., Kandpal, H., Gupta, H.P., Singh, N.B., Gupta, C.M., 1994. Tuftsin-bearing liposomes as rifampin vehicles in treatment of tuberculosis in mice. Antimicrob. Agents Chemother. 38, 588–593. https://doi.org/10.1128/AAC.38.3.588

Ahmad, Z., Pandey, R., Sharma, S., Khuller, G.K., 2006. Pharmacokinetic and pharmacodynamic behaviour of antitubercular drugs encapsulated in alginate nanoparticles at two doses. Int. J. Antimicrob. Agents 27, 409–416. https://doi.org/10.1016/j.ijantimicag.2005.12.009

Ahmad, Z., Sharma, S., Khuller, G.K., 2007. Chemotherapeutic evaluation of alginate nanoparticle-encapsulated azole antifungal and antitubercular drugs against murine tuberculosis. Nanomedicine Nanotechnol. Biol. Med. 3, 239–243. https://doi.org/10.1016/j.nano.2007.05.001

Ahmed, S., Raqib, R., Guðmundsson, G.H., Bergman, P., Agerberth, B., Rekha, R.S., 2020. Host-Directed Therapy as a Novel Treatment Strategy to Overcome Tuberculosis: Targeting Immune Modulation. Antibiotics 9, 21. https://doi.org/10.3390/antibiotics9010021

Akula, P., P. K., L., 2018. Effect of pH on weakly acidic and basic model drugs and determination of their *ex vivo* transdermal permeation routes. Braz. J. Pharm. Sci. 54. https://doi.org/10.1590/s2175-97902018000200070

Alam, Md.S., Phan, K., Karim, R., Jonayed, S.A., Munir, H.K.Md., Chakraborty, S., Alam, T., 2015. Surgery for spinal tuberculosis: a multi-center experience of 582 cases. J. Spine Surg. 1, 65–71. https://doi.org/10.3978/j.issn.2414-469X.2015.07.03

Alaribe, F.N., Manoto, S.L., Motaung, S.C.K.M., 2016. Scaffolds from biomaterials: advantages and limitations in bone and tissue engineering. Biologia (Bratisl.) 71, 353–366. https://doi.org/10.1515/biolog-2016-0056

Alene, K.A., Wangdi, K., Colquhoun, S., Chani, K., Islam, T., Rahevar, K., Morishita, F., Byrne, A., Clark, J., Viney, K., 2021. Tuberculosis related disability: a systematic review and meta-analysis. BMC Med. 19, 203. https://doi.org/10.1186/s12916-021-02063-9

Alqahtani, M.S., Kazi, M., Alsenaidy, M.A., Ahmad, M.Z., 2021. Advances in Oral Drug Delivery. Front. Pharmacol. 12.

Alvarez, K., Nakajima, H., 2009. Metallic Scaffolds for Bone Regeneration. Materials 2, 790–832. https://doi.org/10.3390/ma2030790

Alves, R., Reis, T.V. da S., Silva, L.C.C. da, Storpírtis, S., Mercuri, L.P., Matos, J. do R., 2010. Thermal behavior and decomposition kinetics of rifampicin

polymorphs under isothermal and non-isothermal conditions. Braz. J. Pharm. Sci. 46, 343–351. https://doi.org/10.1590/S1984-82502010000200022

Al-Zanbagi, A.B., Shariff, M.K., 2021. Gastrointestinal tuberculosis: A systematic review of epidemiology, presentation, diagnosis and treatment. Saudi J. Gastroenterol. Off. J. Saudi Gastroenterol. Assoc. 27, 261–274. https://doi.org/10.4103/sjg.sjg_148_21

Arefin, A.M.E., Khatri, N.R., Kulkarni, N., Egan, P.F., 2021. Polymer 3D printing review: materials, process, and design strategies for medical applications. polymers 13, 1499. https://doi.org/10.3390/polym13091499

Bai, D.-P., Lin, X.-Y., Huang, Y.-F., Zhang, X.-F., 2018. Theranostics aspects of various nanoparticles in veterinary medicine. Int. J. Mol. Sci. 19, 3299. https://doi.org/10.3390/ijms19113299

Banks, W.A., 2009. Characteristics of compounds that cross the blood-brain barrier. BMC Neurol. 9, S3. https://doi.org/10.1186/1471-2377-9-S1-S3

Baptista, R., Guedes, M., 2021. Porosity and pore design influence on fatigue behavior of 3D printed scaffolds for trabecular bone replacement. J. Mech. Behav. Biomed. Mater. 117, 104378. https://doi.org/10.1016/j.jmbbm.2021.104378

Baranyai, Z., Soria-Carrera, H., Alleva, M., Millán-Placer, A.C., Lucía, A., Martín-Rapún, R., Aínsa, J.A., de la Fuente, J.M., 2021. Nanotechnology-based targeted drug delivery: an emerging tool to overcome tuberculosis. Adv. Ther. 4, 2000113. https://doi.org/10.1002/adtp.202000113

Bartelds, R., Nematollahi, M.H., Pols, T., Stuart, M.C.A., Pardakhty, A., Asadikaram, G., Poolman, B., 2018. Niosomes, an alternative for liposomal delivery. PLoS ONE 13, e0194179. https://doi.org/10.1371/journal.pone.0194179

Baykan, A.H., Sayiner, H.S., Aydin, E., Koc, M., Inan, I., Erturk, S.M., 2022. Extrapulmonary tuberculosıs: an old but resurgent problem. Insights Imaging 13, 39. https://doi.org/10.1186/s13244-022-01172-0

Beggs, W.H., Andrews, F.A., 1974. Chemical characterization of ethambutol binding to mycobacterium smegmatis. Antimicrob. Agents Chemother. 5, 234–239.

Begines, B., Ortiz, T., Pérez-Aranda, M., Martínez, G., Merinero, M., Argüelles-Arias, F., Alcudia, A., 2020. Polymeric nanoparticles for drug delivery: recent developments and future prospects. Nanomaterials 10, 1403. https://doi.org/10.3390/nano10071403

Beres, D., Meltzer, T., 1938. Tuberculous meningitis and its relation to tuberculous foci in the brain. Am. J. Pathol. 14, 59-70.5.

Bhagyaraj, S., Krupa, I., 2020. Alginate-Mediated synthesis of hetero-shaped silver nanoparticles and their hydrogen peroxide sensing ability. Molecules 25, 435. https://doi.org/10.3390/molecules25030435

Bhalekar, M.R., Madgulkar, A.R., Desale, P.S., Marium, G., 2017. Formulation of piperine solid lipid nanoparticles (SLN) for treatment of rheumatoid arthritis.

Drug Dev. Ind. Pharm. 43, 1003–1010. https://doi.org/10.1080/03639045.2017.1291666

Bhandari, R., Kaur, I.P., 2013. Pharmacokinetics, tissue distribution and relative bioavailability of isoniazid-solid lipid nanoparticles. Int. J. Pharm. 441, 202–212. https://doi.org/10.1016/j.ijpharm.2012.11.042

Bhardwaj, A., Kumar, L., Narang, R.K., Murthy, R.S.R., 2013. Development and characterization of ligand-appended liposomes for multiple drug therapy for pulmonary tuberculosis. Artif. Cells Nanomedicine Biotechnol. 41, 52–59. https://doi.org/10.3109/10731199.2012.702316

Bhargava, A., Shewade, H.D., 2020. The potential impact of the COVID-19 response related lockdown on TB incidence and mortality in India. Indian J. Tuberc. 67, S139–S146. https://doi.org/10.1016/j.ijtb.2020.07.004

Bharti, C., Nagaich, U., Pal, A.K., Gulati, N., 2015. Mesoporous silica nanoparticles in target drug delivery system: A review. Int. J. Pharm. Investig. 5, 124–133. https://doi.org/10.4103/2230-973X.160844

Blumer, M.J.F., 2021. Bone tissue and histological and molecular events during development of the long bones. Ann. Anat. - Anat. Anz. 235, 151704. https://doi.org/10.1016/j.aanat.2021.151704

Caldwell, J., Gardner, I., Swales, N., 1995. An Introduction to Drug Disposition: The Basic Principles of Absorption, Distribution, Metabolism, and Excretion. Toxicol. Pathol. 23, 102–114. https://doi.org/10.1177/019262339502300202

Cao, W., Hench, L.L., 1996. Bioactive materials. Ceram. Int. 22, 493–507. https://doi.org/10.1016/0272-8842(95)00126-3

Chakaya, J., Khan, M., Ntoumi, F., Aklillu, E., Fatima, R., Mwaba, P., Kapata, N., Mfinanga, S., Hasnain, S.E., Katoto, P.D.M.C., Bulabula, A.N.H., Sam-Agudu, N.A., Nachega, J.B., Tiberi, S., McHugh, T.D., Abubakar, I., Zumla, A., 2021. Global Tuberculosis Report 2020 – Reflections on the Global TB burden, treatment and prevention efforts. Int. J. Infect. Dis., Commemorating World Tuberculosis Day March 24th, 2021: “The Clock is Ticking” 113, S7–S12. https://doi.org/10.1016/j.ijid.2021.02.107

Chan, B.P., Leong, K.W., 2008. Scaffolding in tissue engineering: general approaches and tissue-specific considerations. Eur. Spine J. 17, 467–479. https://doi.org/10.1007/s00586-008-0745-3

Chang, B., Quan, Q., Li, Y., Qiu, H., Peng, J., Gu, Y., 2018. Treatment of Osteoporosis, with a Focus on 2 Monoclonal Antibodies. Med. Sci. Monit. Int. Med. J. Exp. Clin. Res. 24, 8758–8766. https://doi.org/10.12659/MSM.912309

Chatterjee, S., 2011. Brain tuberculomas, tubercular meningitis, and post-tubercular hydrocephalus in children. J. Pediatr. Neurosci. 6, S96–S100. https://doi.org/10.4103/1817-1745.85725

Chen, W., Huang, L., Tang, Q., Wang, S., Hu, C., Zhang, X., 2020. Progress on diagnosis and treatment of central nervous system tuberculosis. Radiol. Infect. Dis. 7, 160–169. https://doi.org/10.1016/j.jrid.2020.07.005

Chindamo, G., Sapino, S., Peira, E., Chirio, D., Gonzalez, M.C., Gallarate, M., 2020. Bone Diseases: Current Approach and Future Perspectives in Drug Delivery Systems for Bone Targeted Therapeutics. Nanomaterials 10, 875. https://doi.org/10.3390/nano10050875

Chou Tseng, C., 2014. Tuberculosis arthritis: epidemiology, diagnosis, treatment. Clin. Res. Foot Ankle 02. https://doi.org/10.4172/2329-910X.1000131

Clemens, D.L., Lee, B.-Y., Xue, M., Thomas, C.R., Meng, H., Ferris, D., Nel, A.E., Zink, J.I., Horwitz, M.A., 2012. Targeted intracellular delivery of antituberculosis drugs to *Mycobacterium tuberculosis*-infected macrophages via functionalized mesoporous silica nanoparticles. Antimicrob. Agents Chemother. 56, 2535–2545. https://doi.org/10.1128/AAC.06049-11

Coleman, D., Waddell, S.J., Mitchison, D.A., 2011. Effects of low incubation temperatures on the bactericidal activity of anti-tuberculosis drugs. J. Antimicrob. Chemother. 66, 146–150. https://doi.org/10.1093/jac/dkq414

Cook, G.M., Berney, M., Gebhard, S., Heinemann, M., Cox, R.A., Danilchanka, O., Niederweis, M., 2009. Physiology of Mycobacteria. Adv. Microb. Physiol. 55, 81–319. https://doi.org/10.1016/S0065-2911(09)05502-7

Daemi, H., Barikani, M., 2012. Synthesis and characterization of calcium alginate nanoparticles, sodium homopolymannuronate salt and its calcium nanoparticles. Sci. Iran. 19, 2023–2028. https://doi.org/10.1016/j.scient.2012.10.005

D'Ambrosio, L., Centis, R., Sotgiu, G., Pontali, E., Spanevello, A., Migliori, G.B., 2015. New anti-tuberculosis drugs and regimens: 2015 update. ERJ Open Res. 1, 00010–02015. https://doi.org/10.1183/23120541.00010-2015

Daskalakis, E., Huang, B., Vyas, C., Acar, A.A., Fallah, A., Cooper, G., Weightman, A., Koc, B., Blunn, G., Bartolo, P., 2022. Novel 3D bioglass scaffolds for bone tissue regeneration. Polymers 14, 445. https://doi.org/10.3390/polym14030445

Davis, A.G., Rohlwink, U.K., Proust, A., Figaji, A.A., Wilkinson, R.J., 2019. The pathogenesis of tuberculous meningitis. J. Leukoc. Biol. 105, 267–280. https://doi.org/10.1002/JLB.MR0318-102R

de Castro, R.R., do Carmo, F.A., Martins, C., Simon, A., de Sousa, V.P., Rodrigues, C.R., Cabral, L.M., Sarmento, B., 2021. Clofazimine functionalized polymeric nanoparticles for brain delivery in the tuberculosis treatment. Int. J. Pharm. 602, 120655. https://doi.org/10.1016/j.ijpharm.2021.120655

De Matteis, L., Jary, D., Lucía, A., García-Embid, S., Serrano-Sevilla, I., Pérez, D., Ainsa, J.A., Navarro, F.P., M. de la Fuente, J., 2018. New active formulations against M. tuberculosis: Bedaquiline encapsulation in lipid nanoparticles and chitosan nanocapsules. Chem. Eng. J., Smart nanomaterials and nanostructures for diagnostic and therapy 340, 181–191. https://doi.org/10.1016/j.cej.2017.12.110

Devarajan, P.V., Dawre, S.M., Dutta, R., 2015. Infectious Diseases: Need for Targeted Drug Delivery, in: Devarajan, P.V., Jain, S. (Eds.), Targeted drug delivery : concepts and design, advances in delivery science and technology.

Springer International Publishing, Cham, pp. 113–148. https://doi.org/10.1007/978-3-319-11355-5_3

Dey, S., Fageria, L., Sharma, A., Mukherjee, S., Pande, S., Chowdhury, R., Chowdhury, S., 2022. Silver nanoparticle-induced alteration of mitochondrial and ER homeostasis affects human breast cancer cell fate. Toxicol. Rep. 9, 1977–1984. https://doi.org/10.1016/j.toxrep.2022.10.017

Doig, C., Seagar, A.L., Watt, B., Forbes, K.J., 2002. The efficacy of the heat killing of *Mycobacterium tuberculosis.* J. Clin. Pathol. 55, 778–779.

Domsta, V., Seidlitz, A., 2021. 3D-Printing of drug-eluting implants: an overview of the current developments described in the literature. Molecules 26, 4066. https://doi.org/10.3390/molecules26134066

Dong, J., Zhang, S., Liu, H., Li, X., Liu, Y., Du, Y., 2014. Novel alternative therapy for spinal tuberculosis during surgery: reconstructing with anti-tuberculosis bioactivity implants. Expert Opin. Drug Deliv. 11, 299–305. https://doi.org/10.1517/17425247.2014.872625

Ehrt, S., Schnappinger, D., 2009. Mycobacterial survival strategies in the phagosome: defense against host stresses. Cell. Microbiol. 11, 1170–1178. https://doi.org/10.1111/j.1462-5822.2009.01335.x

El-Ridy, M.S., Abdelbary, A., Nasr, E.A., Khalil, R.M., Mostafa, D.M., El-Batal, A.I., Abd El-Alim, S.H., 2011. Niosomal encapsulation of the antitubercular drug, pyrazinamide. Drug Dev. Ind. Pharm. 37, 1110–1118. https://doi.org/10.3109/03639045.2011.560605

El-Ridy, M.S., Yehia, S.A., Kassem, M.A.-E.-M., Mostafa, D.M., Nasr, E.A., Asfour, M.H., 2015. Niosomal encapsulation of ethambutol hydrochloride for increasing its efficacy and safety. Drug Deliv. 22, 21–36. https://doi.org/10.3109/10717544.2013.868556

Enea, M., Pereira, E., Peixoto de Almeida, M., Araújo, A.M., Bastos, M. de L., Carmo, H., 2020. Gold nanoparticles induce oxidative stress and apoptosis in human kidney cells. Nanomaterials 10, 995. https://doi.org/10.3390/nano10050995

Essa, D., Kondiah, P.P.D., Choonara, Y.E., Pillay, V., 2020. The Design of poly(lactide-co-glycolide) nanocarriers for medical Applications. Front. Bioeng. Biotechnol. 8, 48. https://doi.org/10.3389/fbioe.2020.00048

Falsetti, I., Palmini, G., Aurilia, C., Donati, S., Iantomasi, T., Brandi, M.L., 2022. Selective estrogen receptor modulators in post-menopausal osteoporosis. Int. J. Bone Fragility 2, 93–96. https://doi.org/10.57582/IJBF.220203.093

Fan, J.-H., Li, W.-T., Hung, W.-I., Chen, C.-P., Yeh, J.-M., 2011. Cytotoxicity and differentiation effects of gold nanoparticles to human bone marrow mesenchymal stem cells. Biomed. Eng. Appl. Basis Commun. 23, 141–152. https://doi.org/10.4015/S1016237211002475

Farrell, K.B., Karpeisky, A., Thamm, D.H., Zinnen, S., 2018. Bisphosphonate conjugation for bone specific drug targeting. Bone Rep. 9, 47–60. https://doi.org/10.1016/j.bonr.2018.06.007

Faure, J., Drevet, R., Lemelle, A., Ben Jaber, N., Tara, A., El Btaouri, H., Benhayoune, H., 2015. A new sol–gel synthesis of 45S5 bioactive glass using an organic acid as catalyst. Mater. Sci. Eng. C 47, 407–412. https://doi.org/10.1016/j.msec.2014.11.045

Fernandes, H.R., Gaddam, A., Rebelo, A., Brazete, D., Stan, G.E., Ferreira, J.M.F., 2018. Bioactive glasses and glass-ceramics for healthcare applications in bone regeneration and tissue engineering. Materials 11, 2530. https://doi.org/10.3390/ma11122530

Freire, F.D., Câmara, M.B., Dantas, M.G., Aragão, C.F.S., Lima e Moura, T.F.A. de, Raffin, F.N., 2014. Gastric-resistant isoniazid pellets reduced degradation of rifampicin in acidic medium. Braz. J. Pharm. Sci. 50, 749–755. https://doi.org/10.1590/S1984-82502014000400010

Fu, Y.-C., Fu, T.-F., Wang, H.-J., Lin, C.-W., Lee, G.-H., Wu, S.-C., Wang, C.-K., 2014. Aspartic acid-based modified PLGA–PEG nanoparticles for bone targeting: In vitro and in vivo evaluation. Acta Biomater. 10, 4583–4596. https://doi.org/10.1016/j.actbio.2014.07.015

Fullam, E., J. Young, R., 2021. Physicochemical properties and *Mycobacterium tuberculosis* transporters: keys to efficacious antitubercular drugs? RSC Med. Chem. 12, 43–56. https://doi.org/10.1039/D0MD00265H

Gagneux, S., 2018. Ecology and evolution of *Mycobacterium tuberculosis*. Nat. Rev. Microbiol. 16, 202–213. https://doi.org/10.1038/nrmicro.2018.8

Gambacciani, M., Levancini, M., 2014. Hormone replacement therapy and the prevention of postmenopausal osteoporosis. Przegląd Menopauzalny Menopause Rev. 13, 213–220. https://doi.org/10.5114/pm.2014.44996

Garg, D., Goyal, V., 2020. Spinal tuberculosis treatment: an enduring bone of contention. Ann. Indian Acad. Neurol. 23, 441–448. https://doi.org/10.4103/aian.AIAN_141_20

Garg, R.K., Somvanshi, D.S., 2011. Spinal tuberculosis: A review. J. Spinal Cord Med. 34, 440–454. https://doi.org/10.1179/2045772311Y.0000000023

Garg, S., Alam, M.S., Bajpai, R., Kishan, K.R., Agrawal, P., 2009. Redox biology of *Mycobacterium tuberculosis* H37Rv: protein-protein interaction between GlgB and WhiB1 involves exchange of thiol-disulfide. BMC Biochem. 10, 1. https://doi.org/10.1186/1471-2091-10-1

Garg, T., Singh, O., Arora, S., Murthy, R., 2012. Scaffold: a novel carrier for cell and drug delivery. Crit. Rev. Ther. Drug Carrier Syst. 29, 1–63. https://doi.org/10.1615/critrevtherdrugcarriersyst.v29.i1.10

Gaspar, M.M., Cruz, A., Penha, A.F., Reymão, J., Sousa, A.C., Eleutério, C.V., Domingues, S.A., Fraga, A.G., Filho, A.L., Cruz, M.E.M., Pedrosa, J., 2008. Rifabutin encapsulated in liposomes exhibits increased therapeutic activity in a model of disseminated tuberculosis. Int. J. Antimicrob. Agents 31, 37–45. https://doi.org/10.1016/j.ijantimicag.2007.08.008

Gastrointestinal Tuberculosis Imaging: Practice Essentials, Esophageal Tuberculosis, Gastric and Duodenal Tuberculosis, 2019.

Geszke-Moritz, M., Moritz, M., 2016. Solid lipid nanoparticles as attractive drug vehicles: Composition, properties and therapeutic strategies. Mater. Sci. Eng. C 68, 982–994. https://doi.org/10.1016/j.msec.2016.05.119

Ghosh, R., Mondal, S., Mukherjee, D., Adhikari, A., Ahmed, S.A., Alsantali, R.I., Khder, A.S., Altass, H.M., Moussa, Z., Das, R., Bhattacharyya, M., Pal, S.K., 2022. Oral drug delivery using a polymeric nanocarrier: chitosan nanoparticles in the delivery of rifampicin. Mater. Adv. 3, 4622–4628. https://doi.org/10.1039/D2MA00295G

Gómez-Cerezo, M.N., Peña, J., Ivanovski, S., Arcos, D., Vallet-Regí, M., Vaquette, C., 2021. Multiscale porosity in mesoporous bioglass 3D-printed scaffolds for bone regeneration. Mater. Sci. Eng. C 120, 111706. https://doi.org/10.1016/j.msec.2020.111706

Gopalaswamy, R., Dusthackeer, V.N.A., Kannayan, S., Subbian, S., 2021. Extrapulmonary tuberculosis—an update on the diagnosis, treatment and drug resistance. J. Respir. 1, 141–164. https://doi.org/10.3390/jor1020015

Grotz, E., Tateosian, N., Amiano, N., Cagel, M., Bernabeu, E., Chiappetta, D.A., Moretton, M.A., 2018. Nanotechnology in tuberculosis: state of the art and the challenges ahead. Pharm. Res. 35, 213. https://doi.org/10.1007/s11095-018-2497-z

Gu, Z., Fu, J., Lin, H., He, Y., 2020. Development of 3D bioprinting: From printing methods to biomedical applications. Asian J. Pharm. Sci. 15, 529–557. https://doi.org/10.1016/j.ajps.2019.11.003

Hakkimane, S.S., Shenoy, V.P., Gaonkar, S.L., Bairy, I., Guru, B.R., 2018. Antimycobacterial susceptibility evaluation of rifampicin and isoniazid benz-hydrazone in biodegradable polymeric nanoparticles against *Mycobacterium tuberculosis* H37Rv strain. Int. J. Nanomedicine 13, 4303–4318. https://doi.org/10.2147/IJN.S163925

Haleem, A., Javaid, M., Khan, R.H., Suman, R., 2020. 3D printing applications in bone tissue engineering. J. Clin. Orthop. Trauma 11, S118–S124. https://doi.org/10.1016/j.jcot.2019.12.002

Haulman, N.J., Hawn, T.R., Nolan, C.M., 2008. Chapter 24 - Tuberculosis in travelers and immigrants, in: Jong, E.C., Sanford, C. (Eds.), the travel and tropical medicine manual (Fourth Edition). W.B. Saunders, Edinburgh, pp. 391–406. https://doi.org/10.1016/B978-141602613-6.10024-2

Hegazy, W.A.H., Mamari, R.A., Almazroui, K., Habsi, A.A., Kamona, A., AlHarthi, H., Lawati, A.I.A., AlHusaini, A.H., 2021. Retrospective study of bone-TB in Oman: 2002–2019. J. Epidemiol. Glob. Health 11, 238–245. https://doi.org/10.2991/jegh.k.210420.002

Horne, D.J., Misch, E.A., 2017. Practice Point 18 - Tuberculosis of the Urogenital Tract, in: Cohen, J., Powderly, W.G., Opal, S.M. (Eds.), Infectious Diseases

(Fourth Edition). Elsevier, pp. 555-556.e1. https://doi.org/10.1016/B978-0-7020-6285-8.00213-6

Houben, R.M.G.J., Dodd, P.J., 2016. The global burden of latent tuberculosis infection: a re-estimation using mathematical modelling. PLoS Med. 13, e1002152. https://doi.org/10.1371/journal.pmed.1002152

Houston, A., Macallan, D.C., 2014. Extrapulmonary tuberculosis. Medicine (Baltimore), Infections Part 3 of 3 42, 18–22. https://doi.org/10.1016/j.mpmed.2013.10.008

Hua, L., Qian, H., Lei, T., zhang, yu, Lei, P., Hu, Y., 2022. 3D-Printed porous tantalum coated with antitubercular drugs achieving antibacterial properties and good biocompatibility. Macromol.biosci 22. https://doi.org/10.1002/mabi.202100338

Hua, S., 2019. Physiological and pharmaceutical considerations for rectal drug formulations. Front. Pharmacol. 10, 1196. https://doi.org/10.3389/fphar.2019.01196

Huang, D., Li, D., Wang, T., Shen, H., Zhao, P., Liu, B., You, Y., Ma, Y., Yang, F., Wu, D., Wang, S., 2015. Isoniazid conjugated poly(lactide-co-glycolide): Long-term controlled drug release and tissue regeneration for bone tuberculosis therapy. Biomaterials 52, 417–425. https://doi.org/10.1016/j.biomaterials.2015.02.052

Hussain, M.M., Samir, T.M., Azzazy, H.M.E., 2013. Unmodified gold nanoparticles for direct and rapid detection of *Mycobacterium tuberculosis* complex. Clin. Biochem. 46, 633–637. https://doi.org/10.1016/j.clinbiochem.2012.12.020

Iacobino, A., Piccaro, G., Giannoni, F., Mustazzolu, A., Fattorini, L., 2016. Activity of drugs against dormant *Mycobacterium tuberculosis.* Int. J. Mycobacteriology 5 Suppl 1, S94–S95. https://doi.org/10.1016/j.ijmyco.2016.09.061

Isiguzo, G., Du Bruyn, E., Howlett, P., Ntsekhe, M., 2020. Diagnosis and management of tuberculous pericarditis: what is new? Curr. Cardiol. Rep. 22, 2. https://doi.org/10.1007/s11886-020-1254-1

Iyisan, B., Landfester, K., 2019. Polymeric Nanocarriers, in: Gehr, P., Zellner, R. (Eds.), Biological responses to nanoscale particles: molecular and cellular aspects and methodological approaches, nanoscience and technology. Springer International Publishing, Cham, pp. 53–84. https://doi.org/10.1007/978-3-030-12461-8_3

Jabbar, K.Q., Barzinjy, A.A., Hamad, S.M., 2022. Iron oxide nanoparticles: Preparation methods, functions, adsorption and coagulation/flocculation in wastewater treatment. Environ. Nanotechnol. Monit. Manag. 17, 100661. https://doi.org/10.1016/j.enmm.2022.100661

Jain, A.K., Jaggi, K.R., Bhayana, H., Saha, R., 2018. Drug-resistant spinal tuberculosis. Indian J. Orthop. 52, 100–107. https://doi.org/10.4103/ortho.IJOrtho_306_17

Jensen, A.T., Jensen, S.S., Worsaae, N., 2016. Complications related to bone augmentation procedures of localized defects in the alveolar ridge. A retrospective clinical study. Oral Maxillofac. Surg. 20, 115–122. https://doi.org/10.1007/s10006-016-0551-8

Ji, Z., Lin, G., Lu, Q., Meng, L., Shen, X., Dong, L., Fu, C., Zhang, X., 2012. Targeted therapy of SMMC-7721 liver cancer in vitro and in vivo with carbon nanotubes based drug delivery system. J. Colloid Interface Sci. 365, 143–149. https://doi.org/10.1016/j.jcis.2011.09.013

Jia, S., Zhang, K., Wan, X., Gao, Z., Gong, J., Rohani, S., 2020. Effects of temperature and solvent properties on the liquid–solid phase equilibrium of γ-pyrazinamide. J. Chem. Eng. Data 65, 3667–3678. https://doi.org/10.1021/acs.jced.0c00286

Jin Lee, S., Lee, H.-J., Kim, S.-Y., Min Seok, J., Hee Lee, J., Doo Kim, W., Keun Kwon, I., Park, S.-Y., A Park, S., 2018. In situ gold nanoparticle growth on polydopamine-coated 3D-printed scaffolds improves osteogenic differentiation for bone tissue engineering applications: in vitro and in vivo studies. Nanoscale 10, 15447–15453. https://doi.org/10.1039/C8NR04037K

Jones, J.R., Lin, S., Yue, S., Lee, P.D., Hanna, J.V., Smith, M.E., Newport, R.J., 2010. Bioactive glass scaffolds for bone regeneration and their hierarchical characterisation. Proc. Inst. Mech. Eng. [H] 224, 1373–1387. https://doi.org/10.1243/09544119JEIM836

Jones-Lopez, E.C., Ellner, J.J., 2011. CHAPTER 35 - Tuberculosis and Atypical Mycobacterial Infections, in: Guerrant, R.L., Walker, D.H., Weller, P.F. (Eds.), Tropical infectious diseases: principles, pathogens and practice (Third Edition). W.B. Saunders, Edinburgh, pp. 228–247. https://doi.org/10.1016/B978-0-7020-3935-5.00035-5

Judson, I., Radford, J.A., Harris, M., Blay, J.-Y., van Hoesel, Q., le Cesne, A., van Oosterom, A.T., Clemons, M.J., Kamby, C., Hermans, C., Whittaker, J., Donato di Paola, E., Verweij, J., Nielsen, S., 2001. Randomised phase II trial of pegylated liposomal doxorubicin (DOXIL®/CAELYX®) versus doxorubicin in the treatment of advanced or metastatic soft tissue sarcoma: a study by the EORTC Soft Tissue and Bone Sarcoma Group. Eur. J. Cancer 37, 870–877. https://doi.org/10.1016/S0959-8049(01)00050-8

Kaba, Ö., Kara, M., Odacılar, C.A., Kamer, İ., Sütçü, M., Demir, S.Ö., Çalışkan, E., Törün, S.H., Salman, N., Somer, A., 2019. Evaluation of cases of pediatric extrapulmonary tuberculosis: a single center experience. Turk. Arch. Pediatr. Pediatri Arş. 54, 86–92. https://doi.org/10.14744/TurkPediatriArs.2019.33239

Kakkar, V., Kaur, I.P., 2011. Evaluating potential of curcumin loaded solid lipid nanoparticles in aluminium induced behavioural, biochemical and histopathological alterations in mice brain. Food Chem. Toxicol. 49, 2906–2913. https://doi.org/10.1016/j.fct.2011.08.006

Kalluru, R., Fenaroli, F., Westmoreland, D., Ulanova, L., Maleki, A., Roos, N., Madsen, M.P., Koster, G., Jacobsen, W.E., Wilson, S., Roberg-Larsen, H., Khuller, G.K., Singh, A., Nyström, B., Griffiths, G., 2013. Polylactide-co-

glycolide-rifampicin-nanoparticles efficiently clear *Mycobacterium bovis* BCG infection in macrophages and remain membrane-bound in phago-lysosomes. J. Cell Sci. jcs.121814. https://doi.org/10.1242/jcs.121814

Karadjian, M., Essers, C., Tsitlakidis, S., Reible, B., Moghaddam, A., Boccaccini, A.R., Westhauser, F., 2019. Biological properties of calcium phosphate bioactive glass composite bone substitutes: current experimental evidence. Int. J. Mol. Sci. 20, 305. https://doi.org/10.3390/ijms20020305

Karimi, M., Ghasemi, A., Zangabad, P.S., Rahighi, R., Basri, S.M.M., Mirshekari, H., Amiri, M., Pishabad, Z.S., Aslani, A., Bozorgomid, M., Ghosh, D., Beyzavi, A., Vaseghi, A., Aref, A.R., Haghani, L., Bahrami, S., Hamblin, M.R., 2016. Smart micro/nanoparticles in stimulus-responsive drug/gene delivery systems. Chem. Soc. Rev. 45, 1457. https://doi.org/10.1039/c5cs00798d

Kaufmann, S.H.E., Dorhoi, A., Hotchkiss, R.S., Bartenschlager, R., 2018. Host-directed therapies for bacterial and viral infections. Nat. Rev. Drug Discov. 17, 35–56. https://doi.org/10.1038/nrd.2017.162

Kaur, G., Pandey, O.P., Singh, K., Homa, D., Scott, B., Pickrell, G., 2014. A review of bioactive glasses: their structure, properties, fabrication and apatite formation. J. Biomed. Mater. Res. A 102, 254–274. https://doi.org/10.1002/jbm.a.34690

Kazi, K.M., Mandal, A.S., Biswas, N., Guha, A., Chatterjee, S., Behera, M., Kuotsu, K., 2010. Niosome: A future of targeted drug delivery systems. J. Adv. Pharm. Technol. Res. 1, 374–380. https://doi.org/10.4103/0110-5558.76435

Kerry, R.G., Gouda, S., Sil, B., Das, G., Shin, H.-S., Ghodake, G., Patra, J.K., 2018. Cure of tuberculosis using nanotechnology: An overview. J. Microbiol. 56, 287–299. https://doi.org/10.1007/s12275-018-7414-y

Khatak, S., Mehta, M., Awasthi, R., Paudel, K.R., Singh, S.K., Gulati, M., Hansbro, N.G., Hansbro, P.M., Dua, K., Dureja, H., 2020. Solid lipid nanoparticles containing anti-tubercular drugs attenuate the Mycobacterium marinum infection. Tuberculosis 125, 102008. https://doi.org/10.1016/j.tube.2020.102008

Khiev, D., Mohamed, Z.A., Vichare, R., Paulson, R., Bhatia, S., Mohapatra, S., Lobo, G.P., Valapala, M., Kerur, N., Passaglia, C.L., Mohapatra, S.S., Biswal, M.R., 2021. Emerging nano-formulations and nanomedicines applications for ocular drug delivery. Nanomaterials 11, 173. https://doi.org/10.3390/nano11010173

Khoza, L.J., Kumar, P., Dube, A., Demana, P.H., Choonara, Y.E., 2022. Insights into innovative therapeutics for drug-resistant tuberculosis: Host-directed therapy and autophagy inducing modified nanoparticles. Int. J. Pharm. 622, 121893. https://doi.org/10.1016/j.ijpharm.2022.121893

Kim, B.-S., Yang, S.-S., Kim, C.S., 2018. Incorporation of BMP-2 nanoparticles on the surface of a 3D-printed hydroxyapatite scaffold using an ε-polycaprolactone polymer emulsion coating method for bone tissue engineering. Colloids Surf. B Biointerfaces 170, 421–429. https://doi.org/10.1016/j.colsurfb.2018.06.043

Klein, D.J., Boukouvala, S., McDonagh, E.M., Shuldiner, S.R., Laurieri, N., Thorn, C.F., Altman, R.B., Klein, T.E., 2016. PharmGKB Summary: Isoniazid pathway, pharmacokinetics (PK). Pharmacogenet. Genomics 26, 436–444. https://doi.org/10.1097/FPC.0000000000000232

Kolloli, A., Subbian, S., 2017. Host-Directed Therapeutic Strategies for Tuberculosis. Front. Med. 4.

Kulkarni, P., Rawtani, D., Barot, T., 2019. Formulation and optimization of long acting dual niosomes using Box-Behnken experimental design method for combinative delivery of Ethionamide and D-cycloserine in Tuberculosis treatment. Colloids Surf. Physicochem. Eng. Asp. 565, 131–142. https://doi.org/10.1016/j.colsurfa.2019.01.004

Kumar, G.P., Rajeshwarrao, P., 2011. Nonionic surfactant vesicular systems for effective drug delivery—an overview. Acta Pharm. Sin. B 1, 208–219. https://doi.org/10.1016/j.apsb.2011.09.002

Kumar, S.V., Deka, M.K., Bagga, M., Kala, M.S., Gauthaman, K., 2010. A systematic review of different type of tuberculosis. Eur. Rev. Med. Pharmacol. Sci. 14, 831–843.

Lao, J., Madani, J., Puértolas, T., Álvarez, M., Hernández, A., Pazo-Cid, R., Artal, Á., Antón Torres, A., 2013. Liposomal doxorubicin in the treatment of breast cancer patients: a review. J. Drug Deliv. 2013, 456409. https://doi.org/10.1155/2013/456409

Lee, C.-N., Wang, Y.-M., Lai, W.-F., Chen, T.-J., Yu, M.-C., Fang, C.-L., Yu, F.-L., Tsai, Y.-H., Chang, W.H.-S., Zuo, C.S., Renshaw, P.F., 2012. Super-paramagnetic iron oxide nanoparticles for use in extrapulmonary tuberculosis diagnosis. Clin. Microbiol. Infect. 18, E149–E157. https://doi.org/10.1111/j.1469-0691.2012.03809.x

Lee, J.-H., Baik, J.-M., Yu, Y.-S., Kim, J.H., Ahn, C.B., Son, K.H., Kim, J.-H., Choi, E.S., Lee, J.W., 2020. Development of a heat labile antibiotic eluting 3D printed scaffold for the treatment of osteomyelitis. Sci. Rep. 10, 7554. https://doi.org/10.1038/s41598-020-64573-5

Lee, J.Y., 2015. Diagnosis and treatment of extrapulmonary tuberculosis. Tuberc. Respir. Dis. 78, 47–55. https://doi.org/10.4046/trd.2015.78.2.47

Lee, S.H., 2016. Tuberculosis infection and latent tuberculosis. Tuberc. Respir. Dis. 79, 201–206. https://doi.org/10.4046/trd.2016.79.4.201

Lemmer, Y., Kalombo, L., Pietersen, R.-D., Jones, A.T., Semete-Makokotlela, B., Van Wyngaardt, S., Ramalapa, B., Stoltz, A.C., Baker, B., Verschoor, J.A., Swai, H.S., de Chastellier, C., 2015. Mycolic acids, a promising mycobacterial ligand for targeting of nanoencapsulated drugs in tuberculosis. J. Controlled Release 211, 94–104. https://doi.org/10.1016/j.jconrel.2015.06.005

Li, H., Pan, S., Xia, P., Chang, Y., Fu, C., Kong, W., Yu, Z., Wang, K., Yang, X., Qi, Z., 2020. Advances in the application of gold nanoparticles in bone tissue engineering. J. Biol. Eng. 14, 14. https://doi.org/10.1186/s13036-020-00236-3

Li, Yan, Bai, Y., Pan, J., Wang, H., Li, H., Xu, X., Fu, X., Shi, R., Luo, Z., Li, Yongliang, Li, Q., Fuh, J.Y.H., Wei, S., 2019. A hybrid 3D-printed aspirin-laden liposome composite scaffold for bone tissue engineering. J. Mater. Chem. B 7, 619–629. https://doi.org/10.1039/C8TB02756K

Lin, X., Patil, S., Gao, Y.-G., Qian, A., 2020. The bone extracellular matrix in bone formation and regeneration. Front. Pharmacol. 11, 757. https://doi.org/10.3389/fphar.2020.00757

Liu, P., Guo, B., Wang, S., Ding, J., Zhou, W., 2019. A thermo-responsive and self-healing liposome-in-hydrogel system as an antitubercular drug carrier for localized bone tuberculosis therapy. Int. J. Pharm. 558, 101–109. https://doi.org/10.1016/j.ijpharm.2018.12.083

Lu, R.-M., Hwang, Y.-C., Liu, I.-J., Lee, C.-C., Tsai, H.-Z., Li, H.-J., Wu, H.-C., 2020. Development of therapeutic antibodies for the treatment of diseases. J. Biomed. Sci. 27, 1. https://doi.org/10.1186/s12929-019-0592-z

Mahdy, E.A., Sahbal, K.M., Mostafa Mabrouk, Beherei, H.H., Abdel-Monem, Y.K., 2021. Enhancement of glass-ceramic performance by TiO2 doping: *In-vitro* cell viability, proliferation, and differentiation. Ceram. Int. 47, 6251–6261. https://doi.org/10.1016/j.ceramint.2020.10.203

Majeed, U., Manochakian, R., Zhao, Y., Lou, Y., 2021. Targeted therapy in advanced non-small cell lung cancer: current advances and future trends. J. Hematol. Oncol.J Hematol Oncol 14, 108. https://doi.org/10.1186/s13045-021-01121-2

Makadia, H.K., Siegel, S.J., 2011. Poly Lactic-co-Glycolic Acid (PLGA) as biodegradable controlled drug delivery carrier. Polymers 3, 1377–1397. https://doi.org/10.3390/polym3031377

Malan, S.F., Chetty, D.J., 2002. Physicochemical properties of drugs and membrane permeability. South Afr. J. Sci. 7.

Malaviya, A.N., Kotwal, P.P., 2003. Arthritis associated with tuberculosis. Best Pract. Res. Clin. Rheumatol., Infection and Arthritis 17, 319–343. https://doi.org/10.1016/S1521-6942(02)00126-2

Manallack, D.T., Prankerd, R.J., Yuriev, E., Oprea, T.I., Chalmers, D.K., 2013. The significance of acid/base properties in drug discovery. Chem. Soc. Rev. 42, 485–496. https://doi.org/10.1039/c2cs35348b

Mantica, G., Ambrosini, F., Riccardi, N., Vecchio, E., Rigatti, L., De Rose, A.F., Van der Merwe, A., Terrone, C., Bartoletti, R., Bonkat, G., 2021. Genitourinary tuberculosis: a comprehensive review of a neglected manifestation in low-endemic countries. Antibiotics 10, 1399. https://doi.org/10.3390/antibiotics10111399

Manyelo, C.M., Solomons, R.S., Walzl, G., Chegou, N.N., 2021. Tuberculous meningitis: pathogenesis, immune responses, diagnostic challenges, and the potential of biomarker-based approaches. J. Clin. Microbiol. 59, e01771-20. https://doi.org/10.1128/JCM.01771-20

Maphasa, R.E., Meyer, M., Dube, A., 2021. The macrophage response to *Mycobacterium tuberculosis* and opportunities for autophagy inducing nanomedicines for tuberculosis Therapy. Front. Cell. Infect. Microbiol. 10.

Marrale, J., Morrissey, M.C., Haddad, F.S., 2007. A literature review of autograft and allograft anterior cruciate ligament reconstruction. Knee Surg. Sports Traumatol. Arthrosc. 15, 690–704. https://doi.org/10.1007/s00167-006-0236-1

Mayosi, B.M., Burgess, L.J., Doubell, A.F., 2005. Tuberculous Pericarditis. Circulation 112, 3608–3616. https://doi.org/10.1161/CIRCULATIONAHA.105.543066

Mazlan, M.K.N., Mohd Tazizi, M.H.D., Ahmad, R., Noh, M.A.A., Bakhtiar, A., Wahab, H.A., Mohd Gazzali, A., 2021. Antituberculosis targeted drug delivery as a potential future treatment approach. Antibiotics 10, 908. https://doi.org/10.3390/antibiotics10080908

Meena, L.S., Rajni, 2010. Survival mechanisms of pathogenic *Mycobacterium tuberculosis* H37Rv. FEBS J. 277, 2416–2427. https://doi.org/10.1111/j.1742-4658.2010.07666.

Mehnert, W., Mäder, K., 2012. Solid lipid nanoparticles: Production, characterization, and applications. Adv. Drug Deliv. Rev.., 64, 83–101. https://doi.org/10.1016/j.addr.2012.09.021

Mehta, S.K., Jindal, N., 2013. Formulation of Tyloxapol niosomes for encapsulation, stabilization and dissolution of anti-tubercular drugs. Colloids Surf. B Biointerfaces 101, 434–441. https://doi.org/10.1016/j.colsurfb.2012.07.006

Migliori, G.B., Thong, P.M., Alffenaar, J.-W., Denholm, J., Tadolini, M., Alyaquobi, F., Blanc, F.-X., Buonsenso, D., Cho, J.-G., Codecasa, L.R., Danila, E., Duarte, R., García-García, J.-M., Gualano, G., Rendon, A., Silva, D.R., Souleymane, M.B., Tham, S.M., Thomas, T.A., Tiberi, S., Udwadia, Z.F., Goletti, D., Centis, R., D'Ambrosio, L., Sotgiu, G., Ong, C.W.M., Network, for the G.T., 2021. Gauging the impact of the COVID-19 pandemic on tuberculosis services: a global study. Eur. Respir. J. 58. https://doi.org/10.1183/13993003.01786-2021

Miranda, M.S., Rodrigues, M.T., Domingues, R.M.A., Costa, R.R., Paz, E., Rodríguez-Abreu, C., Freitas, P., Almeida, B.G., Carvalho, M.A., Gonçalves, C., Ferreira, C.M., Torrado, E., Reis, R.L., Pedrosa, J., Gomes, M.E., 2018. Development of inhalable superparamagnetic iron oxide nanoparticles (SPIONs) in microparticulate system for antituberculosis drug delivery. Adv. Healthc. Mater. 7, e1800124. https://doi.org/10.1002/adhm.201800124

Mody, V.V., Siwale, R., Singh, A., Mody, H.R., 2010. Introduction to metallic nanoparticles. J. Pharm. Bioallied Sci. 2, 282–289. https://doi.org/10.4103/0975-7406.72127

Morgan, E.F., Unnikrisnan, G.U., Hussein, A.I., 2018. Bone Mechanical Properties in Healthy and Diseased States. Annu. Rev. Biomed. Eng. 20, 119–143. https://doi.org/10.1146/annurev-bioeng-062117-121139

Nasr, M., Mansour, S., Mortada, N.D., Elshamy, A.A., 2008. Vesicular aceclofenac systems: A comparative study between liposomes and niosomes. J. Microencapsul. 25, 499–512. https://doi.org/10.1080/02652040802055411

Nikolova, M.P., Chavali, M.S., 2019. Recent advances in biomaterials for 3D scaffolds: A review. Bioact. Mater. 4, 271–292. https://doi.org/10.1016/j.bioactmat.2019.10.005

O'Brien, F.J., 2011. Biomaterials & scaffolds for tissue engineering. Mater. Today 14, 88–95. https://doi.org/10.1016/S1369-7021(11)70058-X

Padwal, P., Bandyopadhyaya, R., Mehra, S., 2015. Biocompatible citric acid-coated iron oxide nanoparticles to enhance the activity of first-line anti-TB drugs in Mycobacterium smegmatis. J. Chem. Technol. Biotechnol. 90, 1773–1781. https://doi.org/10.1002/jctb.4766

Paliwal, R., Paliwal, S.R., Kenwat, R., Kurmi, B.D., Sahu, M.K., 2020. Solid lipid nanoparticles: a review on recent perspectives and patents. Expert Opin. Ther. Pat. 30, 179–194. https://doi.org/10.1080/13543776.2020.1720649

Palomino, J.C., Martin, A., 2014. Drug Resistance Mechanisms in *Mycobacterium tuberculosis*. Antibiotics 3, 317–340. https://doi.org/10.3390/antibiotics3030317

Pandey, R., Khuller, G.K., 2006. Oral nanoparticle-based antituberculosis drug delivery to the brain in an experimental model. J. Antimicrob. Chemother. 57, 1146–1152. https://doi.org/10.1093/jac/dkl128

Pandey, R., Khuller, G.K., 2004. Polymer based drug delivery systems for mycobacterial infections. Curr. Drug Deliv. 1, 195–201. https://doi.org/10.2174/1567201043334669

Pang, Y., An, J., Shu, W., Huo, F., Chu, N., Gao, M., Qin, S., Huang, H., Chen, X., Xu, S., 2019. Epidemiology of extrapulmonary tuberculosis among Inpatients, China, 2008–2017. Emerg. Infect. Dis. 25, 457–464. https://doi.org/10.3201/eid2503.180572

Patra, J.K., Das, G., Fraceto, L.F., Campos, E.V.R., Rodriguez-Torres, M. del P., Acosta-Torres, L.S., Diaz-Torres, L.A., Grillo, R., Swamy, M.K., Sharma, S., Habtemariam, S., Shin, H.-S., 2018. Nano-based drug delivery systems: recent developments and prospects. J. Nanobiotechnology 16, 71. https://doi.org/10.1186/s12951-018-0392-8

Pei, P., Tian, Z., Zhu, Y., 2018a. 3D printed mesoporous bioactive glass/metal-organic framework scaffolds with antitubercular drug delivery. Microporous Mesoporous Mater. 272, 24–30. https://doi.org/10.1016/j.micromeso.2018.06.012

Piccaro, G., Poce, G., Biava, M., Giannoni, F., Fattorini, L., 2015. Activity of lipophilic and hydrophilic drugs against dormant and replicating *Mycobacterium tuberculosis*. J.Antibot. (Tokyo) 68, 711–714. https://doi.org/10.1038/ja.2015.52

Piddington, D.L., Kashkouli, A., Buchmeier, N.A., 2000. Growth of *Mycobacterium tuberculosis* in a defined medium is very restricted by acid pH and Mg(2+) levels. Infect. Immun. 68, 4518–4522. https://doi.org/10.1128/IAI.68.8.4518-4522.2000

Pigrau-Serrallach, C., Rodríguez-Pardo, D., 2013. Bone and joint tuberculosis. Eur. Spine J. 22, 556–566. https://doi.org/10.1007/s00586-012-2331-y

Pinheiro, M., Lúcio, M., Lima, J.L., Reis, S., 2011. Liposomes as drug delivery systems for the treatment of TB. Nanomed.6,1413–1428. https://doi.org/10.2217/nnm.11.122

Pohaku Mitchell, K.K., Liberman, A., Kummel, A.C., Trogler, W.C., 2012. Iron(III)-Doped, Silica Nanoshells: A Biodegradable Form of Silica. J. Am. Chem. Soc. 134, 13997–14003. https://doi.org/10.1021/ja3036114

Preethi Soundarya, S., Haritha Menon, A., Viji Chandran, S., Selvamurugan, N., 2018. Bone tissue engineering: Scaffold preparation using chitosan and other biomaterials with different design and fabrication techniques. Int. J. Biol. Macromol. 119, 1228–1239. https://doi.org/10.1016/j.ijbiomac.2018.08.056

Purohit, M., Mustafa, T., 2015. Laboratory diagnosis of extra-pulmonary tuberculosis (EPTB) in resource-constrained settings: state of the art, challenges and the need. J. Clin. Diagn. Res. JCDR 9, EE01–EE06. https://doi.org/10.7860/JCDR/2015/12422.5792

Rajasekaran, S., Kanna, R.M., Shetty, A.P., 2014. Pathophysiology and treatment of spinal tuberculosis. JBJS Rev. 2, e4. https://doi.org/10.2106/JBJS.RVW.M.00130

Rajasekaran, S., Soundararajan, D.C.R., Shetty, A.P., Kanna, R.M., 2018. Spinal tuberculosis: current concepts. Glob. Spine J. 8, 96S-108S. https://doi.org/10.1177/2192568218769053

Rasouli, M.R., Mirkoohi, M., Vaccaro, A.R., Yarandi, K.K., Rahimi-Movaghar, V., 2012. Spinal tuberculosis: diagnosis and management. Asian Spine J. 6, 294–308. https://doi.org/10.4184/asj.2012.6.4.294

Rock, R.B., Olin, M., Baker, C.A., Molitor, T.W., Peterson, P.K., 2008. Central nervous system tuberculosis: pathogenesis and clinical aspects. Clin. Microbiol. Rev. 21, 243–261. https://doi.org/10.1128/CMR.00042-07

Rodriguez-Takeuchi, S.Y., Renjifo, M.E., Medina, F.J., 2019. Extrapulmonary tuberculosis: pathophysiology and imaging findings. RadioGraphics 39, 2023–2037. https://doi.org/10.1148/rg.2019190109

Ryan, C.J., Saylor, P.J., Everly, J.J., Sartor, O., 2014. Bone-targeting radiopharmaceuticals for the treatment of bone-metastatic castration-resistant prostate cancer: exploring the implications of new data. The Oncologist 19, 1012–1018. https://doi.org/10.1634/theoncologist.2013-0472

Sankar, R., Sharda, N., Singh, S., 2003. Behavior of decomposition of rifampicin in the presence of isoniazid in the pH range 1-3. Drug Dev. Ind. Pharm. 29, 733–738. https://doi.org/10.1081/ddc-120021772

Sarathy, J.P., Dartois, V., 2020. Caseum: a Niche for *Mycobacterium tuberculosis* drug-tolerant persisters. Clin. Microbiol. Rev. 33, e00159-19. https://doi.org/10.1128/CMR.00159-19

Sarkar, N., Bose, S., 2019. Liposome-encapsulated curcumin-loaded 3D printed scaffold for bone tissue engineering. ACS Appl. Mater. Interfaces. https://doi.org/10.1021/acsami.9b01218

Schaible, U.E., Sturgill-Koszycki, S., Schlesinger, P.H., Russell, D.G., n.d. Cytokine activation leads to acidification and increases maturation of Mycobacterium avium -containing phagosomes in murine macrophages. J. Immunol. 8.

Sercombe, L., Veerati, T., Moheimani, F., Wu, S.Y., Sood, A.K., Hua, S., 2015. Advances and challenges of liposome assisted drug delivery. Front. Pharmacol. 6, 286. https://doi.org/10.3389/fphar.2015.00286

Seung, K.J., Keshavjee, S., Rich, M.L., 2015. Multidrug-resistant tuberculosis and extensively drug-resistant tuberculosis. Cold Spring Harb. Perspect. Med. 5, a017863. https://doi.org/10.1101/cshperspect.a017863

Shafer, R.W., Kim, D.S., Weiss, J.P., Quale, J.M., 1991. Extrapulmonary tuberculosis in patients with human immunodeficiency virus infection. Medicine (Baltimore) 70, 384–397. https://doi.org/10.1097/00005792-199111000-00004

Sharma, S., Sanpui, P., Chattopadhyay, A., Sankar Ghosh, S., 2012. Fabrication of antibacterial silver nanoparticle —sodium alginate– chitosan composite films. RSC Adv. 2, 5837–5843. https://doi.org/10.1039/C2RA00006G

Sharma, S.K., Mohan, A., Kohli, M., 2021. Extrapulmonary tuberculosis. Expert Rev. Respir. Med. 15, 931–948. https://doi.org/10.1080/17476348.2021.1927718

Sia, J.K., Rengarajan, J., 2019. Immunology of *Mycobacterium tuberculosis* Infections. Microbiol. Spectr. 7, 7.4.6. https://doi.org/10.1128/microbiolspec.GPP3-0022-2018

Siew, A., Le, H., Thiovolet, M., Gellert, P., Schatzlein, A., Uchegbu, I., 2012. Enhanced oral absorption of hydrophobic and hydrophilic drugs using quaternary ammonium palmitoyl glycol chitosan nanoparticles. Mol. Pharm. 9, 14–28. https://doi.org/10.1021/mp200469a

Singh, M., Guzman-Aranguez, A., Hussain, A., Srinivas, C.S., Kaur, I.P., 2019. Solid lipid nanoparticles for ocular delivery of isoniazid: evaluation, proof of concept and in vivo safety & kinetics. Nanomed. 14, 465–491. https://doi.org/10.2217/nnm-2018-0278

Singh, R., Lillard, J.W., 2009. Nanoparticle-based targeted drug delivery. Exp. Mol. Pathol. 86, 215–223. https://doi.org/10.1016/j.yexmp.2008.12.004

Singh, R., Nawale, L., Arkile, M., Wadhwani, S., Shedbalkar, U., Chopade, S., Sarkar, D., Chopade, B.A., 2016. Phytogenic silver, gold, and bimetallic nanoparticles as novel antitubercular agents. Int. J. Nanomedicine 11, 1889–1897. https://doi.org/10.2147/IJN.S102488

Smith, I., 2003. *Mycobacterium tuberculosis* Pathogenesis and molecular determinants of Virulence. Clin. Microbiol. Rev. 16, 463–496. https://doi.org/10.1128/CMR.16.3.463-496.2003

Sousa, S., Clézardin, P., 2018. Bone-Targeted Therapies in Cancer-Induced Bone Disease. Calcif. Tissue Int. 102, 227–250. https://doi.org/10.1007/s00223-017-0353-5

Stillhart, C., Vučićević, K., Augustijns, P., Basit, A.W., Batchelor, H., Flanagan, T.R., Gesquiere, I., Greupink, R., Keszthelyi, D., Koskinen, M., Madla, C.M., Matthys, C., Miljuš, G., Mooij, M.G., Parrott, N., Ungell, A.-L., de Wildt, S.N., Orlu, M., Klein, S., Müllertz, A., 2020. Impact of gastrointestinal physiology on drug absorption in special populations—An UNGAP review. Eur. J. Pharm. Sci. 147, 105280. https://doi.org/10.1016/j.ejps.2020.105280

Suleman, A., Kondiah, P.P.D., Mabrouk, M., Choonara, Y.E., 2021. The application of 3D-printing and nanotechnology for the targeted treatment of osteosarcoma. Front. Mater. 8.

Sun, C., Zhang, X., Wang, J., Chen, Y., Meng, C., 2021. Novel mesoporous silica nanocarriers containing gold; a rapid diagnostic tool for tuberculosis. BMC Complement. Med. Ther. 21, 277. https://doi.org/10.1186/s12906-021-03451-7

Sun, H., Jia, J., Jiang, C., Zhai, S., 2018. Gold nanoparticle-induced cell death and potential applications in nanomedicine. Int. J. Mol. Sci. 19, 754. https://doi.org/10.3390/ijms19030754

Sundaramurthy, V., Korf, H., Singla, A., Scherr, N., Nguyen, L., Ferrari, G., Landmann, R., Huygen, K., Pieters, J., 2017. Survival of *Mycobacterium tuberculosis* and mycobacterium bovis BCG in lysosomes *in-vivo*. Microbes Infect. 19, 515–526. https://doi.org/10.1016/j.micinf.2017.06.008

Sznitowska, M., Gajewska, M., Janicki, S., Radwanska, A., Lukowski, G., 2001. Bioavailability of diazepam from aqueous-organic solution, submicron emulsion and solid lipid nanoparticles after rectal administration in rabbits. Eur. J. Pharm. Biopharm. 52, 159–163. https://doi.org/10.1016/S0939-6411(01)00157-6

Tadolini, M., García-García, J.-M., Blanc, F.-X., Borisov, S., Goletti, D., Motta, I., Codecasa, L.R., Tiberi, S., Sotgiu, G., Migliori, G.B., 2020. On tuberculosis and COVID-19 co-infection. Eur. Respir. J. 56, 2002328. https://doi.org/10.1183/13993003.02328-2020

Tang, K., Li, J., Huang, T., Zhong, W., Luo, X., Quan, Z., 2020a. Clinical efficacy of three types of autogenous bone grafts in treatment of single-segment thoracic tuberculosis: A retrospective cohort study. Int. J. Med. Sci. 17, 2844–2849. https://doi.org/10.7150/ijms.47309

Tang, K., Li, J., Huang, T., Zhong, W., Luo, X., Quan, Z., 2020b. Clinical efficacy of three types of autogenous bone grafts in treatment of single-segment thoracic tuberculosis: A retrospective cohort study. Int. J. Med. Sci. 17, 2844–2849. https://doi.org/10.7150/ijms.47309

Tanner, L., Denti, P., Wiesner, L., Warner, D.F., 2018. Drug permeation and metabolism in *Mycobacterium tuberculosis* : prioritising local exposure as essential criterion in new TB drug development. IUBMB Life 70, 926–937. https://doi.org/10.1002/iub.1866

Tazhbayev, Y., Galiyeva, A., Zhumagaliyeva, T., Burkeyev, M., Karimova, B., 2021. Isoniazid—loaded albumin nanoparticles: taguchi optimization method. Polymers 13, 3808. https://doi.org/10.3390/polym13213808

Tewabe, A., Abate, A., Tamrie, M., Seyfu, A., Abdela Siraj, E., 2021. Targeted drug delivery — from magic bullet to nanomedicine: principles, challenges, and future perspectives. J. Multidiscip. Healthc. 14, 1711–1724. https://doi.org/10.2147/JMDH.S313968

Tuli, S.M., 1975. Results of treatment of spinal tuberculosis by " middle-path" regime. J. Bone Joint Surg. Br. 57-B, 13–23. https://doi.org/10.1302/0301-620X.57B1.13

Ujváry, I., 2001. CHAPTER 3 - Pest control agents from natural products, in: Krieger, R.I., Krieger, W.C. (Eds.), handbook of pesticide toxicology (Second Edition). Academic Press, San Diego, pp. 109–179. https://doi.org/10.1016/B978-012426260-7.50006-9

Ukon, Y., Makino, T., Kodama, J., Tsukazaki, H., Tateiwa, D., Yoshikawa, H., Kaito, T., 2019. Molecular-based treatment strategies for osteoporosis: a literature review. Int. J. Mol. Sci. 20, 2557. https://doi.org/10.3390/ijms20102557

V. K., A.D., Ray, S., Arora, U., Mitra, S., Sionkowska, A., Jaiswal, A.K., 2022. Dual drug delivery platforms for bone tissue engineering. Front. Bioeng. Biotechnol. 10.

Vallet-Regi, M., Salinas, A.J., 2021. Mesoporous bioactive glasses for regenerative medicine. Mater. Today Bio 11, 100121. https://doi.org/10.1016/j.mtbio.2021.100121

Vélez, L.A., Delgado, Y., Ferrer-Acosta, Y., Suárez-Arroyo, I.J., Rodríguez, P., Pérez, D., 2022. Theoretical prediction of gastrointestinal absorption of phytochemicals. Int. J. Plant Biol. 13, 163–179. https://doi.org/10.3390/ijpb13020016

Viswanathan, V., Mehta, H., Pharande, R., Bannalikar, A., Gupta, P., Gupta, U., Mukne, A., 2018. Mannosylated gelatin nanoparticles of licorice for use in tuberculosis: Formulation, in vitro evaluation, in vitro cell uptake, in vivo pharmacokinetics and in vivo anti-tubercular efficacy. J. Drug Deliv. Sci. Technol. 45, 255–263. https://doi.org/10.1016/j.jddst.2018.01.017

Wadowsky, R.M., Wolford, R., McNamara, A.M., Yee, R.B., 1985. Effect of temperature, pH, and oxygen level on the multiplication of naturally occurring Legionella pneumophila in potable water. Appl. Environ. Microbiol. 49, 1197–1205.

Wagner, V., Dullaart, A., Bock, A.-K., Zweck, A., 2006. The emerging nanomedicine landscape. Nat. Biotechnol. 24, 1211–1217. https://doi.org/10.1038/nbt1006-1211

Wang, L., Hu, C., Shao, L., 2017. The antimicrobial activity of nanoparticles: present situation and prospects for the future. Int. J. Nanomedicine 12, 1227–1249. https://doi.org/10.2147/IJN.S121956

Wardhani, I.F., Samudra, R.M.R., Katherine, Hikmawati, D., Aminatun, 2019. Physical characterization of injectable bone substitute associated-3D printed bone scaffold for spinal tuberculosis. J. Phys. Conf. Ser. 1417, 012034. https://doi.org/10.1088/1742-6596/1417/1/012034

Warner, D.F., Mizrahi, V., 2007. The survival kit of *Mycobacterium tuberculosis* . Nat. Med. 13, 282–284. https://doi.org/10.1038/nm0307-282

Webber, M.J., Khan, O.F., Sydlik, S.A., Tang, B.C., Langer, R., 2015. A Perspective on the clinical translation of scaffolds for tissue engineering. Ann. Biomed. Eng. 43, 641–656. https://doi.org/10.1007/s10439-014-1104-7

Wei, B., Wang, W., Liu, X., Xu, C., Wang, Y., Wang, Z., Xu, J., Guan, J., Zhou, P., Mao, Y., 2021. Gelatin methacrylate hydrogel scaffold carrying resveratrol-loaded solid lipid nanoparticles for enhancement of osteogenic differentiation of BMSCs and effective bone regeneration. Regen. Biomater. 8, rbab044. https://doi.org/10.1093/rb/rbab044

Williams, J.M., Adewunmi, A., Schek, R.M., Flanagan, C.L., Krebsbach, P.H., Feinberg, S.E., Hollister, S.J., Das, S., 2005. Bone tissue engineering using polycaprolactone scaffolds fabricated via selective laser sintering. Biomaterials 26, 4817–4827. https://doi.org/10.1016/j.biomaterials.2004.11.057

World Health Organization, 2021a. COVID-19 pandemic slows progress against tuberculosis [WWW Document]. WHO Reg. Off. Afr. URL https://www.afro.who.int/news/covid-19-pandemic-slows-progress-against-tuberculosis (accessed 2.2.22).

World Health Organization, 2021b. Global tuberculosis report 2021.

Wu, C., Chang, J., 2012. Mesoporous bioactive glasses: structure characteristics, drug/growth factor delivery and bone regeneration application. Interface Focus 2, 292–306. https://doi.org/10.1098/rsfs.2011.0121

Yang, L., Liu, Z., 2013. Analysis and therapeutic schedule of the postoperative recurrence of bone tuberculosis. J. Orthop. Surg. 8, 47. https://doi.org/10.1186/1749-799X-8-47

Yang, S.C., Lu, L.F., Cai, Y., Zhu, J.B., Liang, B.W., Yang, C.Z., 1999. Body distribution in mice of intravenously injected camptothecin solid lipid nanoparticles and targeting effect on brain. J. Controlled Release 59, 299–307. https://doi.org/10.1016/S0168-3659(99)00007-3

Yang, Z., Lou, C., Wang, X., Wang, C., Shi, Z., Niu, N., 2022. Preparation, characterization, and in-vitro cytotoxicity of nanoliposomes loaded with anti-tubercular drugs and TGF-β1 siRNA for improving spinal tuberculosis therapy. BMC Infect. Dis. 22, 824. https://doi.org/10.1186/s12879-022-07791-8

Yao, Q., Nooeaid, P., Detsch, R., Roether, J.A., Dong, Y., Goudouri, O.-M., Schubert, D.W., Boccaccini, A.R., 2014. Bioglass®/chitosan–polycaprolactone bilayered

composite scaffolds intended for osteochondral tissue engineering. J. Biomed. Mater. Res. A 102, 4510–4518. https://doi.org/10.1002/jbm.a.35125

Yaqoob, A.A., Ahmad, H., Parveen, T., Ahmad, A., Oves, M., Ismail, I.M.I., Qari, H.A., Umar, K., Mohamad Ibrahim, M.N., 2020. Recent Advances in Metal Decorated Nanomaterials and Their Various Biological Applications: A Review. Front. Chem. 8, 341. https://doi.org/10.3389/fchem.2020.00341

Yin, X.H., Liu, Z.K., He, B.R., Hao, D.J., 2017. Single posterior surgical management for lumbosacral tuberculosis: titanium mesh versus iliac bone graft. Medicine (Baltimore) 96, e9449. https://doi.org/10.1097/MD.0000000000009449

Yu, L., Chen, Y., Lin, H., Du, W., Chen, H., Shi, J., 2018. Ultrasmall mesoporous organosilica nanoparticles: Morphology modulations and redox-responsive biodegradability for tumor-specific drug delivery. Biomaterials 161, 292–305. https://doi.org/10.1016/j.biomaterials.2018.01.046

Yuan, J., Zhen, P., Zhao, H., Chen, K., Li, X., Gao, M., Zhou, J., Ma, X., 2015. The preliminary performance study of the 3D printing of a tricalcium phosphate scaffold for the loading of sustained release anti-tuberculosis drugs. J. Mater. Sci. 50, 2138–2147. https://doi.org/10.1007/s10853-014-8776-0

Zahoor, A., Sharma, S., Khuller, G.K., 2005. Inhalable alginate nanoparticles as antitubercular drug carriers against experimental tuberculosis. Int. J. Antimicrob. Agents 26, 298–303. https://doi.org/10.1016/j.ijantimicag.2005.07.012

Zeng, Y., Fan, Y., Luo, F., Hou, T., Dai, F., Xu, J., Zhang, Z., 2020. Tricortical iliac crest allograft with anterolateral single rod screw instrumentation in the treatment of thoracic and lumbar spinal tuberculosis. Sci. Rep. 10. https://doi.org/10.1038/s41598-020-70007-z

Zhan, Y., Kang, X., Gao, W., Zhang, X., Kong, L., Hao, D., Wang, B., 2022. Efficacy analysis of one-stage posterior-only surgical treatment for thoracic spinal tuberculosis in the T4–6 segments with minimum 5-year follow-up. Sci. Rep. 12, 149. https://doi.org/10.1038/s41598-021-04138-2

Zhang, H., Zeng, K., Yin, X., Huang, J., Tang, M., Guo, C., 2015. Debridement, internal fixation, and reconstruction using titanium mesh for the surgical treatment of thoracic and lumbar spinal tuberculosis via a posterior-only approach: a 4-year follow-up of 28 patients. J. Orthop. Surg. 10, 150. https://doi.org/10.1186/s13018-015-0292-7

Zhang, Y., Wade, M.M., Scorpio, A., Zhang, H., Sun, Z., 2003. Mode of action of pyrazinamide: disruption of *Mycobacterium tuberculosis* membrane transport and energetics by pyrazinoic acid. J. Antimicrob. Chemother. 52, 790–795. https://doi.org/10.1093/jac/dkg446

Zhang, Y., Zhai, D., Xu, M., Yao, Q., Zhu, H., Chang, J., Wu, C., 2017. 3D-printed bioceramic scaffolds with antibacterial and osteogenic activity. Biofabrication 9, 025037. https://doi.org/10.1088/1758-5090/aa6ed6

Zhang, Y., Zhang, J., 2005. Surface modification of monodisperse magnetite nanoparticles for improved intracellular uptake to breast cancer cells. J. Colloid Interface Sci. 283, 352–357. https://doi.org/10.1016/j.jcis.2004.09.042

Zhong, Y., Li, S., 2021. New progress in improving the delivery methods of bisphosphonates in the treatment of bone tumors. Drug Des. Devel. Ther. 15, 4939–4959. https://doi.org/10.2147/DDDT.S337925

Zhou, Z., Yao, Q., Li, L., Zhang, X., Wei, B., Yuan, L., Wang, L., 2018. Antimicrobial activity of 3D-printed poly(ε-Caprolactone) (PCL) composite scaffolds presenting vancomycin-loaded polylactic acid-glycolic Acid (PLGA) Microspheres. Med. Sci. Monit. Int. Med. J. Exp. Clin. Res. 24, 6934–6945. https://doi.org/10.12659/MSM.911770

Zhu, M., Li, K., Zhu, Y., Zhang, J., Ye, X., 2015. 3D-printed hierarchical scaffold for localized isoniazid/rifampin drug delivery and osteoarticular tuberculosis therapy. Acta Biomater. 16, 145–155. https://doi.org/10.1016/j.actbio.2015.01.034

Zhu, M., Wang, H., Liu, J., He, H., Hua, X., He, Q., Zhang, L., Ye, X., Shi, J., 2011. A mesoporous silica nanoparticulate/β-TCP/BG composite drug delivery system for osteoarticular tuberculosis therapy. Biomaterials 32, 1986–1995. https://doi.org/10.1016/j.biomaterials.2010.11.025

Zielińska, A., Carreiró, F., Oliveira, A.M., Neves, A., Pires, B., Venkatesh, D.N., Durazzo, A., Lucarini, M., Eder, P., Silva, A.M., Santini, A., Souto, E.B., 2020. Polymeric nanoparticles: production, characterization, toxicology and ecotoxicology. Molecules 25, 3731. https://doi.org/10.3390/molecules25163731

CHAPTER 3

DEVELOPMENT AND OPTIMIZATION OF BEDAQUILINE-LOADED PLGA NANOPARTICLE FOR POTENTIAL TARGETED BONE DELIVERY

3.1. Introduction

Tuberculosis (TB) is an ancient infectious disease that has afflicted humanity since 2400 BC. The discovery of tubercle bacillus as a causing pathogen in 1882 by Robert Koch revolutionized the treatment of TB, as this resulted in the discovery of the Bacille Calmette-Guérin (BCG) vaccine against TB, which is still in use to date (Barberis et al., 2017; Cioboata et al., 2023; Daniel, 2006). Furthermore, in 1947, different anti-TB drugs were developed (Barberis et al., 2017). To date, the treatment of TB remains a challenge, as the prolonged treatment duration, drug-related toxicities, and non-adherence to therapy have contributed to the rise of drug-resistant TB (Sazali et al., 2023). Multidrug-resistant (MDR) TB, characterized by resistance to isoniazid and rifampicin, and extensively drug-resistant (XDR) TB, involving additional resistance to fluoroquinolones and at least one second-line injectable drug, present treatment challenges (Mphaphuli et al., 2023; World Health Organization, 2024). These strains require prolonged and complex therapeutic regimens, often associated with severe side effects and reduced efficacy (Dartois and Rubin, 2022; Mphaphuli et al., 2023).

One particularly concerning manifestation of TB is bone tuberculosis (bone TB), a form of extrapulmonary TB. Bone TB often affects the spine, causing vertebral destruction and severe deformities, and is associated with high morbidity if not treated promptly and effectively (Hegazy et al., 2021; Mphaphuli et al., 2023). A great clinical challenge in treating bone TB is inadequate drug concentration at the affected site, as well as delivering therapies directly to the bone, where infections may persist even under systemic treatment (Hua et al., 2022; Sharma et al., 2012). Bedaquiline (BQ), a diarylquinoline antimycobacterial agent, is the first anti-TB drug to receive FDA approval in over forty years. BQ offers a novel mechanism of action by inhibiting the ATP synthase enzyme essential for mycobacterial energy metabolism (Bélard et al., 2015; Bhandari et al., 2023). Furthermore, this anti-TB drug can target and eliminate both active and dormant forms of TB, which is crucial for bone TB treatment (Bhandari et al., 2023). Despite its efficacy, BQ has limitations, including poor aqueous solubility, low bioavailability, and potential toxicity, necessitating advanced drug delivery systems

to optimize its therapeutic profile (Bélard et al., 2015; De Matteis et al., 2018; Jahan et al., 2023).

Nanotechnology has emerged as a transformative tool in addressing these challenges, offering opportunities for controlled drug release, enhanced bioavailability, and targeted delivery (Malik et al., 2023). There are several advantages of nano-sized drug delivery over the systemic delivery of drugs, some of which are listed in **Figure 3.1.** In the context of TB, various nanosystem carriers including polymeric nanoparticles (PNs), liposomes, nanoemulsions, dendrimers, polymeric micelles, carbon nanotubes, metallic nanoparticles, solid lipid nanoparticles (SLNs), and nanostructured Lipid Carriers (NLCs) have been employed to deliver different anti-TB drugs, including BQ (Choudhary and Kusum Devi, 2015; Kumar et al., 2023). These nanotechnology-based drug delivery strategies can be used to treat bone diseases that are difficult to treat with conventional clinical therapies.

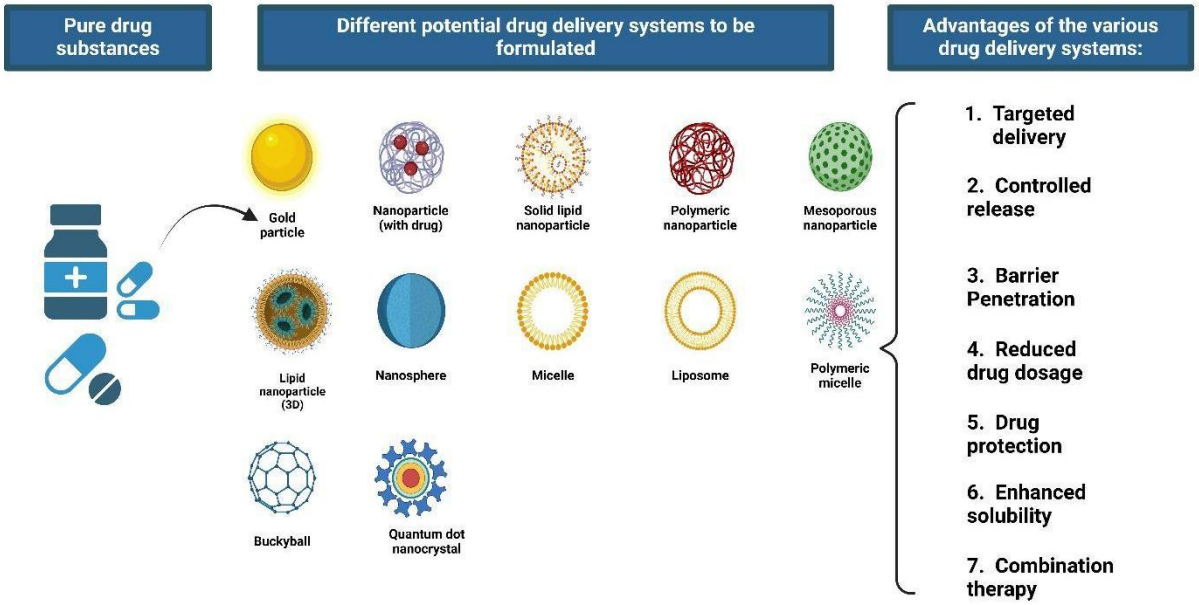


Figure 3.1: Schematic illustration of different nanoparticles and advantages of the nanoparticle systems.

PNs have gained significant interest in drug delivery applications due to their advantageous properties, including small particle size, excellent thermodynamic stability, enhanced solubility for hydrophobic drugs, prolonged drug release, and the ability to evade recognition by the reticuloendothelial system (RES) (Begines et al., 2020). Among the polymers used for these nanoparticles, Poly(lactic-co-glycolic acid) (PLGA) stands out as a particularly promising option. PLGA offers unique benefits,

including tunable degradation rates, efficient drug encapsulation, sustained release profiles, and the potential for targeted delivery to the bone tissues affected by TB (Begines et al., 2020; Liang et al., 2023; Makadia and Siegel, 2011). Furthermore, as a biocompatible and biodegradable polymer approved by regulatory agencies, PLGA has a well-established safety profile and widespread applicability in drug delivery applications, positioning it as a superior choice compared to other polymers like chitosan and alginate (Makadia and Siegel, 2011; Mphaphuli et al., 2023; Poh et al., 2019). The potential of PLGA nanoparticles for bone TB treatment lies in their ability to be tailored for both pulmonary and extrapulmonary TB, including bone infections (Luo et al., 2024). The small size of PLGA nanoparticles enables deep tissue penetration. At the same time, their ability to encapsulate drugs such as BQ allows for controlled release over extended periods, ensuring that therapeutic concentrations are maintained at the site of infection (Abdelghany et al., 2019; Luo et al., 2024; Struzek and Scherließ, 2023). This approach could help overcome the limitations of conventional TB treatments, offering a targeted and sustained release to affected bones, improving drug efficacy, and minimizing systemic side effects.

In addition, the application of Design of Experiments (DoE) within the framework of Quality by Design (QbD) has revolutionized the development and optimization of PLGA nanoparticles (Günday Türeli et al., 2016; Patil et al., 2024; Struzek and Scherließ, 2023). QbD is a systematic approach to pharmaceutical development that emphasizes a deep understanding of the product and process through predefined objectives (Pramod et al., 2016). DoE, a critical tool in the QbD paradigm, identifies and evaluates key formulation and process parameters and their interactions. This approach ensures that the nanoparticle formulation meets predefined quality attributes, such as particle size, drug loading, and release profiles (Pramod et al., 2016; Yu, 2008). This integration underscores the potential of PLGA nanoparticles in achieving precise and targeted drug delivery and meeting the stringent regulatory standards for pharmaceutical products. Patil et al., (2024) employed a QbD strategy to systematically develop multiple-drug-loaded PLGA nanoparticle systems as inhalable dry powders for TB treatment. Furthermore, this research assessed BQ and pretomanid (PTD) in combination as model drugs for TB treatment. The PLGA nanoparticles were developed using the oil-in-water (o/w) single emulsion solvent evaporation method. The nanoparticles demonstrated particle size of 200 ± 17 nm, PDI 0.10 – 0.14, and surface charge of (-) 30 ± 3 mV. The NPs showed high encapsulation efficiency of

82.04 ± 5.40 % and 92.52 ± 4.69 % w/w for BQ and PTD, respectively. Optimization of the PLGA nanoparticles for the inhalable dry powder formulation of BQ and PTD, several critical process parameters (CPPs) played a significant role in ensuring the success of the formulation. The following CPPs were particularly influential: spray drying temperature, feed rate, and inlet air flow rate (Patil et al., 2024). These CPPs were systematically evaluated using the DoE approach, which allowed the researchers to understand their effects on the critical quality attributes (CQAs) of the nanoparticles. By optimizing these parameters, the study successfully developed a formulation with high yield (72 ±2% w/w), low moisture content (<1% w/w), and suitable aerodynamic properties (MMAD of 2.4 μm and an FPF greater than 75%) for inhalation delivery. Furthermore, the optimal drug ratio of 1:4 for BQ to PTD was successfully loaded into the PLGA nanoparticles. This specific ratio is crucial for maximizing the effectiveness of the treatment against TB. Although the study reports on the quality attributes of the dry powder formulation, it does not provide long-term stability data. Stability is crucial for ensuring that the nanoparticles maintain their efficacy and safety over time, especially for inhalable formulations that may be stored for extended periods (Patil et al., 2024).

The primary aim of this chapter was to develop and characterize BQ-loaded PLGA nanoparticles for the management and treatment of TB. This system was designed with the potential for both pulmonary and extrapulmonary TB treatment, taking advantage of the flexible nature of PLGA nanoparticles. Due to their small size, biocompatibility, and ability to encapsulate a variety of drugs, PLGA nanoparticles can be tailored for pulmonary delivery via inhalation or systemic administration for extrapulmonary manifestations. The formulation of BQ-loaded PLGA nanoparticles was optimized using DoE, where both regression modeling and response surface modelling (RSM) were employed to identify key formulation parameters that influence nanoparticle characteristics, such as particle size, drug loading, and encapsulation efficiency.

3.2. Materials and Methods

3.2.1. Materials

Poly(d,l-lactide-co-glycolide) (PLGA) (75:25d, l-lactide:glycolide) were generous gift from Corbion Purac (Singapore). Bedaquiline (BQ) was purchased from Leap Chem (Hong Kong, China). Polyvinyl alcohol (PVA) (30kDa, 87−90% hydrolyzed), methanol

(99.9% purity HPLC grade), acetonitrile (99.9% HPLC grade), potassium dihydrogen orthophosphate (99.0% purity), triethylamine (99.5% purity), dichloromethane (DCM), dimethyl sulfoxide (DMSO), orthophosphoric acid (85% purity) were purchased from Sigma-Aldrich (Pty) Ltd (St. Louis, Missouri, United States). MG63 osteoblast-like cells were obtained from PromoLab (Pty) T/A Separations (Johannesburg, South Africa). Alpha minimum essential medium (α-MEM) was obtained from Gibco and Foetal Bovine Serum (FBS), gentamicin and Penicillin-Streptomycin were obtained from Sigma-Aldrich (Pty) Ltd (St. Louis, Missouri, United States), MTT Cell Proliferation Kit was used (Roche, Basel, Switzerland).

3.2.2. Development and Optimization of PLGA BQ-loaded Nanoparticles

BQ-loaded PLGA nanoparticles were developed and optimized using a four-factorial and a three-level Box-Behnken Design (BBD). The design was selected because it is widely recognized for developing higher-order response surfaces requiring fewer experimental runs than a standard factorial approach. Alongside the central composite design, it eliminates specific runs to preserve the potential for higher-order surface modeling (Jahan et al., 2023; Patil et al., 2024; Yu, 2008). The design was used to investigate the effects of independent variables *viz.,* PVA concentration (X_1; in the range 0.5 - 2.5%), sonication time (X_2; in the range 2-7mins), amplitude (X_3; in the range 40 - 80%), and drug amount (X_4; in the range 5 - 10 mg) (Table 3.1). The three variables were varied at three levels: low (coded as − 1), middle (coded as 0) and high (coded as 1). The critical quality attributes (CQA) of the PLGA nanoparticle formulation included particle size (Y_1), polydispersity index (PDI) (Y_2), drug loading (Y_3), and encapsulation efficiency (EE) (Y_4).

The responses were statistically analyzed using analysis of variance (ANOVA) in DesignExpert® v8 software (Stat-Ease Inc, MN, USA). A total of 29 formulations were generated, as presented in Table 3.1. The selection of optimal mathematical models was based on evaluating statistical parameters, including the p-value, lack-of-fit p-value (non-significant), R^2, adjusted R^2, predicted R^2, coefficient of variation (CV), and predicted residual sum of squares (PRESS). 3D and contour plots were developed based on the derived equations to better understand how the formulation factors influenced the responses. Optimization of the responses was carried out using both numerical and graphical methods. The desirability approach and overlay plots were used to identify an ideal solution with optimal formulation.

Table 3.1: BBD model for the effect of formulation composition on PLGA nanoparticles.

Formulation	X_1	X_2	X_3	X_4
1	1.50 (0)	4.50 (0)	40.00 (-1)	5.00 (-1)
2	1.50 (0)	4.50 (0)	80.00 (1)	10.00 (1)
3	1.50 (0)	4.50 (0)	80.00 (1)	5.00 (-1)
4	1.50 (0)	4.50 (0)	40.00 (-1)	10.00 (1)
5	1.50 (0)	4.50 (0)	60.00 (0)	7.50 (0)
6	0.50 (-1)	2.00 (-1)	60.00 (0)	7.50 (0)
7	1.50 (0)	4.50 (0)	60.00 (0)	7.50 (0)
8	0.50 (-1)	7.00 (1)	60.00 (0)	7.50 (0)
9	2.50 (1)	7.00 (1)	60.00 (0)	7.50 (0)
10	2.50 (1)	2.00 (-1)	60.00 (0)	7.50 (0)
11	2.50 (1)	4.50 (0)	60.00 (0)	5.00 (-1)
12	2.50 (1)	4.50 (0)	60.00 (0)	10.00 (1)
13	1.50 (0)	4.50 (0)	60.00 (0)	7.50 (0)
14	1.50 (0)	4.50 (0)	60.00 (0)	7.50 (0)
15	1.50 (0)	7.00 (1)	40.00 (-1)	7.50 (0)
16	1.50 (0)	2.00 (-1)	80.00 (1)	7.50 (0)
17	1.50 (0)	2.00 (-1)	40.00 (-1)	7.50 (0)
18	0.50 (-1)	4.50 (0)	60.00 (0)	10.00 (1)
19	1.50 (0)	7.00 (1)	80.00 (1)	7.50 (0)
20	0.50 (-1)	4.50 (0)	60.00 (0)	5.00 (-1)
21	1.50 (0)	7.00 (1)	60.00 (0)	10.00 (1)
22	1.50 (0)	4.50 (0)	60.00 (0)	7.50 (0)
23	1.50 (0)	2.00 (-1)	60.00 (0)	5.00 (-1)
24	1.50 (0)	4.50 (0)	60.00 (0)	7.50 (0)
25	2.50 (1)	4.50 (0)	80.00 (1)	7.50 (0)
26	1.50 (0)	2.00 (-1)	60.00 (0)	10.00 (1)
27	0.50 (-1)	4.50 (0)	40.00 (-1)	7.50 (0)
28	0.50 (-1)	4.50 (0)	80.00 (1)	7.50 (0)
29	2.50 (1)	4.50 (0)	40.00 (-1)	7.50 (0)

X_1: PVA conc, **X_2**: sonication time, **X_3**: amplitude, **X_4**: drug amount

3.2.3. Fabrication of optimized BQ-loaded PLGA nanoparticles

BQ-loaded PLGA nanoparticles were prepared using a single emulsion (O/W) method as depicted in **Figure 3.2.** (Poh et al., 2019). Briefly, 50mg of PLGA and different amounts of BQ were dissolved in DCM (2 ml) to form the organic phase. It was then slowly mixed with an aqueous solution containing PVA, and an O/W-type emulsion was formed upon probe sonication at the optimized amplitude (78.4%) for a set time over an ice bath. The emulsion was added dropwise to 20 ml of 0.75% w/v PVA mixture under magnetic stirring (500 rpm) at room temperature. This mixture was left stirring for 3 hours to remove DCM and form nanoparticles and was washed thrice with deionized water followed by centrifugation at 10,000 rpm for 30 minutes. The resulting nanoparticles were freeze-dried over 24 hours under a freeze-dried system to obtain nanoparticles in powder form.

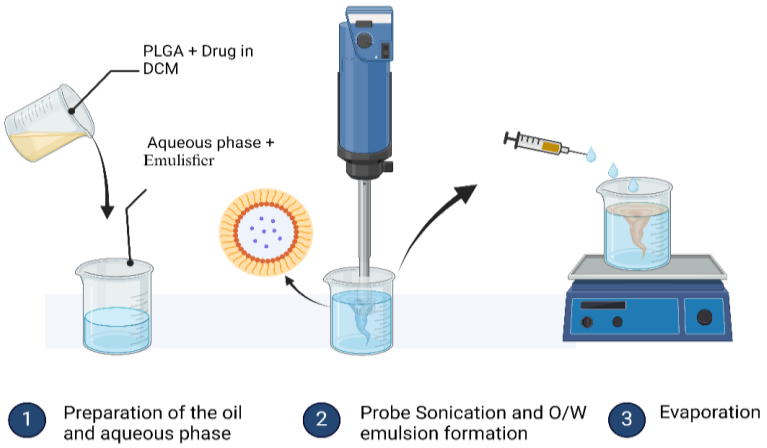


Figure 3.2: Schematic representation of the manufacturing process of BQ-loaded PLGA nanoparticles.

3.2.4. Characterization of the Optimized BQ-loaded PLGA nanoparticles

3.2.4.1. Determination of particle size

Nanoparticle size and distribution profiles were evaluated using a ZetaSizer NanoZS (Malvern Instruments, Malvern, UK), equipped with non-invasive backscatter technology operating at a 173° angle. The zeta potential of the formulated nanoparticles was assessed by subjecting individual samples to a controlled electric field and measuring their mobility through Brownian motion. This analysis utilized a combination of Laser Doppler Velocimetry and Phase Analysis Light Scattering, with the sample conductivity maintained at a maximum of 200 mS/cm.

3.2.4.2. Determination of particle surface morphology

Morphological evaluation of the nanoparticles was performed using scanning electron microscopy (SEM) (ZEISS Electron Microscopy, Carl Zeiss Microscopy Ltd., Cambridge, UK). Samples of the nanoparticle suspension (5 to 10 µL) were dropped onto an aluminium specimen stub and air-dried before coating (×2) with gold-palladium (AuPd). The sample was viewed and captured under low (82.34 KX) and high (314.84 KX) magnification.

3.2.4.3. Analysis of chemical integrity using FTIR spectroscopy analysis

Fourier Transform Infrared (FTIR) spectroscopy (Spectrum 100, PerkinElmer Inc., Waltham, MA, USA) was employed to examine and compare the vibrational transitions

of chemical structures in both individual components and their combinations within the BQ-loaded PLGA nanoparticles. The analysis was performed on pristine BQ, PLGA, and the BQ-loaded nanoparticles. Spectra were acquired under 120 psi pressure, covering the wavelength range of 4000–550 cm^{-1}, with 20 scans conducted to ensure the capture of detailed and relevant spectral information.

3.2.4.4. Analysis of the crystallographic structure

X-ray powder diffraction (XRD) (RIGAKU MiniFlex, RIGAKU Inc., Tokyo, Japan) analysis was performed to examine pure BQ, pristine PLGA, blank PLGA nanoparticles, and lyophilized BQ-loaded PLGA nanoparticles. A scan of 2θ was conducted at a speed of ten degrees per minute, between 10 and 90 degrees. This was followed by diffraction analyses, which allowed for the observation of the nanoparticles' degree of crystallinity.

3.2.4.5. Analysis of thermal behaviour using differential scanning calorimetry (DSC)

Pristine BQ, pure PLGA, blank PLGA nanoparticles, and lyophilized BQ-loaded PLGA nanoparticles were analyzed using differential scanning calorimetry (DSC) with a DSC-60 instrument (TA-60 WS, Shimadzu, Kyoto, Japan). Approximately 3–10 mg of each sample was placed in aluminium pans, then crimp-sealed for analysis. The DSC measurements were conducted at a heating rate of 10 °C/min under an inert nitrogen atmosphere with a 50 mL/min flow rate. An empty aluminium pan served as the reference. The DSC thermogram of free BQ was compared with that of the lyophilized BQ-loaded PLGA nanoparticles to assess potential changes in the physicochemical properties of BQ and its interaction with the PLGA polymer.

3.2.4.6. Analysis of thermal stability assessment using thermogravimetric analysis (TGA)

The composition of BQ-loaded PLGA nanoparticles was determined using thermogravimetric analysis (TGA) conducted on a TGA 4000 instrument (PerkinElmer, Llantrisant, Wales, UK). The analysis was performed within a temperature range of 30 °C to 900 °C under a continuous nitrogen flow. Samples were heated at a constant rate of 10 °C per minute. The resulting thermograms, represented as percentage weight loss versus temperature, were analyzed using Pyris™ software (PerkinElmer, Llantrisant, Wales, UK).

3.2.4.7. Determination of BQ content in the PLGA nanoparticles

The BQ content in the PLGA nanoparticles was evaluated by high-performance liquid chromatography (HPLC) (Waters, Milford, Massachusetts, USA) following the method described by Ayodele et al., (2024). The HPLC system was equipped with Waters symmetry300™ C18 5 µm, 4.6 x 150mm column, a UV-detector, and a Waters binary HPLC pump. 95:5 ($^{v}/_{v}$) mixtures of acetonitrile/methanol and phosphate buffer (pH 7.4) were used as the mobile phase with a flow rate of 1.0mL/min, at a wavelength of 275 nm. For measuring BQ content in PLGA nanoparticles, 5mg of freeze-dried nanoparticles was dissolved in DMSO and vortexed for 1 minute to completely solubilize the PLGA nanoparticles. The solution was centrifuged at 13,000 rpm for 10 minutes at 4 °C. The supernatant was then collected for analysis of BQ concentration by HPLC. Entrapment efficiency (EE%) and drug loading (DL%) were calculated with equation 3.1 and 3.2. The measurements were performed in triplicate.

$$EE\ (\%) = \frac{Weight\ of\ drug\ in\ nanoparticles}{Initial\ weight\ of\ feeding\ drug}\ X\ 100 \qquad \textbf{(3.1)}$$

$$DL\ (\%) = \frac{Weight\ of\ drug\ in\ nanoparticles}{Weight\ of\ nanoparticles}\ X\ 100 \qquad \textbf{(3.2)}$$

3.2.4.8. Stability studies

The optimized freeze-dried BQ-loaded PLGA nanoparticles were kept in sealed air-tight vials at 25 ± 2 °C and relative humidity (RH) of 60 ± 5% in the stability chamber (Labcon, South Africa) and studied for their stability over 3 months. The stability samples were evaluated monthly to assess any variations in particle size, PDI, EE%, and DL% of the optimized lyophilized BQ-loaded PLGA nanoparticles. The data obtained from the samples collected every month was compared with the freshly prepared BQ-loaded PLGA nanoparticles (time zero sample). All determinations were run in triplicate and reported as mean±S.D.

3.2.4.9. Evaluation of *in-vitro* release of BQ from the PLGA nanoparticles

The *In-vitro* drug release behaviour of BQ-loaded PLGA nanoparticles was evaluated at pH 7.4 for 48 hours at 37 °C, mimicking the physiological conditions of the bone environment. The freeze-dried BQ-loaded PLGA nanoparticles (5mg) were dispersed in 2ml of prepared 0.1 M PBS (pH 7.4) containing 0.5% v/v Tween 80. The inclusion of Tween 80 was essential for improving the solubility and stability of the nanoparticles in

the release medium, ensuring consistent release behaviour. The samples were then loaded into a dialysis membrane (SnakeSkin™, 3500 MWCO) and submerged into the drug release phosphate buffer (100 mL) of pH of 7.4 and incubated in an orbital shaking incubator (YIHDER LM-530, YIHDER Co., Ltd., Taipei, Taiwan). The dialysis membrane was used to facilitate the diffusion of only BQ into the release medium for quantification. Sampling (2 mL) was undertaken at different time intervals (t = 1, 2, 4, 8, 12, 24 and 48 hours). The cumulative amount of BQ release at different time points was evaluated by the HPLC method. The data of *In-vitro* release were fitted into different kinetic models to know the mechanism and kinetics of BQ release from PLGA nanoparticles (Najib et al., 2023).

3.2.4.10. *In-vitro* assays for cytotoxicity studies of PLGA nanoparticles

The osteoblast-like cell line (MG63) was employed for the cytotoxicity study. The osteoblast-like MG63 cells were chosen because they express several characteristic features of osteoblast, and they are a great candidate for evaluation of cell viability, cell adhesion, and cell proliferation in bone tissue engineering. Briefly, cells were grown in Alpha Minimum Essential Medium (α-MEM, 82% *v/v*) supplemented with Foetal Bovine Serum (FBS, 14% *v/v*), 2% (*v/v*) gentamicin, and 2% (*v/v*) penicillin-streptomycin in a T-25 culture flask (Sigma-Aldrich; St. Louis, MO, USA). Cells were allowed to grow, and when a 90% confluence was reached, cultured cells were dissociated from the culture flask with 0.25% trypsin. The cells were seeded in a 96-well plate, at a seeding density of 2.5×10^4. To each well, a cell suspension of 90 µL was added followed by incubation at 37°C, 5% CO_2 for 24 hours to allow adequate cell adherence.

The experimental cells were treated in triplicate (n=3) with 10 µL of PLGA nanoparticles, BQ, and BQ-loaded PLGA nanoparticles at concentrations of 5 µg/ml, 10 µg/ml, 20 µg/ml, 40 µg/ml, and 60 µg/ml. The negative control consisted of untreated cells. After treatment, the cells were incubated for 72 hours before performing the MTT cell viability assay. The MTT assay was carried out using the MTT Cell Proliferation Kit I (Roche, Basel, Switzerland). A 10 µL solution of MTT (5 mg/mL) was added to each well, followed by a 4-hour incubation at 37°C with 5% CO_2. Afterward, 100 µL of the solubilizing agent (acid-isopropanol, 0.04 N HCl in isopropanol) was added to dissolve the formed formazan crystals, and the plate was incubated overnight at 37°C with 5% CO_2. Absorbance was measured at 570 nm with a reference wavelength of 620 nm

using a multimodal microplate reader (Victor X3, PerkinElmer, Waltham, MA, USA). The absorbance values were recorded (mean ± standard deviation) and used to calculate % cell viability using Equation 3.3.

$$\%\ Cell\ viability = \frac{A_{test} - A_{blank}}{A_{control} - A_{blank}}\ X\ 100 \qquad \textbf{(3.3)}$$

where A_{test} is the test absorbance, A_{blank} is the blank absorbance, and $A_{control}$ is the control absorbance in nm.

3.3. Results and Discussion

3.3.1. Statistical Optimization

The 29 experimental runs conducted for the BQ-loaded PLGA nanoparticles are summarized in **Table 3.2**, detailing the results for particle size, PDI, encapsulation efficiency, and drug loading. The effects of PVA concentration, sonication time, amplitude percentage, and drug amount on these responses are analyzed and illustrated using 2D contour plots, 3D response surface plots, and corresponding polynomial equations.

Table 3.2: Experimental design and characteristics of BQ-loaded PLGA nanoparticles.

Std	Experimental run	Y_1	Y_2	Y_3	Y_4
5	**1**	225.5	0.06	9.0	67.5
8	**2**	252.2	0.05	16.3	38.0
6	**3**	238.5	0.08	9.4	74.1
7	**4**	244.0	0.07	16.8	76.9
9	**5**	238.4	0.06	13.3	78.1
1	**6**	317.8	0.19	13.2	83.5
10	**7**	233.4	0.04	13.3	69.5
3	**8**	316.4	0.21	12.9	59.7
4	**9**	182.9	0.07	12.8	68.4
2	**10**	216.6	0.07	13.1	67.3
12	**11**	198.0	0.05	9.2	54.1
14	**12**	193.2	0.06	17.1	59.3
19	**13**	233.0	0.05	13.0	59.3
20	**14**	234.0	0.08	13.1	54.5
16	**15**	209.1	0.04	13.1	62.0
17	**16**	389.6	0.18	13.0	52.1
15	**17**	400.5	0.20	13.1	55.3
13	**18**	324.8	0.17	16.6	48.9
18	**19**	228.2	0.07	12.8	58.1
11	**20**	318.1	0.22	9.1	60.9
27	**21**	323.6	0.23	16.4	50.3
28	**22**	235.0	0.07	13.1	56.0
25	**23**	223.5	0.05	9.1	56.0
29	**24**	234.0	0.05	13.1	42.4
24	**25**	197.2	0.05	13.0	37.9

26	**26**	231.0	0.07	13.4	35.8
21	**27**	323.2	0.19	13.1	31.0
23	**28**	323.8	0.21	13.2	33.6
22	**29**	238.4	0.08	13.0	33.7

Y_1:particle size**, Y_2:** polydispersity index**, Y_3:** drug loading**, Y_4:** entrapment efficiency

3.3.1.1. Evaluation of model adequacy and ANOVA for particle size (Y_1)

The model's reliability and accuracy were confirmed through various statistical metrics, as summarized in Table 3.3. An R^2 value near 1 indicates a strong data fit, while adequate precision, with a value of 41.044 (well above the threshold of >4), confirms the model's strong predictive capability. A low coefficient of variation (C.V.) of 5.70% (below the 10% threshold) demonstrates high reproducibility. Together, these metrics validate the model's robustness and precision. To further confirm the adequacy, validity, and robustness of the regression model, a graphical representation of the model for particle size was analyzed. The graphical representations include the normal probability plot of residuals depicted in **Figure 3.3a** which exhibits the linearity of the data. The plot of the measured and model-predicted values depicted in **Figure 3.3b** shows data that is linear, suggesting that the model is adequate.

Table 3.3 Model adequacy measures and values summary.

Fit statistics	**Values**
Std Dev	4.12E-009
Mean	7.236E-008
% C. V	5.70
R^2	0.99
Adjusted R^2	0.99
Adequate Precision	41.04

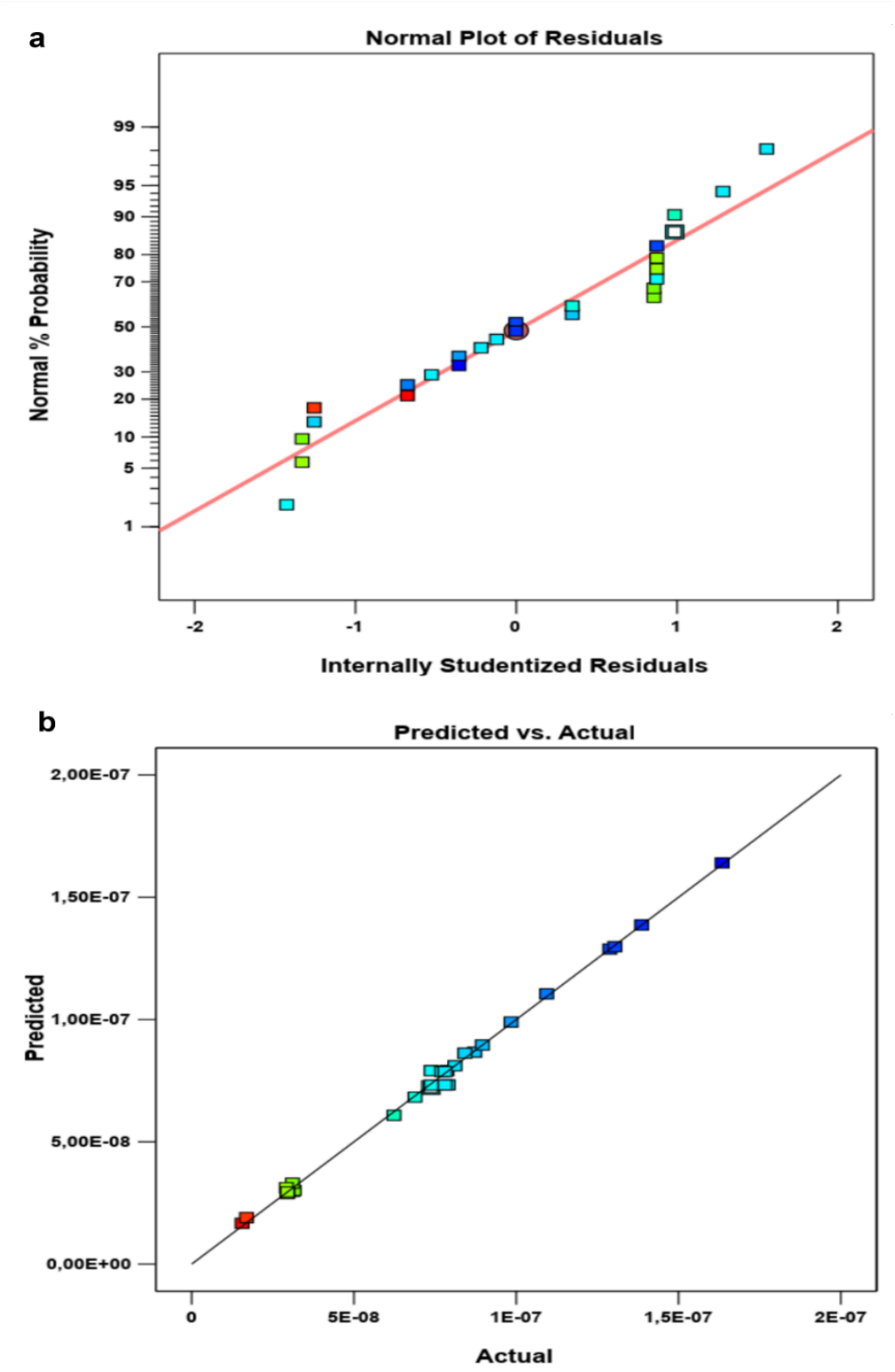


Figure 3.3: (a) Normal plot of residuals depicting the impact of model terms on particle size, **(b)** Observed versus predicted response for particle size.

To meet the validity requirements of ANOVA, the experimental data concerning Y_1 response was transformed. The power transformation was utilized for this response. Hence, after transformation, the statistical model used with a significant value ($p<0.05$)

was linear as summarized in **Table 3.4**. The F-value is 125.78 and the low probability of p<0.0001 indicates that there is a 0.01% chance that the F-value is due to noise, resulting in the model being significant. The effects of **X_1, X_2, X_3, X_4, X_1X_2, X_1X_3, X_2X_3, X_2X_4, X^2_3, X^2_4, $X^2_1X_2$, $X^2_1X_3$, $X^2_1X_4$, $X_1X^2_3$, $X_2X^2_4$, and $X^2_3X_4$** are significant to the linear model (shaded in grey). The absence of a significant lack-of-fit further emphasizes the high predictive capability of the model.

Table 3.4: Statistical measures of model adequacy.

Source	Sum of Squares	Df	Mean Square	F-value	p-value
Model	4.059E-014	19	2.137E-015	125.78	< 0.0001
X_1	2.064E-014	1	2.064E-014	1215.19	< 0.0001
X_2	6.485E-015	1	6.485E-015	381.76	< 0.0001
X_3	2.407E-016	1	2.407E-016	14.17	0.0070
X_4	8.113E-016	1	8.113E-016	47.76	0.0002
X_1X_2	1.044E-015	1	1.044E-015	61.45	0.0001
X_1X_3	8.054E-016	1	8.054E-016	47.42	0.0002
X_2X_3	3.437E-017	1	3.437E-017	2.02	0.1979
X_2X_4	1.765E-016	1	1.765E-016	10.39	0.0146
X^2_3	6.084E-016	1	6.084E-016	35.82	0.0006
X^2_4	1.225E-017	1	1.225E-017	0.72	0.4239
$X^2_1X_2$	1.405E-017	1	1.405E-017	0.83	0.3934
$X^2_1X_3$	1.225E-015	1	1.225E-015	72.10	< 0.0001
$X^2_1X_4$	2.922E-016	1	2.922E-016	17.20	0.0043
$X_1X^2_3$	1.143E-015	1	1.143E-015	67.26	< 0.0001
$X_2X^2_4$	1.024E-015	1	1.024E-015	60.27	0.0001
$X^2_3X_4$	7.614E-016	1	7.614E-016	44.82	0.0003
Lack of fit	1,062E-16	4	2,654E-17	6,25	0,0821

X_1: PVA conc, **X_2**: sonication time, **X_3**: amplitude, **X_4**: drug amount

The relationship between the particle size of PLGA nanoparticles and other input variables, including their interaction, is described by **Equation 3.4.**

$$Y_1^3 = +7.704E008+5.080E008X_1+4.026E008X_2 - 5.485E009X_3 - 3.149E008X_4+1.615E008X_1 X_2 +1.419E008X_1 X_3+2.931E009X_1 X_4 - 6.643E009X_2 X_3 - 2.727E008X_2 X_4+1.750E009X_3 X_4+1.623E009X_1^2 -1.515E008X_3^2+8.058E009X_4^2-2.390E008X_1^2 X_2+3.348E008X_1^2 X_4-1.451E008X_1 X_3^2-3.880E008X_2 X_4^2+2.450E008X_3^2 X_4 \quad \textbf{(3.4)}$$

Where,

Y_1 = particle size

X_1 = PVA Concentration

X_2 = Sonication time

X_3= Amplitude

X_4 = drug amount

The polynomial equation was employed to draw conclusions based on the magnitude and mathematical sign of the coefficients. In **Equations 3.4**, PVA concentration, sonication time, amplitude, and drug amount are recognized as the primary factors influencing the response (Y_1). PVA concentration and sonication time positively impacted the response, while the amplitude and drug amount exhibited a negative effect.

The contour and three-dimensional (3D) plots were generated to study the relationship between the input variables and the responses. The shape and color of the plots reveal the interaction between the variables being investigated. The particle size of the BQ-loaded PLGA nanoparticles ranged from 182.9d.nm to 400.5d. nm as shown in **Figure 3.4 a,b**. Notably, formulations with high PVA concentration (F9 and F12, 182.9d.nm and 193.2d.nm, respectively) showed a decrease in size compared to those with low PVA concentration (F17, F18, F27, and F28,400.5d.nm; 324.8d.nm; 323.2d.nm; 323.8d.nm, respectively). Pharmaceutically, PVA has a variety of functions and is commonly used as a surfactant and stabilizer (Cortés et al., 2021; Higazy et al., 2021). For the BQ-loaded PLGA nanoparticles, PVA is suggested to have reduced the interfacial tension between the organic solution and aqueous medium, increasing the emulsion stability and acting as a steric stabilizer, increasing particle size as illustrated in **Figure 3.4 a,b** (Menon et al., 2012). The results achieved in this study are in agreement with previous findings done by other groups (Günday Türeli et al., 2016; Menon et al., 2012; Struzek and Scherließ, 2023).

Furthermore, a decrease in the nanoparticle size was observed when increasing the sonication time. This is consistent with a study conducted by Madani et al., (2018) (Madani et al., 2018). This effect can be attributed to that a higher sonication time promotes a rapid diffusion of the organic solution in the aqueous phase (Kolahi et al., 2022; Madani et al., 2018).

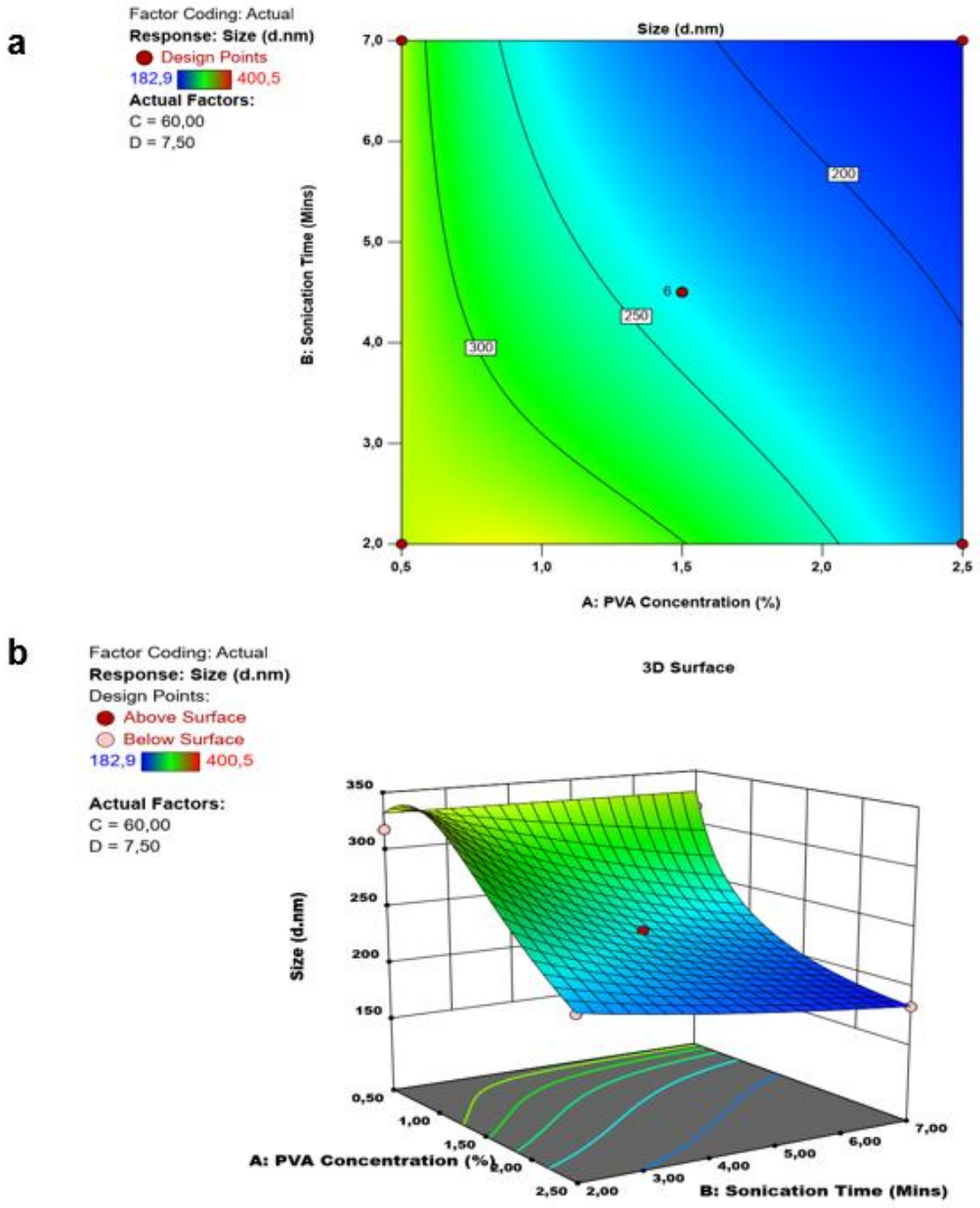


Figure 3.4: (a) 2D contour plot depicting the impact of X_1 and X_2 on particle size, **(b)** 3D response surface plot depicting the impact of X_1 and X_2 on the particle size of the BQ-loaded PLGA nanoparticles.

An ideal nanoparticle size for targeted bone drug delivery is 0-100 nm, as this allows the nanoparticles to travel within the bone sinusoids efficiently and deliver a substantial quantity of the drug into the cells via endocytosis. However, it has been shown that a nanoparticle size of 200 nm is sufficient for bone-targeted delivery, as this particle size can penetrate cellular barriers and enhance endocytosis (Posadowska et al., 2015).

3.3.1.2. Evaluation of model adequacy and ANOVA for polydispersity index (Y_2)

The model adequacy was confirmed according to the specifications detailed in **Table 3.5**. The predicted R^2 is in reasonable agreement with the adjusted R^2, and the adequate precision is greater than 4, indicating that the model is robust and can be used. The graphical representations of the model adequacy for PDI are summarized in **Appendix A**.

Table 3.5: Model adequacy measures and values summary.

Fit statistics	Values
Std Dev	0.0445
Mean	0.3073
Predicted R^2	0,6184
PRESS	0,1035
% C. V	14.49
R^2	0.8831
Adjusted R^2	0.8100
Adequate Precision	9.847

The suggested PDI (Y_2) model was square root, and the ANOVA data are summarized in **Table 3.6**. The model terms that exerted a significant effect are shaded in grey

Table 3.6: ANOVA analysis model for PDI.

Source	Sum of Squares	Df	Mean Square	F-value	p-value
Model	0,2396	10	0,0240	12,08	< 0.0001
X_1	0,1189	1	0,1189	59,94	< 0.0001
X_2	0,0148	1	0,0148	7,47	0,0147
X_3	0,0001	1	0,0001	0,0719	0,7920
X_4	0,0004	1	0,0004	0,2157	0,6486
X_1X_3	0,0019	1	0,0019	0,9460	0,3452
X_2X_3	0,0006	1	0,0006	0,3179	0,5807
X^2_1	0,0349	1	0,0349	17,61	0,0007
X^2_2	0,0240	1	0,0240	12,08	0,0031
X^2_3	0,0024	1	0,0024	1,19	0,2917
$X_2X^2_3$	0,0603	1	0,0603	30,38	< 0.0001
Lack of fit	0.0271	13	0.0021	1.36	0.4507

X_1: PVA conc, **X_2**: sonication time, **X_3**: amplitude, **X_4**: drug amount

The PVA concentration and sonication time exert significant effects on PDI, and this effect is better understood using a mathematical representation shown by Equation 3.5. The effect of the input variables on PDI is mathematically represented by **Equation 3.5.**

$$\sqrt{Y_2} = 0.2489 - 0.0995X_1 + 0.0473X_2 - 0.0034X_3 + 0.0064X_4 - 0.0217X_1X_3 + 0.0126X_2X_3$$

$$+ 0.071X_1^2 + 0.0602X_2^2 + 0.0187X_3^2 - 0.1554X_2X_3^2 \quad \textbf{(3.5)}$$

Where,

Y_2 = PDI

X_1 = PVA Concentration

X_2 = Sonication time

X_3= Amplitude

X_4 = drug amount

PDI is an indicator of the size distribution of PLGA nanoparticles, lower PDI values (0.1-0.25) indicate monodisperse samples whereas polydisperse samples have higher values (>0.5) of PDI and this indicates a wider particle size distribution (Ruiz et al., 2022). The PDI for the BQ-loaded PLGA nanoparticles ranged from 0.038 to -0.23. The increase in PVA concentrations, which reduces PDI by stabilizing the nanoparticles during formation, is suggested as the reason for the low PDI values.

The impact of PVA concentration and amplitude on PDI was further interpreted using response surface plots, as depicted in **Figure 3.5a,b.** An increase in PVA concentration resulted in a significant decrease in PDI compared to the effect of amplitude, as shown in **Figure 3.5a,b**, where increasing the amplitude caused a slight increase in the PDI of the BQ-loaded PLGA nanoparticles. There was no combinatory effect between PVA concentration and amplitude, as observed by the little to no change in PDI due to amplitude throughout the concentrations.

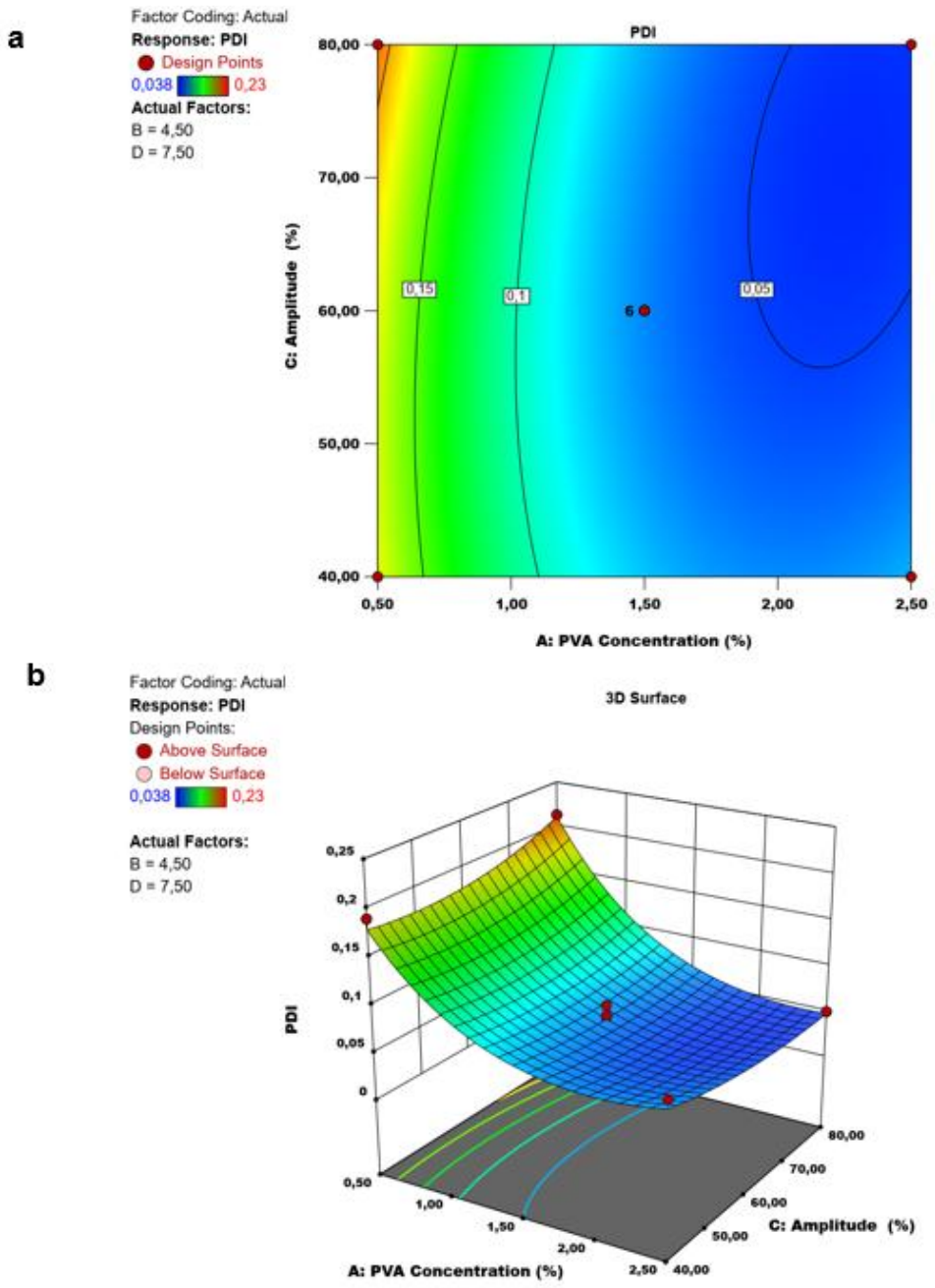


Figure 3.5: (a) 2D contour plot depicting the impact of X_1 and X_3 on PDI, **(b)** 3D response surface plot depicting the impact of X_1 and X_3 on the PDI of the BQ-loaded PLGA nanoparticles.

3.3.1.3. Evaluation of model adequacy and ANOVA for drug loading (%) (Y_3)

The value and a Prob > F value was used to determine the significance of the model at a 0.05 level of confidence. The ANOVA data for the linear mixture model for DL (%) (Y_3) are summarized in **Table 3.7**. The significant model terms were **X_1, X_2, X_4, X_1X_4, X_3X_4, X^2_1, X^2_3, X^2_4, $X^2_1X_2$, $X^2_1X_4$, $X_1X^2_2$, $X_1X^2_3$, $X^2_2X_4$, $X_2X^2_3$, and $X^2_1X^2_2$** (highlighted in

grey). The significance of response surface models was investigated using ANOVA and model F.

Table 3.7: ANOVA analysis model for DL (%).

Source	Sum of Squares	Df	Mean Square	F-value	p-value
Model	141,60	22	6,44	2852,82	<0.0001
X_1	0,0657	1	0,0657	29,10	0,0057
X_2	0,5250	1	0,5250	232,69	0,0001
X_3	0,0002	1	0,0002	0,0684	0,8065
X_4	54,44	1	54,44	24131,25	<0.0001
X_1X_2	0,0003	1	0,0003	0,1112	0,7556
X_1X_3	0,0031	1	0,0031	1,3570	0,3088
X_1X_4	0,0470	1	0,0470	20,8103	0,0103
X_2X_3	0,0070	1	0,0070	3,0883	0,1537
X_2X_4	0,0054	1	0,0054	2,4127	0,1953
X_3X_4	0,1686	1	0,1686	74,7388	0,0010
X^2_1	0,0438	1	0,0438	19,4224	0,0116
X^2_2	0,0017	1	0,0017	0,7694	0,4299
X^2_3	0,0516	1	0,0516	22,8831	0,0088
X^2_4	0,0989	1	0,0989	43,8476	0,0027
$X^2_1X_2$	0,5894	1	0,5894	261,2458	<0,0001
$X^2_1X_4$	0,0462	1	0,0462	20,4729	0,0106
$X_1X^2_2$	0,0485	1	0,0485	21,5135	0,0097
$X_1X^2_3$	0,0633	1	0,0633	28,0556	0,0061
$X^2_2X_3$	0,0149	1	0,0149	6,5993	0,0620
$X^2_2X_4$	0,5050	1	0,5050	223,8135	0,0001
, $X_2X^2_3$	0,5257	1	0,5257	233,0250	0,0001
$X^2_1X^2_2$	0,0554	1	0,0554	24,5669	0,0077
Lack of fit	0.0039	1	0.0039	2.33	0,2244

X_1: PVA conc, X_2: sonication time, X_3: amplitude, X_4: drug amount

The model F-value of 2852.82 and *p*-value <0.0001 indicate that the model was significant. Furthermore, the lack of fit was not significant for the generated data, confirming that the model is acceptable. The adequacy of the model was investigated by examining normal probability, studentized residuals, and Box-Cox plots for DL(%) (Y_3), as depicted in **Figures 3.6a-c**. The normal probability and studentized residual plots reveal a linear distribution and scatter of data, confirming that the data was normal. The Box-Cox plot shows that the data were in the optimum region of the parabola and that transformation of the data was not required. From the results obtained from the diagnostic plots of the linear model, it is evident that the model fits the criteria of model adequacy. This implies that the linear model is adequate to be used to describe the relationship between input variables and zeta potential.

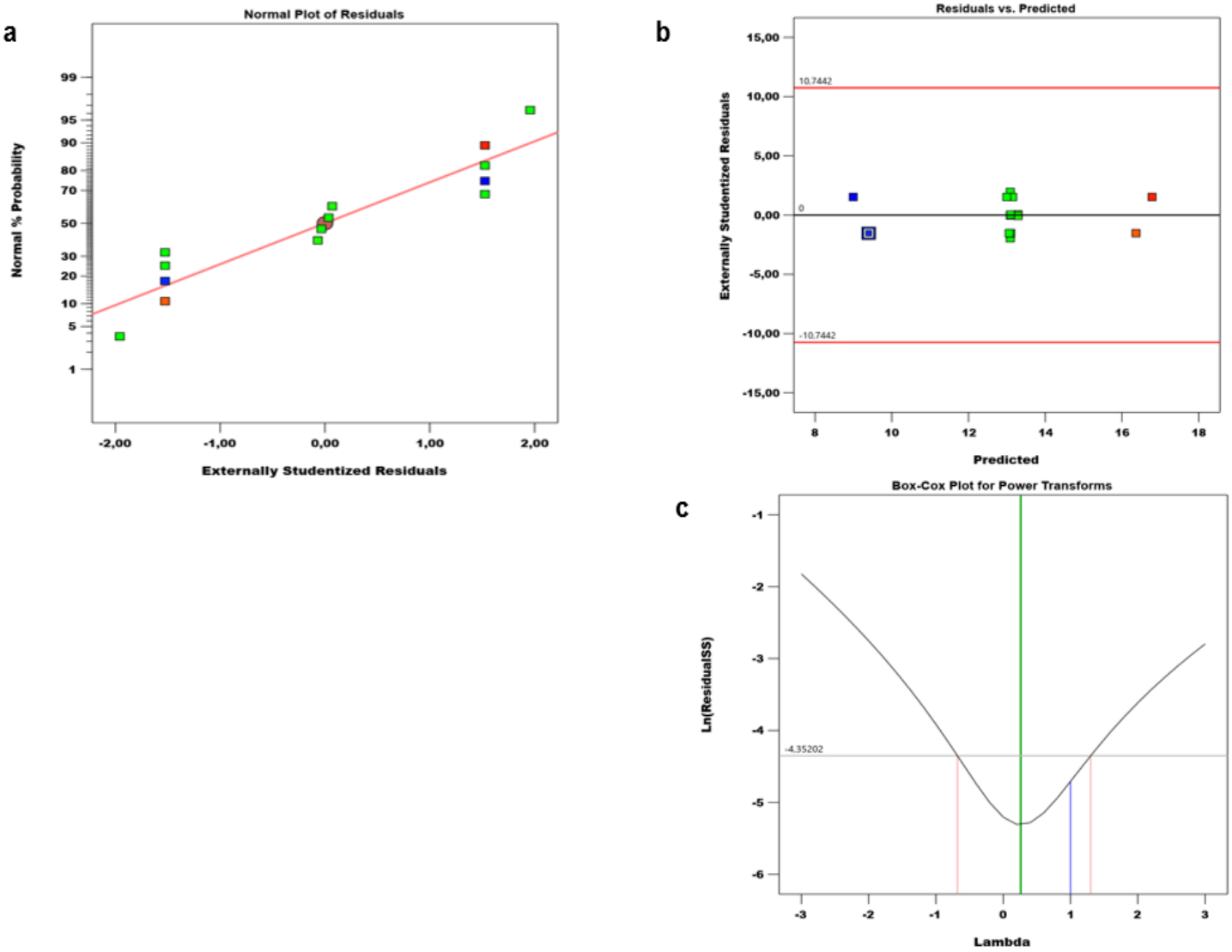


Figure 3.6: (a) Normal probability plot of residuals for DL, **(b)** plot of studentized residuals versus predicted responses for DL, **(c)** Box-cox plot for power transformation for DL.

The Box-Cox plot generated includes the blue line within the 95% confidence interval, confirming that the data were in the optimum region of the parabola and model adequacy. The determination of DL (%) was evaluated to establish nanoparticles with a high drug loading percentage as this would require fewer nanoparticles to achieve the therapeutic level. This approach results in minimal adverse effects caused by excessive carrier materials (Khalbas et al., 2024; Shen et al., 2017). The final equation for the DL is reported as **Equation 3.6.**

$$Y_3 = 13.16+0.1281X_1+1.66X_2-0.0044X_3+3.69X_4+0.0079X_1X_2-0.0277X_1X_3+0.1083X_1X_4-0.0417X_2X_3-0.1690X_2X_4-0.2053X_3X_4+0.1570X_1^2+0.0561X_2^2-0.1704X_3^2-0.2359X_4^2-1.80X_1^2X_2+0.1520X_1^2X_4-0.1558X_1X_2^2-0.1779X_1X_3^2-0.0747X_2^2X_3-1.67X_2^2X_4-1.70X_2X_3^2-0.5264X_1^2X_2^2 \quad \textbf{(3.6)}$$

Where,

Y_3 = Drug loading (%)
X_1 = PVA Concentration
X_2 = Sonication time
X_3= Amplitude
X_4 = drug amount

Contour plots that show the impact of drug amount, PVA concentration, and sonication time on the DL(%) are depicted in **Figure 3.7a, b**. The plots show that X_4 has a positive effect with DL(%), evidently as more drug is added, the higher the DL(%), indicating better incorporation efficiency. DL(%) of BQ in the prepared PLGA nanoparticles was noted to range from 9.02% to 17.09% proving to be satisfactory as most polymeric nanoparticles have a DL(%) ranging from 0.2% to 35% (Troiano et al., 2013). A hypothesized cause for this phenomenon is that BQ is highly hydrophobic due to its aromatic rings and long aliphatic chains. Its hydrophobic nature makes it poorly soluble in aqueous environments but highly compatible with hydrophobic polymers like PLGA (75:25), which has a high proportion of lactic acid residues (Preiss et al., 2015; Van Hemelryck et al., 2021). This results in the hydrophobic regions of BQ interacting with the hydrophobic segments of PLGA through van der Waals forces and hydrophobic interactions (Lee and Pokorski, 2018). This leads to BQ embedding itself in the polymer matrix, increasing DL(%). **Figure 3.7a** shows a slight decrease in DL(%) with higher PVA concentration, this is due to that PVA concentration affects the stability of the nanoparticle formation.

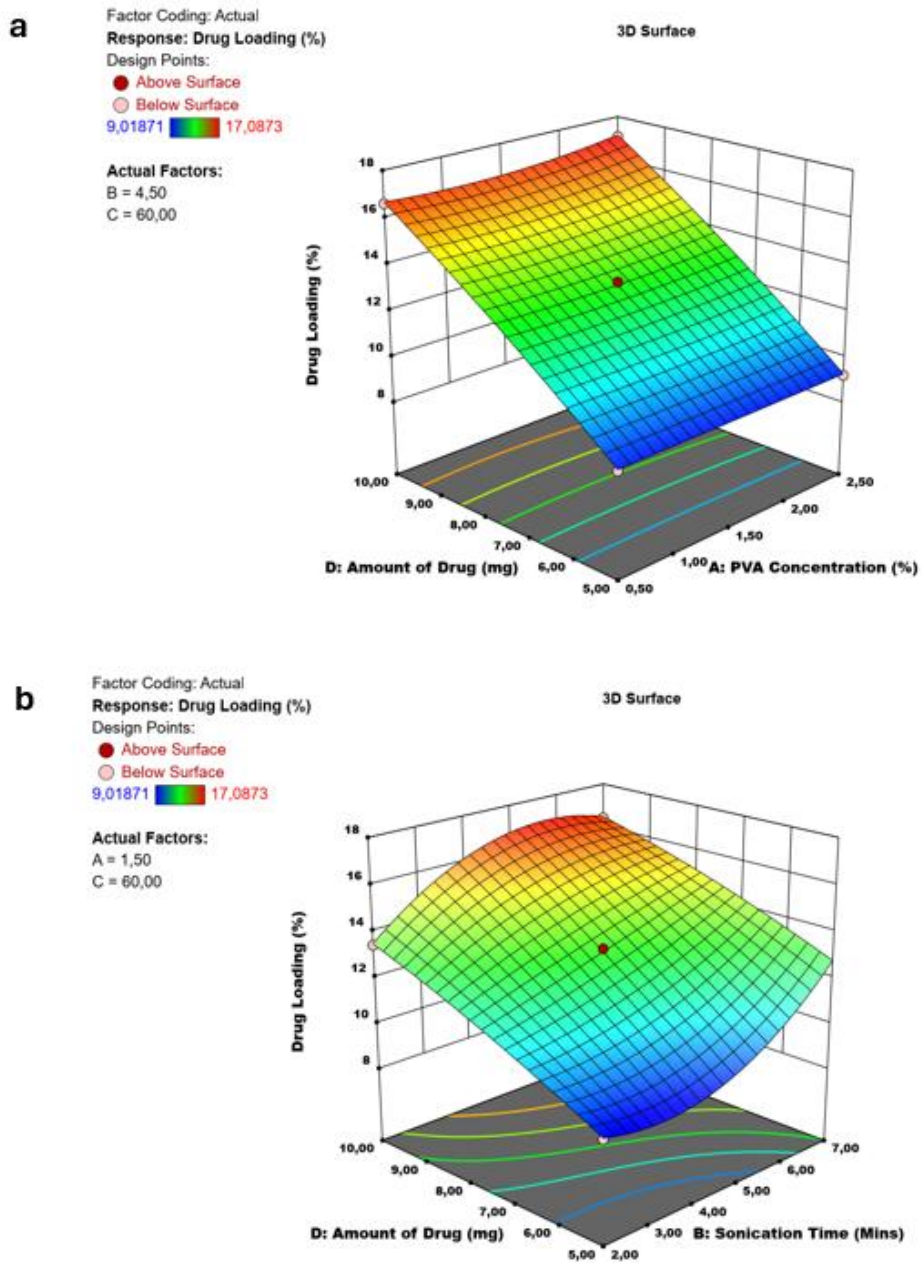


Figure 3.7: (a) 3D response surface plot showing the impact of X_1 and X_4 on DL(%), **(b)** 3D response surface plot depicting the impact of X_2 and X_4 on the DL(%) of the BQ-loaded PLGA nanoparticles.

3.3.1.4. Evaluation of model adequacy and ANOVA for entrapment efficiency (Y_4)

Table 3.8 summarizes the ANOVA data for the two-factor interaction (2FI) model for entrapment efficiency (EE) (Y4). The model F-value was 4.74, and the p-value was much lower than 0.05 (p=0.0029), which indicates that the model was significant. In this model, the **X_4, X_3X_4, X^2_1, X^2_3, and $X^2_1X_2$** were considered significant terms. The 2FI response surface equation for EE is represented by **Equation 3.7**.

Table 3.8: ANOVA analysis model for EE.

	Source	Sum of Squares	Df	Mean Square	F-value	p-value
Model		1688,60	9	187,62	4,74	0,0029
X_1		0,8401	1	0,8401	0,0212	0,8859
X_2		85,87	1	85,87	2,17	0,1591
X_3		88,52	1	88,52	2,24	0,1531
X_4		274,06	1	274,06	6,92	0,0175
X_1X_2		154,11	1	154,11	3,89	0,0650
X_3X_4		516,70	1	516,70	13,05	0,0021
X^2_1		216,05	1	216,05	5,46	0,0320
X^2_3		426,03	1	426,03	10,76	0,0044
$X^2_1X_2$		215,01	1	215,01	5,43	0,0323
Lack of fit		532.36	14	38.03	0.8116	0.6649

X_1: PVA conc, **X_2**: sonication time, **X_3**: amplitude, **X_4**: drug amount

$$Y_4=-53.81505-44.05657X_1-10.63150X_2+3.94080X_3+11.664X_4+13.60248X_1X_2-0.227309X_3X_4+11.04953X_1^2-0.019765X_3^2-3.70656X_1^2X_2 \quad \textbf{(3.7)}$$

Where,

Y_4 = EE (%)

X_1 = PVA Concentration

X_2 = Sonication time

X_3= Amplitude

X_4 = drug amount

The model was established to be adequate as depicted by the normal probability, studentized residuals, and Box-Cox plots as the points on the normal probability, as shown in **Figures 3.8a,b,** respectively. The plot of residuals fell on or close to the straight line, and the Box-Cox plot did not require transformations. The EE ranged from 30,97% to 83,49% with X_4 having the most significant effect as shown in the above equation, the effect is agonistic as an increase in BQ amount results in better entrapment efficiency to a certain point. However, as depicted by the one-factor plot **(Figure 3.9a)**, an increase in drug amount from 6-10mg results in a linear decline in EE. Furthermore, the decline in EE is observed in the interaction between X_1 and X_4 **(Figure 3.9b,c),** where a decline in EE occurs when the BQ amount is increased beyond 8mg, especially when combined with higher PVA concentrations. This phenomenon is suggested to be caused by the higher PVA concentration, which alters the interfacial tension and negatively affects the droplet formation in emulsions (Otte et al., 2020; Song et al., 2008). This leads to more BQ partitioning into the aqueous phase (Song et al., 2008).

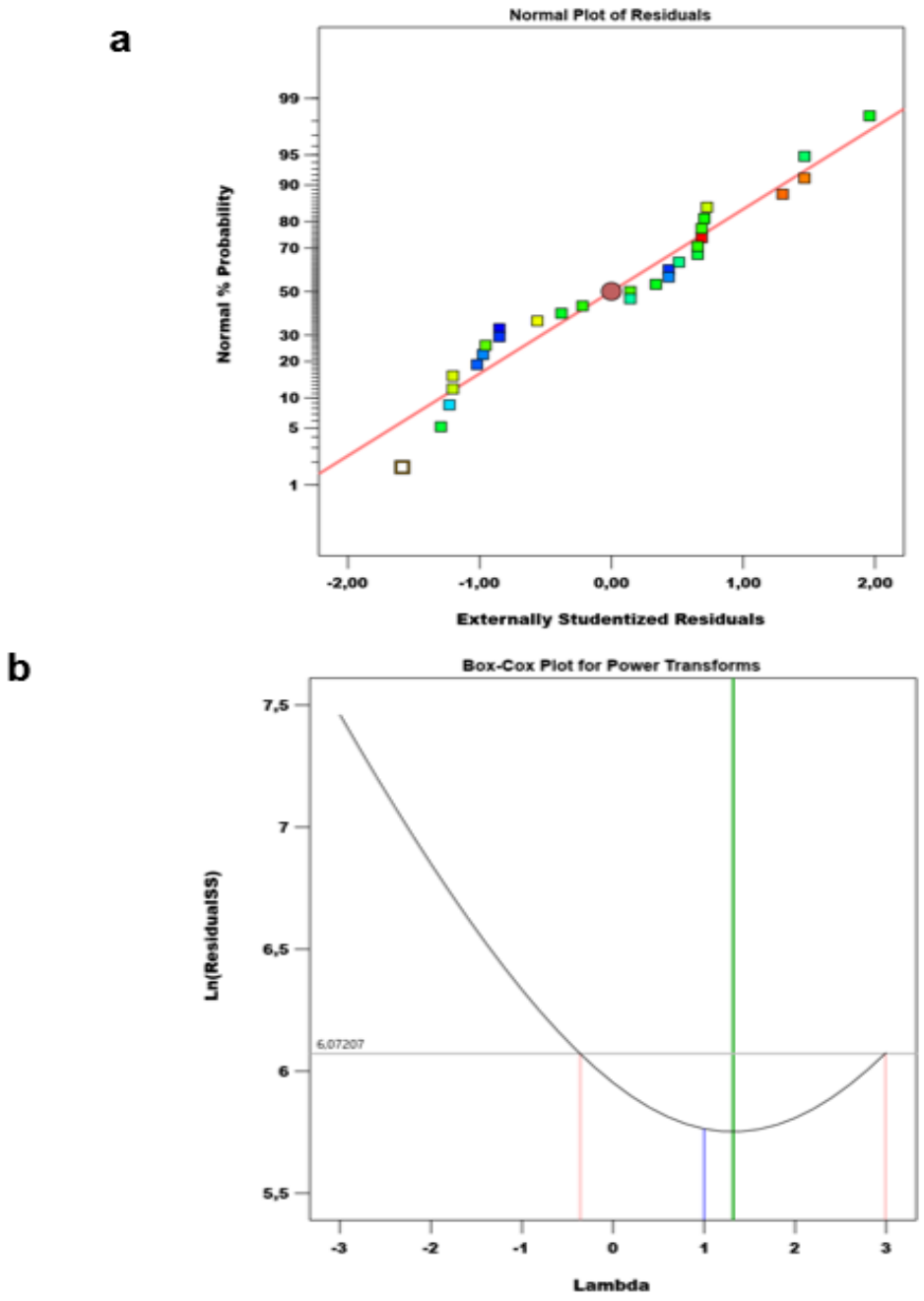


Figure 3.8: (a) Normal probability plot of residuals for EE, **(b)** Box-cox plot for power transformation for EE.

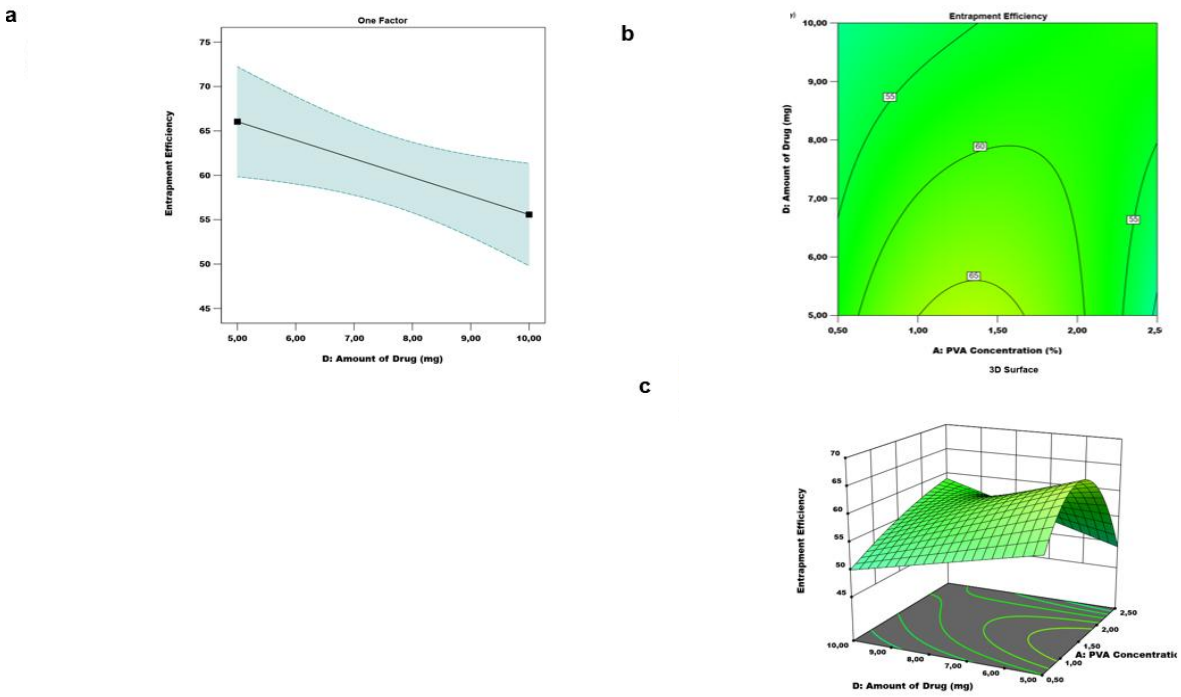


Figure 3.9: (a) One-factor plot depicting the impact of X_4 on EE, **(b)** 2D contour plot depicting the impact of X_1 and X_4 on EE, **(c)** 3D response surface plot depicting the impact of X_1 and X_4 on the EE of the BQ-loaded PLGA nanoparticles.

3.3.1.5. Formulation Optimization

The major objective of this part of the study was to design and develop stable BQ-loaded PLGA nanoparticles with appropriate particle size (Y_1), PDI (Y_2), DL(%) (Y_3), and EE (Y_4). The use of numerical optimization techniques is a highly effective approach to achieving a continuous optimization process (Campbell et al., 2019). Numerical optimization locates a point in space in which the desirability function is at a maximum for which the characteristics of the target can be modified by adjusting the relative importance of that target (Pasandideh and Niaki, 2006; Shishir and Chen, 2017; Yeom et al., 2017). Numerical optimization was undertaken using Design Expert® software to select an optimum formulation composition that would lead to the development of the desired microemulsion. The optimized input variable generated and the predicted desired target level for each output response are summarised in **Table 3.9**.

Table 3.9: Optimized formulation variables and predicted responses.

Formulation variable				**Predicted responses**				**Desirability**
X_1 %	X_2 Mins	X_3 %	X_4 Mg	Y1 d.nm	Y2	Y3 %	Y4 %	
2.12	7	78.4	5	200	0.038	10.18	70.5	0.924

X_1: PVA conc, **X_2**: sonication time, **X_3**: amplitude, **X_4**: drug amount; **Y_1:**particle size**, Y_2:** polydispersity index**, Y_3:** drug loading**, Y_4:** entrapment efficiency

The model's desirability was 0.942, the highest desirability value observed. Henceforth this composition was selected as the optimum formulation. A summary of the predicted response values and experimental responses with the corresponding percent prediction error is listed in **Table 3.10**.

Table 3.10: Results BQ-loaded PLGA nanoparticles developed using the optimum process variables.

Response	**Prediction value**	**Experimental**	**Prediction Error**
Y_1	200	183.8	8.8
Y_2	0.038	0.053	28.30
Y_3	10.18	12.5	18.56
Y_4	70.5	69.5	1.47

Y_1: particle size**, Y_2:** polydispersity index**, Y_3:** drug loading**, Y_4:** entrapment efficiency

The low values of the calculated percentage prediction error indicate the mathematical model's robustness. In addition, the efficacy of RSM's predictive ability is also demonstrated, suggesting its efficiency as a tool for process optimization (Veza et al., 2023).

3.3.2. Characterization of optimized BQ-loaded PLGA nanoparticles

3.3.2.1. Assessment of BDQ-loaded PLGA nanoparticles in terms of particle size, PDI, and morphology

BQ-loaded PLGA nanoparticles were prepared by a simple solvent evaporation method using PVA as a stabilizer as previously reported (Patil et al., 2024). The technique was selected over other methods due to its ability to be able to produce nanoparticles with relatively mono-dispersed size distribution, which is crucial for consistent drug delivery performance (Budhian et al., 2007; Günday Türeli et al., 2016; Kızılbey, 2019). In addition, the choice of the PLGA (75:25) polymer was selected based on the hydrophobicity of both the polymer and drug, which would result in higher drug loading (Budhian et al., 2007; Lee and Pokorski, 2018).

The average hydrodynamic particle size and PDI of pristine optimized PLGA nanoparticles were found to be 124±102.3 nm, and 0.412±2.03 respectively **(Appendix A**). Meanwhile, the optimized BQ-loaded PLGA nanoparticles had a hydrodynamic size of 183.8±54.54 nm and a PDI of 0.053± 0.02 **(Figure 3.10a)**. In addition, the zeta potential of the pristine optimized PLGA nanoparticles and optimized BQ-loaded PLGA nanoparticles was -11.6 mV **(Appendix A**) and -5.5mV **(Figure 3.10b)**. , respectively. The reason for the decrease in zeta potential is due to the surface interaction of free BQ and the free carboxylic groups on the surface of the PLGA, which then results in the masking of the negative groups of PLGA (Jamali et al., 2018; Rafiei and Haddadi, 2019). Furthermore, the use of PVA as a surfactant is suggested to affect the zeta potential of the PLGA nanoparticles as the residuals after washing partially cover the surface charge of the PLGA (Chumakova et al., 2008; Mura et al., 2011). However, the low PDI is indicative of monodispersed particles with lower possibilities of aggregation, while the hydrodynamic size is at an optimal range for enhanced permeability and retention (EPR) effects (Budhian et al., 2007; Cortés et al., 2021).

The optimized BQ-loaded PLGA nanoparticles had a well-defined spherical overall morphology **(Figure 3.10c,d)**. These findings show that the synthesized BQ-loaded PLGA nanoparticles are desirable for potential bone-targeted delivery, as their particle size, shape, PDI, and zeta potential play crucial roles in cellular uptake, circulation stability, and bioavailability.

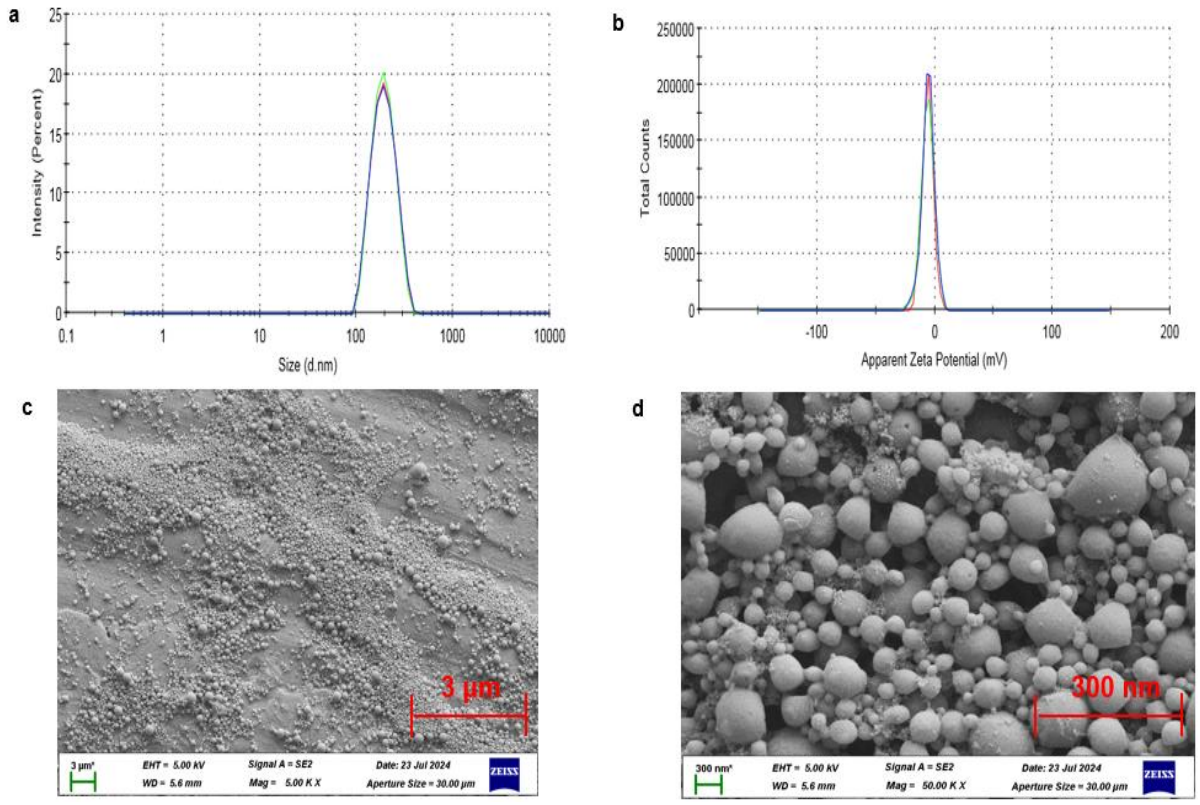


Figure 3.10: A visualization of the morphological attributes of the optimized BQ-loaded PLGA nanoparticles, showing (**a**) average hydrodynamic particle size of 183.8±54.54 nm (PDI = 0.05 ± 0.02), (**b**) zeta potential of -5.5± 5.44 mV, and (**c**) SEM image showing overall morphology at 3 µg/ml scale (5.00 KX magnification), and **(d)** a higher magnification SEM image at 300 nm scale (50.00 KX magnification), showing a spherical nanoparticle morphology.

3.3.2.2. Determination of structural integrity of the optimized BQ-loaded PLGA nanoparticles

The FTIR spectra of pure PVA, PLGA, BQ, and optimized BQ-loaded PLGA nanoparticles are presented in **Figure 3.11a-d**. The infrared spectrum of PVA **(Figure 3.11a)** showed a broad peak at 3300-3400 cm^{-1}, which corresponds to the presence

of OH stretching, and at 2900-2950 cm^{-1} C-H stretching bands are observed. Furthermore, at around 1090 and 1150 cm^{-1} a shoulder stretching of the C-O is evident (Jipa et al., 2012).The PLGA spectrum **(Figure 3.11b)** on the other hand revealed absorption peaks at 1750 cm^{-1}, 1080-1170 $cm^{-1,}$ and 2850-2950 cm^{-1} regions which correspond to C=O, C-O-C, and CH asymmetric and symmetric stretching vibrations, respectively (Pirooznia et al., 2012). Three bands were observed on the spectrum of pure BQ **(Figure 3.11c)** at around 3200 cm^{-1}, 1500 cm^{-1}, and 600-900 cm^{-1}, which were ascribed to the N–H or O–H stretching, possibly due to hydrogen bonding, aromatic C=C stretching vibrations and C–N and C–Cl stretching, respectively, confirming the presence of functional groups associated with BQ (Momin et al., 2019). The Lyophilized BQ-loaded PLGA nanoparticles **(Figure 3.11d)** exhibit the C=O stretching peak at around 1750 cm-1, confirming the presence of PLGA. In addition, the reduction in O-H and N-H peaks indicates successful drug entrapment within the polymer and the preservation of major peaks of BQ suggests stability of BQ in the nanoparticles. It is important to note that PVA peaks in **Figure 3.11d** have a reduced intensity and this is because PVA serves as a stabilizer during the emulsification process, therefore the low detected amount is typical due to PVA bounded to the nanoparticle surface (Higazy et al., 2021).

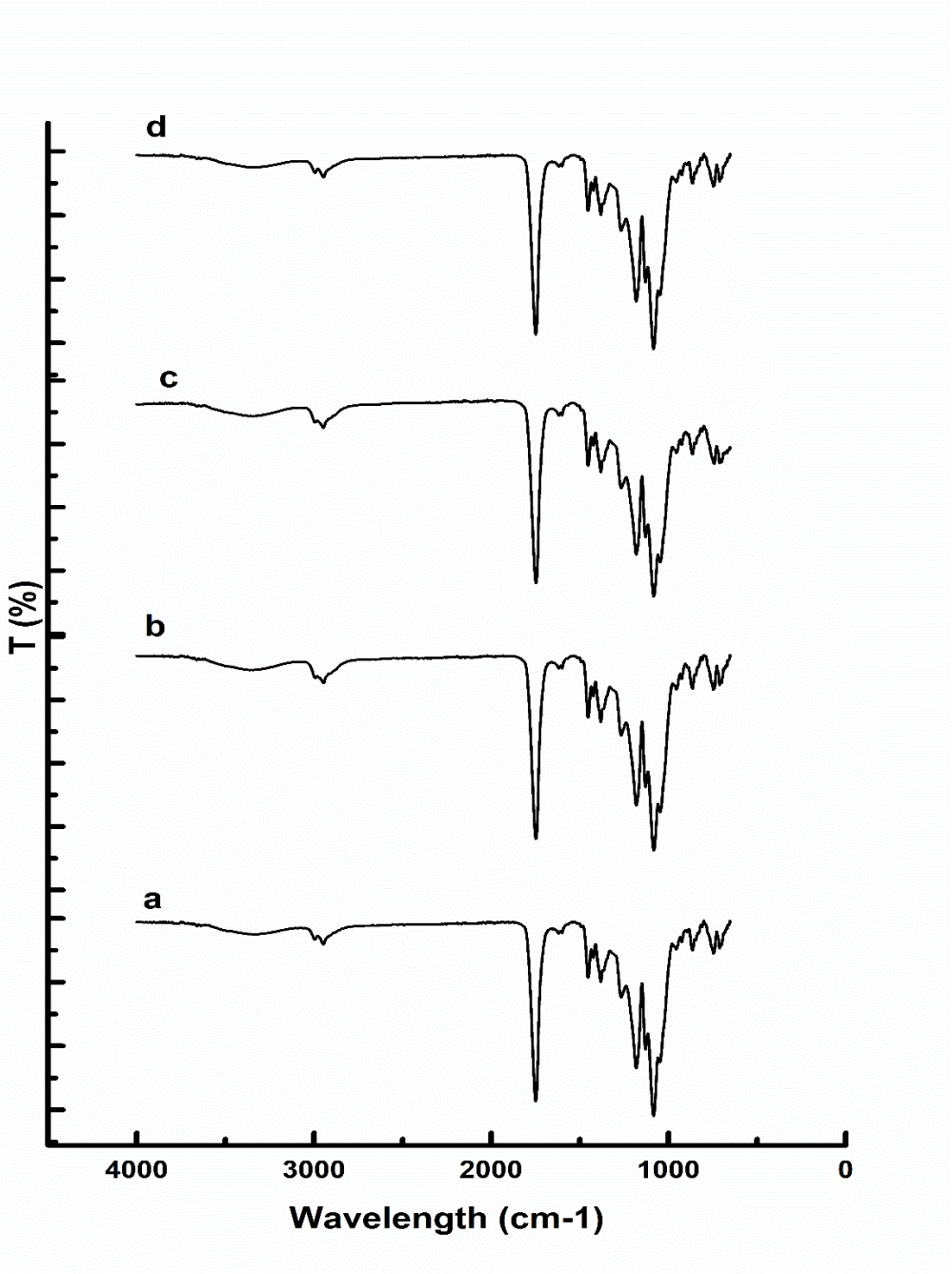


Figure 3.11: FTIR spectra of the **(a)** PVA, **(b)** PLGA, **(c)** BQ, and **(d)** optimized lyophilized BQ-loaded PLGA nanoparticles.

3.3.2.3. Assessment of the crystalline structural properties of optimized BQ-loaded PLGA nanoparticles

The crystallization of BQ in the optimized formulation was investigated by utilizing XRD. **Figure 3.12** shows the XRD results of PVA, PLGA, BQ, and optimized BQ-loaded PLGA nanoparticles. The pattern of plain PVA **(Figure 3.12a)** indicates a Broad

peak at approximately 2θ = 19.5° and a secondary diffuse peak around 40.5° that characterizes the semi-crystalline nature of the PVA (Kaur et al., 2024; Nerkar D. M et al., 2018; Sun et al., 2022). On the contrary, PLGA **(Figure 3.12b)** shows characteristics of an amorphous structure between 2θ = 15-30° and no sharp crystalline peaks. These results correspond to those reported by (Zhang et al., 2020). In the diffractogram of BQ **(Figure 3.12c)** powder, distinct sharp peaks are present at diffraction angles of 2θ = 7.2°, 14.4°, 15.8°, and 20.2° indicating its crystalline nature (Okezue et al., 2020). Furthermore, these characteristic peaks are not observed in the optimized BQ-loaded PLGA nanoparticles **(Figure 3.12d)**. This suggests that BQ is no longer retained in its crystalline state within the optimized BQ-loaded PLGA nanoparticles; instead, it adopts an amorphous structure. These findings align with the FTIR results, further supporting the absence of crystalline BQ within the nanoparticles. Additionally, this is consistent with previous studies on nanoparticles produced using the solvent-antisolvent precipitation technique, where drug molecules are generally distributed in an amorphous form within the polymer matrix (Kolahi et al., 2022; Li et al., 2024; Verma et al., 2021).

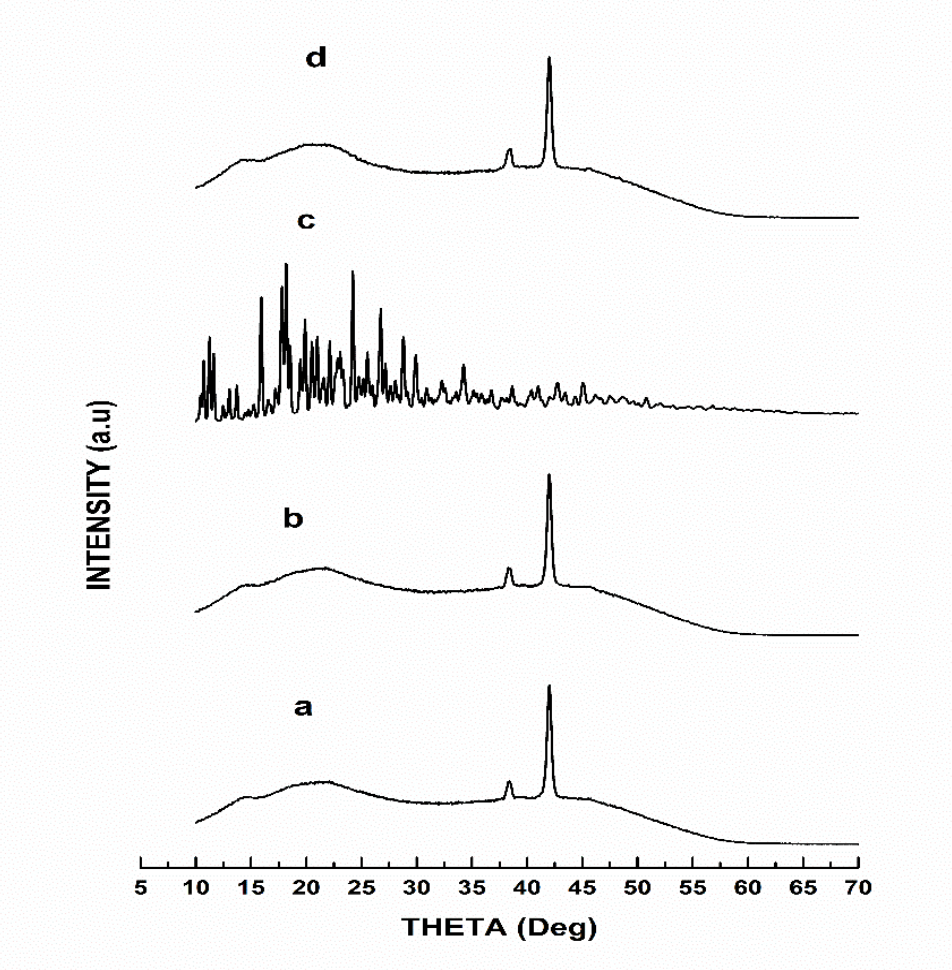


Figure 3.12: XRD diffraction pattern of **the (a)** PVA, **(b)** PLGA, **(c)** BQ, and **(d)** optimized lyophilized BQ-loaded PLGA nanoparticles.

3.3.2.4. Evaluation of thermal behaviour using differential scanning calorimetry (DSC) of optimized BQ-loaded PLGA nanoparticles

Pharmaceutically, DSC has been used to identify the potential instability of various APIs in different dosage forms (Bharate et al., 2010). The DSC thermograms of the PVA, PLGA, BQ, and optimized BQ-loaded PLGA nanoparticles are presented in **Figure 3.13a-d**. For PVA **(Figure 3.13a)**, an endothermic peak at 190-200°C represents PVA's melting point (Gupta et al., 2009; Nerkar D. M et al., 2018). This indicates that PVA is a semi-crystalline structure, where crystalline regions provide rigidity and stability (Sun et al., 2022). Furthermore, the high melting point ensures formulation stability during processing and storage (Chen et al., 2007). The glass transition temperature (Tg) for PLGA **(Figure 3.13b)** is observed around 45–50°C. In

contrast with PVA, PLGA usually does not have a distinct melting point because it is largely amorphous (Jia et al., 2021; Menon et al., 2012; Song et al., 2008). For BQ **(Figure 3.13c)**, the DSC thermogram shows a sharp endothermic peak around 180°C for pristine BQ. This suggests that the drug is largely crystalline and these results are in agreement with those observed with XRD data (Momin et al., 2019). The thermogram of the optimized BQ-loaded PLGA nanoparticles **(Figure 3.13d)** shows a reduction in BQ melting peak intensity which suggests successful molecular dispersion of the drug within the PLGA matrix and conversion of BQ from crystalline to amorphous. Furthermore, the shift in PLGA's Tg indicates drug-polymer molecular interactions, the formation of a stable drug-polymer matrix, and successful encapsulation of BQ which is corroborated by the FTIR and XRD results (Momin et al., 2019; Patil et al., 2024).

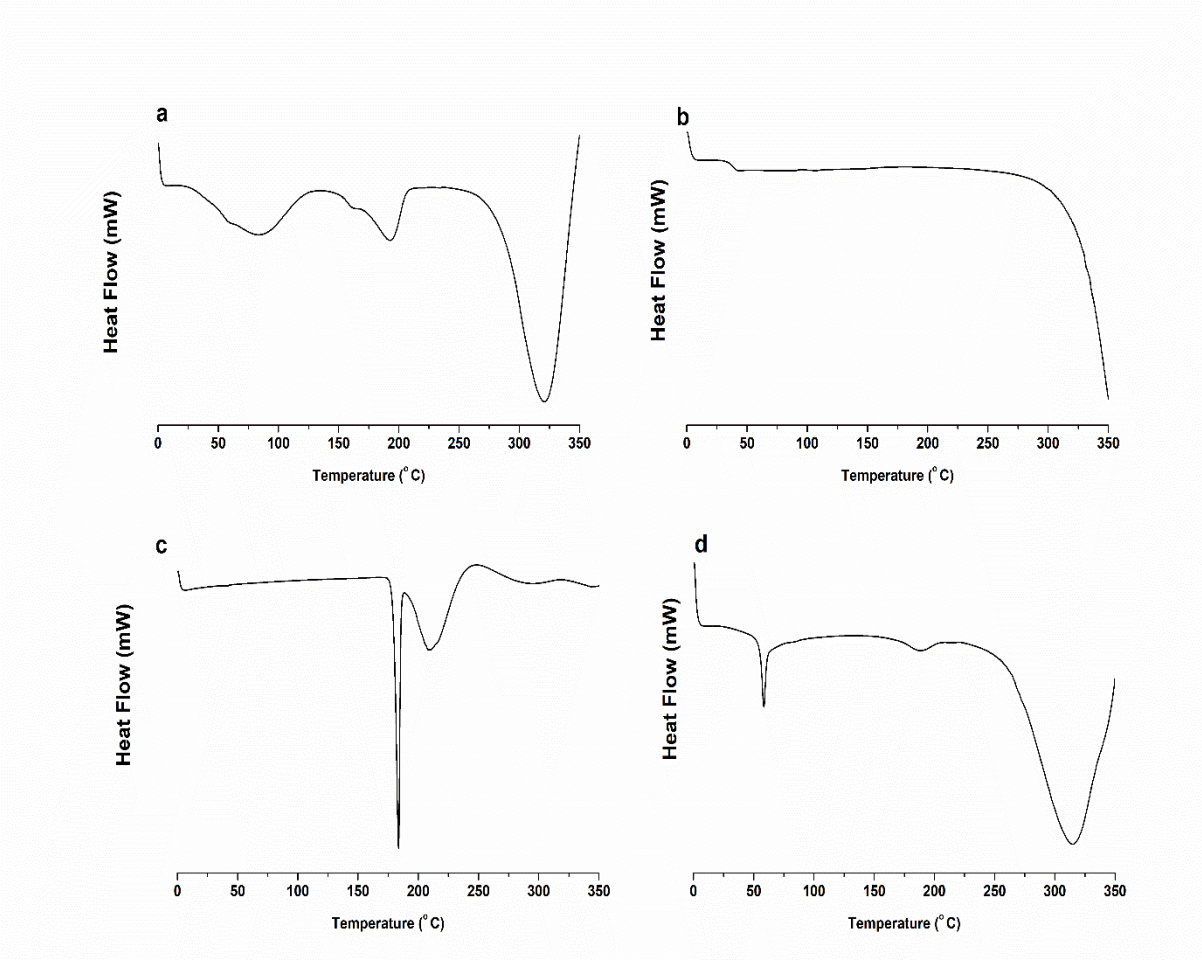


Figure 3.13: DSC thermogram patterns of the **(a)** PVA, **(b)** PLGA, **(c)** BQ, and **(d)** optimized lyophilized BQ-loaded PLGA nanoparticles.

3.3.2.5. Assessment of the thermal stability properties of optimized BQ-loaded PLGA nanoparticles release from the optimized PLGA nanoparticles

The thermograms in **Figure 3.14a-d** show the degradation of PVA, PLGA, BQ, and optimized PLGA nanoparticles. PVA **(Figure 3.14a)** shows a two-step degradation: initial moisture loss around 100°C, followed by main decomposition at 250-350°C (Nerkar D. M et al., 2018). The thermal degradation of PLGA **(Figure 3.14b)** begins at temperatures greater than 200 °C and reaches full degradation by around 400 °C, noticeably up to 900 °C, there is no additional major weight loss event observed, suggesting that the residuals formed after complete degradation remain stable over higher temperatures (Silva et al., 2015)**.** Moreover, pristine BQ **(Figure 3.14c)** displays a gradual weight loss around 180-200 °C. The TGA curve of the optimized formulation **(Figure 3.14d)** follows a similar degradation profile to PLGA indicating that the formulation's behaviour is dominated by the polymer matrix. However, the presence of BQ modifies the onset and progression slightly. The weight loss observed between 250 °C and 300 °C is indicative of the combined effect of both the drug and the polymer undergoing degradation. Similar trends were observed in the FTIR, DSC, and XRD data, further confirming the successful encapsulation of BQ within the polymer matrix and its influence on the formulation's physicochemical properties.

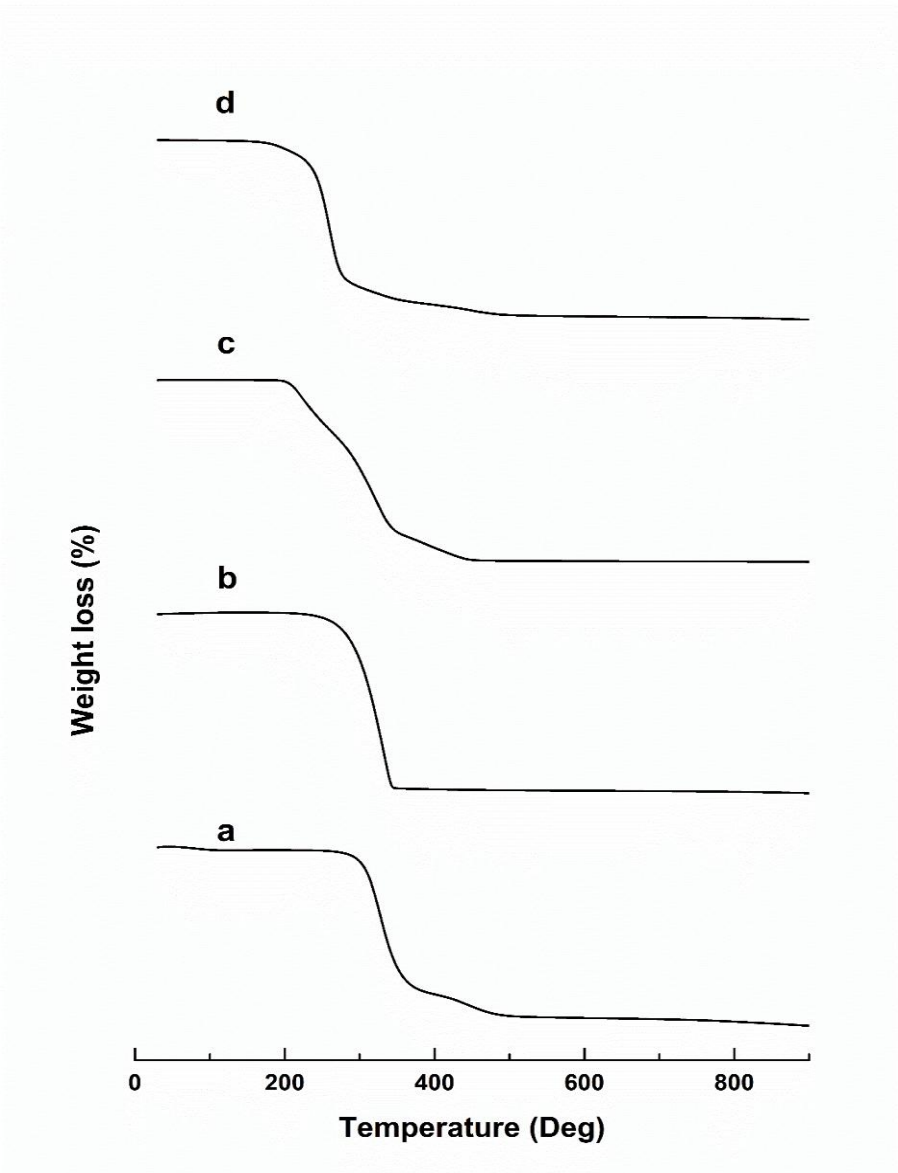


Figure 3.14: TGA thermogram patterns of the **(a)** PVA, **(b)** PLGA, **(c)** BQ, and **(d)** optimized lyophilized BQ-loaded PLGA nanoparticles.

3.3.2.6. Evaluation of BQ entrapment efficiency, drug loading, and *In-vitro* release from optimized BQ-loaded PLGA nanoparticles

DL and EE are two crucial concepts concerning drug delivery systems as a high percentage of both is associated with the effectiveness of the drug delivery system (Freitas et al., 2019). Although BQ is clinically indicated for MDR-TB in combination with other anti-TB drugs, it has not been indicated for bone TB. However (De Vito et al., 2022) conducted a study in an attempt to assess the effectiveness of BQ in patients with bone TB and BQ was found to be effective with no severe adverse effects (De

Vito et al., 2022). Despite its promises, the dosing of BQ has been met with a lot of controversy in practice as the current use of BQ has been accompanied by serious side effects and potential drug interactions, necessitating careful monitoring and consideration of resistance development (Bélard et al., 2015; Veziris et al., 2017). Therefore, to minimize those as mentioned above, loading the drug in a PLGA nanoparticle system would be more beneficial. Furthermore, targeting BQ to bone can lead to dose reduction (Pirooznia et al., 2012; Song et al., 2008). In the present study, BQ was successfully loaded into the optimized PLGA nanoparticles, achieving an EE (%) of 69.5% and DL (%) of 12.5%. A consistent challenge in formulation development is the encapsulation of hydrophobic drugs and achieving controlled drug release (Ezike et al., 2023). However, the high EE and DL for BQ were observed due to the interaction between PLGA and the drug, supporting its potential as an effective delivery system

The *in-vitro* drug release study was conducted to quantify the amount of BQ released from the optimized PLGA nanoparticles at pH 7.4 representing the physiology pH of bone. The BQ release over 48 hours is presented in **Figure 3.15**. and the release profile from the nanoparticles exhibited a biphasic pattern, consisting of an initial burst release followed by a sustained release phase. A maximum cumulative release of 67+2.68% was obtained over 48 hours. The sustained release was achieved by the gradual diffusion of BQ from the nanoparticle core through interconnected pores and channels within the polymeric matrix.

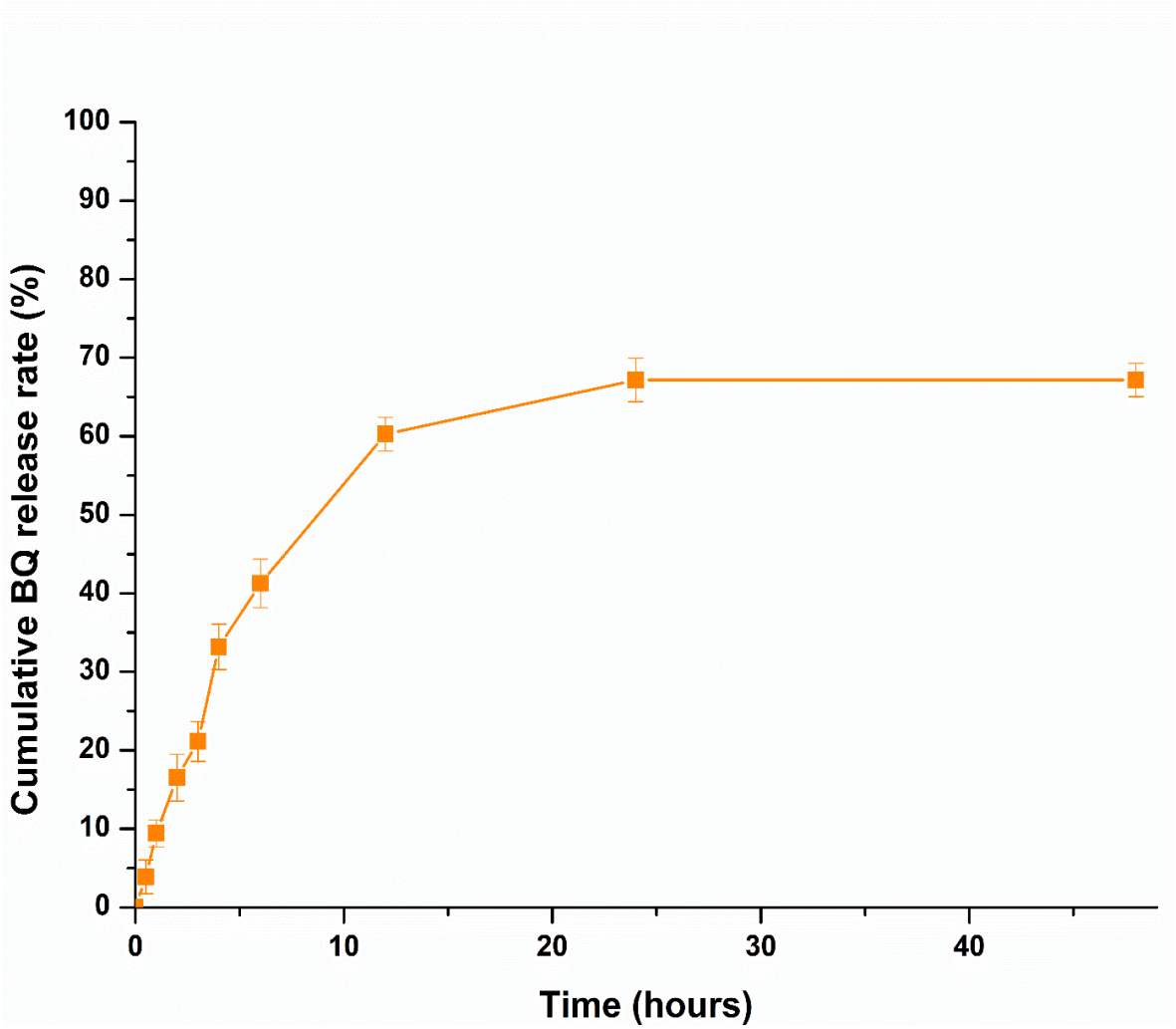


Figure 3.15: *In-vitro* BQ release profiles from the optimized PLGA nanoparticles at pH 7.4. Experiment data are presented as the mean ± SD, *n* = 3.

In drug delivery research, mathematical modelling has become increasingly common to promote predicting and identifying the kinetics and mechanism of API release from drug delivery systems (Khalbas et al., 2024). Zero-order, first-order, Higuchi and Korsmeyer-Peppas and Hixson-Crowell models are mathematical models that have been widely used to characterize *in-vitro* API release (Ofori-Kwakye et al., 2016; Ojsteršek et al., 2024). To elucidate the kinetics of BQ release, *In-vitro* release data were fitted to mathematical models. To determine the model that best fits the experimental data, R^2 values were generated from zero-order, first-order, Higuchi, Korsmeyer-Peppas, and Hixson-Crowell models. This was achieved by plotting the graphs of cumulative % BQ released versus time (zero-order model), the natural logarithm of cumulative % BQ remaining in the matrix versus time (first-order model), cumulative % BQ released versus square root of time (Higuchi model), the natural

logarithm of cumulative % BQ released versus the natural logarithm of time (Korsmeyer-Peppas model) and cube root of the initial concentration minus cube root of % BQ remaining versus time (Hixson-Crowell model). The R^2 was used as an indicator of the best model that defined the release of BQ from the optimized PLGA nanoparticles.

Table 3.11: Results of fitting in-vitro data for BQ release from optimized BQ-loaded PLGA nanoparticles to different mathematical models.

Formulation	R^2 for kinetic model				
	Zero-order	**First-order**	**Higuchi**	**Korsmeyer-Peppas**	**Hixson-Crowell**
Optimized BQ-loaded PLGA nanoparticles	0.6381	0.7146	0.8592	0.7105	0.6907

The highest R^2 value (0.8592) suggests that the Higuchi model best describes the release behaviour. The model elucidates that drug release is primarily controlled by diffusion through a polymeric matrix. This suggests that BQ gradually diffuses out of the polymer matrix.

3.3.2.7. Assessment of long-term stability of optimized BQ-loaded PLGA nanoparticles

The evaluation of long-term stability in formulation development is crucial, as this elucidates the physicochemical integrity, efficacy, and safety of the particular formulation over time (Evers et al., 2022). The guidelines on how to conduct such studies are described in the International Conference on Harmonisation (ICH) guidelines (Abraham, 2010). This study assessed long-term stability by evaluating particle size, PDI, EE(%), and DL(%) as depicted in **Figures 3.16a-b**. Statistically, no significant changes were observed in particle size, PDI, EE (%) and DL (%) when optimized lyophilized BQ-loaded PLGA nanoparticles were stored at 25 ± 2 °C/60 ± 5% relative humidity over the 3 months. The particle size and PDI **(Figure 3.16a** had slightly increased after 30 days, then both factors stabilized to a similar level of the freshly prepared optimized BQ-loaded nanoparticles after 60 and 90 days. This occurrence is suggested to be caused by the fact that the nanoparticles might have undergone some physical changes, such as aggregation or fusion. However, the fact

that the particle size and PDI recovered between days 60 and 90 suggests the nanoparticles were able to regain stability over time, possibly due to the disruption of some of the particles (Masarudin et al., 2015). Additionally, the low values of the PDI suggest that nanoparticles maintain a uniform size distribution and resist significant aggregation (Madani et al., 2018; Masarudin et al., 2015). This demonstrates the overall physical stability of the PLGA nanoparticle formulations during long-term storage which is crucial for bone-targeted delivery (Wu et al., 2024).

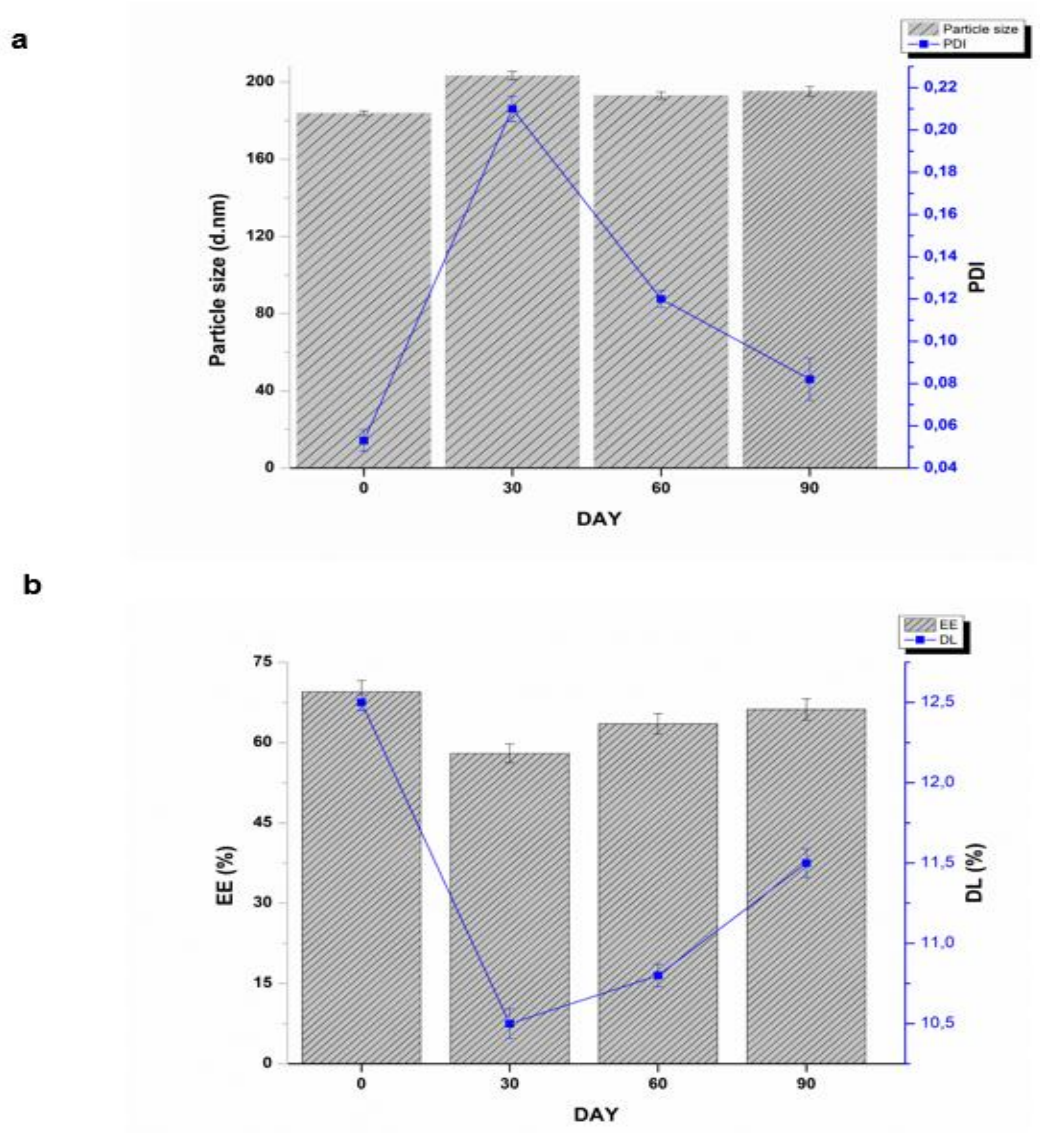


Figure 3.16: Stability data of optimized BQ-loaded PLGA nanoparticles evaluating **(a)** particle size and PDI, **(b)** EE (%) and DL (%) at 25 ± 2 °C and 60 ± 5% relative humidity.

The change in the EE (%) and DL (%) within the nanoparticulate systems for 90 days was examined as shown in **Figure 3.16b**. The EE (%) and DL (%) of the loaded BQ in the nanosystem dropped slightly from 69.5% to 58% and 12.5% to 10% after 30 days of incubation, respectively. Similar to the size and PDI, the EE (%) and DL (%) did stabilize between days 30 and 90. Moreover, the stabilization of EE (%) and DL (%) suggests that the optimized BQ-loaded PLGA nanoparticles can retain sufficient drug payload, preventing premature drug loss and enhancing localized drug concentration within bone tissues. This is especially beneficial for treating chronic bone infections such as bone TB or osteomyelitis, where prolonged exposure to the therapeutic agent is essential for bacterial eradication and bone regeneration (Haider et al., 2020).

3.3.2.8. Evaluation of cytotoxicity of the optimized BQ-loaded PLGA nanoparticles on MG-63 cell line

The cell growth rate was evaluated by exposing cells to different concentrations of free BQ and optimized BQ-loaded PLGA nanoparticles (ranging from 5 to 60 µg/ml) over 72 hours, using the MTT assay. The pristine cells were used as a negative control; thus, the cell viability was set at 100% to compare against the experimental samples **(Figure 3.17).** The results showed dose-dependent cytotoxicity for both free BQ and BQ-loaded PLGA nanoparticles, with increasing concentrations leading to reduced cell viability. For the BQ-loaded PLGA nanoparticles, cell viability at the lowest concentration of 5 µg/mL was approximately 80%, dropping to around 32% at the highest concentration of 60 µg/mL. In contrast, free BQ induced a steeper decline in cell viability, decreasing from about 65% at 5 µg/mL to roughly 25% at 60 µg/mL. This observation aligns with previous findings indicating toxicity across various cell lines (Jahan et al., 2023; Najib Ullah et al., 2023). The slower rate of cell death seen with the encapsulated formulation suggests that PLGA encapsulation provides a controlled release profile, mitigating the immediate cytotoxic effects of free BQ while maintaining therapeutic efficacy. Collectively, these results indicate that BQ-loaded PLGA nanoparticles offer a promising strategy for bone-targeted therapy, balancing efficacy and safety.

To further support the above, BQ-loaded PLGA nanoparticles were assessed for their potential to reduce cell viability of MG-63 cells **(Table 3.12)**. A lower IC50 value

indicates higher drug potency, while a higher IC50 suggests lower potency (Garcia-Molina et al., 2022). In our study, the free drug has a lower IC50, indicating that it is more toxic to MG-63 cells, whereas the loaded nanoparticles have a higher IC50, suggesting that the sustained release of the drug as shown in **Figure 3.15**, reduces immediate cytotoxicity. These findings suggest that PLGA nanoparticles enhance drug delivery, reduce side effects, and improve therapeutic outcomes for bone infection treatments.

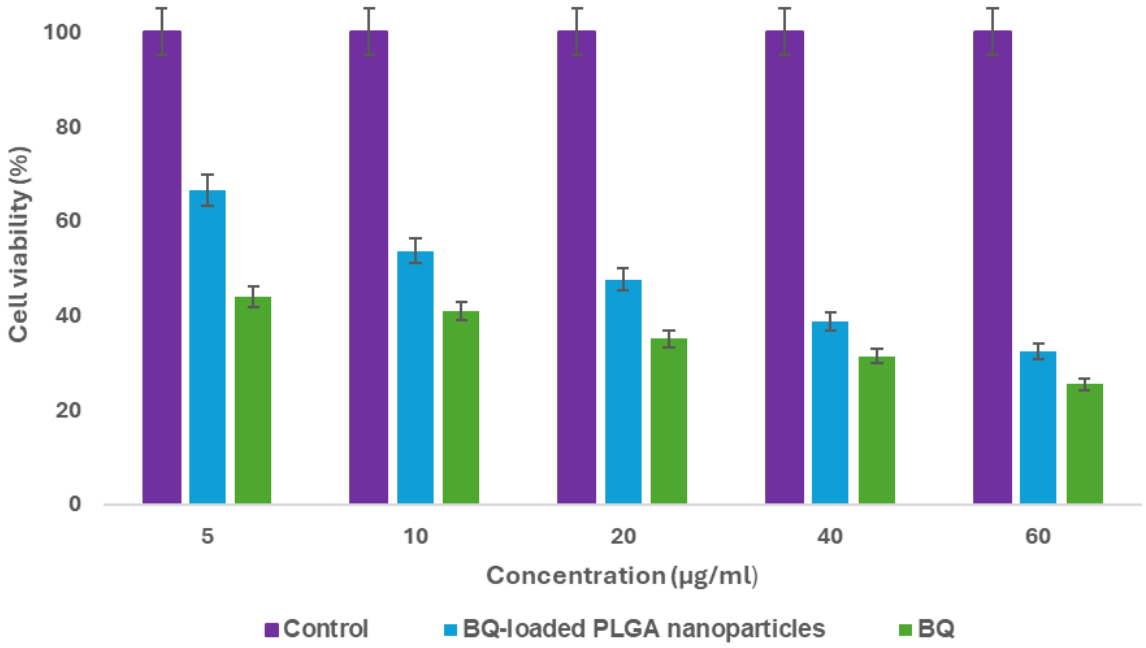


Figure 3.17: Cell viability of MG-63 cell line treated with BQ-loaded PLGA nanoparticles and free BQ incubated at 37°C for 72 hours. Data presented as mean ± SD, *n* = 4 ($p<0.0001$).

Table 3.12: IC50 values for the BQ-loaded PLGA nanoparticles and free BQ incubated. Data are presented as mean ± SD (n=4).

	Free-BQ	BQ-loaded nanoparticles	PLGA
IC50 (µg/ml)	1.3406 ± 2.56	16.2902 ± 2.6	

3.4. Concluding Remarks

In this chapter, BQ-loaded PLGA nanoparticles were successfully fabricated using the single emulsion (O/W) method, aiming for potential application in bone-TB therapy. The box-Behnken design was employed in this study to systematically optimize the formulation and this approach allowed for the effective evaluation of critical factors influencing nanoparticle size, polydispersity index, encapsulation efficiency, and drug loading while minimizing the number of experimental runs. Furthermore, model adequacy was rigorously validated using statistical parameters, confirming the developed models' reliability. This optimized approach enhances the reproducibility and potential applicability of the nanoparticle system for bone-TB therapy.

The statistical results revealed that an increase in both PVA and sonication time decreased particle size, while the effects of amplitude and drug amount were negligible. Furthermore, the effect of the PVA concentration on PDI was observed as a negative correlation. The EE (%) and DL (%) were both statistically influenced by the drug amount and the relationship between the polymer and the drug. This synergistic effect suggests that the polymer matrix provided a favourable environment for drug entrapment, potentially due to improved drug-polymer affinity, reduced drug diffusion out of the emulsion system, or optimized polymer precipitation dynamics during nanoparticle formation. The statistical analysis further confirmed that this interaction had a significant positive effect, contributing to higher EE and DL values in the optimized formulation.

The optimized formulation was achieved by utilizing a median concentration of PVA and a moderate drug amount while maintaining high sonication time and amplitude. This combination resulted in a particle size of 200 nm, a polydispersity index (PDI) of 0.038, a drug loading (DL) of 10.18%, and an encapsulation efficiency (EE) of 70.5%, demonstrating the effectiveness of the optimized formulation in achieving desirable nanoparticle characteristics. Furthermore, the nanosystem exhibited sustained drug release, with 67% of the drug released over 48 hours, indicating its potential for prolonged therapeutic action. Stability studies demonstrated that the system remained stable over three months, maintaining its physicochemical properties. Additionally, cytotoxicity studies confirmed the biocompatibility of the nanoparticles, suggesting that the formulation is safe for further biomedical applications.

Expanding on these findings, **Chapter 4** will focus on the development of a novel drug delivery system, a 3D-printed scaffold incorporating the BQ-loaded PLGA nanoparticles. This scaffold-based approach aims to provide a localized and sustained drug release platform, enhancing bone regeneration while effectively delivering anti-TB therapy to the affected site. The integration of nanoparticles into the scaffold is expected to improve drug retention, prolong release kinetics, and offer a multifunctional system for targeted bone-TB treatment.

3.5. References

Abdelghany, S., Parumasivam, T., Pang, A., Roediger, B., Tang, P., Jahn, K., Britton, W.J., Chan, H.-K., 2019. Alginate modified-PLGA nanoparticles entrapping amikacin and moxifloxacin as a novel host-directed therapy for multidrug-resistant tuberculosis. J. Drug Deliv. Sci. Technol. 52, 642–651. https://doi.org/10.1016/j.jddst.2019.05.025

Abraham, J., 2010. International conference on harmonisation of technical requirements for registration of pharmaceuticals for human use, in: Tietje, C., Brouder, A. (Eds.), handbook of transnational economic governance regimes. Brill | Nijhoff, pp. 1041–1053. https://doi.org/10.1163/ej.9789004163300.i-1081.897

Ayodele, S., Eyk, A.D. van, Kumar, P., E. Choonara, Y., 2024. A sensitive, rapid and cost-effective RP-HPLC-UV method for detection and quantification of bedaquiline in physiological fluid (pH 7.4). Anal. Methods 16, 7169–7177. https://doi.org/10.1039/D4AY01143K

Barberis, I., Bragazzi, N.L., Galluzzo, L., Martini, M., 2017. The history of tuberculosis: from the first historical records to the isolation of Koch's bacillus. J. Prev. Med. Hyg. 58, E9–E12.

Begines, B., Ortiz, T., Pérez-Aranda, M., Martínez, G., Merinero, M., Argüelles-Arias, F., Alcudia, A., 2020. Polymeric nanoparticles for drug delivery: recent developments and future prospects. Nanomaterials 10, 1403. https://doi.org/10.3390/nano10071403

Bélard, S., Heuvelings, C.C., Janssen, S., Grobusch, M.P., 2015. Bedaquiline for the treatment of drug-resistant tuberculosis. Expert Rev. Anti Infect. Ther. 13, 535–553. https://doi.org/10.1586/14787210.2015.1021785

Bhandari, M., Soria-Carrera, H., Wohlmann, J., Knudsen Dal, N.-J., Fuente, J.M. de la, Martín-Rapún, R., Griffiths, G., Fenaroli, F., 2023. Subcellular localization and therapeutic efficacy of polymeric micellar nanoparticles encapsulating bedaquiline for tuberculosis treatment in zebrafish. Biomater. Sci. 11, 2103–2114. https://doi.org/10.1039/D2BM01835G

Bharate, S.S., Bharate, S.B., Bajaj, A.N., 2010. Interactions and incompatibilities of pharmaceutical excipients with active pharmaceutical ingredients: a comprehensive review.

Budhian, A., Siegel, S.J., Winey, K.I., 2007. Haloperidol-loaded PLGA nanoparticles: Systematic study of particle size and drug content. Int. J. Pharm. 336, 367–375. https://doi.org/10.1016/j.ijpharm.2006.11.061

Campbell, S.D., Sell, D., Jenkins, R.P., Whiting, E.B., Fan, J.A., Werner, D.H., 2019. Review of numerical optimization techniques for meta-device design [Invited]. Opt. Mater. Express 9, 1842–1863. https://doi.org/10.1364/OME.9.001842

Chen, N., Li, L., Wang, Q., 2007. New technology for thermal processing of poly(vinyl alcohol). Plast. Rubber Compos. 36, 283–290. https://doi.org/10.1179/174328907X237575

Choudhary, S., Kusum Devi, V., 2015. Potential of nanotechnology as a delivery platform against tuberculosis: Current research review. J. Controlled Release 202, 65–75. https://doi.org/10.1016/j.jconrel.2015.01.035

Chumakova, O.V., Liopo, A.V., Andreev, V.G., Cicenaite, I., Evers, B.M., Chakrabarty, S., Pappas, T.C., Esenaliev, R.O., 2008. Composition of PLGA and PEI/DNA nanoparticles improves ultrasound-mediated gene delivery in solid tumors in vivo. Cancer Lett. 261, 215–225. https://doi.org/10.1016/j.canlet.2007.11.023

Cioboata, R., Biciusca, V., Olteanu, M., Vasile, C.M., 2023. COVID-19 and tuberculosis: unveiling the dual threat and shared solutions perspective. J. Clin. Med. 12, 4784. https://doi.org/10.3390/jcm12144784

Cortés, H., Hernández-Parra, H., Bernal-Chávez, S.A., Prado-Audelo, M.L.D., Caballero-Florán, I.H., Borbolla-Jiménez, F.V., González-Torres, M., Magaña, J.J., Leyva-Gómez, G., 2021. Non-ionic surfactants for stabilization of polymeric nanoparticles for biomedical uses. Materials 14, 3197. https://doi.org/10.3390/ma14123197

Daniel, T.M., 2006. The history of tuberculosis. Respir. Med. 100, 1862–1870. https://doi.org/10.1016/j.rmed.2006.08.006

Dartois, V.A., Rubin, E.J., 2022. Anti-tuberculosis treatment strategies and drug development: challenges and priorities. Nat. Rev. Microbiol. 20, 685–701. https://doi.org/10.1038/s41579-022-00731-y

De Matteis, L., Jary, D., Lucía, A., García-Embid, S., Serrano-Sevilla, I., Pérez, D., Ainsa, J.A., Navarro, F.P., M. de la Fuente, J., 2018. New active formulations against M. tuberculosis: Bedaquiline encapsulation in lipid nanoparticles and chitosan nanocapsules. Chem. Eng. J., Smart nanomaterials and nanostructures for diagnostic and therapy 340, 181–191. https://doi.org/10.1016/j.cej.2017.12.110

De Vito, A., Fiore, V., Urru, V., Bozzi, E., Geremia, N., Princic, E., Canu, D., Molicotti, P., Are, R., Babudieri, S., Madeddu, G., 2022. Use of bedaquiline in spinal osteomyelitis and soft tissue abscess caused by multidrug-resistant Mycobacterium tuberculosis : A case report. Braz. J. Infect. Dis. 26, 102701. https://doi.org/10.1016/j.bjid.2022.102701

Evers, A., Clénet, D., Pfeiffer-Marek, S., 2022. Long-term stability prediction for the development assessment of biopharmaceutics using advanced kinetic modeling. Pharmaceutics 14, 375. https://doi.org/10.3390/pharmaceutics14020375

Ezike, T.C., Okpala, U.S., Onoja, U.L., Nwike, C.P., Ezeako, E.C., Okpara, O.J., Okoroafor, C.C., Eze, S.C., Kalu, O.L., Odoh, E.C., Nwadike, U.G., Ogbodo,

J.O., Umeh, B.U., Ossai, E.C., Nwanguma, B.C., 2023. Advances in drug delivery systems, challenges and future directions. Heliyon 9, e17488. https://doi.org/10.1016/j.heliyon.2023.e17488

Freitas, E.D. de, Lima, B.M., Rosa, P.C.P., da Silva, M.G.C., Vieira, M.G.A., 2019. Evaluation of proanthocyanidin-crosslinked sericin/alginate blend for ketoprofen extended release. Adv. Powder Technol. 30, 1531–1543. https://doi.org/10.1016/j.apt.2019.04.031

Garcia-Molina, P., Garcia-Molina, F., Teruel-Puche, J.A., Rodriguez-Lopez, J.N., Garcia-Canovas, F., Muñoz-Muñoz, J.L., 2022. The Relationship between the IC50 Values and the Apparent Inhibition Constant in the Study of Inhibitors of Tyrosinase Diphenolase Activity Helps Confirm the Mechanism of Inhibition. Molecules 27, 3141. https://doi.org/10.3390/molecules27103141

Günday Türeli, N., Türeli, A.E., Schneider, M., 2016. Optimization of ciprofloxacin complex loaded PLGA nanoparticles for pulmonary treatment of cystic fibrosis infections: Design of experiments approach. Int. J. Pharm. 515, 343–351. https://doi.org/10.1016/j.ijpharm.2016.10.025

Gupta, S., Pramanik, A.K., Kailath, A., Mishra, T., Guha, A., Nayar, S., Sinha, A., 2009. Composition dependent structural modulations in transparent poly(vinyl alcohol) hydrogels. Colloids Surf. B Biointerfaces 74, 186–190. https://doi.org/10.1016/j.colsurfb.2009.07.015

Haider, M., Elsherbeny, A., Jagal, J., Hubatová-Vacková, A., Saad Ahmed, I., 2020. Optimization and Evaluation of Poly(lactide-co-glycolide) Nanoparticles for enhanced cellular uptake and efficacy of paclitaxel in the treatment of head and neck cancer. Pharmaceutics 12, 828. https://doi.org/10.3390/pharmaceutics12090828

Hegazy, W.A.H., Mamari, R.A., Almazroui, K., Habsi, A.A., Kamona, A., AlHarthi, H., Lawati, A.I.A., AlHusaini, A.H., 2021. Retrospective study of bone-TB in Oman: 2002–2019. J. Epidemiol. Glob. Health 11, 238–245. https://doi.org/10.2991/jegh.k.210420.002

Higazy, I.M., Mahmoud, A.A., Ghorab, M.M., Ammar, H.O., 2021. Development and evaluation of polyvinyl alcohol stabilized polylactide-co-caprolactone-based nanoparticles for brain delivery. J. Drug Deliv. Sci. Technol. 61, 102274. https://doi.org/10.1016/j.jddst.2020.102274

Hua, L., Qian, H., Lei, T., zhang, yu, Lei, P., Hu, Y., 2022. 3D-Printed porous tantalum coated with antitubercular drugs achieving antibacterial properties and good biocompatibility. Macromol.biosci 22. https://doi.org/10.1002/mabi.202100338

Jahan, R.N., Khan, Z., Akhtar, Md.S., Ansari, M.D., Solanki, P., Ahmad, F.J., Aqil, M., Sultana, Y., 2023. Development of bedaquiline-loaded snedds using quality by design (qbd) approach to improve biopharmaceutical attributes for the management of multidrug-resistant Tuberculosis (MDR-TB). Antibiotics 12, 1510. https://doi.org/10.3390/antibiotics12101510

Jamali, Z., Khoobi, M., Hejazi, S.M., Eivazi, N., Abdolahpour, S., Imanparast, F., Moradi-Sardareh, H., Paknejad, M., 2018. Evaluation of targeted curcumin (CUR) loaded PLGA nanoparticles for in vitro photodynamic therapy on human glioblastoma cell line. Photodiagnosis Photodyn. Ther. 23, 190–201. https://doi.org/10.1016/j.pdpdt.2018.06.026

Jia, Z., Ma, C., Zhang, H., 2021. PLGA coatings and PLGA drug-loading coatings for cardiac stent samples: degradation characteristics and blood compatibility. Coatings 11, 1427. https://doi.org/10.3390/coatings11111427

Jipa, I., Stoica, A., Stroescu, M., Dobre, L.-M., Dobre, T., Jinga, S., Tardei, C., 2012. Potassium sorbate release from poly(vinyl alcohol)-bacterial cellulose films. Chem. Pap. 66. https://doi.org/10.2478/s11696-011-0068-4

Kaur, H., Singh, S., Rode, S., Chaudhary, P.K., Khan, N.A., Ramamurthy, P.C., Gupta, D.N., Kumar, R., Das, J., Sharma, A.K., 2024. Fabrication and characterization of polyvinyl alcohol-chitosan composite nanofibers for carboxylesterase immobilization to enhance the stability of the enzyme. Sci. Rep. 14, 19615. https://doi.org/10.1038/s41598-024-67913-x

Khalbas, A.H., Albayati, T.M., Ali, N.S., Salih, I.K., 2024. Drug loading methods and kinetic release models using of mesoporous silica nanoparticles as a drug delivery system: A review. South Afr. J. Chem. Eng. 50, 261–280. https://doi.org/10.1016/j.sajce.2024.08.013

Kızılbey, K., 2019. Optimization of rutin-loaded PLGA nanoparticles synthesized by single-emulsion solvent evaporation method. ACS Omega 4, 555–562. https://doi.org/10.1021/acsomega.8b02767

Kolahi, P., Shekarchizadeh, H., Nasirpour, A., 2022. Effect of combination of ultrasonic treatment and anti-solvent methods as a high-efficiency method of nanoparticle production on the tragacanth gum properties. J. Food Sci. Technol. 59, 1131–1139. https://doi.org/10.1007/s13197-021-05117-1

Kumar, M., Virmani, T., Kumar, G., Deshmukh, R., Sharma, A., Duarte, S., Brandão, P., Fonte, P., 2023. Nanocarriers in tuberculosis treatment: challenges and delivery strategies. Pharmaceuticals 16, 1360. https://doi.org/10.3390/ph16101360

Lee, P.W., Pokorski, J.K., 2018. PLGA devices: production and applications for sustained protein delivery. Wiley Interdiscip. Rev. Nanomed. Nanobiotechnol. 10, e1516. https://doi.org/10.1002/wnan.1516

Li, Z., Gong, Z., Zhang, B., Nawaz, A., 2024. Investigation of the influence of anti-solvent precipitation parameters on the physical stability of amorphous solids. Molecules 29, 1275. https://doi.org/10.3390/molecules29061275

Liang, Q., Zhang, P., Zhang, L., Luan, H., Li, X., Xiang, H., Jing, S., Song, X., 2023. Development of tetracycline-modified nanoparticles for bone-targeted delivery of anti-tubercular drug. Front. Bioeng. Biotechnol. 11. https://doi.org/10.3389/fbioe.2023.1207520

Luo, Y., Chen, Hongwei, Chen, Hua, Xiu, P., Zeng, J., Song, Y., Li, T., 2024. Recent advances in nanotechnology-based strategies for bone tuberculosis management. Pharmaceuticals 17, 170. https://doi.org/10.3390/ph17020170

Madani, F., Esnaashari, S.S., Mujokoro, B., Dorkoosh, F., Khosravani, M., Adabi, M., 2018. Investigation of effective parameters on size of paclitaxel loaded plga nanoparticles. Adv. Pharm. Bull. 8, 77–84. https://doi.org/10.15171/apb.2018.010

Makadia, H.K., Siegel, S.J., 2011. Poly Lactic-co-Glycolic Acid (PLGA) as biodegradable controlled drug delivery carrier. Polymers 3, 1377–1397. https://doi.org/10.3390/polym3031377

Malik, S., Muhammad, K., Waheed, Y., 2023. Emerging applications of nanotechnology in healthcare and medicine. Molecules 28, 6624. https://doi.org/10.3390/molecules28186624

Masarudin, M.J., Cutts, S.M., Evison, B.J., Phillips, D.R., Pigram, P.J., 2015. Factors determining the stability, size distribution, and cellular accumulation of small, monodisperse chitosan nanoparticles as candidate vectors for anticancer drug delivery: application to the passive encapsulation of [14C]-doxorubicin. Nanotechnol. Sci. Appl. 8, 67–80. https://doi.org/10.2147/NSA.S91785

Menon, J.U., Kona, S., Wadajkar, A.S., Desai, F., Vadla, A., Nguyen, K.T., 2012. Effects of surfactants on the properties of PLGA nanoparticles. J. Biomed. Mater. Res. A 100A, 1998–2005. https://doi.org/10.1002/jbm.a.34040

Momin, M.A.M., Rangnekar, B., Sinha, S., Cheung, C.-Y., Cook, G.M., Das, S.C., 2019. Inhalable dry powder of bedaquiline for pulmonary tuberculosis: in vitro physicochemical characterization, antimicrobial activity and safety studies. Pharmaceutics 11, 502. https://doi.org/10.3390/pharmaceutics11100502

Mphaphuli, M.T., Sithole, M.N., Kumar, P., Kondiah, P.P.D., Mabrouk, M., Choonara, Y.E., 2023. Multi-purpose prototypes for extrapulmonary Mycobacterium tuberculosis targeting: A regenerative medicine perspective. J. Drug Deliv. Sci. Technol. 89, 105039. https://doi.org/10.1016/j.jddst.2023.105039

Mura, S., Hillaireau, H., Nicolas, J., Le Droumaguet, B., Gueutin, C., Zanna, S., Tsapis, N., Fattal, E., 2011. Influence of surface charge on the potential toxicity of PLGA nanoparticles towards Calu-3 cells. Int. J. Nanomedicine 6, 2591–2605. https://doi.org/10.2147/IJN.S24552

Najib Ullah, S.N.M., Afzal, O., Altamimi, A.S.A., Alossaimi, M.A., Almalki, W.H., Alzahrani, A., Barkat, M.A., Almeleebia, T.M., Alshareef, H., Shorog, E.M., Khan, G., Singh, T., Singh, J.K., 2023. Bedaquiline-loaded solid lipid nanoparticles drug delivery in the management of non-small-cell lung cancer (NSCLC). Pharmaceuticals 16, 1309. https://doi.org/10.3390/ph16091309

Nerkar D. M, Jadhav V. P, Chakraborty C. T, 2018. Nanoparticle-embedded polymer: preparation and characterization of PVA-PPY-AU nanocomposite free standing films. Int. J. Sci. Res. Rev. 7, 136–147.

Ofori-Kwakye, K., Mfoafo, K.A., Kipo, S.L., Kuntworbe, N., Boakye-Gyasi, M.E., 2016. Development and evaluation of natural gum-based extended-release matrix tablets of two model drugs of different water solubilities by direct compression. Saudi Pharm. J. 24, 82–91. https://doi.org/10.1016/j.jsps.2015.03.005

Ojsteršek, T., Vrečer, F., Hudovornik, G., 2024. comparative fitting of mathematical models to carvedilol release profiles obtained from hypromellose matrix tablets. Pharmaceutics 16, 498. https://doi.org/10.3390/pharmaceutics16040498

Okezue, M., Smith, D., Zeller, M., Byrn, S.R., Smith, P., Bogandowich-Knipp, S., Purcell, D.K., Clase, K.L., 2020. Crystal structures of salts of bedaquiline. Acta Crystallogr. Sect. C Struct. Chem. 76, 1010–1023. https://doi.org/10.1107/S2053229620013455

Otte, A., Sharifi, F., Parka, K., 2020. Interfacial tension effects on the properties of PLGA microparticles. Colloids Surf. B Biointerfaces 196, 111300. https://doi.org/10.1016/j.colsurfb.2020.111300

Pasandideh, S.H.R., Niaki, S.T.A., 2006. Multi-response simulation optimization using genetic algorithm within desirability function framework. Appl. Math. Comput. 175, 366–382. https://doi.org/10.1016/j.amc.2005.07.023

Patil, S.M., Diorio, A.M., Kommarajula, P., Kunda, N.K., 2024. A quality-by-design strategic approach for the development of bedaquiline-pretomanid nanoparticles as inhalable dry powders for TB treatment. Int. J. Pharm. 653, 123920. https://doi.org/10.1016/j.ijpharm.2024.123920

Pirooznia, N., Hasannia, S., Lotfi, A.S., Ghanei, M., 2012. Encapsulation of Alpha-1 antitrypsin in PLGA nanoparticles: *In-vitro* characterization as an effective aerosol formulation in pulmonary diseases. J. Nanobiotechnology 10, 20. https://doi.org/10.1186/1477-3155-10-20

Poh, W., Ab Rahman, N., Ostrovski, Y., Sznitman, J., Pethe, K., Loo, S.C.J., 2019. Active pulmonary targeting against tuberculosis (TB) via triple-encapsulation of Q203, bedaquiline and superparamagnetic iron oxides (SPIOs) in nanoparticle aggregates. Drug Deliv. 26, 1039–1048. https://doi.org/10.1080/10717544.2019.1676841

Posadowska, U., Parizek, M., Filova, E., Wlodarczyk-Biegun, M., Kamperman, M., Bacakova, L., Pamula, E., 2015. Injectable nanoparticle-loaded hydrogel system for local delivery of sodium alendronate. Int. J. Pharm. 485, 31–40. https://doi.org/10.1016/j.ijpharm.2015.03.003

Pramod, K., Tahir, M.A., Charoo, N.A., Ansari, S.H., Ali, J., 2016. Pharmaceutical product development: A quality by design approach. Int. J. Pharm. Investig. 6, 129–138. https://doi.org/10.4103/2230-973X.187350

Preiss, L., Langer, J.D., Yildiz, Ö., Eckhardt-Strelau, L., Guillemont, J.E.G., Koul, A., Meier, T., 2015. Structure of the mycobacterial ATP synthase Fo rotor ring in

complex with the anti-TB drug bedaquiline. Sci. Adv. 1, e1500106. https://doi.org/10.1126/sciadv.1500106

Rafiei, P., Haddadi, A., 2019. A robust systematic design: Optimization and preparation of polymeric nanoparticles of PLGA for docetaxel intravenous delivery. Mater. Sci. Eng. C 104, 109950. https://doi.org/10.1016/j.msec.2019.109950

Ruiz, E., Orozco, V.H., Hoyos, L.M., Giraldo, L.F., 2022. Study of sonication parameters on PLA nanoparticles preparation by simple emulsion-evaporation solvent technique. Eur. Polym. J. 173, 111307. https://doi.org/10.1016/j.eurpolymj.2022.111307

Sazali, M.F., Rahim, S.S.S.A., Mohammad, A.H., Kadir, F., Payus, A.O., Avoi, R., Jeffree, M.S., Omar, A., Ibrahim, M.Y., Atil, A., Tuah, N.M., Dapari, R., Lansing, M.G., Rahim, A.A.A., Azhar, Z.I., 2023. Improving tuberculosis medication adherence: the potential of integrating digital technology and health belief model. Tuberc. Respir. Dis. 86, 82–93. https://doi.org/10.4046/trd.2022.0148

Sharma, S., Sanpui, P., Chattopadhyay, A., Sankar Ghosh, S., 2012. Fabrication of antibacterial silver nanoparticle —sodium alginate– chitosan composite films. RSC Adv. 2, 5837–5843. https://doi.org/10.1039/C2RA00006G

Shen, S., Wu, Y., Liu, Y., Wu, D., 2017. High drug-loading nanomedicines: progress, current status, and prospects. Int. J. Nanomedicine 12, 4085–4109. https://doi.org/10.2147/IJN.S132780

Shishir, M.R.I., Chen, W., 2017. Trends of spray drying: A critical review on drying of fruit and vegetable juices. Trends Food Sci. Technol. 65, 49–67. https://doi.org/10.1016/j.tifs.2017.05.006

Silva, M.F., Hechenleitner, A.A.W., Irache, J.M., Oliveira, A.J.A. de, Pineda, E.A.G., 2015. Study of thermal degradation of PLGA, PLGA nanospheres and plga/maghemite superparamagnetic nanospheres. Mater. Res. 18, 1400–1406. https://doi.org/10.1590/1516-1439.045415

Song, X., Zhao, Y., Hou, S., Xu, F., Zhao, R., He, J., Cai, Z., Li, Y., Chen, Q., 2008. Dual agents loaded PLGA nanoparticles: Systematic study of particle size and drug entrapment efficiency. Eur. J. Pharm. Biopharm. 69, 445–453. https://doi.org/10.1016/j.ejpb.2008.01.013

Struzek, A.-M., Scherließ, R., 2023. Quality by design as a tool in the optimisation of nanoparticle preparation—a case study of PLGA nanoparticles. Pharmaceutics 15, 617. https://doi.org/10.3390/pharmaceutics15020617

Sun, M., Wang, Y., Yao, L., Li, Y., Weng, Y., Qiu, D., 2022. Fabrication and characterization of gelatin/polyvinyl alcohol composite scaffold. Polymers 14, 1400. https://doi.org/10.3390/polym14071400

Troiano, G., Figa, M., Sabnis, A., 2013. Drug loaded polymeric nanoparticles and methods of making and using same. US8420123B2.

Van Hemelryck, S., Wens, R., van Poppel, H., Luijks, M., Shahidi, K., Marczak, M., Kahnt, A., Holm, R., Mannaert, E., Langguth, P., 2021. In Vitro Evaluation of Poly(lactide-co-glycolide) in situ forming gels for bedaquiline fumarate salt and pharmacokinetics following subcutaneous injection in rats. Pharmaceutics 13, 1231. https://doi.org/10.3390/pharmaceutics13081231

Verma, V., Ryan, K.M., Padrela, L., 2021. Production and isolation of pharmaceutical drug nanoparticles. Int. J. Pharm. 603, 120708. https://doi.org/10.1016/j.ijpharm.2021.120708

Veza, I., Spraggon, M., Fattah, I.M.R., Idris, M., 2023. Response surface methodology (RSM) for optimizing engine performance and emissions fueled with biofuel: Review of RSM for sustainability energy transition. Results Eng. 18, 101213. https://doi.org/10.1016/j.rineng.2023.101213

Veziris, N., Bernard, C., Guglielmetti, L., Du, D.L., Marigot-Outtandy, D., Jaspard, M., Caumes, E., Lerat, I., Rioux, C., Yazdanpanah, Y., Tiotiu, A., Lemaitre, N., Brossier, F., Jarlier, V., Robert, J., Sougakoff, W., Aubry, A., 2017. Rapid emergence of Mycobacterium tuberculosis bedaquiline resistance: lessons to avoid repeating past errors. Eur. Respir. J. 49. https://doi.org/10.1183/13993003.01719-2016

World Health Organization, 2024. Global tuberculosis report 2024. Geneva.

Wu, Y., Sun, B., Tang, Y., Shen, A., Lin, Y., Zhao, X., Li, J., Monteiro, M.J., Gu, W., 2024. Bone targeted nano-drug and nano-delivery. Bone Res. 12, 1–22. https://doi.org/10.1038/s41413-024-00356-2

Yeom, D.W., Chae, B.R., Son, H.Y., Kim, J.H., Chae, J.S., Song, S.H., Oh, D., Choi, Y.W., 2017. Enhanced oral bioavailability of valsartan using a polymer-based supersaturable selfmicroemulsifying drug delivery system. Int. J. Nanomedicine 12, 3533–3545. https://doi.org/10.2147/IJN.S136599

Yu, L.X., 2008. Pharmaceutical Quality by Design: Product and Process Development, Understanding, and Control. Pharm. Res. 25, 781–791. https://doi.org/10.1007/s11095-007-9511-1

Zhang, Y., Zhang, R., Illangakoon, U.E., Harker, A.H., thrasivoulou, c., parhizkar, m., edirisinghe, m., luo, c., 2020. copolymer composition and nanoparticle configuration enhance in vitro drug release behavior of poorly water-soluble progesterone for oral formulations. Int. J. Nanomedicine Volume 15, 5389–5403. https://doi.org/10.2147/IJN.S257353

CHAPTER 4
DEVELOPMENT, AND *IN-VITRO*, CHARACTERIZATION OF THE NOVEL MULTI-COMPONENT 3D-PRINTED SCAFFOLD EMBEDDED WITH BQ-LOADED PLGA NANOPARTICLES FOR BONE TB THERAPY

4.1. Introduction

Bone tuberculosis (TB) has significant clinical, socioeconomic, and healthcare implications, especially in regions with high TB prevalence. Its impact extends beyond bone destruction, affecting mobility, quality of life, and healthcare systems (Ferreira et al., 2023; Foster et al., 2015; Nidoi et al., 2021). Bone TB primarily affects the spine and long bones, leading to severe complications such as bone destruction, deformities, and chronic pain (Pigrau-Serrallach, 2013). The current treatment strategies for bone TB involve prolonged systemic antibiotic therapy and, in severe cases, surgical debridement or bone grafting. However, these approaches have several limitations, including poor drug penetration into infected bone tissue, systemic toxicity from high-dose antibiotics, and limited regenerative capacity following bone loss (Mphaphuli et al., 2023; Pandita et al., 2020; Ruparel et al., 2022). These challenges necessitate the development of novel therapeutic strategies that not only deliver localized, sustained drug release but also promote bone regeneration.

Bone tissue engineering (BTE) is used as one of the solutions to circumvent the specified limitations through the development of an implantable scaffold. BTE has improved the prognosis of major bone deformities by employing 3D printing technology as one strategy for addressing these challenges (Haleem et al., 2020). Utilizing existing components, 3D printing techniques construct new scaffolds with enhanced mechanical properties for load-bearing applications (Arefin et al., 2021; Haleem et al., 2020; Nikolova and Chavali, 2019a). In addition, among the various 3D printing techniques, extrusion printing has been the most widely recognized technique for creating 3D printed scaffolds for bone tissue regeneration (Do et al., 2015; Kim et al., 2018; Martin et al., 2019; Turnbull et al., 2018; Zhang et al., 2020; Zhu et al., 2016).

To ensure optimal scaffold performance for bone applications, novel inks used in 3D printing must possess critical properties such as biocompatibility, biodegradability, mechanical strength, and rheological properties that facilitate precise printing and

maintain scaffold integrity (Rezania et al., 2022). These biomaterial ink properties are vital for promoting cell growth, tissue infiltration, and bone regeneration. The scaffold must also exhibit adequate porosity and interconnectivity to support nutrient diffusion and vascularization. Therefore, biomaterials are commonly used to fabricate these scaffolds, combining biopolymers, bioceramics, and biodegradable metals to provide the best qualities for bone regeneration (Loh and Choong, 2013; Nikolova and Chavali, 2019a; Zhang et al., 2021). However, selecting the appropriate biomaterial for 3D printing remains a significant challenge (Kumar et al., 2019). This can be addressed through the development of a multi-component scaffold using a combination of biomaterials, ensuring excellent mechanical and biological properties that closely mimic natural bone (Alaribe et al., 2016; Kumar et al., 2019; Ogueri et al., 2019).

Few studies on the design and development of a 3D-printed multi-component scaffold for bone TB have been conducted over the past decade. Yuan et al., (2015) emphasized the necessity of selecting appropriate biomaterials for a spinal TB scaffold, highlighting that these materials must release drugs at a concentration high enough to kill TB bacteria but low enough not to impair osteogenesis. In addition, the biomaterials must be biocompatible, and have a slow, consistent drug release rate to synchronize with bacterial clearance and bone regeneration (Yuan et al., 2015). While bioactive glasses (BG) have been explored as a potential biomaterial due to their ability to bond with native bone tissue and support angiogenesis and tissue regeneration, their rapid ion dissolution and resulting hydroxyapatite layer formation may not always provide optimal, sustained drug release (Distler et al., 2020; Shah and Czechowska, 2018; Yazdanpanah et al., 2022). The improvement of BGs for medical use is ongoing, with titanium (Ti)-containing bioactive glasses (BGTs) gaining attention for their enhanced mechanical strength and antibacterial properties, as well as their ability to promote bone regeneration (Han et al., 2019; Smith et al., 2021). Pei et al., (2018) developed a 3D printed scaffold for spinal TB composed of mesoporous bioactive glass (MBG), however, to avoid the brittleness of the scaffold, polycaprolactone (PCL) was added to improve the mechanical strength and to enhance drug delivery properties, Metal−Organic Frameworks (MOFs) were incorporated to the MBG (Pei et al., 2018). Similarly, Zhu et al., (2015) combined MBG with mesoporous silica nanoparticles (MSN) to improve drug loading, while PHBHHx polymer was added to facilitate adhesion between bioceramics and drug powders.

These studies highlight the importance of combining different biomaterials to achieve scaffolds with desirable properties for bone regeneration and drug delivery (Zhu et al., 2015). However, these approaches still face significant limitations, such as inconsistent drug release profiles, limited mechanical strength, and lack of comprehensive biocompatibility across multiple stages of bone regeneration.

Our study proposes the development of a novel multi-component scaffold using 3D printing for bone TB therapy. This scaffold will incorporate BGTs to enhance bioactivity. Furthermore, synthetic polymers such as PCL and polyvinyl alcohol (PVA) will be used to improve the scaffold's mechanical strength, with PVA also functioning as a stabilizing agent in the novel ink (Rezania et al., 2022; Uma Maheshwari et al., 2014; Xu et al., 2022). The addition of natural polymers like sodium alginate is essential to enhance the biocompatibility, and biodegradability, of the scaffold (Heo et al., 2017). Unlike previous designs, our prototype combines natural, synthetic, and bioactive components, addressing the limitations of earlier studies by offering superior mechanical strength, controlled drug release, and enhanced biocompatibility, ensuring more consistent therapeutic effects and better bone regeneration outcomes for bone TB treatment. This study reports on a comprehensive fabrication approach to achieve a targeted 3D-printed multi-component scaffold for bone TB therapy, ensuring safety by design. This includes the formulation of BQ-loaded PLGA nanoparticles as discussed in **Chapter 3**, embedded in a 3D-printed scaffold, with *In-vitro* evaluations conducted to assess its efficacy and biocompatibility.

4.2. Materials and methods

4.2.1. Materials

Sodium alginate (NaAlg, Product number: W201502) was obtained from Sigma-Aldrich, Gillingham, UK. Poly (vinyl alcohol) (PVA, Mw 19 000) and Polycaprolactone (PCL, Mw 80 000) were also obtained from Sigma-Aldrich. The bioactive glass titanium (BGT) containing (10%) titanium was kindly donated by the National Research Centre (Cairo, Egypt). MG63 osteoblast-like cells were sourced from PromoLab (Pty) T/A Separations (Johannesburg, South Africa). Alpha minimum essential medium (α-MEM) was obtained from Gibco, while fetal bovine serum (FBS), gentamicin, and penicillin-streptomycin were purchased from Sigma-Aldrich (St. Louis, Missouri, USA).

The MTT Cell Proliferation Kit I was acquired from Roche (Basel, Switzerland). Chemicals were utilized without further purification unless stated.

4.2.2. Fabrication of the novel multi-component 3D-printed scaffold

The BGT-PCL-PVA-NaALG scaffold was fabricated using the 4th generation 3D Bioplotter™ (EnvisionTEC, Germany). First, PCL was dissolved in chloroform (30% w/v). Sodium alginate (10% w/v) was hydrated in deionized water and homogenized at 17,000 rpm for 10 minutes before being slowly mixed with the PCL solution and homogenized at 18,000 rpm for 15 minutes in an ice bath. Bioactive glass titanium (1.5 g) and water (10 mL) were then added gradually, followed by homogenization at 20,000 rpm. Meanwhile, PVA (10% w/v) was dissolved in deionized water at 65°C for 1 hour and then slowly mixed in.

Additionally, 10% (v/v) of BQ-loaded PLGA nanoparticles were incorporated into the final novel ink to enhance the scaffold's drug delivery properties. This volume was chosen based on preliminary optimization studies to ensure a uniform distribution of nanoparticles without compromising the structural integrity or printability of the scaffold. The specified concentration was selected to achieve a balance between adequate drug loading and maintaining the physical characteristics of the ink for successful 3D printing. Uniform nanoparticle distribution is critical for ensuring consistent release of BQ while retaining the mechanical properties of the scaffold. Printability was a key consideration to guarantee that the ink could flow smoothly through the 3D printer nozzle, avoiding issues like clogging or poor layer adhesion. The final novel ink, which was in the form of a paste, was loaded into a cartridge and 3D-printed into a petri dish containing propanol as a solidifying solution. **Figure 4.1** illustrates the fabrication process. The parameters in Table 4.1 were used in fabricating the novel multi-component 3D-printed scaffold.

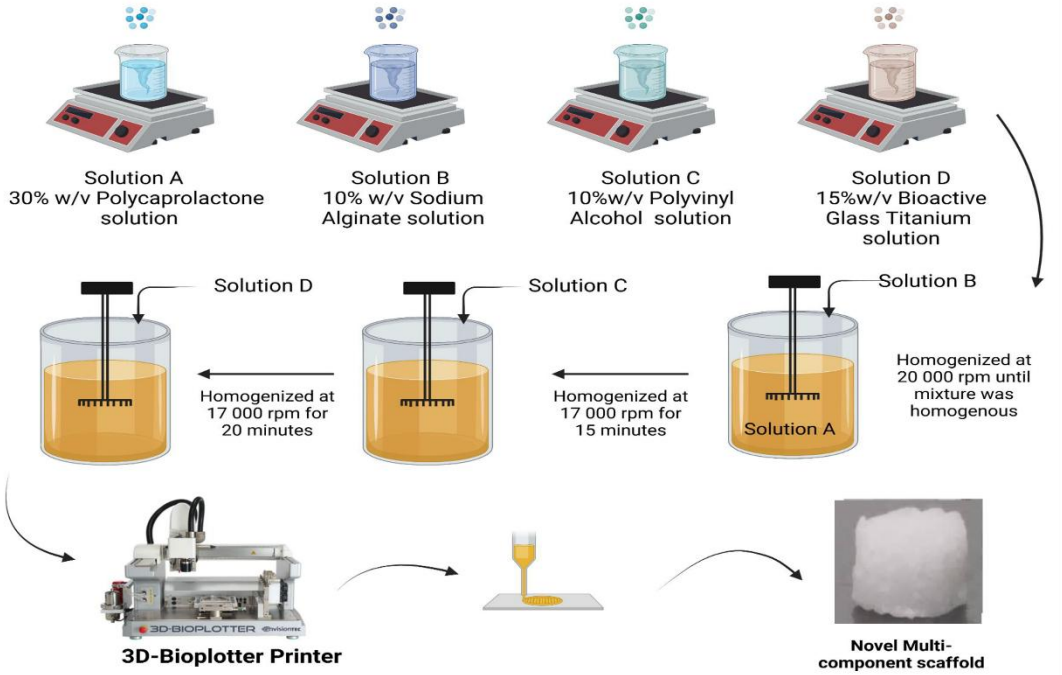


Figure 4.1: Schematic and photographic depiction of the development of the novel multi-component 3D-printed scaffold.

Table 4.1: Parameters for the novel multi-component 3D-printed scaffold

Parameter	Value
Printing pressure	2 Bar
Printing speed	35.1 mm/s
Nozzle size	25 µm
Temperature	20°c
Waiting period	15 seconds

4.3. Characterisation studies of the loaded and unloaded novel multi-component 3D-printed scaffold

4.3.1. Physicochemical properties of the novel multi-component 3D-printed scaffold

Fourier transform infrared spectroscopy (Spectrum 100, PerkinElmer Inc., Waltham, MA, USA) was employed to identify the molecular vibrations indicative of chemical changes within the 3D-printed scaffold samples. FTIR measurements were conducted over a wavenumber range of 4000–650 cm^{-1}. X-ray diffraction (XRD) analysis was performed using a Rigaku 600 X-ray diffractometer (RIGAKU MiniFlex, RIGAKU Inc., Tokyo, Japan) to examine the phase composition (crystalline and/or amorphous) of

the prepared 3D-printed scaffold. The XRD spectra were recorded within a range of 10° to 90°.

4.3.2. Thermal properties of the novel multi-component 3D-printed scaffold

A thermogravimetric analyzer (TGA 400, PerkinElmer, MA) was used to analyze the thermal decomposition of the 3D printed scaffold and the native materials. Samples (10–20 mg) were placed in a ceramic pan under a nitrogen gas atmosphere. Thermograms were recorded in a range of 30–900°C and revealed the thermal decomposition of the materials.

4.3.3. Microstructure and morphology of the novel multi-component 3D-printed scaffold

To investigate the surface morphology, the 3D-printed multi-component scaffolds were first coated with a thin layer of gold using an EPI coater. The gold was sputtered onto the samples, which were mounted on aluminum stubs, using an SPI Model sputter-coater and control unit (Hester, PA). After a 60-second coating process, the samples were imaged and analyzed using an FEI Nova NanoLab SEM (FEI Company, Hillsboro, OR).

4.3.4. Porosity and pore size distribution of the novel multi-component 3D-printed scaffold

The porosimetric analysis of the 3D-printed multi-component scaffolds was conducted using an ASAP 2020 porositometer (Micromeritics Instrument Company (Pty) Ltd., Norcross, GA, USA) equipped with research-grade ASAP 2020 V3.01 software (n = 3). This analysis was performed to quantify the porous characteristics of the scaffolds, including surface area, pore size distribution, and total pore volume. Briefly, scaffold samples (~10.5 mg) were evacuated with nitrogen gas (N_2) to remove surface moisture and residual gas particles before analysis. The samples were then enclosed in an isothermal jacket and degassed for approximately 18 hours. Following degassing, the samples were transferred to the analysis port and immersed in liquid nitrogen for porosity measurements. The Barrett–Joyner–Halenda (BJH) and Brunauer–Emmett–Teller (BET) adsorption-desorption models were subsequently

applied to determine pore size distribution and surface area characteristics (Govender et al., 2018).

4.3.5. Biomineralization of the novel multi-component 3D-printed scaffold

The SBF immersion test is commonly used to evaluate the ion release behavior (and bioactivity) of samples in the field of bioactive glasses. With the assumption that the ion release kinetics in SBF and in cell culture medium are comparable, we conducted the SBF immersion test to investigate the bioactivity and ion release profiles (Kokubo and Takadama, 2006; Mabrouk et al., 2019). The immersion of the novel multi-component 3D-printed scaffold was conducted as follows: Briefly, 10 mg of the scaffold was immersed in 15 mL of SBF following the procedure described (Kokubo and Takadama, 2006) for 0, 7, 14, 21, and 28 days at 37 °C. After immersion, samples were examined by X-ray diffraction, and FTIR as described in **section 4.3.1**.

4.3.6. Swelling analysis of the novel multi-component 3D-printed scaffold

The swelling behaviour of the 3D-printed multi-component scaffolds was evaluated by immersing the samples in phosphate-buffered saline (PBS, Ph 7.4, 37°C) to simulate physiological conditions. At predetermined time intervals, the scaffolds were carefully removed, gently blotted with filter paper to remove excess surface moisture and weighed. The initial dry weight of each scaffold was recorded as W_i, while the wet weight at each time point was noted as W_f. **Equation 4.1** shows the determination of the swelling ratio (mean ±SD) (n=3):

$$Swelling\ ratio\ \% = \frac{(w_f - w_i)}{w_i} x100 \ldots\ldots\ldots\ldots\ldots \textbf{(4.1)}$$

This analysis provided insights into the scaffold's water absorption capacity, structural stability, and potential for fluid uptake in biological environments**.**

4.3.7. Biodegradation of the novel multi-component 3D-printed scaffold

Degradation studies of the 3D-printed scaffolds were performed under physiological conditions to assess their biodegradability and suitability for tissue engineering applications. The scaffolds were carefully prepared to ensure uniform weight (1g). The degradation capability of the engineered scaffolds was evaluated in simulated body fluid (SBF) at 37°C over 30 days. The SBF fluid was changed after every seven days.

The scaffolds were dried at 90°C and weighed after being removed from the SBF at specific intervals (Chen et al., 2021). The weight loss was calculated using **Equation 4.2**.

$$Degradation\ rate\ \% = \frac{(w_o - w_t)}{w_0}\ x\ 100 \text{.....} \textbf{(4.2)}$$

Where;

W_0 = the initial mass of the scaffolds (before immersion),

W_t = Final weight of the scaffold at a specific time point

4.3.8. Compressive strength analysis of the novel multi-component 3D-printed scaffold

The mechanical properties of the 3D-printed multi-component scaffolds were evaluated using a Texture Analyzer (Ta.XTplus, Stable Micro Systems, Surrey, UK) to assess their compressive strength and structural integrity. Furthermore, to investigate the impact of BGT on mechanical performance, an unloaded 3D-printed scaffold without bioactive glass titanium was also assessed for comparison.

Before testing, scaffolds were incubated for 24 hours at 37°C in a cell culture medium composed of Alpha Minimum Essential Medium (α-MEM, 82% v/v), supplemented with 14% (v/v) fetal bovine serum (FBS), 2% (v/v) gentamicin, and 2% (v/v) penicillin-streptomycin. Following incubation, compressive force was applied using a texture probe at a pre-test speed of 0.5 mm/s and an initial compression force of 1 kg. Compression continued at a test speed of 1 mm/s until scaffold fracture occurred, with data recorded at an acquisition rate of 200 points/s. Scaffold mechanical failure was identified as the point of structural breakage (Cuadros et al., 2015; Diaz-Gomez et al., 2022). Mechanical strength was conducted in triplicate and data was recorded as a mean ± SD (n=3).

4.3.9. Bedaquilline release from the novel multi-component 3D-printed scaffold

A drug-loaded multi-component 3D-printed scaffold weighing 1g was placed in 20 mL of SBF and incubated in an orbital shaking incubator (YIHDER LM-530, YIHDER Co., Ltd., Taipei, Taiwan) at 37 °C to simulate physiological conditions. Samples were collected over a period of 4 weeks. Fresh SBF was replenished after each sampling

to maintain sink conditions (Ji et al., 2024; Jin Lee et al., 2018). A high-performance liquid chromatography (HPLC) (Waters, Milford, Massachusetts, USA) was used to analyze the drug release profile, following the method described by Ayodele et al. (2024). The HPLC system was equipped with a Waters Symmetry300™ C18 (5 µm, 4.6 × 150 mm) column, a UV detector, and a Waters binary HPLC pump. The mobile phase consisted of a 95:5 (v/v) mixture of acetonitrile/methanol and phosphate buffer (pH 7.4), with a flow rate of 1.0 mL/min and a detection wavelength of 275 nm.

4.3.10. *In-vitro* Cytotoxicity analysis of the novel multi-component 3D-printed scaffold

In this study, the newly synthesized scaffolds were subject to cell viability evaluation using a 3-(4,5-dimethylthiazole2-yl)-2,5-diphenyltetrazolium bromide (MTT) assay. Osteoblast-like cells were utilized to assess the cell viability of the 3D-printed scaffolds, before implanting the 3D-printed scaffolds in a living organism. The standard culture medium served as the control in this study. The primary aim of the assay was to determine whether the cells remained metabolically active on the 3D-printed scaffold, ensuring its biocompatibility for further applications (Gong et al., 2020).

4.3.11. Cell culture and experimental setup

Osteoblast-like MG63 cells, derived from human osteosarcoma, were selected for their osteoblast-like properties, making them an ideal model for evaluating cell viability, adhesion, and proliferation in BTE (Dvorakova et al., 2023). Briefly, cells were cultured in Alpha Minimum Essential Medium (α-MEM, 82% v/v) supplemented with 14% (v/v) fetal bovine serum (FBS), 2% (v/v) gentamicin, and 2% (v/v) penicillin-streptomycin in a T-75cm^2 culture flask (Sigma-Aldrich, St. Louis, MO, USA). containing 15ml. The flask was incubated at 37°C in a 5% CO_2 environment. The cell culturing medium was changed every second day (Sithole et al., 2018).

4.3.11.1. Cell viability evaluation for the novel multi-component 3D-printed scaffold

Before conducting cytotoxicity studies, the 3D-printed scaffolds (0.6 g/well) were washed with 70% ethanol and thoroughly rinsed with PBS. The scaffolds were then exposed to continuous UV-C light (254 nm) for 30 minutes using a UV EQUIP system

(South Africa) to ensure surface sterilization (Łopianiak and Butruk-Raszeja, 2020; Tohamy et al., 2018). The sterilized 3D-printed scaffolds were first placed in cell culture medium within sterilized polytops to allow for proper wetting of the scaffold before transferring them to the well plates. Once the osteoblast-like MG63 cells had reached the confluence of 80-90%, the cells were detached using 0.25% trypsin solution following the cell supplier protocol. Then cells were centrifuged and re-suspended in a prepared culture medium and counted using a hemocytometer. Aliquots (1mL) containing $1x10^5$ cells were seeded on top of the novel multi-component 3D-printed scaffolds which were transferred in 24-well plates. The following was then incubated at 37°C in a 5% CO_2 environment for 2 hours. After Incubation, the medium was removed and replaced with 1ml of fresh culture medium (Sithole et al., 2018; Tavakoli et al., 2024).

At the end of each designated time point (1, 3, and 7 days), the medium was removed and replaced with MTT solution (20 µL) was added to each well plate, followed by the addition of acid-isopropanol solubilizing agent (100 µL) after 4 hours, and incubation overnight under standard culture conditions. Absorbance measurements were carried out in triplicates using the Victor™ X3 microplate reader. Absorbances were read at 570 nm, with the background measurement taken at 690 nm. **Equation 4.3** was applied to calculate the cell viability (Kondiah et al., 2017; Tohamy et al., 2018).

$$(\%)Cell\ Viability = \frac{A_{test} - A_{blank}}{A_{control} - A_{blank}}\ X\ 100 \quad \textbf{.....(4.3)}$$

Where;

A_{test} = absorbance from the 3D-printed scaffolds

$A_{control}$ = absorbance from control (medium with cells)

A_{blank} = absorbance from blank (medium only)

4.3.12. Cell adhesion onto the novel multi-component 3D-printed scaffold

The assessment of the adhesion of cells to the surface of the scaffold is a crucial measure in BTE, as it provides fundamental details on the biocompatibility of the scaffold and its potential to support cell proliferation, differentiation, and integration (Tupe et al., 2024). A positive cell adhesion of cells to the scaffold indicates the scaffold's effectiveness in promoting BTE (Nikolova and Chavali, 2019b; Tupe et al.,

2024). In this study, the adhesion of osteoblast-like MG-63 cells on the surface of the scaffolds was investigated after day 7 of the culture period, with a seeding density of $2x10^5$ cells per scaffold. The cells were first fixed using a 1.5%v/v glutaraldehyde in PBS solution for 30 minutes to preserve the cells and facilitate the analysis. The scaffolds were then dehydrated through a series of ethanol washes with increasing concentrations to maintain the integrity of the cell morphology. SEM was employed to examine the detailed surface interactions between the cells and the scaffold material. To ensure high-quality imaging and accurate visualization, the scaffold surface was coated with a thin layer of gold before imaging (Sithole et al., 2018; Tavakoli et al., 2024). This method allowed for the clear observation of the cellular attachment, spread, and morphology on the scaffold surface, providing valuable information on its suitability for supporting osteoblast-like cell growth.

4.3.13. Statistical analysis

GraphPad Prism 9 (GraphPad Software, Inc., San Diego, CA, USA) two-tailed Student's t-test was used for data analysis, with $p< 0.05$ deemed statistically significant. Data are presented as mean values of biological triplicates (n=3) ± standard deviation.

4.4. Results and discussion

4.4.1. Chemical integrity evaluation of the novel multi-component 3D-printed scaffold

Figure 4.2 presents the FTIR spectra of the drug-loaded and unloaded novel multicomponent scaffold and its components, highlighting key functional groups that contribute to its suitability for BTE. The **(Figure 4.2a)** bioactive glass titanium (BGT 10%) spectrum features Si-O-Si bending (490 cm^{-1}) and symmetric stretching (778 cm^{-1}) vibrations, confirming SiO_2 as a network former, which is crucial for osteoconductivity and hydroxyapatite (HA) formation. The P-O stretching (1043–1024 cm^{-1}) supports bone mineralization, while the Ti-O vibration (635 cm^{-1}) indicates titanium incorporation, which enhances osteoinduction by promoting cell adhesion and differentiation (Mabrouk et al., 2021; Mahdy et al., 2021).

The FTIR spectrum of the unloaded novel multi-component scaffold **(Figure 4.2F)** exhibits characteristic peaks from its polymeric and inorganic components. The ester groups of **(Figure 4.2b)** PCL contribute to its distinct carbonyl stretching band at 1722 cm^{-1}, ensuring mechanical stability and controlled degradation for gradual bone replacement (She et al., 2021; Uma Maheshwari et al., 2014). Hydroxyl and carbocyclic groups from **(Figure 4.2c)** PVA are evident in the broad O–H stretching (3550–3200 cm^{-1}), which supports hydration and cell viability, while **(Figure 4.2d)** NaAlg COO vibrations (1594, 1406 cm^{-1}) enhance hydrophilicity and cell adhesion, facilitating extracellular matrix formation (Kim et al., 2018, 2018; Tohamy et al., 2018). **(Figure 4.2a)** BGT 10% introduces additional signals, confirming its integration into the polymeric network.

The **(Figure 4.2g)** drug-loaded novel multi-component scaffold displays additional spectral contributions from the drug and inorganic bioglass component. The incorporation of **(e)** BQ-loaded PLGA nanoparticles is confirmed by characteristic peaks described in Chapter 3, indicating successful drug loading within the system. The presence of bioglass and titanium introduces new silicon-oxygen (Si–O) stretching bands within the 1000–1100 cm^{-1} region. The interactions between organic and inorganic components may result in slight shifts or peak broadening, suggesting hydrogen bonding or electrostatic interactions, which enhance scaffold stability and bioactivity. These molecular interactions contribute to osteointegration, controlled degradation, and localized drug release, making the scaffold highly effective for bone tissue regeneration by promoting cell adhesion, proliferation, and new bone formation (Mabrouk et al., 2019).

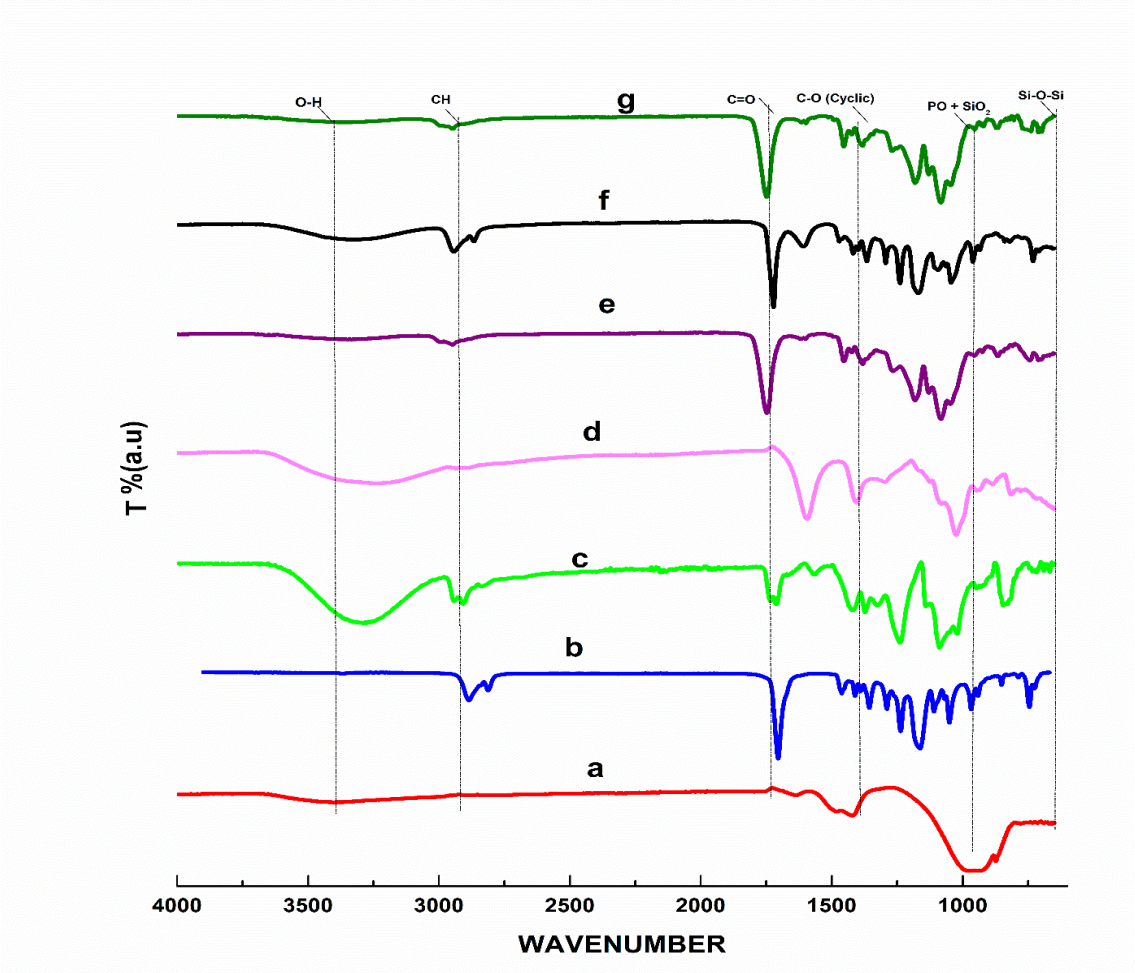
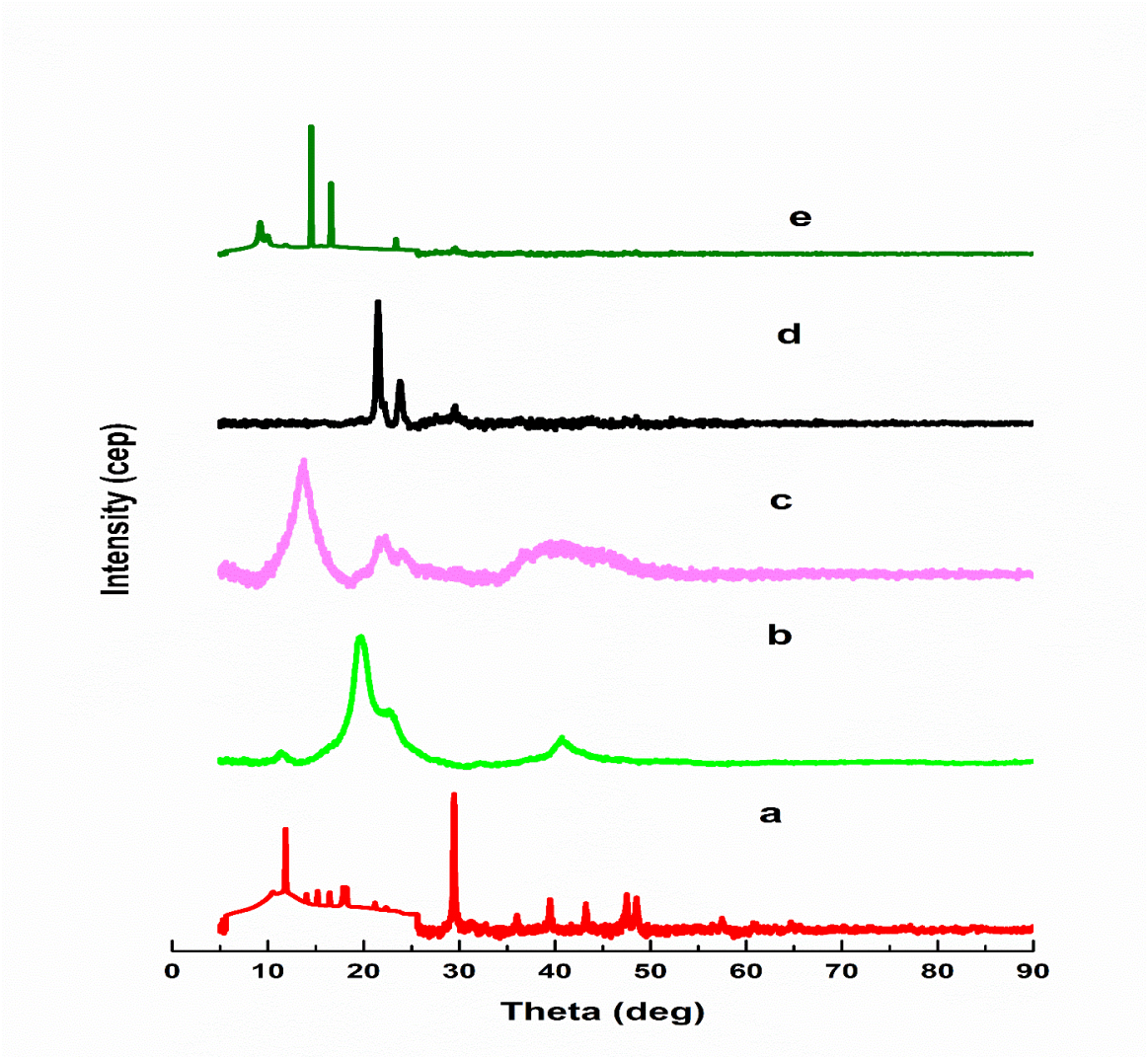


Figure 4.2: FTIR spectra of **(a)** native BGT 10%, **(b)** native polycaprolactone (PCL), **(c)** native polyvinyl alcohol (PVA), **(d)** native sodium alginate (NaAlg), **(e)** BQ-loaded PLGA nanoparticles **(f)** Unloaded 3D-printed scaffold and **(g)** Drug loaded 3D-printed scaffold.

The XRD diffractograms of the drug-loaded and unloaded novel multicomponent scaffold and its components are shown in **Figure 4.3** to ascertain the scaffold's physicochemical state. The X-ray diffraction analysis of **(Figure 4.3a)** pure BGT10% reveals distinct peaks within the 28°–30° range (2θ), indicating a degree of crystallinity within the bio-glass matrix. The **(Figure 4.3b)** native PVA exhibits a broad peak at 19°–20°, characteristic of its semicrystalline nature, while **(Figure 4.3c)** NaAlg displays peaks at approximately 14°, 22°, and 38°, confirming its partially ordered structure (Mabrouk et al., 2014). The XRD of the **(Figure 4.3d)** unloaded novel multi-component scaffold shows overlapping diffraction features from its components, with peaks associated with PVA (18° and 23°) exhibiting increased crystallinity due to polymer interactions. Upon **(e)** BQ-loaded PLGA nanoparticles, the scaffold displays subtle

peak shifts and intensity variations, suggesting molecular interactions between the delivery system and the scaffold matrix. These modifications may indicate partial disruption of crystallinity or structural rearrangements, potentially influencing drug release behaviour and scaffold integrity. Overall, the XRD analysis confirms the composite scaffold's balance between crystalline and amorphous phases, crucial for mechanical strength, bioactivity, and controlled drug release in bone tissue regeneration.



.

Figure 4.3: XRD spectra of **(a)** native BGT (10%) **(b)** native PVA, **(c)** native NaAlg**, (d)** unloaded novel multicomponent scaffold and **(e)** drug-loaded novel multicomponent scaffold.

4.4.2. Assessment of thermal stability and composition of the 3D-printed scaffold

Thermogravimetric analysis (TGA) plays a crucial role in evaluating the thermal stability and the TGA curves of the individual components and the novel multi-component 3D-printed scaffolds (both unloaded and drug-loaded) are presented in **Figure 4.4.** The TGA analysis provides valuable insights into the material's thermal stability and degradation behaviour, which is crucial for tissue engineering applications. The **(Figure 4.4a)** BGT 10% exhibited a straight-line thermogram, indicating no weight loss and confirming its high thermal stability, which is expected for an inorganic material (Mabrouk et al., 2021). The thermogram for **(Figure 4.4b)** PCL showed an initial weight loss at ~350°C, corresponding to its polymer backbone decomposition, while **(Figure 4.4c)** PVA degraded at ~300°C, due to dehydration and polymer chain (Uma Maheshwari et al., 2014; Zhou et al., 2018). The thermogram for **(d)** NaAlg was the least thermally stable, with decomposition starting at ~240°C, attributed to the breakdown of its carboxyl and hydroxyl functional groups (Valido et al., 2020).

The **(e)** unloaded novel multi-component 3D-printed scaffold exhibited an initial weight loss at ~340°C, indicating strong polymer-polymer interactions through hydrogen bonding and possible cross-linking. The slightly higher thermal stability compared to the individual polymer components suggests that BGT incorporation reinforces the scaffold’s structural integrity (Mabrouk et al., 2014; Smith et al., 2021). However, in the **(f)** drug-loaded novel multi-component 3D-printed scaffold, the initial degradation shifted to ~310°C, indicating that BQ-loaded PLGA nanoparticles influenced the thermal stability. This earlier degradation may be due to the weakening of polymer-polymer interactions, where the drug disrupts the original hydrogen bonding network or reduces crystallinity, leading to an earlier thermal breakdown (Madorsky and Straus, 1959). Together, these results confirm that the thermal behavior observed in the TGA aligns with the structural characteristics identified by the XRD and FTIR spectra.

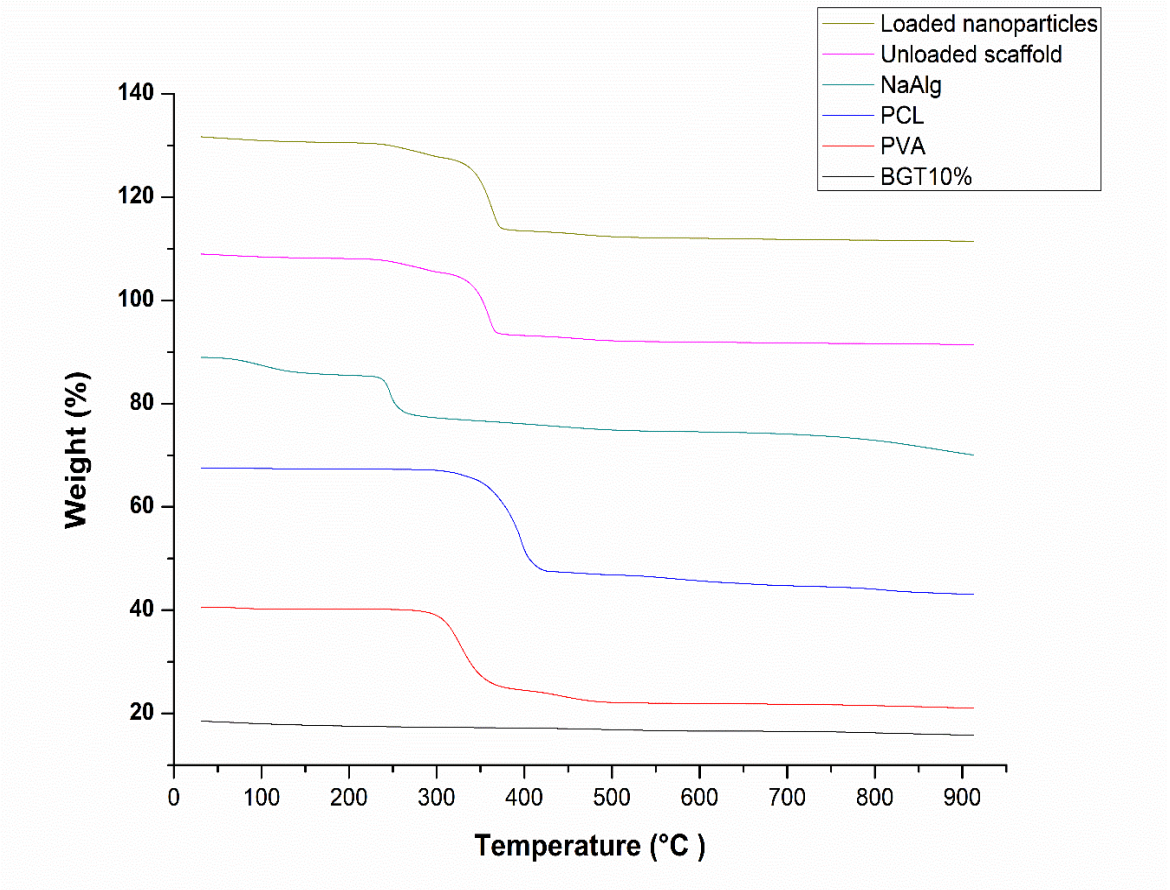


Figure 4.4: TGA thermograms of **(a)** native BGT 10%, **(b)** native polycaprolactone (PCL), **(c)** native polyvinyl alcohol (PVA), **(d)** native sodium alginate (NaAlg), **(e)** Unloaded 3D-printed scaffold and **(f)** Drug loaded 3D-printed scaffold.

4.4.3. Evaluation of microstructure, morphology, and porosity of the novel multi-component 3D-printed scaffold.

The microstructural, morphological, and porosity evaluation of the 3D-printed scaffold is crucial for understanding its surface characteristics and overall structural integrity. This section presents macroscopic and microscopic analyses, incorporating visual assessment through captured images, high-resolution structural insights via scanning electron microscopy (SEM), and porosity measurements conducted using a porosimeter, with SEM also used to confirm porosity.

Figure 4.5 (a,b) illustrates the microstructure characteristic of the novel multi-component 3D-printed scaffold, which is indicative of both drug-loaded and unloaded scaffold. The scaffold exhibits a distinct grid-like pattern with uniformly distributed pores, indicative of a controlled and precise printing process. Small droplets or surface

irregularities are visible, which could be remnants of material deposition during printing. The scaffold's surface appears moist and reflective, which can be attributed to its recent removal from propanol, which is the solidifying solvent used during the printing process and was observed before the drying stage. Furthermore, **Figure 4.5 (c-f**) depicted images of the loaded and unloaded 3D printed scaffolds further confirming and expanding upon the macroscopic observations previously described. Both scaffolds maintain a highly interconnected porous structure at the microscopic level, corresponding closely with the uniform, grid-like morphology observed macroscopically. The loaded scaffold **(Figure 4.5 e,f)** distinctly reveals spherical nanoparticulate structures evenly distributed on its surface and within its internal pores, confirming the successful incorporation of drug-loaded nanoparticles. In contrast, the unloaded scaffold **(Figure 4.5 c,d)** presents a clear, unobstructed porous network without these nanoparticulate structures, highlighting the morphological changes induced by nanoparticle loading. The rough texture observed in both scaffold types through SEM analysis is consistent with the earlier macroscopic assessment, indicating favourable surface characteristics for cell adhesion and proliferation (Baptista and Guedes, 2021; Calore et al., 2021; Pei et al., 2018). Overall, SEM imaging validates the macroscopic evaluations and demonstrates that nanoparticle loading does not compromise the scaffold's structural integrity but rather improves its functional attributes for targeted biomedical applications.

The SEM and BET analyses offered complementary insights into the scaffold's porosity characteristics (Bardestani et al., 2019). The SEM image **(Figure 4.6 a),** analyzed through ImageJ, revealed macropores with sizes ranging from approximately 415.7 µm to 562.3 µm which falls within the optimal pore size range of >300 µm known to support effective cell infiltration, tissue integration, and nutrient diffusion in BTE applications (Baptista and Guedes, 2021; Sithole et al., 2018; Zhang et al., 2022). It should be noted that pore size measurements and pore size distributions obtained from SEM and BET analyses were comparable for both the loaded and unloaded scaffolds. Therefore, representative images and data for only one scaffold type are presented to avoid redundancy.

The BET analysis provided information about the scaffold's surface area, pore size, and pore volume, as displayed in **Figure 4.6 (b)** (Lapczyna et al., 2014). The

combination of the different biomaterials resulted in an isotherm that exhibits a hysteresis loop, indicative of a mesoporous structure. The inset pore-size distribution confirms pores predominantly in the nanometer range (below 200 nm), suggesting the presence of additional micro- and mesoporous features on the scaffold surface (Bardestani et al., 2019; Mndlovu et al., 2019; Zhu et al., 2015). Such hierarchical porosity improves the scaffold's functional properties by promoting cell attachment, proliferation, and efficient drug delivery (Mirhadi et al., 2018). BET analysis further supports these findings, revealing a high specific surface area (75.549 m^2/g), substantial total pore volume (0.396 cm^3/g), and an average pore diameter of approximately 166.130 nm. Collectively, these parameters indicate that the scaffold possesses a favourable porous architecture capable of facilitating enhanced drug-loading capacity, sustained drug release, efficient mass transport, and robust cell infiltration, making it particularly advantageous for targeted drug delivery and tissue engineering applications (Mirhadi et al., 2018; Mndlovu et al., 2019).

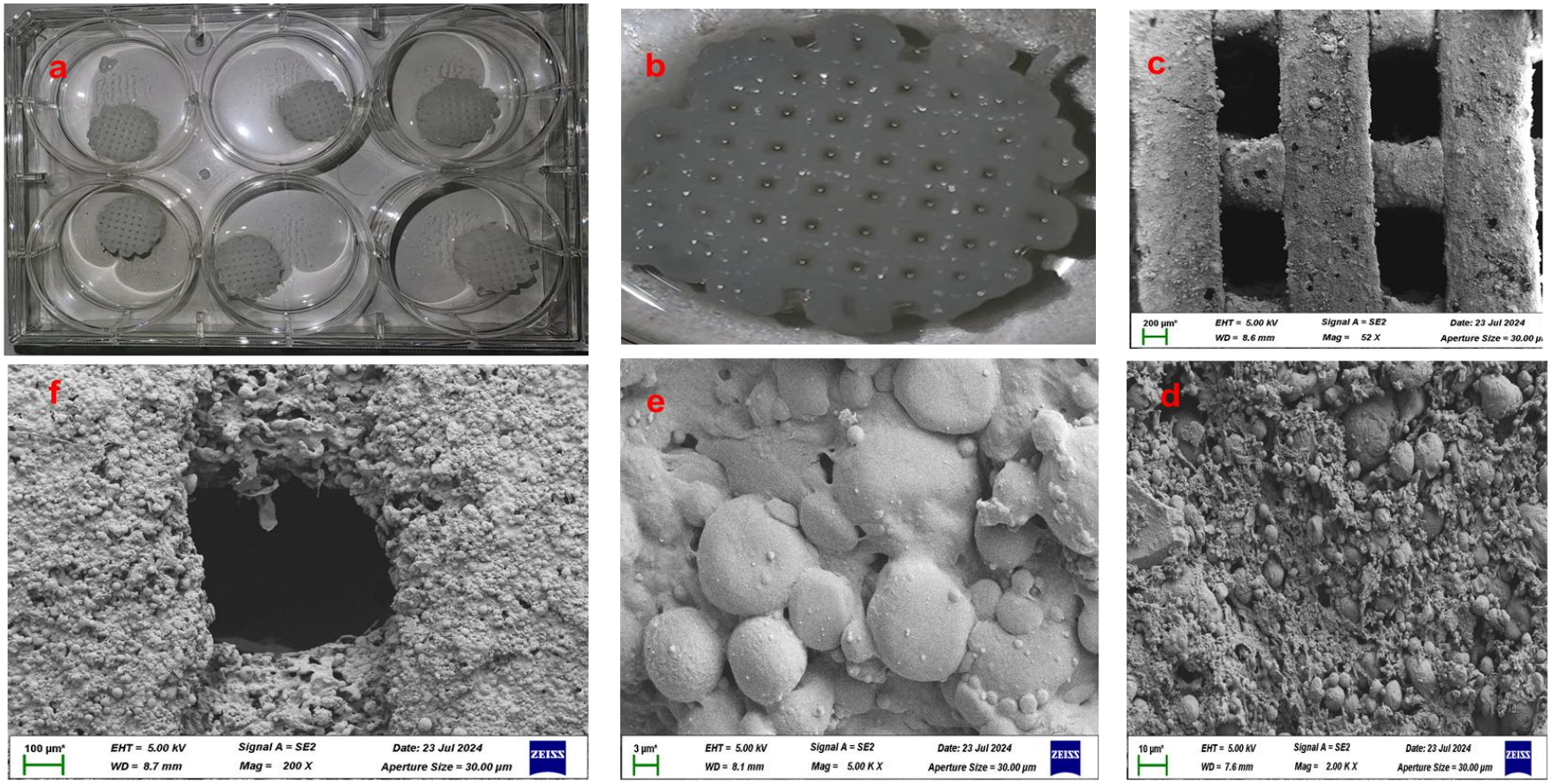


Figure 4.5: Visual and microscopic evaluation of the novel multi-component 3D-printed scaffold. **(a, b)** Macroscopic images showing the microstructure of the 3D-printed scaffold, highlighting its uniform grid-like pattern and structural integrity. **(c, d)** SEM images of the unloaded 3D-printed scaffold, displaying its porous architecture and surface morphology. **(e, f)** SEM images of the drug-loaded 3D-printed scaffold show spherical nanoparticulate structures distributed on the scaffold surface and within its internal pores, confirming successful nanoparticle incorporation.

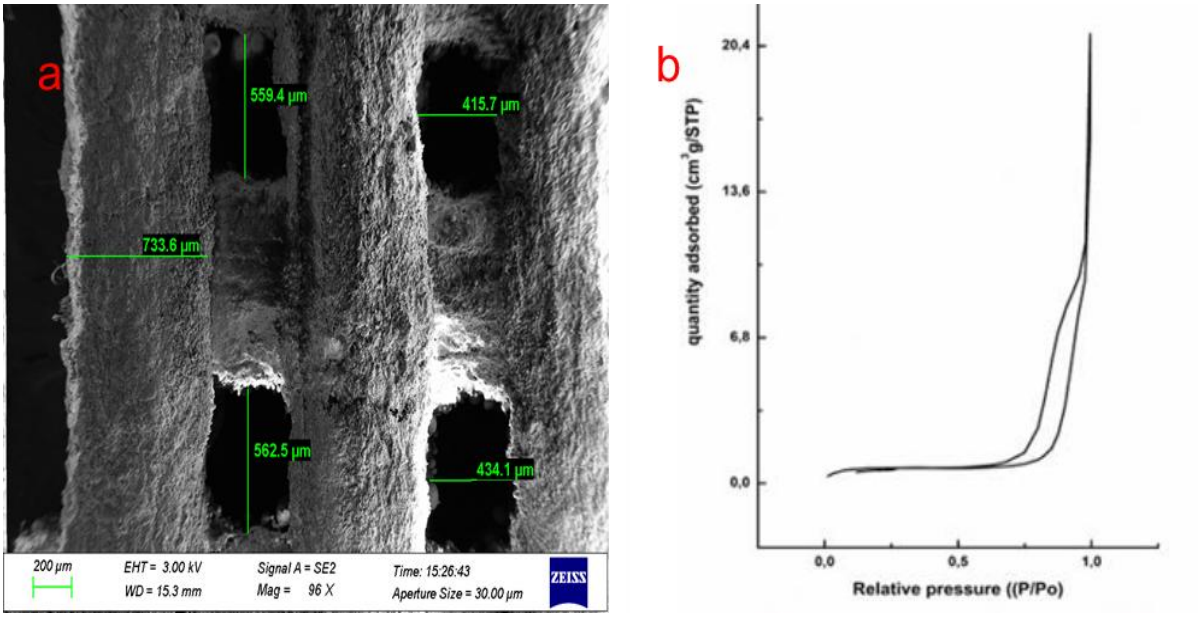


Figure 4.6: Structural and porosity evaluation of the novel multi-component 3D-printed scaffold. **(a)** SEM image showing the scaffold's macroporous architecture with pore sizes ranging from approximately 415.7 µm to 562.3 µm. **(b)** BET isotherm curve illustrating the scaffold's adsorption-desorption behavior, indicative of a mesoporous structure with a hysteresis loop, further supporting its suitability for controlled drug delivery and biomedical applications.

4.4.4. Evaluation of biomineralization of the Novel Multi-Component 3D-Printed Scaffold

The primary role of a 3D-printed scaffold in bone tissue engineering is to serve as a supportive framework that facilitates cell attachment, proliferation, and differentiation, ultimately promoting bone regeneration (Hasan et al., 2022; She et al., 2021; Yoo et al., 2011). To achieve this, the scaffold must closely mimic the composition and structural properties of natural bone tissue. Incorporating minerals such as hydroxyapatite (HA), the primary mineral found in bone, plays a crucial role in achieving this biomimetic design (Rezania et al., 2022; Tohamy et al., 2018). The biomineralization of the 3D-printed scaffold improves the scaffold's biocompatibility and promotes better cell adhesion, proliferation, and differentiation, which ultimately enhances tissue regeneration (Hasan et al., 2022).

SBF soaking experiments were performed to assess the biomineralization and biodegradation of the novel multi-component 3D-printed scaffolds. For both studies, the scaffolds were assessed for over 28 days. For the biomineralization study, XRD

and FTIR **(Figure 4.7 a,b**) were used to evaluate the scaffold mineralization over time. The FTIR spectrum **(Figure 4.7a)** initially displayed prominent polymer peaks (C-H, C=O) characteristic of PCL and PVA, with no evidence of mineral deposition on day 0. By day 7, phosphate (PO_4^{3-}) bands appeared between 900-1200 cm^{-1}, suggesting early calcium phosphate formation, while O-H bands indicated possible hydration layers resulting from bioactive glass (BG) interaction (Mabrouk et al., 2014; Pei et al., 2018). BG undergoes controlled dissolution, releasing calcium and silicate ions that form a silica-rich (SiO_2) layer, which acts as a template for apatite deposition. By day 14, increased PO_4^{3-} intensity and the emergence of a C-O (cyclic) peak suggested carbonate incorporation, resembling bone-like carbonated apatite (Fu et al., 2011; Pei et al., 2018). By day 21 and day 28, stronger PO_4^{3-} peaks alongside well-defined O-H bands confirmed apatite formation, with an enhanced SiO_2 peak indicating ongoing BG degradation and sustained ion exchange (Mabrouk et al., 2014).

The XRD pattern **(Figure 4.7b)** showed distinct PCL, PVA, and titanium peaks on day 0, with no evidence of calcium phosphate phases. By day 7, weak and broad peaks characteristic of amorphous calcium phosphate emerged. On day 14, increased peak intensity near $2\theta = 25.8°$ indicated early apatite crystal growth. By day 21, sharper and more intense apatite peaks confirmed improved crystallinity and mineralization, while by day 28, well-defined apatite peaks indicated the formation of mature, crystalline apatite. The progressive increase in apatite peak intensity and sharpness reflects successful biomineralization, driven by BG dissolution, ion exchange, and subsequent apatite deposition (Lopez-Fontal and Gin, 2025; Tohamy et al., 2018).

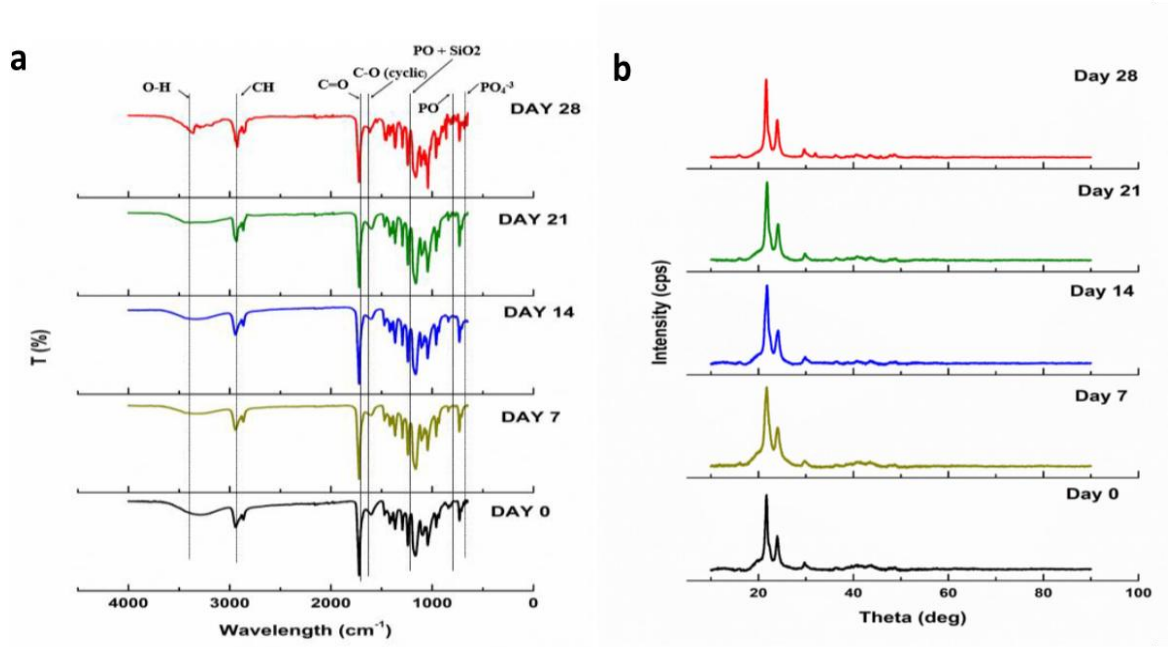


Figure 4.7: Spectra of **(a)** FTIR and **(b)** XRD of the novel multi-component 3D-printed scaffolds before immersion in SBF (pH 7.4, 37°C) and after immersion for over 28 days.

To further elucidate surface biomineralization, energy-dispersive X-ray (EDX) was employed on the novel multi-component 3D-printed scaffold before and after immersion (**Figure 4.8a,b)** in SBF (pH 7.4, 37°C). The EDX spectra before and after immersion confirm successful biomineralization and align with the FTIR and XRD data. Before immersion, the absence of calcium (Ca) and phosphorus (P) peaks in the EDX spectrum corresponds with the day 0 FTIR and XRD data. After immersion, the EDX spectrum reveals prominent Ca, P, Si, and O peaks, indicating mineral deposition. This aligns with the appearance of phosphate (PO_4^{3-}) bands in the FTIR spectrum from day 7 onward. The presence of Si further supports bioactive glass degradation and the formation of a silica-rich layer, which facilitates calcium phosphate nucleation. Together, these results confirm the successful formation of an appetite layer, enhancing the scaffold's bioactivity and suitability for bone regeneration (He et al., 2023; Kumar et al., 2019).

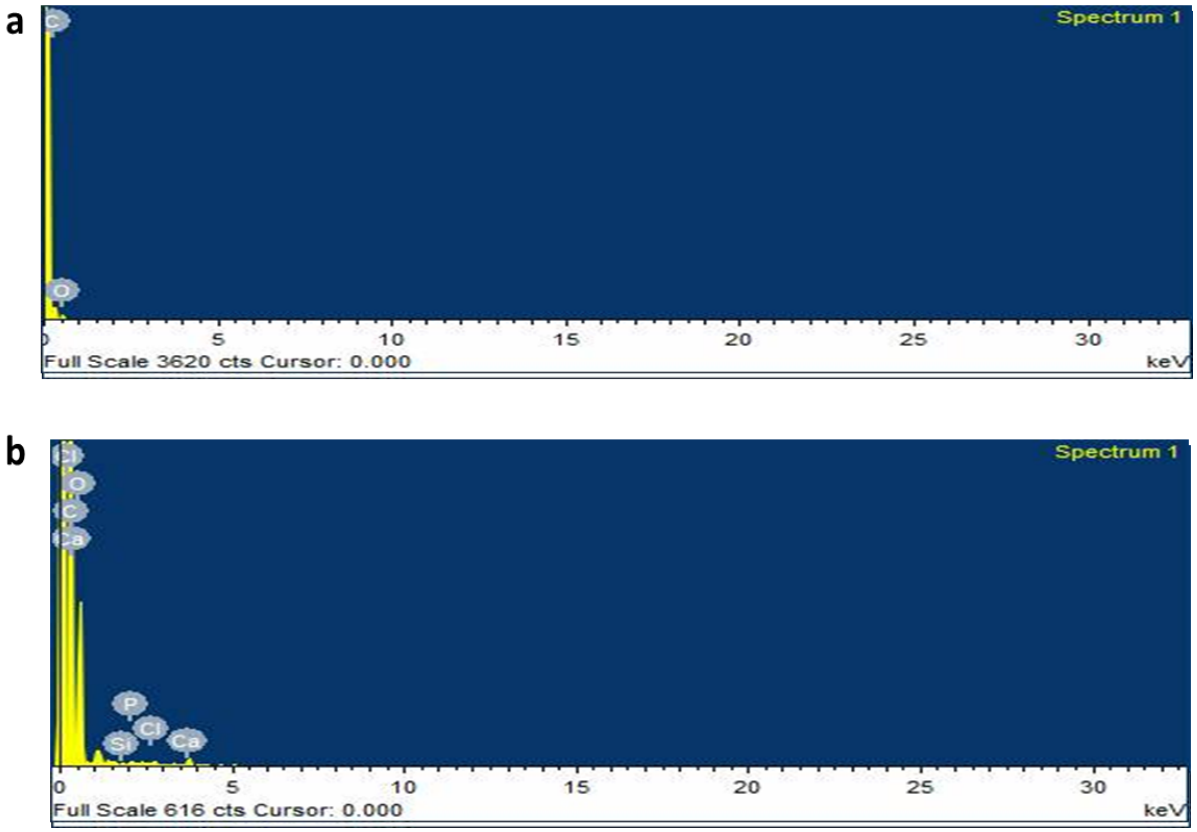


Figure 4.8: EDX of the novel multi-component 3D-printed scaffold **(a)** before immersion in SBF and **(b)** after immersion in SBF for 28 days. The presence of Ca and P can be attributed to the formation of apatite on the surfaces of the scaffolds.

4.4.5. Evaluation of biodegradation and swelling of the Novel Multi-Component 3D-printed Scaffold

Controlled biodegradation is crucial in ensuring the gradual breakdown of scaffold, as new bone tissue forms, maintaining mechanical support during healing. In BTE, it is necessary to achieve a balance between biomineralization and biodegradation to ensure effective bone tissue regeneration and scaffold integration (Gómez-Cerezo et al., 2021; Tupe et al., 2024). The degradation profile **(Figure 4.9)** demonstrates a controlled decrease in scaffold mass over the 30 days, characterized by rapid initial degradation, reducing from 100% at day 0 to approximately 42% by day 5, followed by a slower, stabilized degradation to around 30% at day 10, 26% at day 20, and ultimately reaching approximately 20% by day 30. This initial rapid degradation aligns closely with FTIR, XRD, and EDX data, reflecting early-stage bioactive glass dissolution, calcium and silicate ion release, and initiation of calcium phosphate

nucleation with the formation of a silica-rich layer promoting apatite deposition (Ebrahimi and Sipaut, 2022). The subsequent reduction in degradation rate, particularly after day 10, corresponds to the progressive crystallization of apatite, confirmed by sharper apatite peaks in XRD and prominent Ca and P signals in EDX. The stable apatite mineralization reinforces scaffold integrity, slowing further degradation. This controlled biodegradation, together with successful biomineralization, optimizes scaffold performance for bone regeneration by balancing scaffold resorption with new bone formation (Chen et al., 2021; Hartley et al., 2022).

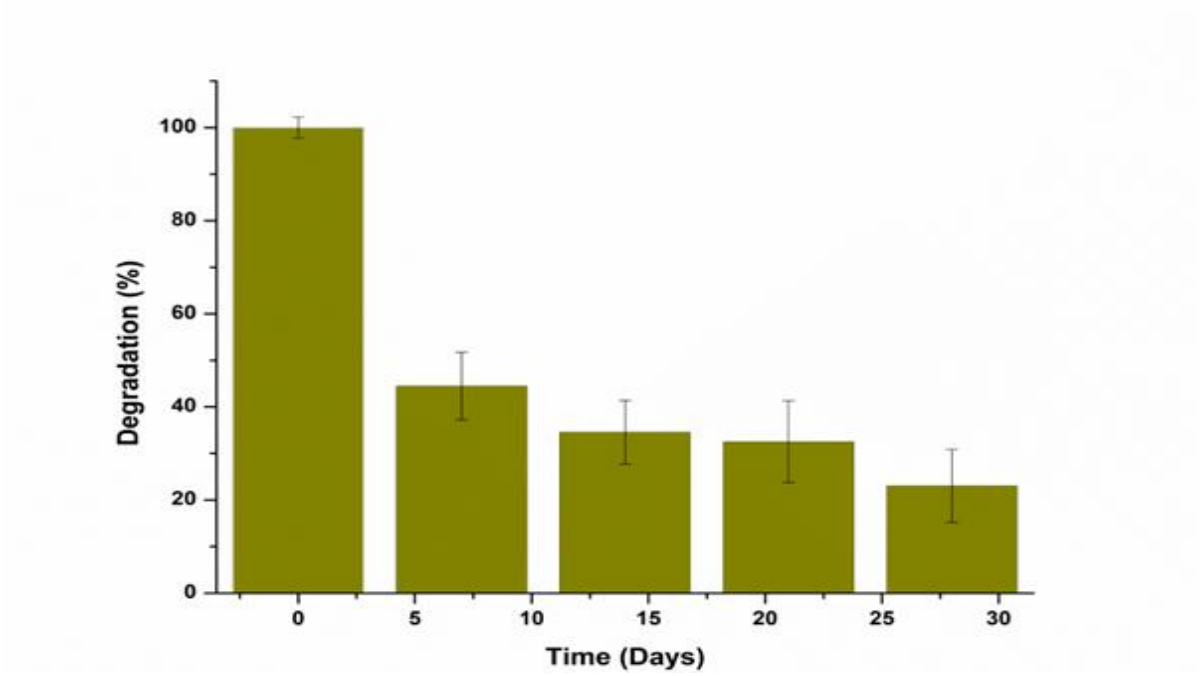


Figure 4.9: Degradation of novel multi-component 3D-printed scaffolds over 30 days.

The swelling rate refers to the reversible fluid uptake influencing scaffold volume, porosity, and cellular activity (Su et al., 2020). Both scaffolds maintained their shape and structural integrity during incubation, with the loaded scaffold **(Figure 4.10 a)** remaining intact until day 10 and the unloaded scaffold **(Figure 4.10 b)** until day 19. However, the unloaded 3D-printed scaffolds displayed a higher swelling ratio compared to the loaded scaffolds, as observed in **Figure 4.10(a,b)**. The presence of BQ-loaded PLGA nanoparticles in the loaded scaffolds restricted water absorption and limited swelling, causing these drug-containing scaffolds to absorb less fluid and maintain a tighter structure with reduced flexibility (Bittner et al., 2021; Su et al., 2020).

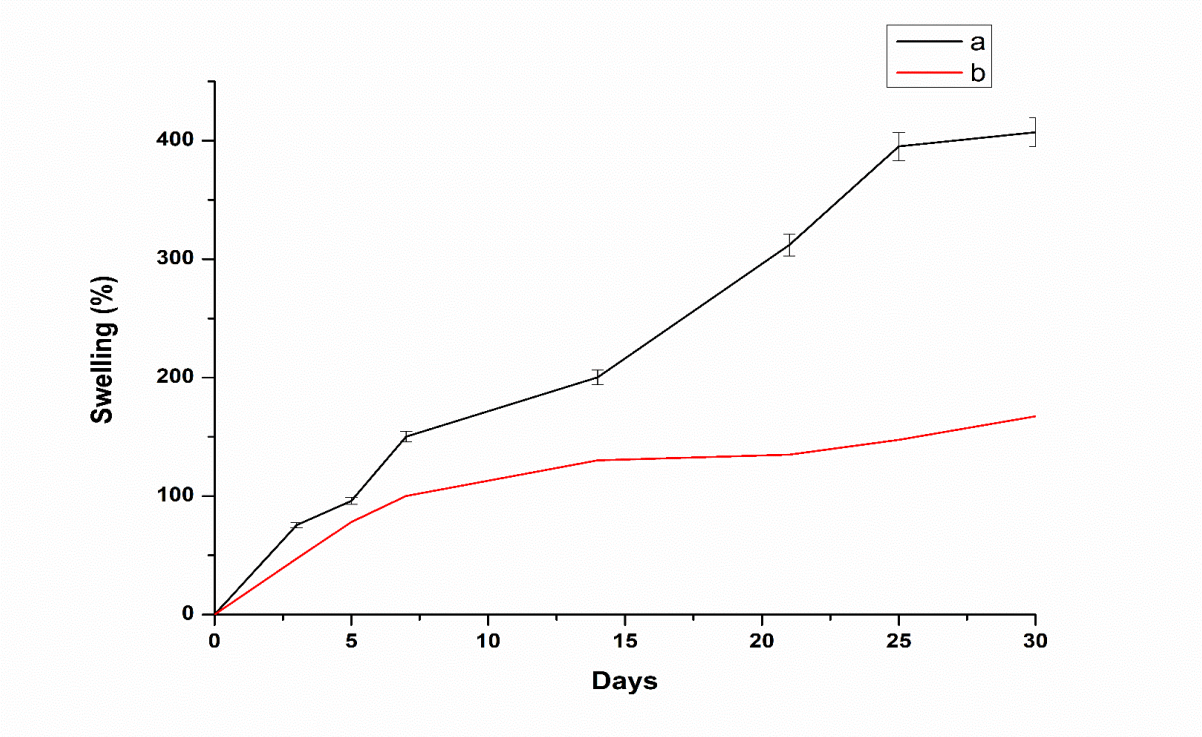


Figure 4.10: Swelling profiles of **(a)** unloaded novel multi-component 3D-printed scaffold and **(b**) drug-loaded novel multi-component 3D-printed scaffold measured over 30 days.

4.4.6. Compressive strength of the novel multi-component 3D-printed scaffold.

The compressive strength of the novel 3D-printed scaffolds was determined using a Texture analyzer and illustrated in **Figure 4.11**. Exposure to physiological fluids can significantly affect the mechanical strength of scaffolds. Consequently, this study examined the changes between the loaded and unloaded 3D-printed scaffold strength following incubation in a culture medium over 24 hours, to better understand the mechanical scaffold performance. To assess the mechanical role of Bioglass Titanium (BGT), an unloaded multi-component scaffold was fabricated without BGT. This allowed direct comparison to isolate BGT's effect as a mechanical enhancer. Known for its bioactivity and ability to improve interfacial bonding and rigidity, the absence of BGT led to a notable drop in compressive strength whichconfirming its critical role in reinforcing the scaffold structure.

The acceptable compressive strength of trabecular bone typically ranges between 2–12 MPa (Zhu et al., 2015). In this study, the unloaded 3D-printed scaffold demonstrated significantly higher compressive strength (7.24 MPa) compared to the

drug-loaded scaffold (4.13 MPa) as shown in **Figure 4.11**. This reduction in mechanical strength in the drug-loaded scaffold is likely attributed to BQ-loaded PLGA nanoparticles, which may have increased the scaffold's porosity, weakening its overall structural integrity. Since higher porosity generally leads to decreased mechanical strength, this structural change likely contributed to the observed difference (Martínez-García et al., 2022; Zhang et al., 2022). In contrast, the unloaded scaffold maintained a denser, uninterrupted structure with a stronger polymer network, resulting in improved compressive strength (Zhang et al., 2022). Both observations are consistent with previous studies, which have similarly reported a reduction in mechanical strength due to increased porosity in drug-loaded systems and enhanced strength in denser, drug-free scaffolds (Amini et al., 2012; Lu et al., 2014; Yekeler et al., 2024).

The incorporation of BGT played a crucial role in reinforcing the mechanical strength of the scaffolds. As evident in **Figure 4.11**, the exclusion of BGT resulted in a significant drop in compressive strength, confirming its structural contribution. Bioglass enhances mechanical stability by forming strong interfacial bonds with the polymer matrix, improving load transfer efficiency, and reducing localized stress concentrations (Fu et al., 2011; Pei et al., 2018). Additionally, titanium provides excellent strength and stiffness, further contributing to the scaffold’s ability to resist compressive forces (Mabrouk et al., 2021; Smith et al., 2021). These synergistic effects of BGT components accounted for the improved mechanical performance observed in the scaffolds.

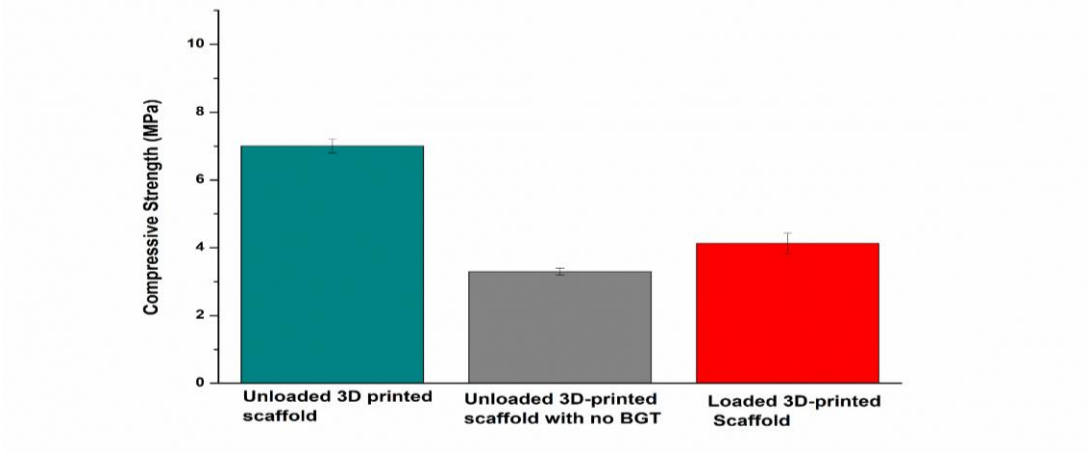


Figure 4.11: Compressive strength (MPa) of various 3D-printed scaffolds.

4.4.7. *In-vitro* drug release of bedaquiline in the novel multi-component 3D-printed scaffold

The release of BQ from the optimized PLGA nanoparticles is illustrated in Chapter 3, where 67±2.68% of the drug was released over 48 hours. The release profile exhibited sustained release characteristics, and the entrapment efficiency (EE%) and drug loading (DL%) were 69.5% and 12.5%, respectively. In this study, we investigated the release profile of BQ loaded into optimized PLGA nanoparticles integrated within the novel multi-component 3D-printed scaffold.

The cumulative BQ release percentages of the 3D-printed scaffold over four weeks **(Figure 12)** showed an extraordinary, sustained release profile. During the initial days, no burst release was observed. This is a positive indication for a sustained release profile, as a burst release is often deemed undesirable due to its associated risk of toxicity from high local concentrations and the potential loss of long-term effectiveness. Between days 10 and 21, approximately 24% of the drug was released, likely attributable to the polymer degradation and subsequent scaffold breakdown. This observation aligns with the swelling study, which indicated that the scaffold maintained structural stability up to day 10 but began to become brittle thereafter. After day 21, the release continued at a slower pace, pointing toward a more gradual, sustained release phase.

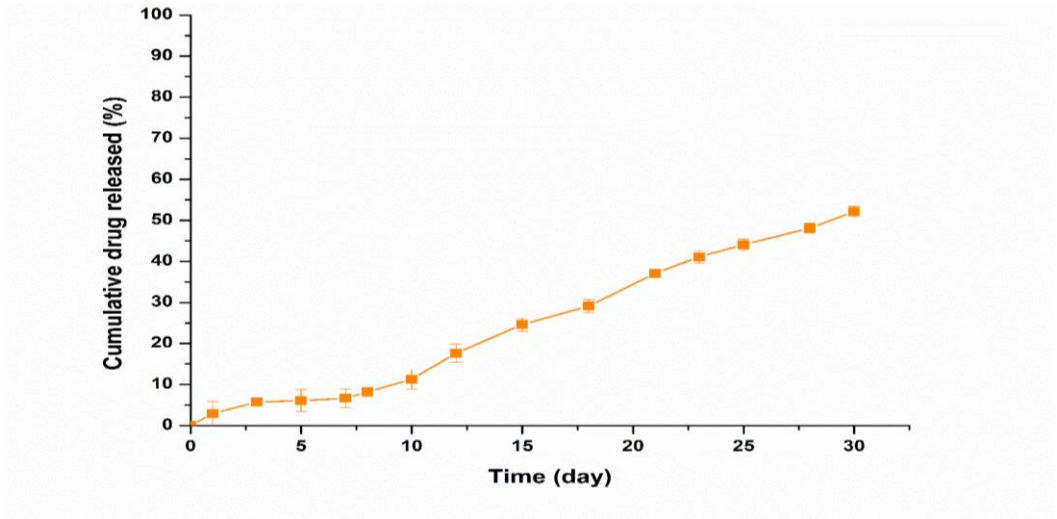


Figure 4.12: *In-vitro* BQ release profile from the 3D-printed scaffold at pH 7.4. Experiment data are presented as the mean ± SD, n = 3.

4.4.8. *In-vitro* cell compatibility of loaded and unloaded novel multi-component 3D-printed scaffold

The in vitro cytocompatibility of the drug-loaded and unloaded novel multicomponent 3D-printed scaffolds was assessed by evaluating the cell viability of osteoblast-like MG63 cells. The MG63 cells were successfully cultured and allowed to differentiate until they reached approximately 90% confluence, as shown in **Figure 4.13**. The cell culture medium served as a negative control, with cell viability set at 100% to provide a reference for comparison with the test samples.

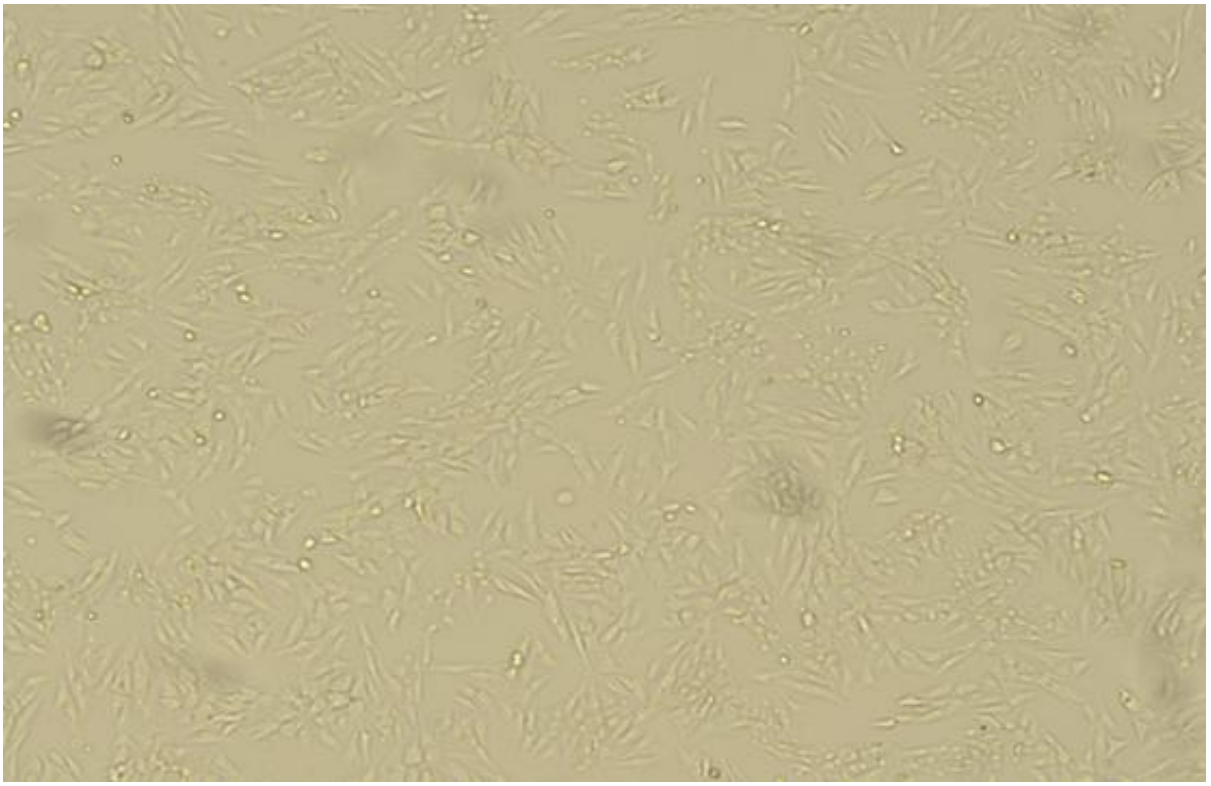


Figure 4.13: Assessment of osteoblast-like MG63 cell differentiation at ~90 confluence.

As shown in **Figure 4.14a**, the MTT assay demonstrates that both unloaded, and drug-loaded 3D-printed scaffolds support high cell viability over the 7-day evaluation period. The results indicate that the differences are statistically significant across all tested days (day 1, day 3, and day 7), with p-values < 0.05. Notably, cells grown on the unloaded scaffolds displayed viability exceeding 140% on day 1, rising to approximately 200% by day 7. Although the drug-loaded scaffolds also exhibited viability well above 100%, their values were slightly lower than those of the unloaded

scaffolds at each time point. This marginal reduction in cell viability could be due to localized drug release, which can transiently modulate cell proliferation or metabolic activity. **Figure 4.14 b,c** shows SEM images SEM images of loaded and unloaded 3D-printed scaffolds after 7 days of culture with osteoblast-like MG63 cells, demonstrating the scaffolds' ability to support cellular attachment and growth.

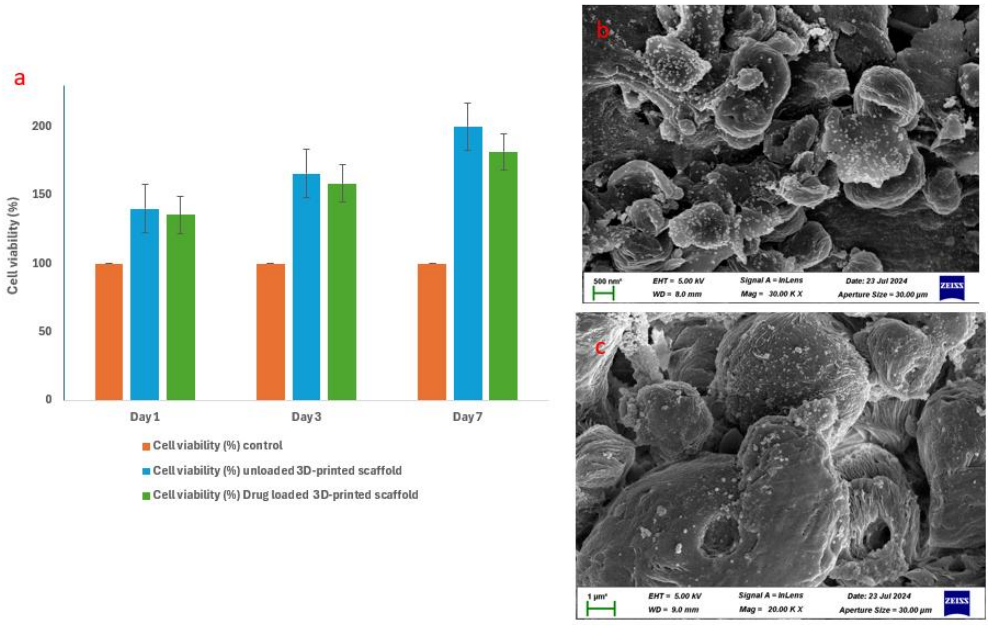


Figure 4.14: (a) Viability of osteoblast-like MG63 cells, assessed using an MTT assay, in the presence of the optimal drug-free and drug-loaded 3D-printed scaffolds. **(b, c**) SEM images of the unloaded and loaded 3D-printed scaffolds, respectively, after 7 days of culture with osteoblast-like MG63 cells.

4.5. Concluding Remarks

In this chapter, a novel multi-component 3D printed scaffold composed of bioactive glass titanium, polycaprolactone, polyvinyl alcohol, and sodium alginate was successfully developed for localized bone TB therapy. The scaffold demonstrated excellent printability, a tailored porous architecture, clinically relevant mechanical strength, and a well-controlled biodegradation profile. Incorporating bedaquiline loaded PLGA nanoparticles achieved a sustained drug release pattern, effectively mitigating burst release. Furthermore, the scaffold promoted robust MG63 osteoblast like cell viability, indicating its biocompatibility and potential for bone regeneration.

Chapter 5 will detail the i*n vivo* animal studies undertaken to further assess the safety, efficacy, and therapeutic potential of this scaffold under physiologically relevant conditions. This is a critical step for validating its clinical promise in bone TB therapy and advancing its potential for real-world applications**.**

4.6. References

Alaribe, F.N., Manoto, S.L., Motaung, S.C.K.M., 2016. Scaffolds from biomaterials: advantages and limitations in bone and tissue engineering. Biologia (Bratisl.) 71, 353–366. https://doi.org/10.1515/biolog-2016-0056

Amini, A.R., Adams, D.J., Laurencin, C.T., Nukavarapu, S.P., 2012. Optimally porous and biomechanically compatible scaffolds for large-area bone regeneration. Tissue Eng. Part A 18, 1376–1388. https://doi.org/10.1089/ten.tea.2011.0076

Arefin, A.M.E., Khatri, N.R., Kulkarni, N., Egan, P.F., 2021. Polymer 3D printing review: materials, process, and design strategies for medical applications. Polymers 13, 1499. https://doi.org/10.3390/polym13091499

Baptista, R., Guedes, M., 2021. Porosity and pore design influence on fatigue behavior of 3D printed scaffolds for trabecular bone replacement. J. Mech. Behav. Biomed. Mater. 117, 104378. https://doi.org/10.1016/j.jmbbm.2021.104378

Bardestani, R., Patience, G.S., Kaliaguine, S., 2019. Experimental methods in chemical engineering: specific surface area and pore size distribution measurements—BET, BJH, and DFT. Can. J. Chem. Eng. 97, 2781–2791. https://doi.org/10.1002/cjce.23632

Bittner, S.M., Pearce, H.A., Hogan, K.J., Smoak, M.M., Guo, J.L., Melchiorri, A.J., Scott, D.W., Mikos, A.G., 2021. Swelling behaviors of 3d printed hydrogel and hydrogel-microcarrier composite scaffolds. Tissue Eng. Part A 27, 665–678. https://doi.org/10.1089/ten.tea.2020.0377

Calore, A.R., Srinivas, V., Anand, S., Albillos-Sanchez, A., Looijmans, S.F.S.P., van Breemen, L.C.A., Mota, C., Bernaerts, K., Harings, J.A.W., Moroni, L., 2021. Shaping and properties of thermoplastic scaffolds in tissue regeneration: The effect of thermal history on polymer crystallization, surface characteristics and cell fate. J. Mater. Res. 36, 3914–3935. https://doi.org/10.1557/s43578-021-00403-2

Chen, H., Shi, Q., Shui, H., Wang, P., Chen, Q., Li, Z., 2021. Degradation of 3D-printed porous polylactic acid scaffolds under mechanical stimulus. Front. Bioeng. Biotechnol. 9, 691834. https://doi.org/10.3389/fbioe.2021.691834

Cuadros, T.R., Erices, A.A., Aguilera, J.M., 2015. Porous matrix of calcium alginate/gelatin with enhanced properties as scaffold for cell culture. J. Mech. Behav. Biomed. Mater. 46, 331–342. https://doi.org/10.1016/j.jmbbm.2014.08.026

Diaz-Gomez, L., Gonzalez-Prada, I., Millan, R., Da Silva-Candal, A., Bugallo-Casal, A., Campos, F., Concheiro, A., Alvarez-Lorenzo, C., 2022. 3D printed carboxymethyl cellulose scaffolds for autologous growth factors delivery in wound healing. Carbohydr. Polym. 278, 118924. https://doi.org/10.1016/j.carbpol.2021.118924

Distler, T., Fournier, N., Grünewald, A., Polley, C., Seitz, H., Detsch, R., Boccaccini, A.R., 2020. Polymer-bioactive glass composite filaments for 3d scaffold manufacturing by fused deposition modeling: fabrication and characterization. Front. Bioeng. Biotechnol. 8.

Do, A.-V., Khorsand, B., Geary, S.M., Salem, A.K., 2015. 3D-Printing of scaffolds for tissue regeneration applications. Adv. Healthc. Mater. 4, 1742–1762. https://doi.org/10.1002/adhm.201500168

Dvorakova, J., Wiesnerova, L., Chocholata, P., Kulda, V., Landsmann, L., Cedikova, M., Kripnerova, M., Eberlova, L., Babuska, V., 2023. Human cells with osteogenic potential in bone tissue research. Biomed. Eng. OnLine 22, 33. https://doi.org/10.1186/s12938-023-01096-w

Ebrahimi, S., Sipaut, C.S., 2022. Synthesis of hydroxyapatite/bioglass composite nanopowder using design of experiments. Nanomaterials 12, 2264. https://doi.org/10.3390/nano12132264

Ferreira, M.R.L., Bonfim, R.O., Bossonario, P.A., Maurin, V.P., Valença, A.B.M., Abreu, P.D. de, Andrade, R.L. de P., Fronteira, I., Monroe, A.A., 2023. Social protection as a right of people affected by tuberculosis: a scoping review and conceptual framework. Infect. Dis. Poverty 12, 103. https://doi.org/10.1186/s40249-023-01157-1

Foster, N., Vassall, A., Cleary, S., Cunnama, L., Churchyard, G., Sinanovic, E., 2015. The economic burden of TB diagnosis and treatment in South Africa. Soc. Sci. Med. 130, 42–50. https://doi.org/10.1016/j.socscimed.2015.01.046

Fu, Q., Saiz, E., Rahaman, M.N., Tomsia, A.P., 2011. Bioactive glass scaffolds for bone tissue engineering: state of the art and future perspectives. Mater. Sci. Eng. C Mater. Biol. Appl. 31, 1245–1256. https://doi.org/10.1016/j.msec.2011.04.022

Gómez-Cerezo, M.N., Peña, J., Ivanovski, S., Arcos, D., Vallet-Regí, M., Vaquette, C., 2021. Multiscale porosity in mesoporous bioglass 3D-printed scaffolds for bone regeneration. Mater. Sci. Eng. C 120, 111706. https://doi.org/10.1016/j.msec.2020.111706

Gong, X., Liang, Z., Yang, Y., Liu, H., Ji, J., Fan, Y., 2020. A resazurin-based, nondestructive assay for monitoring cell proliferation during a scaffold-based 3D culture process. Regen. Biomater. 7, 271–281. https://doi.org/10.1093/rb/rbaa002

Govender, M., Indermun, S., Kumar, P., Choonara, Y.E., Pillay, V., 2018. 3D-printed, pva–paa hydrogel loaded-polycaprolactone scaffold for the delivery of hydrophilic in-situ formed sodium indomethacin. Materials 11, 1006. https://doi.org/10.3390/ma11061006

Haleem, A., Javaid, M., Khan, R.H., Suman, R., 2020. 3D printing applications in bone tissue engineering. J. Clin. Orthop. Trauma 11, S118–S124. https://doi.org/10.1016/j.jcot.2019.12.002

Han, Q., Wang, C., Chen, H., Zhao, X., Wang, J., 2019. Porous tantalum and titanium in orthopedics: a review. ACS Biomater. Sci. Eng. 5, 5798–5824. https://doi.org/10.1021/acsbiomaterials.9b00493

Hartley, E., Moon, H., Neves, A., 2022. Biodegradable synthetic polymers for tissue engineering: a mini review. Reinvention Int. J. Undergrad. Res. 15. https://doi.org/10.31273/reinvention.v15i1.801

Hasan, A., Bagnol, R., Owen, R., Latif, A., Rostam, H.M., Elsharkawy, S., Rose, F.R.A.J., Rodríguez-Cabello, J.C., Ghaemmaghami, A.M., Eglin, D., Mata, A., 2022. Mineralizing coating on 3d printed scaffolds for the promotion of osseointegration. Front. Bioeng. Biotechnol. 10, 836386. https://doi.org/10.3389/fbioe.2022.836386

He, L., Yin, J., Gao, X., 2023. Additive manufacturing of bioactive glass and its polymer composites as bone tissue engineering scaffolds: a review. Bioengineering 10, 672. https://doi.org/10.3390/bioengineering10060672

Heo, E.Y., Ko, N.R., Bae, M.S., Lee, S.J., Choi, B.-J., Kim, J.H., Kim, H.K., Park, S.A., Kwon, I.K., 2017. Novel 3D printed alginate–BFP1 hybrid scaffolds for enhanced bone regeneration. J. Ind. Eng. Chem. 45, 61–67. https://doi.org/10.1016/j.jiec.2016.09.003

Ji, J., Zhao, C., Hua, C., Lu, L., Pang, Y., Sun, W., 2024. 3D Printing cervical implant scaffolds incorporated with drug-loaded carboxylated chitosan microspheres for long-term anti-hpv protein delivery. ACS Biomater. Sci. Eng. 10, 1544–1553. https://doi.org/10.1021/acsbiomaterials.3c01594

Jin Lee, S., Lee, H.-J., Kim, S.-Y., Min Seok, J., Hee Lee, J., Doo Kim, W., Keun Kwon, I., Park, S.-Y., A Park, S., 2018. In situ gold nanoparticle growth on polydopamine-coated 3D-printed scaffolds improves osteogenic differentiation for bone tissue engineering applications: in vitro and in vivo studies. Nanoscale 10, 15447–15453. https://doi.org/10.1039/C8NR04037K

Kim, H., Yang, G.H., Choi, C.H., Cho, Y.S., Kim, G., 2018. Gelatin/PVA scaffolds fabricated using a 3D-printing process employed with a low-temperature plate for hard tissue regeneration: Fabrication and characterizations. Int. J. Biol. Macromol. 120, 119–127. https://doi.org/10.1016/j.ijbiomac.2018.07.159

Kokubo, T., Takadama, H., 2006. How useful is SBF in predicting in vivo bone bioactivity? Biomaterials 27, 2907–2915. https://doi.org/10.1016/j.biomaterials.2006.01.017

Kondiah, P.J., Choonara, Y.E., Kondiah, P.P.D., Kumar, P., Marimuthu, T., du Toit, L.C., Pillay, V., 2017. Development of an injectable pseudo-bone thermo-gel for application in small bone fractures. Int. J. Pharm. 520, 39–48. https://doi.org/10.1016/j.ijpharm.2017.01.039

Kumar, A., Kargozar, S., Baino, F., Han, S.S., 2019. Additive manufacturing methods for producing hydroxyapatite and hydroxyapatite-based composite scaffolds: a review. Front. Mater. 6.

Lapczyna, H., Galea, L., Wüst, S., Bohner, M., Jerban, S., Sweedy, A., Doebelin, N., Van Garderen, N., Hofmann, S., Baroud, G., Müller, R., Von Rechenberg, B., 2014. Effect of grain size and microporosity on the in vivo behaviour of β-tricalcium phosphate scaffolds. Eur. Cell. Mater. 28, 299–319. https://doi.org/10.22203/eCM.v028a21

Loh, Q.L., Choong, C., 2013. Three-dimensional scaffolds for tissue engineering applications: role of porosity and pore size. Tissue Eng. Part B Rev. 19, 485–502. https://doi.org/10.1089/ten.teb.2012.0437

Lopez-Fontal, E., Gin, S., 2025. Insights into calcium phosphate formation induced by the dissolution of 45s5 bioactive glass. ACS Biomater. Sci. Eng. 11, 875–890. https://doi.org/10.1021/acsbiomaterials.4c01680

Łopianiak, I., Butruk-Raszeja, B.A., 2020. Evaluation of sterilization/disinfection methods of fibrous polyurethane scaffolds designed for tissue engineering applications. Int. J. Mol. Sci. 21, 8092. https://doi.org/10.3390/ijms21218092

Lu, L., Zhang, Q., Wootton, D.M., Chiou, R., Li, D., Lu, B., Lelkes, P.I., Zhou, J., 2014. Mechanical study of polycaprolactone-hydroxyapatite porous scaffolds created by porogen-based solid freeform fabrication method. j. appl. Biomater. Funct. Mater. 12, 145–154. https://doi.org/10.5301/jabfm.5000163

Mabrouk, M., Beherei, H.H., Tanaka, Y., Tanaka, M., 2021. Investigating the intermediate water feature of hydrated titanium containing bioactive glass. Int. J. Mol. Sci. 22, 8038. https://doi.org/10.3390/ijms22158038

Mabrouk, M., ElShebiney, S.A., Kenawy, S.H., El-Bassyouni, G.T., Hamzawy, E.M., 2019. Novel, cost-effective, Cu-doped calcium silicate nanoparticles for bone fracture intervention: Inherent bioactivity and in vivo performance. J. Biomed. Mater. Res. B Appl. Biomater. 107, 388–399. https://doi.org/10.1002/jbm.b.34130

Mabrouk, M., Mostafa, A.A., Oudadesse, H., Mahmoud, A.A., El-Gohary, M.I., 2014. Effect of ciprofloxacin incorporation in PVA and PVA bioactive glass composite scaffolds. Ceram. Int. 40, 4833–4845. https://doi.org/10.1016/j.ceramint.2013.09.033

Madorsky, S.L., Straus, S., 1959. Thermal degradation of polymers at high temperatures. J. Res. Natl. Bur. Stand. Sect. Phys. Chem. 63A, 261–268. https://doi.org/10.6028/jres.063A.020

Mahdy, E.A., Sahbal, K.M., Mostafa Mabrouk, Beherei, H.H., Abdel-Monem, Y.K., 2021. Enhancement of glass-ceramic performance by TiO2 doping: In vitro cell viability, proliferation, and differentiation. Ceram. Int. 47, 6251–6261. https://doi.org/10.1016/j.ceramint.2020.10.203

Martin, V., Ribeiro, I.A., Alves, M.M., Gonçalves, L., Claudio, R.A., Grenho, L., Fernandes, M.H., Gomes, P., Santos, C.F., Bettencourt, A.F., 2019. Engineering a multifunctional 3D-printed PLA-collagen-minocycline-nanoHydroxyapatite scaffold with combined antimicrobial and osteogenic

effects for bone regeneration. Mater. Sci. Eng. C 101, 15–26. https://doi.org/10.1016/j.msec.2019.03.056

Martínez-García, R., Sánchez de Rojas, M.I., Jagadesh, P., López-Gayarre, F., Morán-del-Pozo, J.M., Juan-Valdes, A., 2022. Effect of pores on the mechanical and durability properties on high strength recycled fine aggregate mortar. Case Stud. Constr. Mater. 16, e01050. https://doi.org/10.1016/j.cscm.2022.e01050

Mirhadi, S.M., Hassanzadeh Nemati, N., Tavangarian, F., Daliri Joupari, M., 2018. Fabrication of hierarchical meso/macroporous TiO2 scaffolds by evaporation-induced self-assembly technique for bone tissue engineering applications. Mater. Charact. 144, 35–41. https://doi.org/10.1016/j.matchar.2018.06.035

Mndlovu, H., du Toit, L.C., Kumar, P., Marimuthu, T., Kondiah, P.P.D., Choonara, Y.E., Pillay, V., 2019. Development of a fluid-absorptive alginate-chitosan bioplatform for potential application as a wound dressing. Carbohydr. Polym. 222, 114988. https://doi.org/10.1016/j.carbpol.2019.114988

Mphaphuli, M.T., Sithole, M.N., Kumar, P., Kondiah, P.P.D., Mabrouk, M., Choonara, Y.E., 2023. Multi-purpose prototypes for extrapulmonary *Mycobacterium tuberculosis* targeting: A regenerative medicine perspective. J. Drug Deliv. Sci. Technol. 89, 105039. https://doi.org/10.1016/j.jddst.2023.105039

Nidoi, J., Muttamba, W., Walusimbi, S., Imoko, J.F., Lochoro, P., Ictho, J., Mugenyi, L., Sekibira, R., Turyahabwe, S., Byaruhanga, R., Putoto, G., Villa, S., Raviglione, M.C., Kirenga, B., 2021. Impact of socio-economic factors on Tuberculosis treatment outcomes in north-eastern Uganda: a mixed methods study. BMC Public Health 21, 2167. https://doi.org/10.1186/s12889-021-12056-1

Nikolova, M.P., Chavali, M.S., 2019a. Recent advances in biomaterials for 3D scaffolds: A review. Bioact. Mater. 4, 271–292. https://doi.org/10.1016/j.bioactmat.2019.10.005

Nikolova, M.P., Chavali, M.S., 2019b. Recent advances in biomaterials for 3D scaffolds: A review. Bioact. Mater. 4, 271–292. https://doi.org/10.1016/j.bioactmat.2019.10.005

Ogueri, K.S., Jafari, T., Escobar Ivirico, J.L., Laurencin, C.T., 2019. POLYMERIC BIOMATERIALS FOR SCAFFOLD-BASED BONE REGENERATIVE ENGINEERING. Regen. Eng. Transl. Med. 5, 128–154. https://doi.org/10.1007/s40883-018-0072-0

Pandita, A., Madhuripan, N., Pandita, S., Hurtado, R.M., 2020. Challenges and controversies in the treatment of spinal tuberculosis. J. Clin. Tuberc. Mycobact. Dis. 19, 100151. https://doi.org/10.1016/j.jctube.2020.100151

Pei, P., Tian, Z., Zhu, Y., 2018. 3D printed mesoporous bioactive glass/metal-organic framework scaffolds with antitubercular drug delivery. Microporous

Mesoporous Mater. 272, 24–30. https://doi.org/10.1016/j.micromeso.2018.06.012

Pigrau-Serrallach, C., 2013. Bone and joint tuberculosis. Eur. Spine J. 22, 556–566. https://doi.org/10.1007/s00586-012-2331-y

Rezania, N., Asadi-Eydivand, M., Abolfathi, N., Bonakdar, S., Mehrjoo, M., Solati-Hashjin, M., 2022. Three-dimensional printing of polycaprolactone/hydroxyapatite bone tissue engineering scaffolds mechanical properties and biological behavior. J. Mater. Sci. Mater. Med. 33, 31. https://doi.org/10.1007/s10856-022-06653-8

Ruparel, S., Tanaka, M., Mehta, R., Yamauchi, T., Oda, Y., Sonawane, S., Chaddha, R., 2022. Surgical management of spinal tuberculosis—the past, present, and future. Diagnostics 12, 1307. https://doi.org/10.3390/diagnostics12061307

Shah, F.A., Czechowska, J., 2018. 9 - Bioactive glass and glass-ceramic scaffolds for bone tissue engineering, in: Ylänen, H. (Ed.), Bioactive glasses (second edition), woodhead publishing series in biomaterials. Woodhead Publishing, pp. 201–233. https://doi.org/10.1016/B978-0-08-100936-9.00011-3

She, Y., Fan, Z., Wang, L., Li, Y., Sun, W., Tang, H., Zhang, L., Wu, L., Zheng, H., Chen, C., 2021. 3D Printed biomimetic pcl scaffold as framework interspersed with collagen for long segment tracheal replacement. Front. Cell Dev. Biol. 9.

Sithole, M.N., Kumar, P., du Toit, L.C., Marimuthu, T., Choonara, Y.E., Pillay, V., 2018. A 3D bioprinted in situ conjugated-co-fabricated scaffold for potential bone tissue engineering applications. J. Biomed. Mater. Res. A 106, 1311–1321. https://doi.org/10.1002/jbm.a.36333

Smith, S., ElKashty, O., Tamimi, F., Tran, S.D., Cerruti, M., 2021. Titanium-containing silicate-based sol–gel bioactive glass: development, characterization, and applications. Langmuir 37, 14243–14253. https://doi.org/10.1021/acs.langmuir.1c01593

Su, X., Chen, L., Han, S., Niu, G., Ren, J., Ke, C., 2020. Preparation and characterization of a novel triple composite scaffold containing silk fiborin, chitosan, and alginate for 3d culture of colonic carcinoma cells in vitro. med. Sci. Monit. Int. Med. J. Exp. Clin. Res. 26, e922935-1-e922935-17. https://doi.org/10.12659/MSM.922935

Tavakoli, M., Salehi, H., Emadi, R., Varshosaz, J., Labbaf, S., Seifalian, A.M., Sharifianjazi, F., Mirhaj, M., 2024. 3D printed polylactic acid-based nanocomposite scaffold stuffed with microporous simvastatin-loaded polyelectrolyte for craniofacial reconstruction. Int. J. Biol. Macromol. 258, 128917. https://doi.org/10.1016/j.ijbiomac.2023.128917

Tohamy, K.M., Mabrouk, M., Soliman, I.E., Beherei, H.H., Aboelnasr, M.A., 2018. Novel alginate/hydroxyethyl cellulose/hydroxyapatite composite scaffold for bone regeneration: *In-vitro* cell viability and proliferation of human

mesenchymal stem cells. Int. J. Biol. Macromol. 112, 448–460. https://doi.org/10.1016/j.ijbiomac.2018.01.181

Tupe, A., Patole, V., Ingavle, G., Kavitkar, G., Mishra Tiwari, R., Kapare, H., Baheti, R., Jadhav, P., 2024. Recent advances in biomaterial-based scaffolds for guided bone tissue engineering: challenges and future directions. Polym. Adv. Technol. 35, e6619. https://doi.org/10.1002/pat.6619

Turnbull, G., Clarke, J., Picard, F., Riches, P., Jia, L., Han, F., Li, B., Shu, W., 2018. 3D bioactive composite scaffolds for bone tissue engineering. Bioact. Mater. 3, 278–314. https://doi.org/10.1016/j.bioactmat.2017.10.001

Uma Maheshwari, S., Samuel, V.K., Nagiah, N., 2014. Fabrication and evaluation of (PVA/HAp/PCL) bilayer composites as potential scaffolds for bone tissue regeneration application. Ceram. Int. 40, 8469–8477. https://doi.org/10.1016/j.ceramint.2014.01.058

Valido, D.P., Júnior, W.D.G., de Andrade, M.E., Rezende, A.A., de Andrade de Carvalho, F.M., de Lima, R., das Graças Gomes Trindade, G., de Alcântara Campos, C., Oliveira, A.M.S., de Souza, E.P.B.S.S., Frank, L.A., Guterres, S.S., Sussuchi, E.M., Matos, C.R.S., Polloni, A., de Souza Araújo, A.A., Padilha, F.F., Severino, P., Souto, E.B., de Albuquerque Júnior, R.L.C., 2020. Otoliths-composed gelatin/sodium alginate scaffolds for bone regeneration. Drug Deliv. Transl. Res. 10, 1716–1728. https://doi.org/10.1007/s13346-020-00845-x

Xu, Z., Wang, N., Ma, Y., Dai, H., Han, B., 2022. Preparation and study of 3D printed dipyridamole/β-tricalcium phosphate/ polyvinyl alcohol composite scaffolds in bone tissue engineering. J. Drug Deliv. Sci. Technol. 68, 103053. https://doi.org/10.1016/j.jddst.2021.103053

Yazdanpanah, Z., Johnston, J.D., Cooper, D.M.L., Chen, X., 2022. 3D Bioprinted Scaffolds for Bone Tissue Engineering: State-Of-The-Art and Emerging Technologies. Front. Bioeng. Biotechnol. 10.

Yekeler, H.B., Guler, E., Beato, P.S., Priya, S., Abobakr, F.K.M., Dogan, M., Uner, B., Kalaskar, D.M., Cam, M.E., 2024. Design and *in-vitro* evaluation of curcumin-loaded PLGA nanoparticle-embedded sodium alginate/gelatin 3D printed scaffolds for Alzheimer's disease. Int. J. Biol. Macromol. 268, 131841. https://doi.org/10.1016/j.ijbiomac.2024.131841

Yoo, J.-W., Irvine, D.J., Discher, D.E., Mitragotri, S., 2011. Bio-inspired, bioengineered and biomimetic drug delivery carriers. Nat. Rev. Drug Discov. 10, 521–535. https://doi.org/10.1038/nrd3499

Yuan, J., Zhen, P., Zhao, H., Chen, K., Li, X., Gao, M., Zhou, J., Ma, X., 2015. The preliminary performance study of the 3D printing of a tricalcium phosphate scaffold for the loading of sustained release anti-tuberculosis drugs. J. Mater. Sci. 50, 2138–2147. https://doi.org/10.1007/s10853-014-8776-0

Zhang, B., Wang, L., Song, P., Pei, X., Sun, H., Wu, L., Zhou, C., Wang, K., Fan, Y., Zhang, X., 2021. 3D printed bone tissue regenerative PLA/HA scaffolds with comprehensive performance optimizations. Mater. Des. 201, 109490. https://doi.org/10.1016/j.matdes.2021.109490

Zhang, W., Shi, W., Wu, S., Kuss, M., Jiang, X., Untrauer, J.B., Reid, S.P., Duan, B., 2020. 3D printed composite scaffolds with dual small molecule delivery for mandibular bone regeneration. Biofabrication 12, 035020. https://doi.org/10.1088/1758-5090/ab906e

Zhang, Y., Sun, N., Zhu, M., Qiu, Q., Zhao, P., Zheng, C., Bai, Q., Zeng, Q., Lu, T., 2022. The contribution of pore size and porosity of 3D printed porous titanium scaffolds to osteogenesis. Biomater. Adv. 133, 112651. https://doi.org/10.1016/j.msec.2022.112651

Zhou, Z., Yao, Q., Li, L., Zhang, X., Wei, B., Yuan, L., Wang, L., 2018. Antimicrobial activity of 3d-printed poly(ε-caprolactone) (pcl) composite scaffolds presenting vancomycin-loaded polylactic acid-glycolic acid (plga) microspheres. Med. Sci. Monit. Int. Med. J. Exp. Clin. Res. 24, 6934–6945. https://doi.org/10.12659/MSM.911770

Zhu, M., Li, K., Zhu, Y., Zhang, J., Ye, X., 2015. 3D-printed hierarchical scaffold for localized isoniazid/rifampin drug delivery and osteoarticular tuberculosis therapy. Acta Biomater. 16, 145–155. https://doi.org/10.1016/j.actbio.2015.01.034

Zhu, W., Ma, X., Gou, M., Mei, D., Zhang, K., Chen, S., 2016. 3D printing of functional biomaterials for tissue engineering. Curr. Opin. Biotechnol., Tissue, cell & pathway engineering (2016) 40, 103–112. https://doi.org/10.1016/j.copbio.2016.03.014

CHAPTER 5

IN-VIVO EVALUATION OF THE NOVEL MULTI-COMPONENT 3D-PRINTED SCAFFOLD EMBEDDED WITH BQ-LOADED PLGA NANOPARTICLES FOR BONE TUBERCULOSIS THERAPY.

The In vivo study received approval from the University of the Witwatersrand's Animal Research Ethics Committee (AREC), clearance certificate number 2309004C (see Appendix B).

5.1. Introduction

Bone tuberculosis (TB), a form of extrapulmonary TB caused by *Mycobacterium tuberculosis*, remains a significant clinical concern due to its complex pathology and the prolonged duration of treatment required (Garg and Goyal, 2020; Hegazy et al., 2021; Mphaphuli et al., 2023). Conventional systemic chemotherapy is often inadequate for eradicating the infection within the dense and poorly vascularized bone environment, leading to high relapse rates and the potential emergence of drug-resistant strains (Luo et al., 2024). Consequently, the development of localized drug delivery systems that can consistently achieve therapeutic concentrations of anti-TB agents at the lesion site has become a critical objective in orthopedic and infectious disease research.

Recent studies have demonstrated a growing interest in the integration of nanotechnology and three-dimensional (3D) printing for the management of bone tuberculosis, underscoring the clinical relevance and translational potential of such multifunctional therapeutic platforms (Luo et al., 2024; Vinogradova et al., 2023; Yahia et al., 2023). 3D printing enables the fabrication of scaffolds with patient-specific geometries and tailored pore architectures conducive to bone regeneration (Bose et al., 2013). Furthermore, Hua et al. (2022) reported the successful development of 3D printed porous tantalum scaffolds coated with antitubercular agents, which exhibited effective antibacterial activity and favourable biocompatibility, demonstrating the viability of embedding therapeutic agents within metallic scaffolds for localized infection control. In alignment with these advances, the present study introduces a novel multi-component 3D printed scaffold embedded with bedaquiline (BQ) loaded PLGA nanoparticles designed to provide both osteoconductive support and sustained,

localized anti-TB drug release. Using a rabbit critical sized femoral defect model, selected for its clinical relevance to skeletal TB, the scaffold's bone-regenerative capacity and therapeutic performance were assessed by comparing drug-loaded and drug-free variants. This approach aims to establish a dual-function biomaterial capable of promoting functional bone repair while delivering targeted antimycobacterial therapy at the defect site.

5.2. Materials and Methods

5.2.1. Materials

Ketamine HCL (a dissociative anesthetic) and lignocaine were purchased from Bayer (Pty) Ltd Animal Health Div (Wrench, Isando, SA). Xylazine HCl (sedation, anesthesia, muscle relaxation, and analgesia) was purchased from in vervet S.A. (Pty) Ltd. (Isando, SA), sodium pentobarbitone, antisedan, meloxican were purchased from Dechra Veterinary Products Limited (Hadnall, Shrewsbury, UK) and temgesic® was purchased from Mundipharma (Pty) Ltd. (Claremont, Cape Town, SA). Fetal bovine serum (FBS; Biochrom, Berlin, Germany), dulbecco's modified eagle's medium (DMEM), bone morphogenic protein 7 (Osteogenicprotein 1) were purchased from Sigma-Aldrich (St. Louis, MO, USA). All other reagents were of standard analytical grade and were used as procured.

5.2.2. Animal welfare, housing, and habituation before study experiment

Prior to the main experiment, a pilot study was conducted with a smaller cohort of New Zealand White rabbits to optimize and confirm the overall methodology. Insights gained from this preliminary phase informed the design and execution of the full experimental study, including refinements to animal handling techniques, scaffold implantation procedures, and data collection protocols.

For the experimental study, twenty-eight male New Zealand White rabbits (12–16 weeks old, weighing 2.5–3.0 kg) were sourced from the University of the Witwatersrand Central Animal Service (CAS) unit. As depicted in **Figure 5.1(a–b),** each rabbit was housed individually in a separate cage, maintained under a 12-hour light/12-hour dark cycle. A seven-day habituation process was implemented under the supervision of trained CAS staff and the researcher to acclimate the animals to their

environment and handling routines. This daily habituation involved twice-daily visits, ensuring the rabbits' food and water were sufficient, and routine weighing before the surgical procedure and throughout the study. Such acclimatization minimizes stress and facilitates smoother surgical interventions. Environmental enrichments were provided according to CAS standard operating procedures, further ensuring optimal animal welfare and study conditions.

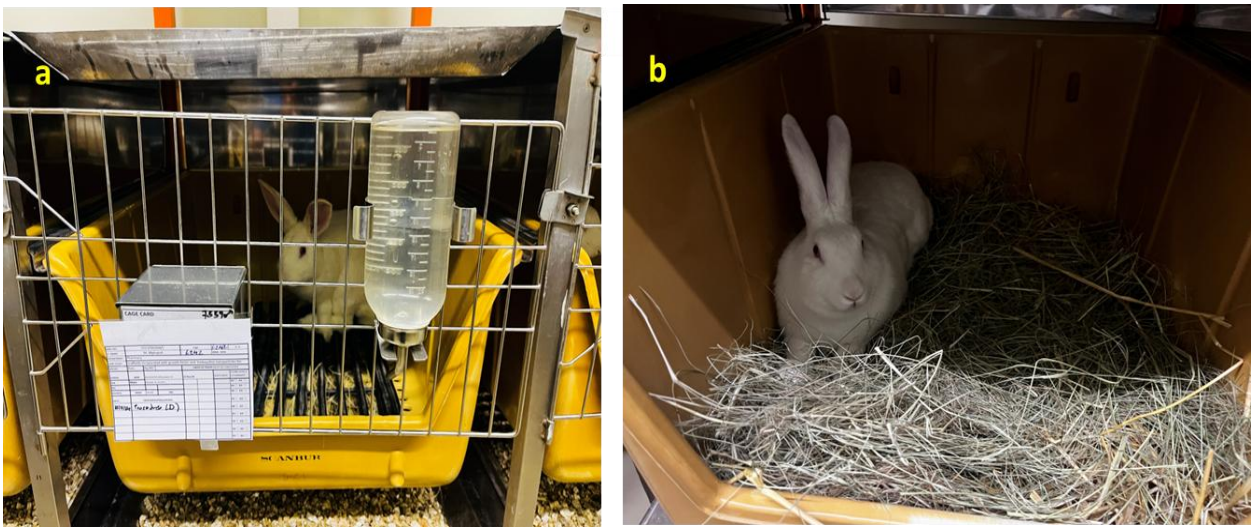


Figure 5.1: Photographic representation of **(a-b)** housing of the New Zealand white Rabbits.

5.2.3. The novel multi-component 3D-printed scaffolds preparation prior implantation

The novel multi-component 3D-printed scaffolds were sterilized with ethanol and then exposed to UV light for 24 hours. To confirm the effectiveness of the sterilization, a qualitative sterility test was performed whereby the scaffolds were incubated in sterile PBS, vortexed, and the supernatant plated onto nutrient-rich Tryptic Soy Agar (TSA). The plates were incubated at 37 °C for 48 hours, with no microbial growth observed for both loaded and unloaded 3D-printed scaffolds, confirming sterility (see images in Appendix A) (United States Pharmacopeial Convention, 2008). A known culture of *Staphylococcus aureus* was used as a positive control to confirm the capacity of the TSA plates to support microbial growth. All handling procedures were conducted using aseptic techniques, by USP <71> guidelines for sterility testing. Afterwards, the scaffolds were soaked in Alpha Minimum Essential Medium (α-MEM, 82% v/v) supplemented with 14% (v/v) fetal bovine serum (FBS), 2% (v/v), and incubated at 37 °C in a 5% CO_2 atmosphere for 24 hours to equilibrate before implantation into the rabbits with induced critical-sized femoral bone defects.

5.2.4. Design and surgical procedure for the pilot intervention

To refine and validate the surgical technique required for creating critical-sized bone defects, pilot tests were conducted using white New Zealand rabbits to optimize the procedure for developing a critical-sized defect (6x8 mm) on the right femur. A preliminary *in vivo* study was performed involving four New Zealand white rabbits under approved ethical guidelines. The pilot study included four distinct intervention groups: one rabbit served as the defect-only control, one received the defect implanted with a scaffold containing BQ-loaded PLGA nanoparticles, another received a drug-free scaffold, and the final rabbit received a scaffold integrated with BQ-loaded PLGA nanoparticles and bone morphogenetic protein (BMP).

The pilot results confirmed that rabbits are suitable animal models, demonstrating excellent survival rates, absence of noticeable adverse effects, and typical behavioural patterns throughout the 4-week study duration. Furthermore, the pilot study provided valuable insight, indicating that complete defect healing could be achieved within 4 weeks, prompting the main study to be shortened to a 4-week duration rather than the

initially planned 12 weeks. Following these successful pilot outcomes, the main study was conducted accordingly with twelve rabbits assessed at 4 weeks as approved by the ethics committee.

5.2.5. The design of the main study

Group 1 (Control Group, n=4): In the control group, comprising 4 young New Zealand rabbits, each animal underwent surgery to create a 6x8 mm surgical defect on the right femur at week 0. Rabbits were terminated sequentially, with one animal terminated each week over 4 weeks. Subsequent analyses were conducted on the bone defect site to assess bone formation and pharmacokinetic parameters.

Group 2 (Intervention Group, n=24): The intervention group comprised 24 young New Zealand rabbits, each animal receiving surgery to induce a 6x8 mm surgical defect on the right femur at week 0. This group was divided into two subgroups of 12 rabbits each:

- Twelve rabbits (n =12) received implantation with a 3D-printed multi-component scaffold without any drug.
- Twelve rabbits (n = 12) received implantation with a 3D-printed multi-component scaffold loaded with PLGA nanoparticles containing bedaquiline.

Rabbits from each subgroup were terminated weekly, with 3 rabbits from each subgroup terminated at weeks 1, 2, 3, and 4, respectively. Subsequent analyses were performed to evaluate bone formation and conduct pharmacokinetic studies. **Figure 5.2** illustrates this experimental design, clearly depicting rabbit groupings, surgical interventions, scaffold treatments, and the weekly termination schedule.

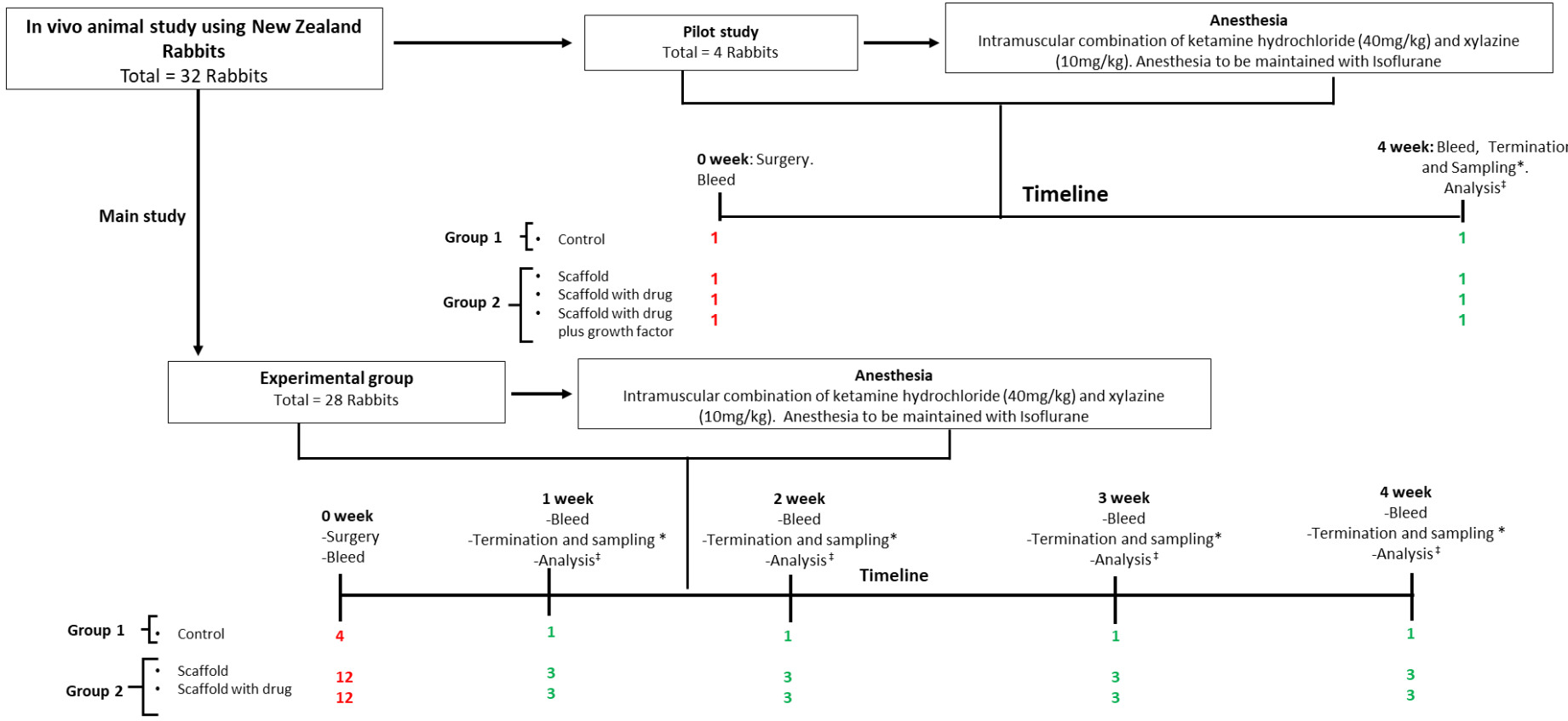


Figure 5.2: Schematic showing the *in vivo* studied model for the implanted scaffold.

5.2.5.1. Surgical procedure for the intervention

All surgical procedures were performed under sterile conditions. The critical-size bone defect was induced as previously described by Zhu et al., (2015) with minor modifications (Zhu et al., 2015). Briefly, New Zealand White Rabbits were anesthetized using an intramuscular combination of ketamine hydrochloride (40 mg/kg) and xylazine (10 mg/kg), with anaesthesia maintained using isoflurane (1-3%) in oxygen. The hair above the right femur was shaved, and the skin was surgically prepared using F10 Skin Prep Solution. F10 Skin Prep Solution was utilized as the ready-to-use disinfectant for the skin. It is a surgical spray with pre- and postoperative broad-spectrum capabilities. This non-staining formula was easy to use, effectively preventing the spread of infections and destroying microorganisms. It did not irritate the skin and was brightly colored, making it easily identifiable and highly beneficial in preventing post-surgical infections. The right femoral recipient site was accessed using a sharp scalpel, and the disto-medial metaphysis of the femur was cleared of soft tissue using a Woodson or Freer periosteal elevator. A surgical drill (6 mm outer diameter) was then employed to prepare an 8 mm deep defect for scaffold insertion. One drug-loaded scaffold was embedded into the groove. A picture was taken to illustrate the surgical procedure **(Figure 5.3)**. After surgery, the surgical site was sutured closed, antibiotics were administered to prevent bone infections, and pain management was provided with meloxicam (Zhu et al., 2015).

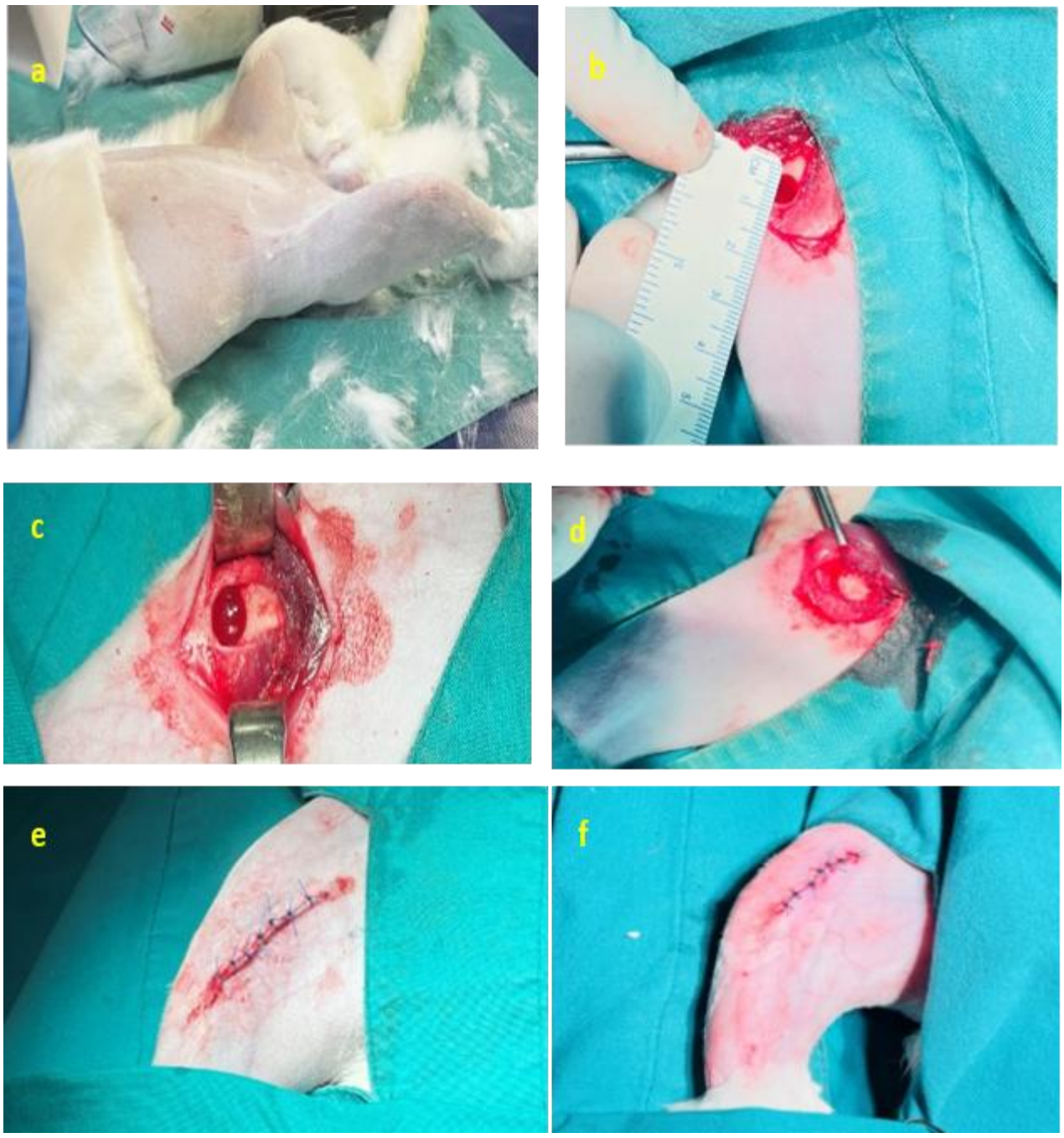


Figure 5.3: Surgical procedure demonstrating the creation of a critical-sized bone defect and scaffold implantation in Rabbits. **(a)** preparation of the rabbit pre-surgery, **(b-c)** creation of surgical defect before scaffold implantation with measurements to ensure defect dimension accuracy, **(d)** placement of 3D-printed scaffold into the defect, **(e-f)** surgical closure and suturing of the site post-implantation.

5.2.5.2. Post-operative Care of the New Zealand White Rabbits

Post-surgery, the rabbits were closely monitored to ensure optimal recovery immediately following the surgical procedures. Each rabbit was housed individually in separate cages maintained at ±25°C under a 12-hour light: 12-hour dark cycle.

Throughout the study, rabbits were fed according to the Wits CAS feeding standard operating procedures (SOPs). No indication of insufficient food or water intake was observed during the entire study period. The rabbits were weighed twice a week, cared for according to the WRAF protocol, and continuously monitored by both the researcher and the veterinarian until the study's completion. No postoperative restrictions on activity or supportive orthotic devices were necessary. The rabbits were inspected twice daily, assessing parameters such as behavior, posture, weight, feeding, and drinking patterns, with observations recorded for future reference.

5.2.5.3. Procedure for euthanasia and sample collection

Blood samples were collected from the rabbits via the ear vein immediately before euthanasia at each termination point (weeks 1, 2, 3, and 4). The withdrawn blood samples were immediately placed in heparinized tubes to prevent clotting. The blood samples were centrifuged at 5000rpm, and the supernatant was transferred into 2mL Eppendorf tubes and stored in the -80 °C freezer for further analysis. Following blood collection, the rabbits were euthanized via intravenous injection of sodium pentobarbitone (2 mL/kg) administered through the ear vein, ensuring minimal anatomical and physiological disruption and discomfort. Euthanasia occurred at 1,2, 3, and 4 weeks following scaffold implantation. Immediately post-euthanasia, implanted scaffolds and samples from empty femoral bone defects were carefully extracted and temporarily stored in 10% buffered formalin before histological processing as depicted in **Figure 5.4**.



Figure 5.4: Procedure for femoral bone extraction and sample preparation post-euthanasia: **(a)** isolated hind limb immediately post-euthanasia; **(b)** muscle tissue removal exposing femoral bone; **(c)** cleaned femur clearly showing the defect region; **(d)** femoral bone segment containing defect region; **(e)** extracted bone segment demonstrating intact and healthy bone marrow, and **(f)** samples stored in 10% buffered formalin awaiting histological analysis.

5.2.5.4. Mechanical strength and computed tomography (CT) assessment

The mechanical strength of the extracted femoral bones was assessed at each termination point (weeks 1, 2, 3, and 4) using a Texture Analyzer (TA.XTplus, Stable Micro Systems, Surrey, UK), enabling comparison between control bones and bones with different scaffold treatments. The method was adopted from Belill K et al. (2014) with some modifications. Briefly, A calibrated textural analyzer (TA.XT.plus; Stable Micro Systems, Surrey, UK), equipped with a 5 mm diameter ball probe coupled with a 10 mm inserter indenter, was used to press the surface of the horizontally mounted femur bone at the defect site, which was either left empty or filled with scaffold material. An average femur specimen was utilized, with an 8 mm diameter and pre-cut to a length of 50 mm **(Figure 5.5a-d)**. tissue from rabbit femur tissue was maintained in 0.9% NaCl-soaked gauze and stored at –80 °C until immediately before testing. Data acquisition was performed using Texture Exponent Software (Version 6.1.16.0), and the specific parameter configurations employed for the analysis are provided in **Table 5.1**. The maximum force generated during the indentation of the segment matrix at a depth of 0.5 mm was determined and regarded as the matrix hardness or indentation resistance (Belill et al., 2014).

Table 5.1: Textural configurations for determining bone hardness.

Parameters	Setting
Test mode	Compression
Test speed	1 mm/s
Post-test speed	5 mm/s
Indentation depth	0.5 mm
Target mode	Distance
Load cell	100 kg

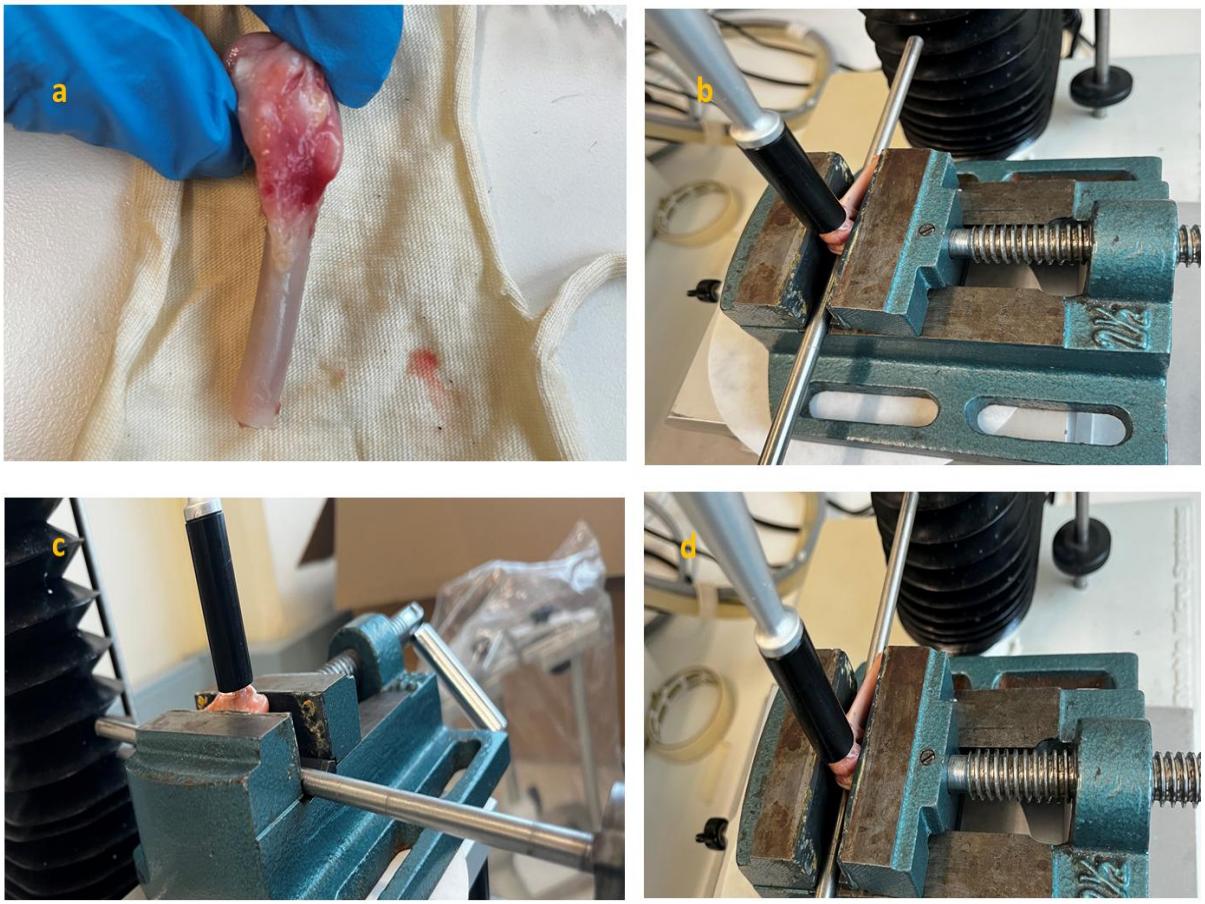


Figure 5.5: (a) Rabbit femur specimen immediately after retrieval from storage**, (b)** clamping of the horizontally oriented femur in a vise under the textural analyzer, **(c)** positioning of the 5 mm diameter ball probe at the defect site, and **(d)** performing the indentation test to determine the bone's matrix hardness or indentation resistance.

5.2.5.5. Evaluation of micro-computed tomography scan of rabbit femur

Micro-CT scans were conducted on the same bone samples at each termination point to evaluate the healing process and structural integration of the scaffolds. The scans were performed using a Skyscan 1278 micro-CT instrument, which provided high-resolution imaging of the femoral architecture and scaffold incorporation. For image reconstruction, NRecon software (Bruker) was employed (Bartos et al., 2018).

5.2.5.6. Sample preparation for histological examination

The specimens collected were fixed in 10% buffered formalin and subsequently demineralized using 14% EDTA for 4 weeks. Following demineralization, representative samples were sectioned according to Idexx standard operating procedure (IdexxSA-AP-26) and processed through routine automated histological tissue processing (IdexxSA-AP-SOP-27). Processed tissues were embedded, and

transverse sections of 5 µm thickness were prepared (IdexxSA-AP-SOP-30), mounted onto slides, and stained using an automated Haematoxylin and Eosin tissue stainer (IdexxSA-AP-SOP-205) in preparation for histological evaluation.

5.2.5.7. Quantification of bedaquiline concentration in plasma using high-pressure liquid chromatography

Bedaquiline (BQ) concentration in blood samples was quantified using High-Performance Liquid Chromatography (HPLC). Blood samples collected from rabbits were subjected to liquid-liquid extraction to isolate the drug from plasma. Briefly, plasma samples were mixed with an organic solvent diethyl ether, vortexed vigorously, and centrifuged at ~4000 rpm for 10 minutes to separate organic and aqueous phases. The organic layer containing the drug was carefully transferred into a clean tube and evaporated under nitrogen gas at room temperature. The residue was reconstituted with the mobile phase, filtered, and analyzed using HPLC following the method described by Ayodele et al., (2024). The HPLC system (Waters, Milford, Massachusetts, USA) had a Waters Symmetry300™ C18 (5 µm, 4.6 × 150 mm) column, a UV detector, and a Waters binary HPLC pump. The mobile phase consisted of a 95:5 (v/v) mixture of acetonitrile/methanol and phosphate buffer (pH 7.4), with a 1.0 mL/min flow rate and a detection wavelength of 275 nm. BQ concentrations were determined by comparing peak areas of samples to a calibration curve ranging from 1 to 60 µg/mL, prepared under identical analytical conditions.

5.3. Results and discussion

5.3.1. Pilot study assessment

The pilot study validated the feasibility of the experimental (surgical) procedures and confirmed previous findings (Hua et al., 2022; Pei et al., 2018; Zhu et al., 2015) indicating that rabbits are a suitable experimental model for this type of research. Rabbits tolerated the surgical interventions well, showing no observable adverse effects throughout the 4-week duration of the pilot study. All rabbits successfully survived the full duration of the study. Histological analyses conducted during the pilot study confirmed bone healing, as illustrated in **Figure 5.6**. Additionally, findings from the pilot study demonstrated no significant difference in bone healing between the scaffold with drug alone and the scaffold with drug plus growth factor (BMP). Consequently, the scaffold incorporating the drug plus growth factor was excluded from

the main study. Following these successful pilot outcomes and after receiving approval from the ethics committee of the University of the Witwatersrand, the main study was conducted for 4 weeks to assess the healing duration and efficacy of scaffold treatments.

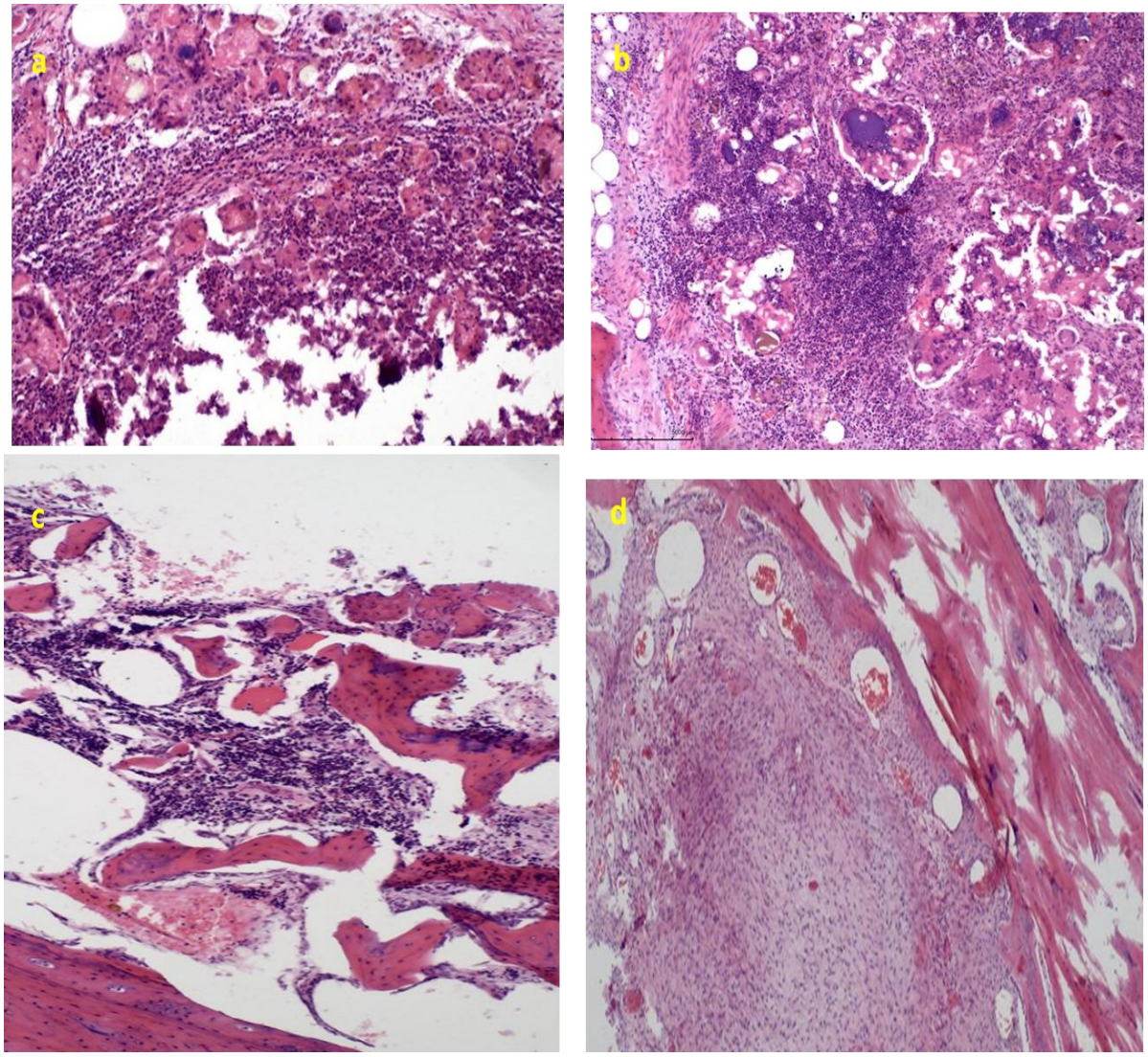


Figure 5.6: Histological evaluation of femoral defect healing after 4 weeks post-implantation (H&E staining): **(a)** Scaffold loaded with BQ showing moderate bone regeneration and inflammatory response; **(b)** Scaffold loaded with BQ plus BMP illustrating similar regenerative activity and inflammation to the drug-only scaffold; **(c)** Drug-free scaffold exhibiting reduced bone formation activity; **(d)** Untreated defect (control) predominantly characterized by fibrous tissue and minimal bone regeneration.

5.3.2. Clinical and histological analysis for main study

5.3.2.1. Clinical examination

During the four-week observation period, there were no post-operative complications

or adverse reactions, such as abnormal bleeding, at any of the surgical sites. Inflammation was minimal (e.g., slight swelling), and after a brief resting period of three to six days post-operation, the rabbits were able to move and leap without notable pain or restriction. Pain levels and recovery were assessed using the grimace scale, while vital signs were monitored, and weight measurements were taken weekly to ensure overall health; these findings are detailed in **Appendix A**. At the time of termination and sample collection, the novel multi-component 3D-printed scaffolds remained intact within the defects, indicating stable integration. Overall, healing progressed smoothly throughout the study period.

5.3.2.2. Histological evaluation of right femur following various interventions

5.3.2.2.1. Histological examination for week *1*

In Week 1, early healing responses were evident in all samples, though the presence of the 3D-printed scaffolds appeared to enhance the extent of woven bone formation compared to the defect control. In the control Rabbit **(Figure 5.7a)**, a focal, segmental full-thickness defect in the cortical bone was filled predominantly with haemorrhage and fibrin, with only peripheral fibroplasia and early woven bone formation emanating from the adjacent endosteum. In contrast, the scaffold-only Rabbit **(Figure 5.7b)** demonstrated a focal defect in the cortical bone that was filled with woven bone lined by osteoblasts; the periosteal surface showed mild fibroplasia while the endosteal surface revealed amorphous, basophilic, slightly crystalline structures—occasionally calcified—and infiltrated by histiocytic cells, including some multinucleated giant cells, with the marrow cavity maintaining a mixture of adipose tissue and hematopoietic precursors alongside mild hemorrhage. The scaffold infused with BQ-loaded PLGA nanoparticles **(Figure 5.7c)** also exhibited a focal defect in the cortical bone, but with more prominent periosteal fibroplasia and significant histiocytic infiltration; the endosteal surface contained amorphous, slightly crystalline, basophilic material with calcification, and variably sized grey crystalline structures were observed within the matrix, together with abundant histiocytic cells including multinucleated forms, hemorrhage, and fibrin. Overall, while the free and drug-loaded scaffolds displayed similar patterns of early woven bone formation, the infused scaffold was distinguished by the more pronounced crystalline structures, suggesting subtle differences in material integration without a significant impact on the overall osteogenic response.

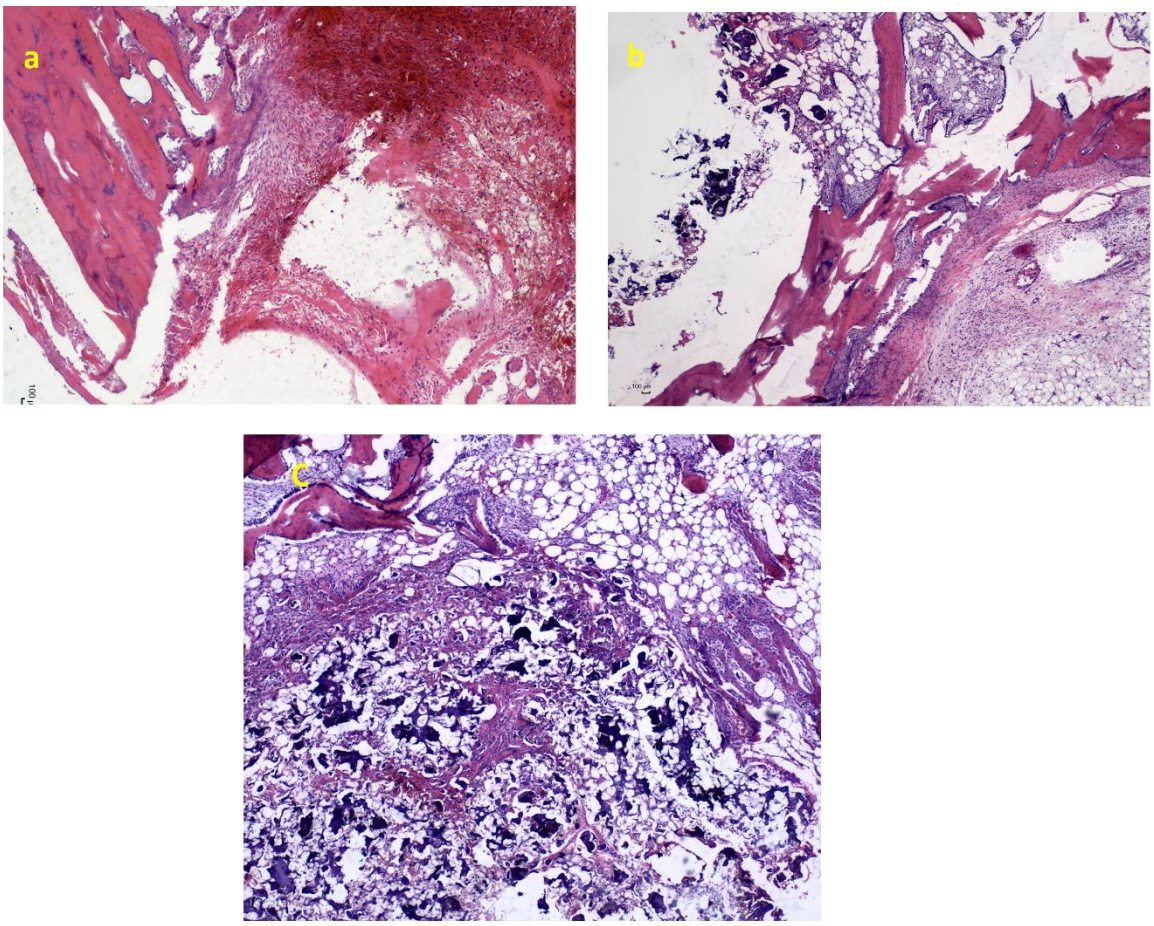


Figure 5.7: Histological sections of rabbit femoral defects at Week 1, comparing **(a)** control defects, **(b)** defects treated with a 3D-printed scaffold only, and (**c)** defects treated with a 3D-printed scaffold loaded with BQ-loaded PLGA nanoparticles.

5.3.2.2.2. Histological examination for week 2

During Week 2, the histological appearance of the defects varied according to whether scaffolds were present or not. For Rabbits with scaffold only **(Figure 5.8a)** a segmental full-thickness cortical bone defect contained a basophilic, crystalline scaffold extending into the marrow cavity, accompanied by small numbers of histiocytoid cells, occasional multinucleated giant cells, and mild haemorrhage and fibrin. Early woven bone formation was evident at the periphery, while extensive hyaline cartilage within the periosteum and endosteum suggested active endochondral ossification. In the Rabbit with scaffold plus BQ-loaded PLGA nanoparticles **(Figure 5.8b)**, the cortical bone defect likewise contained basophilic scaffold material interspersed with spicules of calcification. Fibroblasts, histiocytoid cells, and pronounced multinucleated cells populated the periphery, with mild periosteal woven bone and fibroplasia extending into the adjacent marrow space, where scattered lymphoplasmacytic infiltrates were noted. By contrast, Rabbit with defect **(Figure 5.8c)** showed no scaffold material but displayed a segment of mildly thickened woven bone replacing part of the cortical bone,

with mild periosteal reaction and fibrosis. The marrow cavity contained both adipose tissue and hematopoietic elements. Overall, the Week 2 scaffolds showed a mild foreign-body type reaction alongside early-stage bone formation and cartilage development, while the control group reflected a straightforward, unassisted bone repair process.

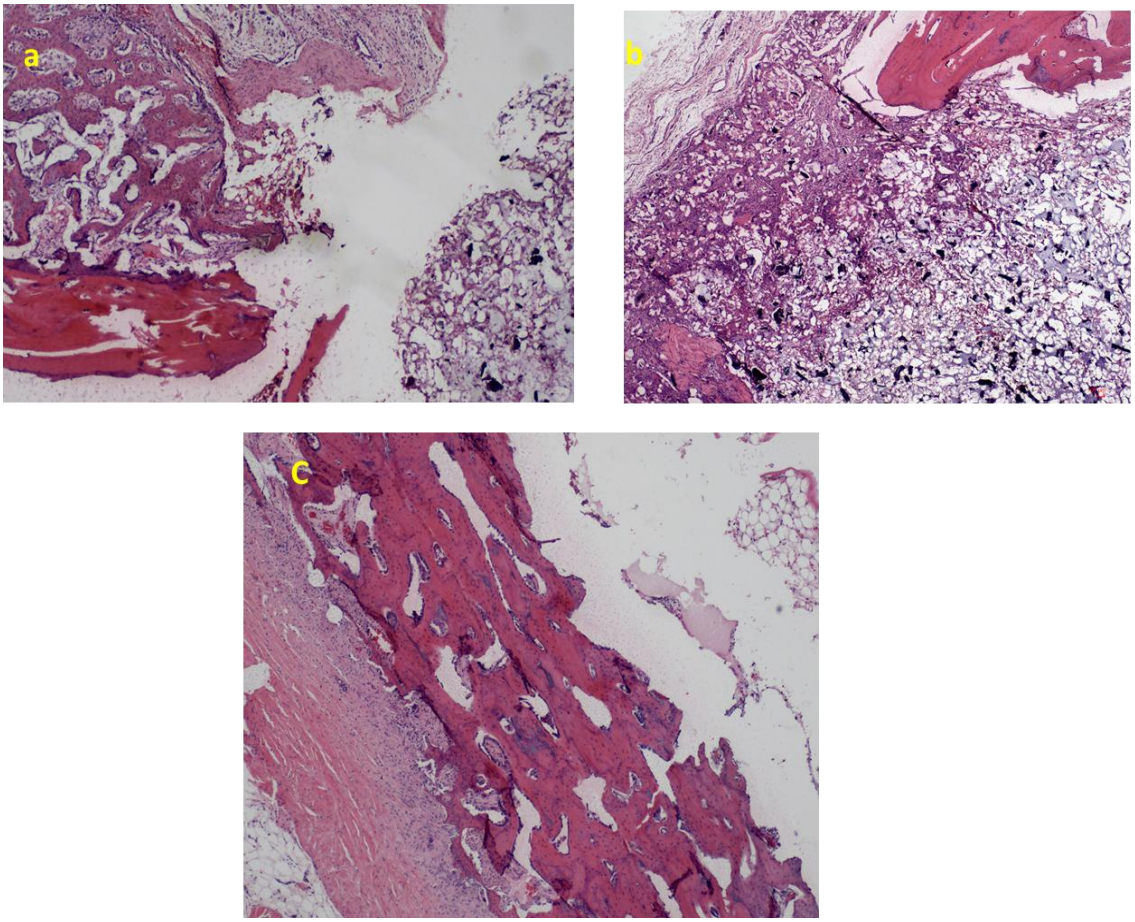


Figure 5.8: Histological sections of rabbit femoral defects at Week 2, comparing **(a)** defects treated with a 3D-printed scaffold only **(b)** defects treated with a 3D-printed scaffold loaded with BQ-loaded PLGA nanoparticles, and **(c)** control defects.

5.3.2.2.3. Histological examination for week 3

By Week 3, both the scaffold and control groups demonstrated progress in bone healing, although the scaffold structures remained visible in the treated groups. **Figure 5.9a** depicts a histological image of Rabbit with scaffold only, a persistent cortical bone defect was filled with a basophilic, slightly crystalline scaffold, surrounded by histiocytoid and multinucleated giant cells. Peripheral fibroplasia and woven bone formation became more pronounced, with a notably thickened periosteum laying down new bone. For Rabbit with scaffold plus BQ-loaded PLGA nanoparticles **(Figure 5.9b),** a similar basophilic scaffold was found within the marrow cavity, showing infiltration by

histiocytes, scattered multinucleated cells, and calcified spicules. Peripheral fibroplasia and woven bone formation were evident, and the cortex itself remained largely intact, although mild periosteal thickening was observed. Meanwhile, Rabbit with defect **(Figure 5.9c)** exhibited a segmental cortical defect filled with fibroblasts and woven bone extending into the marrow cavity, alongside mild to moderate new bone formation in the periosteal and endosteal regions. Small areas of hyaline cartilage within the periosteum underwent endochondral ossification. Overall, the Week 3 samples indicated ongoing integration of the scaffold in the treated groups and a typical intermediate stage of callus formation in the control group.

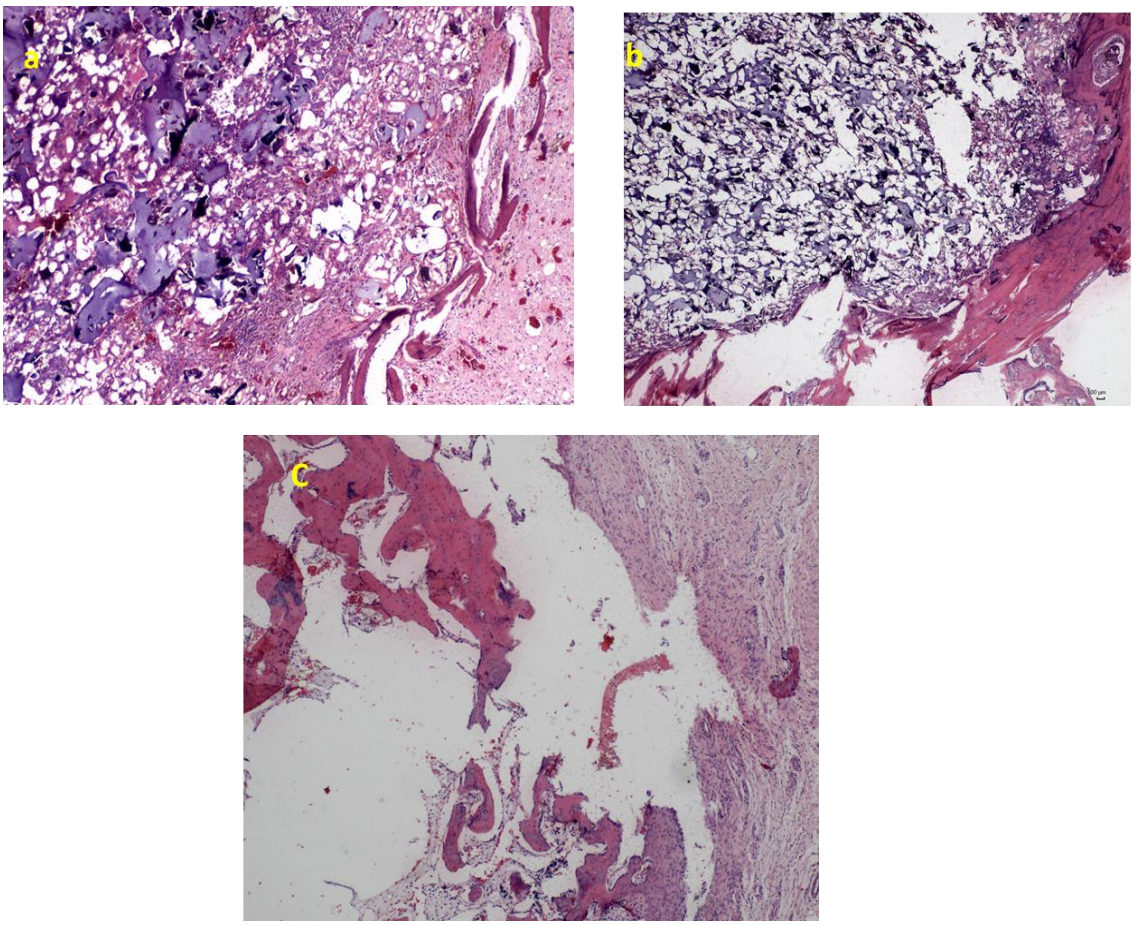


Figure 5.9: Histological sections of rabbit femoral defects at Week 3, comparing **(a)** defects treated with a 3D-printed scaffold only **(b)** defects treated with a 3D-printed scaffold loaded with BQ-loaded PLGA nanoparticles, and **(c)** control defects.

5.3.2.2.4. Histological examination for week 4

At Week 4, the scaffold groups exhibited advanced woven bone formation and an ongoing mild inflammatory response, while the control defect showed further maturation of the repair tissue. Rabbit with scaffold only **(Figure 5.10a)**, a basophilic crystalline scaffold persisted in the cortical defect space, interspersed with histiocytoid

cells, multinucleated giant cells, and scattered neutrophils. Pronounced woven bone extended from the endosteum into the marrow cavity, accompanied by marked periosteal bone formation and mild lymphoplasmacytic infiltrates. **Figure 5.10b** demonstrates Rabbit with scaffold plus BQ-loaded PLGA nanoparticles, a similar scaffold occupied the segmental defect and elicited a foreign-body reaction marked by numerous histiocytes, multinucleated giant cells, and scattered neutrophils. A robust shell of woven bone extended from the endosteum, with periosteal fibrosis and moderate to marked peripheral fibroplasia providing structural support. In contrast, Rabbit with defect **(Figure 5.10c)** presented a segmental defect largely bridged by reactive woven bone and mild periosteal fibrosis, with the adjacent marrow cavity containing normal fat and scattered hematopoietic elements. Collectively, the Week 4 findings demonstrated that both scaffold-only and scaffold-plus-drug interventions supported considerable bone ingrowth around the material, whereas the control defect continued to mature naturally with substantial woven bone formation but lacked the mild foreign-body reaction observed in scaffold-treated groups.

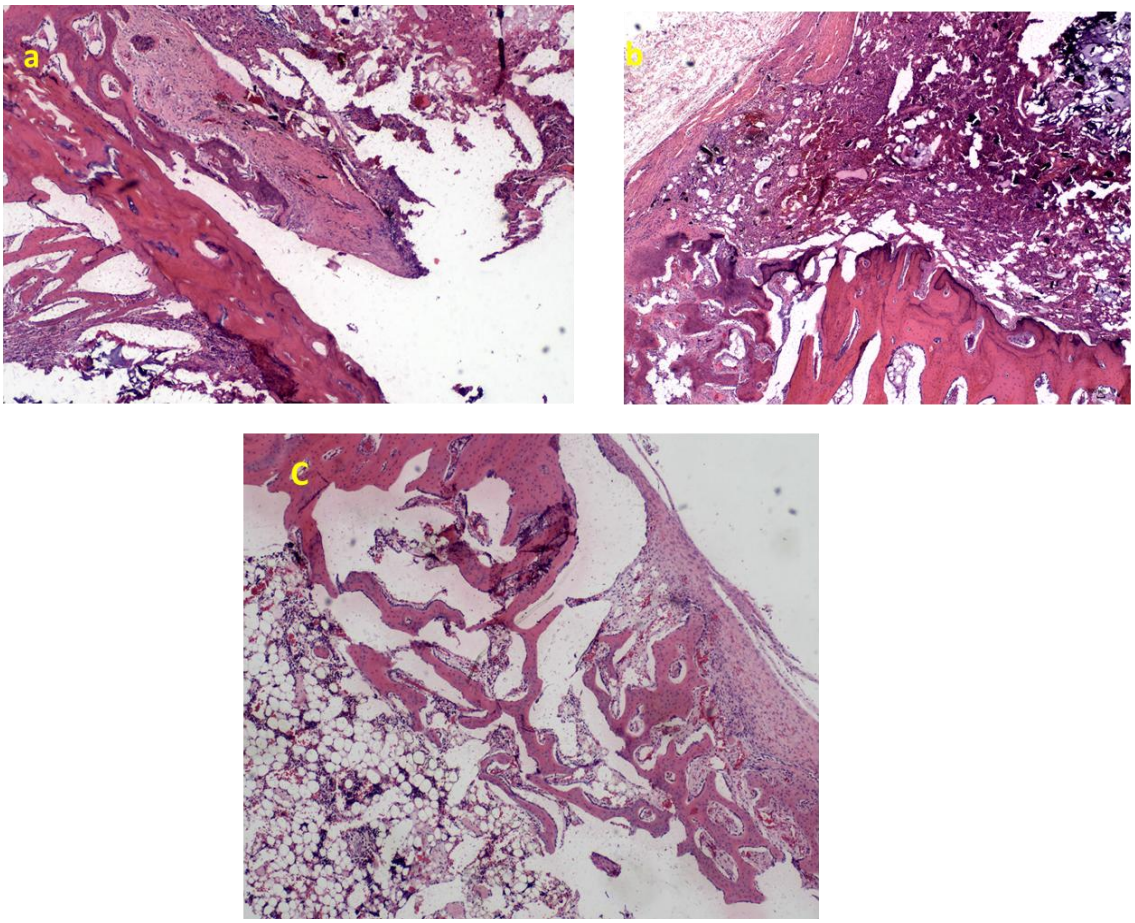


Figure 5.10: Histological sections of rabbit femoral defects at Week 4, comparing **(a)** defects treated with a 3D-printed scaffold only **(b)** defects treated with a 3D-printed scaffold loaded with BQ-loaded PLGA nanoparticles, and **(c)** control defects.

5.3.3. Assessment of mechanical strength

The mechanical integrity of the healing bone defects was quantitatively assessed using a texture analyzer, providing a functional perspective on the osteogenic process. Measurements were performed weekly (Weeks 1–4) across three experimental groups: defect control, free 3D-printed scaffold, and 3D-printed scaffold infused with anti-TB drug. This systematic evaluation aimed to correlate histological healing with biomechanical performance, offering insights into how scaffold integration and drug delivery impact the structural stability and overall mechanical strength of the regenerated tissue over time.

Figure 5.11 illustrates the mechanical strength of the defect control, scaffold only, and scaffold with BQ PLGA nanoparticles, over the four weeks. The graph demonstrates that the scaffold-treated groups consistently exhibit significantly higher force measurements compared to the control group, with statistical analysis confirming these differences ($p < 0.05$) at each time point. In the early weeks, the scaffold groups already showed an elevated load-bearing capacity, suggesting that the structural support provided by the scaffold enhances the initial phase of bone repair. As the healing process progresses, both the scaffold only and the scaffold with nanoparticles groups display a marked increase in mechanical strength, reflecting more advanced woven bone formation and integration of the scaffold material. Although the addition of nanoparticles yields only subtle differences during the early stages, the overall trend indicates that the combined approach may offer a long-term advantage in bone regeneration. This statistically robust data supports the conclusion that scaffold-based strategies significantly improve the mechanical stability of healing bone defects compared to natural, unassisted repair (Alonzo et al., 2021; Bartos et al., 2018; Blumer, 2021).

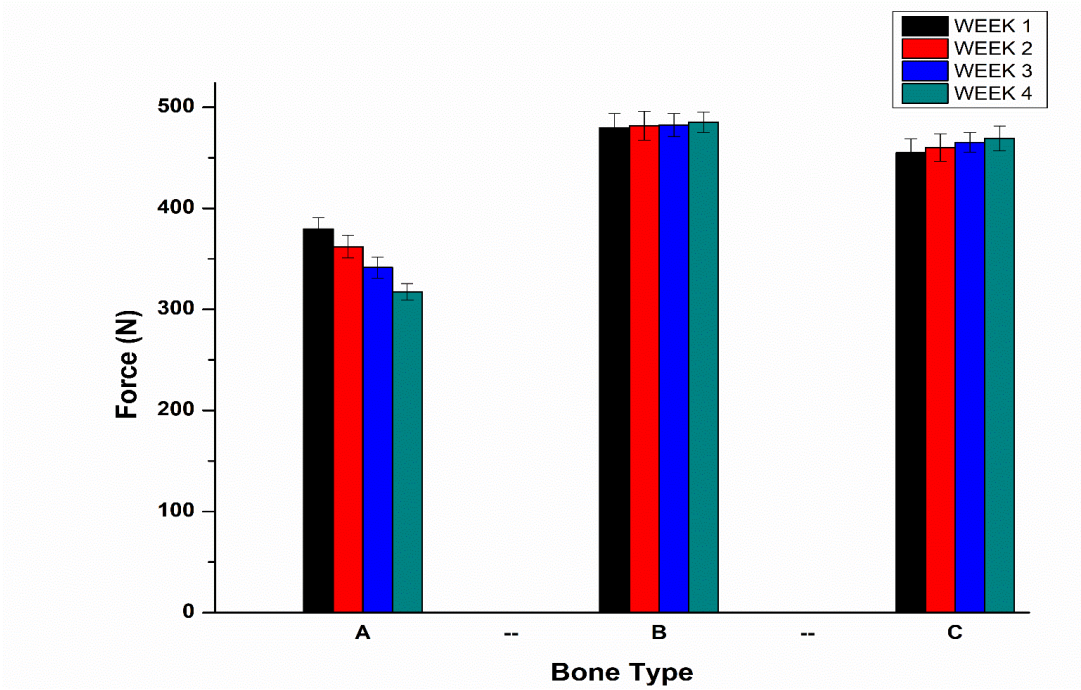


Figure 5.11: Analysis of indentation force of rabbit femoral defects over four weeks, comparing **(a)** control defects, **(b)** defects treated with a 3D-printed scaffold only, and **(c)** defects treated with a 3D-printed scaffold loaded with BQ-loaded PLGA nanoparticles.

5.3.4. Assessment of micro-CT scans of right femur following various interventions

Figure 5.12a (Defect Bone), a radiolucent region indicates a segmental or partial defect with limited new bone formation. The surrounding cortical bone remains intact, but the central gap shows minimal bridging, suggesting incomplete or ongoing healing in the absence of a scaffold. In contrast, In **Figure 5.12b-c** both exhibits more radiodense tissue within the defect area, reflecting new bone formation around or within the scaffold material. Although some radiolucent pockets persist, the overall density is notably higher than in the defect-only image, indicating that the drug-infused scaffold provides a supportive matrix for enhanced osteogenesis (Beaman et al., 2006). Between the two scaffold-treated, **Figure 5.12c** appears to have more robust bone in-growth and denser mineralization, implying a more advanced stage of healing. Taken together, these findings demonstrate that the drug-loaded scaffold promotes greater bone formation and partial bridging of the defect site compared to the untreated defect.

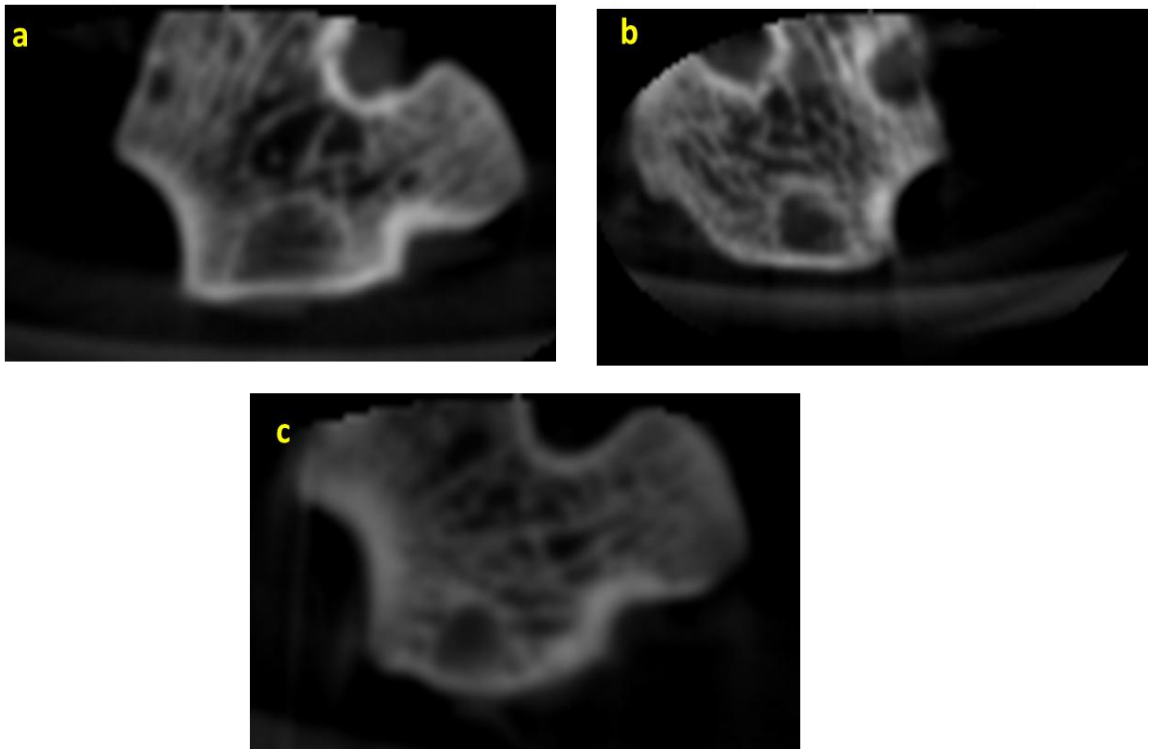


Figure 5.12: Micro-CT images of femoral **(a)** defect, **(b)** implantation of scaffold only, and **(c)** scaffold with BQ-loaded PLGA nanoparticles.

5.3.5. Concentration of Bedaquiline in the blood of the Rabbitt model

The released concentrations of BQ in blood was monitored over time as illustrated in **Figure 5.13**. The scaffold exhibits a slow rise in BQ plasma levels that peaks around Week 3 (approximately 8–9 µg/mL) before slightly declining at Week 4. This profile reflects not only the scaffold's release characteristics but also the body's distribution, metabolism, and excretion of the drug. In **Chapter 4**, the *in-vitro* environment shows a mild burst within the first few days, while *in vivo* measurements at Week 1 remain relatively low, followed by a steady climb that indicates release balanced by physiological clearance. Despite these differences in magnitude and timing, both the *in-vitro* and *in vivo* data confirm that the scaffold is designed for long-term, controlled delivery, rather than a rapid, high concentration burst.

BQ has been minimum inhibitory concentration (MIC) of BQ for *Mycobacterium tuberculosis* can be as low as 0.03–0.12 µg/mL, and even for slightly higher MICs, therapeutic targets typically remain under 1 µg/Ml (Ayodele et al., 2024; Kaniga et al., 2022). The *in vivo* scaffold achieves plasma levels of around 8–9 µg/mL at its peak, which far exceeds the typical MIC. This suggests that the concentrations delivered are

not only sufficient but likely more than adequate to exert an antimicrobial effect (Kaniga et al., 2022). Since the scaffold continues releasing drugs up to at least Week 4, and the plasma levels remain in the multi-microgram-per-milliliter range, local and systemic concentrations appear to stay above the MIC for an extended period. Such sustained coverage is crucial for preventing or treating infections in bone defects, where localized antibiotic delivery can significantly enhance therapeutic outcomes (Pei et al., 2018; Zhu et al., 2015).

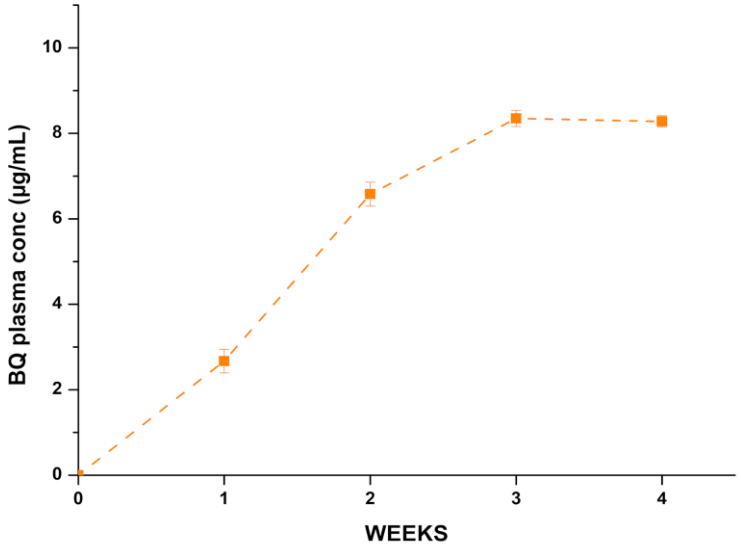


Figure 5.13: Bedaquiline distribution with respect to weeks in blood.

5.4. Concluding Remarks

The in vivo evaluation of the novel multi-component 3D-printed scaffold embedded with BQ-loaded PLGA nanoparticles demonstrates its significant potential for bone tuberculosis therapy. The data show that the scaffold not only greatly improves bone regeneration and mechanical strength compared to untreated controls but also provides sustained local delivery of BQ, keeping plasma concentrations well above the MIC for *Mycobacterium tuberculosis*. Histological and micro-CT analyses confirm strong new bone formation and scaffold integration, while mechanical testing indicates superior load-bearing capacity throughout the healing process. Overall, these findings highlight the scaffold's promise as an effective platform for localized drug delivery and targeted osteogenic support, offering a practical alternative to traditional systemic chemotherapy in managing bone TB. This approach aligns with emerging strategies in

tissue engineering that emphasize multifunctional scaffolds capable of simultaneously addressing infection control and defect repair. Chen et al. (2023) and Zhu et al. (2021) demonstrated 3D-printed systems targeting infection and osteosarcoma or osteomyelitis, while Huang et al. (2024) introduced nitric oxide-releasing PEEK implants with multimodal therapeutic effects. Furthermore, Hua et al. (2022) validated the concept using a porous tantalum scaffold coated with antitubercular drugs. Collectively, these advances reinforce the clinical relevance of integrated therapeutic platforms. The current study contributes to this growing body of work by offering a bioengineered scaffold that combines the mechanical, biological, and pharmacological features necessary for effective bone TB management.

5.5. References

Alonzo, M., Primo, F.A., Kumar, S.A., Mudloff, J.A., Dominguez, E., Fregoso, G., Ortiz, N., Weiss, W.M., Joddar, B., 2021. Bone tissue engineering techniques, advances and scaffolds for treatment of bone defects. Curr. Opin. Biomed. Eng. 17, 100248. https://doi.org/10.1016/j.cobme.2020.100248

Ayodele, S., Eyk, A.D. van, Kumar, P., E. Choonara, Y., 2024. A sensitive, rapid and cost-effective RP-HPLC-UV method for detection and quantification of bedaquiline in physiological fluid (pH 7.4). Anal. Methods 16, 7169–7177. https://doi.org/10.1039/D4AY01143K

Bartos, M., Suchy, T., Zbynek, T., Rene, F., Marie, H.K., 2018. Micro-ct in tissue engineering scaffolds designed for bone regeneration: principles and application. Ceram.-Silikáty 62, 194–199. https://doi.org/10.13168/cs.2018.0012

Beaman, F.D., Bancroft, L.W., Peterson, J.J., Kransdorf, M.J., Menke, D.M., DeOrio, J.K., 2006. Imaging characteristics of bone graft materials. RadioGraphics 26, 373–388. https://doi.org/10.1148/rg.262055039

Belill, K.A., Settle, T.L., Angel, C.R., Kim, S.-W., Rothwell, S.W., 2014. Femoral strength after induced lesions in rats (Rattus norvegicus). Comp. Med. 64, 186–192.

Blumer, M.J.F., 2021. Bone tissue and histological and molecular events during development of the long bones. Ann. Anat. - Anat. Anz. 235, 151704. https://doi.org/10.1016/j.aanat.2021.151704

Bose, S., Vahabzadeh, S., Bandyopadhyay, A., 2013. Bone tissue engineering using 3D printing. Mater. Today 16, 496–504. https://doi.org/10.1016/j.mattod.2013.11.017

Chen, J., Zhou, H., Fan, Y., Gao, G., Ying, Y., Li, J., 2023. 3D printing for bone repair: Coupling infection therapy and defect regeneration. Chem. Eng. J. 471, 144537. https://doi.org/10.1016/j.cej.2023.144537

Garg, D., Goyal, V., 2020. Spinal tuberculosis treatment: an enduring bone of contention. Ann. Indian Acad. Neurol. 23, 441–448. https://doi.org/10.4103/aian.AIAN_141_20

Hegazy, W.A.H., Mamari, R.A., Almazroui, K., Habsi, A.A., Kamona, A., AlHarthi, H., Lawati, A.I.A., AlHusaini, A.H., 2021. Retrospective study of bone-TB in Oman: 2002–2019. J. Epidemiol. Glob. Health 11, 238–245. https://doi.org/10.2991/jegh.k.210420.002

Hua, L., Qian, H., Lei, T., zhang, yu, Lei, P., Hu, Y., 2022. 3D-Printed porous tantalum coated with antitubercular drugs achieving antibacterial properties and good biocompatibility. Macromol.biosci 22. https://doi.org/10.1002/mabi.202100338

Huang, L., Feng, G., Zhang, L., 2024. Propelling Multi-Modal Therapeutics of PEEK Implants through the Power of NO evolving Covalent Organic Frameworks (COFs). Small 20, 2306508. https://doi.org/10.1002/smll.202306508

Kaniga, K., Hasan, R., Jou, R., Vasiliauskienė, E., Chuchottaworn, C., Ismail, N., Metchock, B., Miliauskas, S., Viet Nhung, N., Rodrigues, C., Shin, S., Simsek, H., Smithtikarn, S., Ngoc, A.L.T., Boonyasopun, J., Kazi, M., Kim, S., Kamolwat, P., Musteikiene, G., Sacopon, C.A., Tahseen, S., Vasiliauskaitė, L., Wu, M.-H., Vally Omar, S., 2022. Bedaquiline drug resistance emergence assessment in multidrug-resistant tuberculosis (MDR-TB): a 5-Year prospective in vitro surveillance study of bedaquiline and other second-line drug susceptibility testing in mdr-tb isolates. J. Clin. Microbiol. 60, e02919-20. https://doi.org/10.1128/JCM.02919-20

Luo, Y., Chen, Hongwei, Chen, Hua, Xiu, P., Zeng, J., Song, Y., Li, T., 2024. Recent advances in nanotechnology-based strategies for bone tuberculosis management. Pharmaceuticals 17, 170. https://doi.org/10.3390/ph17020170

Mphaphuli, M.T., Sithole, M.N., Kumar, P., Kondiah, P.P.D., Mabrouk, M., Choonara, Y.E., 2023. Multi-purpose prototypes for extrapulmonary *Mycobacterium tuberculosis* targeting: A regenerative medicine perspective. J. Drug Deliv. Sci. Technol. 89, 105039. https://doi.org/10.1016/j.jddst.2023.105039

Pei, P., Tian, Z., Zhu, Y., 2018. 3D printed mesoporous bioactive glass/metal-organic framework scaffolds with antitubercular drug delivery. Microporous Mesoporous Mater. 272, 24–30. https://doi.org/10.1016/j.micromeso.2018.06.012

United States Pharmacopeial Convention (USP), 2008. *Sterility Tests <71>: Sixth Interim Revision Announcement*. Pharmacopeial Forum, 34(6). Available at: http://www.usppf.com/pf/pub/index.html

Vinogradova, T.I.; Serdobintsev, M.S.; Korzhikova-Vlakh, E.G.; Korzhikov-Vlakh, V.A.; Kaftyrev, A.S.; Blum,N.M.; Semenova, N.Y.; Esmedlyaeva, D.S.; Dyakova, M.E.; Nashchekina, Y.A.; et al. Comparison of autografts and biodegradable 3D-printed composite scaffolds with osteoconductive properties for tissue regeneration in bone tuberculosis. Biomedicines 2023, 11, 2229.https://doi.org/10.3390/biomedicines11082229

Yahia, Sarah, et al. 3D-bioimplants mimicking the structure and function of spine units for the treatment of spinal tuberculosis." RSC advances 13.25 (2023): 17340-17353.

Zhu, M., Li, K., Zhu, Y., Zhang, J., Ye, X., 2015. 3D-printed hierarchical scaffold for localized isoniazid/rifampin drug delivery and osteoarticular tuberculosis therapy. Acta Biomater. 16, 145–155. https://doi.org/10.1016/j.actbio.2015.01.034

Li, Z., Hu, B., Song, Y., Li, Y., Feng, G., Liu, L., Zhang, L., 2021. 3D-Printed Multifunctional Polyetheretherketone Bone Scaffold for Multimodal Treatment of Osteosarcoma and Osteomyelitis. ACS Appl. Mater. Interfaces 13, 47327–47340. https://doi.org/10.1021/acsami.1c10898

CHAPTER 6

CONCLUSIONS AND RECOMMENDATIONS

6.1. Conclusion

Bone tuberculosis (TB) is a serious extrapulmonary manifestation of tuberculosis caused by the bacterium *Mycobacterium tuberculosis*, primarily affecting the spine, long bones, and joints. It presents significant challenges due to its insidious onset, nonspecific clinical features, and complications such as bone destruction, deformities, neurological impairment, and potential drug resistance. Conventional treatment methods that involve long-term systemic administration of anti-TB drugs often have limitations, including poor drug penetration into bone tissue, systemic side effects, and issues related to patient adherence.

This study successfully developed and validated a novel 3D-printed multi-component scaffold incorporating bedaquiline (BQ)-loaded PLGA nanoparticles, specifically designed for the targeted treatment of bone tuberculosis-related defects. Addressing a critical gap in current bone TB treatments, this scaffold provides a unique combination of localized sustained drug delivery and enhanced bone regeneration, minimizing systemic side effects and reducing the risk of drug resistance.

Correlating with the initial aim and objectives, this research demonstrated the successful development and optimization of BQ-loaded PLGA nanoparticles utilizing the solvent evaporation method and Box-Behnken design. The nanoparticles exhibited suitable physicochemical properties, sustained drug release profiles, and favourable *in-vitro* cytotoxicity towards MG-63 cell lines, confirming their therapeutic potential for bone regeneration applications. Furthermore, the study effectively integrated natural (sodium alginate), synthetic (polycaprolactone), metal (titanium), and bioactive (bioactive glass) biomaterials into an optimal ink formulation suitable for 3D printing, achieving the essential characteristics of osteointegration, mechanical strength, biocompatibility, and controlled degradation necessary for bone tissue engineering. Incorporation of the optimized bedaquiline-loaded nanoparticles into this bioink led to the fabrication of a customized, patient-specific scaffold that demonstrated excellent physicochemical, mechanical, and morphological properties, supporting both bone regeneration and localized therapeutic delivery.

In vivo evaluations employing a rabbit femoral defect model provided robust evidence of the scaffold's efficacy in promoting bone repair and sustained localized drug delivery. Histological, micro-CT, and mechanical testing confirmed significant enhancement of bone regeneration and integration, alongside effective management of local TB infection, underscoring its potential clinical applicability. These results validate the scaffold as an innovative solution for localized, effective, and sustained treatment of bone TB-related defects.

6.2. Recommendations

Based on these findings, the recommendations for future research are proposed:

- Long-Term *In Vivo* Studies: Extended studies should be conducted to thoroughly assess long-term scaffold biocompatibility, biodegradation behaviour, bone remodelling dynamics, and sustained therapeutic efficacy beyond the initial healing period observed in this study.

- Mechanistic Studies: Detailed mechanistic investigations are recommended to elucidate cellular and molecular pathways involved in scaffold-mediated bone regeneration and the interaction dynamics between scaffold materials and BQ-loaded nanoparticles in promoting local therapeutic effects.

- Clinical Translation Studies: Pre-clinical studies involving larger animal models and humanized physiological conditions should be pursued to further validate safety, efficacy, and dose optimization, paving the way for subsequent clinical trials.

- Enhancement of Scaffold Functionalization: Future investigations could explore incorporating additional bioactive agents or growth factors into the scaffold system, potentially further enhancing therapeutic outcomes, bone regeneration, and anti-TB efficacy.

- Scalability and Manufacturing Feasibility: While 3D printing offers strong potential for patient-specific applications, future work should evaluate the scalability of the scaffold fabrication process using good manufacturing practice compliant systems. This includes assessing reproducibility, process validation, and cost-effectiveness at a manufacturing scale suitable for clinical translation.

- Safety and Regulatory Considerations: Although titanium provides desirable mechanical strength and bioactivity, potential safety and regulatory hurdles must be considered for human application, including metal ion release, immunogenicity, and compatibility with long-term implantation. Additionally, the cost implications of multi-material scaffolds should be evaluated in the context of widespread accessibility and affordability, particularly in TB-burdened low-resource settings.

In summary, this research successfully introduces a highly promising multi-component scaffold with significant potential to revolutionize the targeted treatment of bone TB, providing a comprehensive and robust platform for future clinical translation.

CHAPTER 7

NOVARTIS NEXT GENERATION PROGRAM EXPERIENCE

7.1. Overview of the Program

The Next Generation Scientist (NGS) Program is a prestigious initiative held at the Novartis Campus in Basel, Switzerland, created to empower talented young scientists worldwide. The program provides selected researchers a unique chance to participate in advanced scientific research projects under the guidance of leading Novartis scientists and mentors, fostering an inspiring environment for innovation, collaboration, and professional development. Participants go through a highly competitive selection process and receive extensive support, including access to cutting-edge research facilities, scientific seminars, networking events, mentorship programs, and customized training workshops. I was honoured to be part of the 2023 cohort of the NGS Program, spending three months at the Novartis Campus working with a dynamic research team focused on advanced analytical techniques for pharmaceutical and biomedical applications.

7.2. Research Focus of Program

The research group at Novartis, which hosted me during the NGS Program, specializes in developing advanced fluorescence-based analytical techniques to study polymeric and proteinate materials used in drug delivery systems. The team is dedicated to understanding and optimizing thermosensitive drug delivery systems (DDS), particularly focusing on the dynamics of conformational changes within these systems under various physiological conditions. Their innovative research aims at unravelling mechanisms of drug encapsulation, controlled release, and delivery efficiency using sophisticated fluorescence spectroscopy, imaging, and quantitative analysis tools. This is essential for enhancing targeted therapies, reducing adverse effects, and improving therapeutic outcomes. During my tenure, I contributed to research activities that investigated these conformational dynamics, gaining invaluable skills and knowledge in fluorescence-based quantitative analyses, polymer chemistry, and pharmaceutical biotechnology applications.

7.3. Achievements and Work Undertaken During the NGS Program Period

During my participation in the NGS Program at Novartis, I had the opportunity to present my research to fellow scientists and mentors within Novartis, facilitating insightful discussions and exchange of ideas that significantly enhanced my understanding and professional network.

- **Quantitative Fluorescence Analysis of Conformational Dynamics in Thermosensitive Polymeric Drug Carriers**

This study explored fluorescence-based quantitative methods to investigate the conformational changes occurring in polymeric drug carriers responsive to thermal stimuli. Employing advanced Förster resonance energy transfer (FRET) and time-resolved fluorescence spectroscopy, we quantified structural rearrangements in polymer chains at various temperatures, closely simulating physiological conditions. Results highlighted significant temperature-dependent structural shifts correlating with drug encapsulation efficiency and controlled release profiles, providing key insights into the optimization of thermosensitive polymer systems for targeted pharmaceutical applications.

- **Fluorescence-Based Monitoring of Protein Stability in Thermoresponsive Drug Delivery Systems**

We developed and validated novel fluorescence assays to quantitatively monitor the stability and structural integrity of protein therapeutics encapsulated within thermosensitive delivery platforms. By analyzing intrinsic protein fluorescence alongside extrinsic fluorescent labelling techniques, we elucidated critical temperature thresholds affecting protein conformation and bioactivity. Our findings demonstrated the precise conditions under which proteins remain stable and therapeutically effective, significantly contributing to the rational design of advanced protein-based DDSs.

7.4. Highlights and Impact of the Work

The research conducted during the NGS Program significantly advanced our understanding of fluorescence-based analytical methods in pharmaceutical sciences, particularly regarding the precise monitoring of conformational dynamics in thermosensitive drug delivery systems. The innovative approaches developed and validated during this period have potential implications for optimizing targeted

therapies and improving patient outcomes by ensuring greater precision and control in drug delivery. Furthermore, the experience and skills gained through the NGS Program have enriched my professional development, fostering collaboration and innovation that align closely with global healthcare research objectives.

Appendix A: Supplementary Material

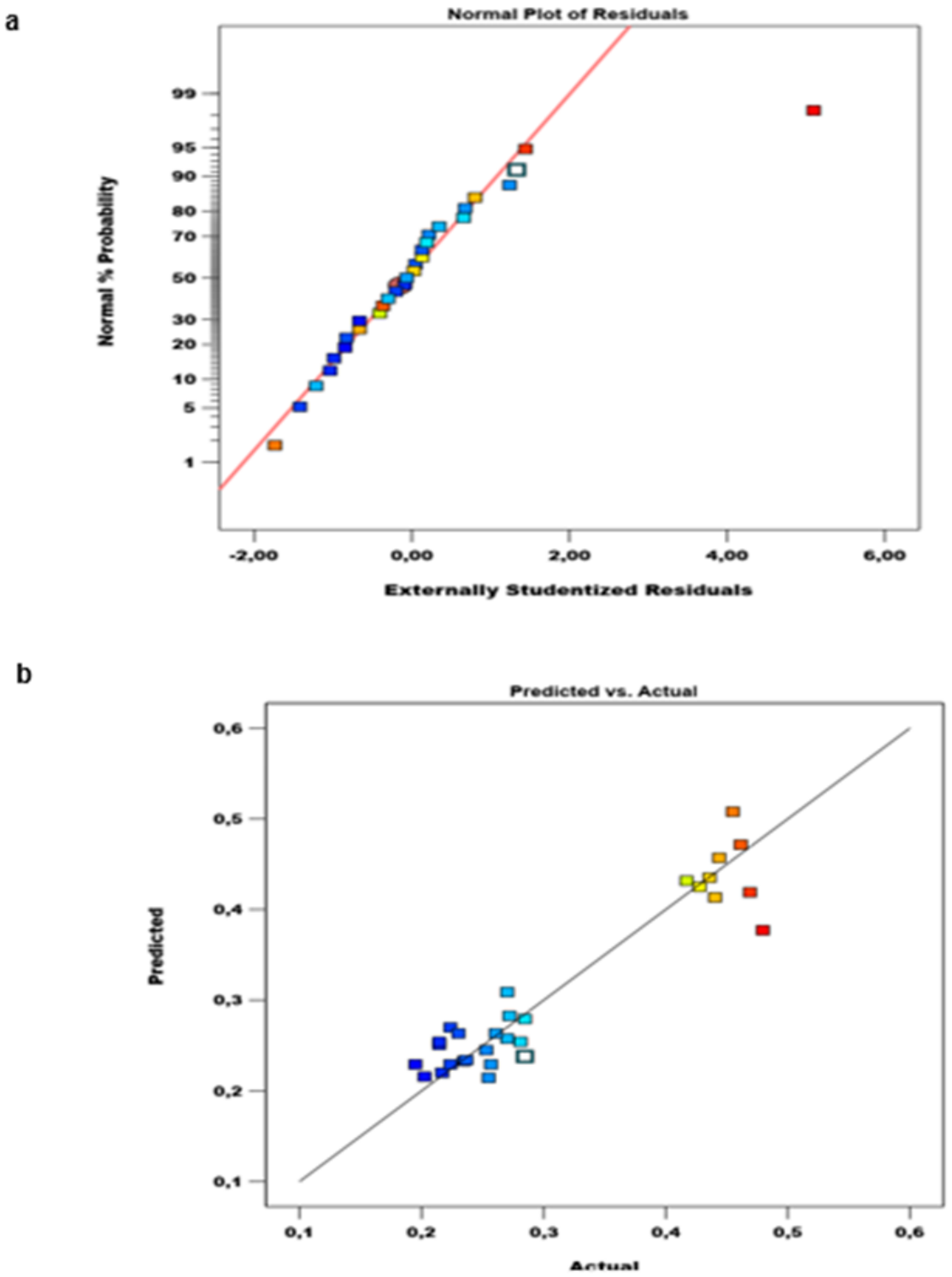


Figure S1 (a) Normal plot of residuals depicting the impact of model terms on PDI, **(b)** Observed versus predicted response for PDI.

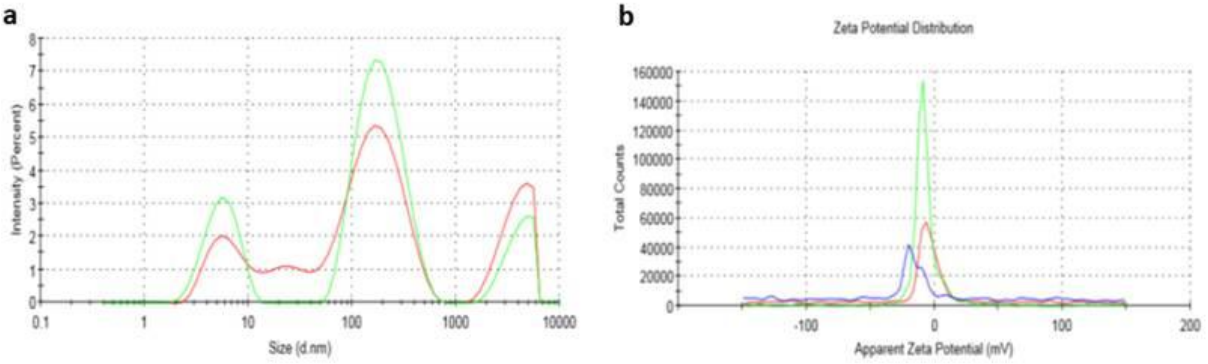


Figure S2 (**a**) average hydrodynamic particle size of 124±102.3nm (PDI 0.412±2.03), (**b**) zeta potential of -11.6 mV

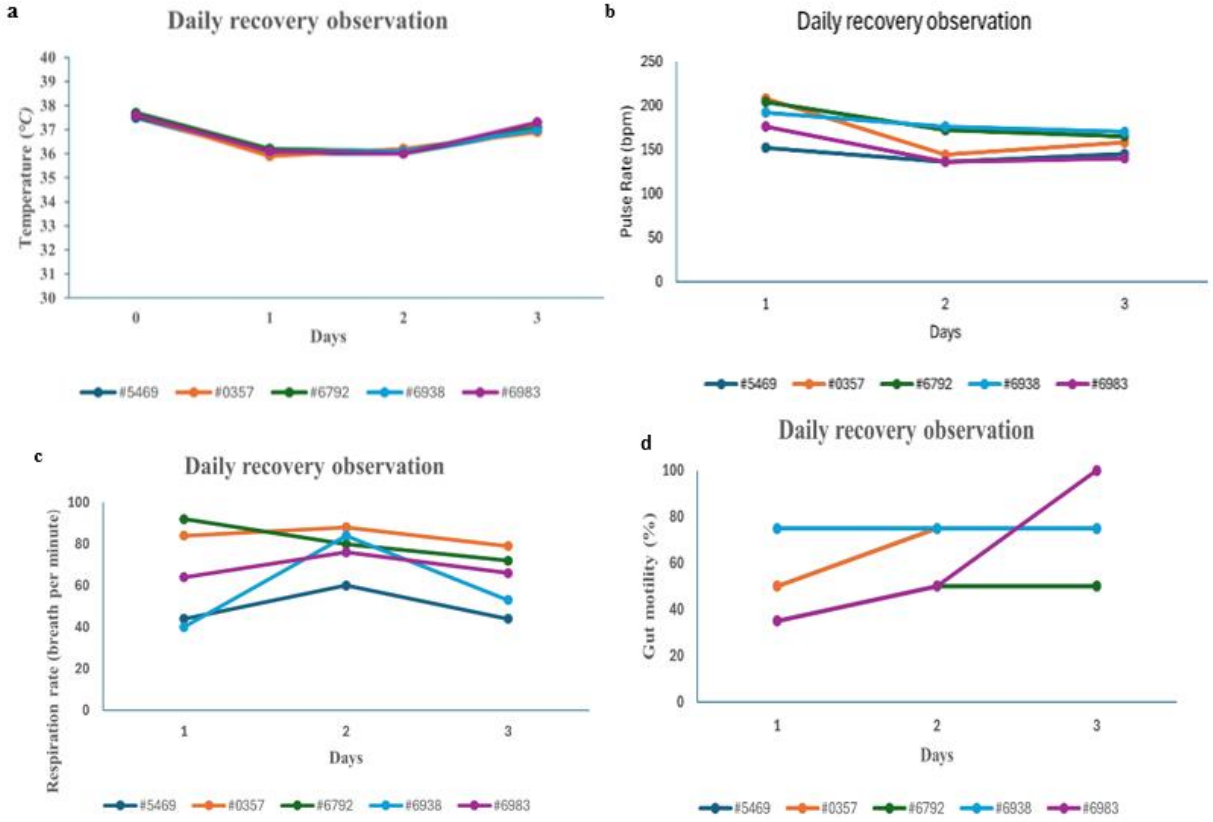


Figure S3 Images depicting daily recovery observations over the first three days post-surgery, including **(a)** body temperature, **(b)** pulse rate, **(c)** respiratory rate, and **(d)** gut motility.

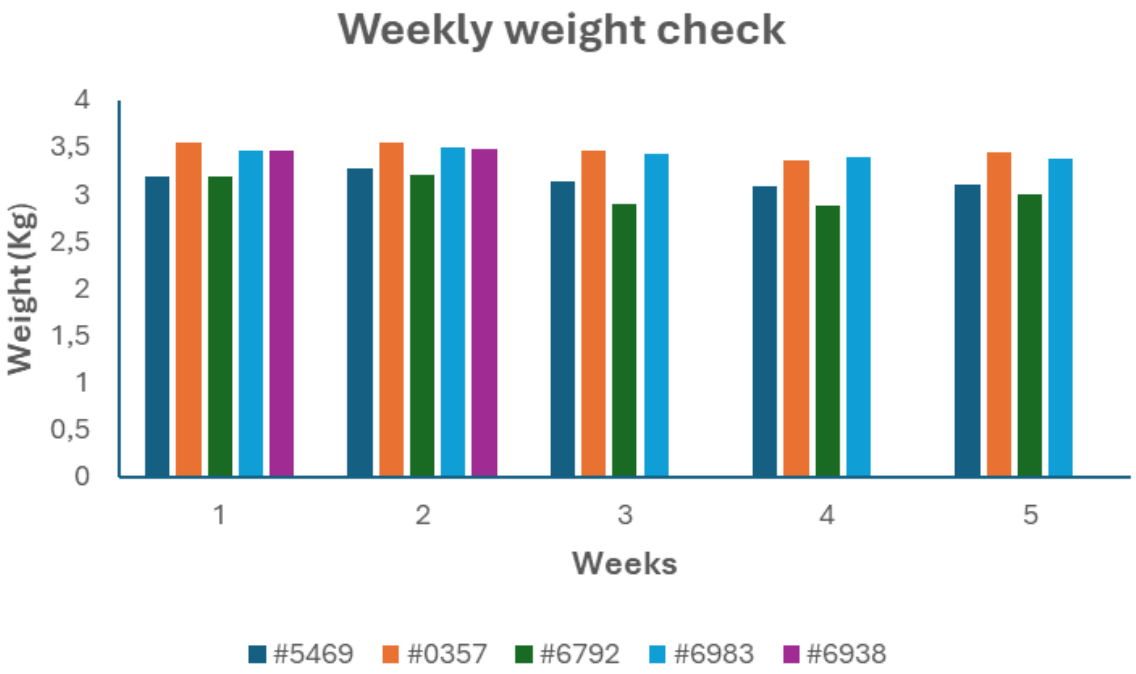


Figure S4 Weekly weight of the rabbits, with weeks 1 and 2 representing pre-surgery measurements and weeks 3 to 5 representing post-surgery measurements.

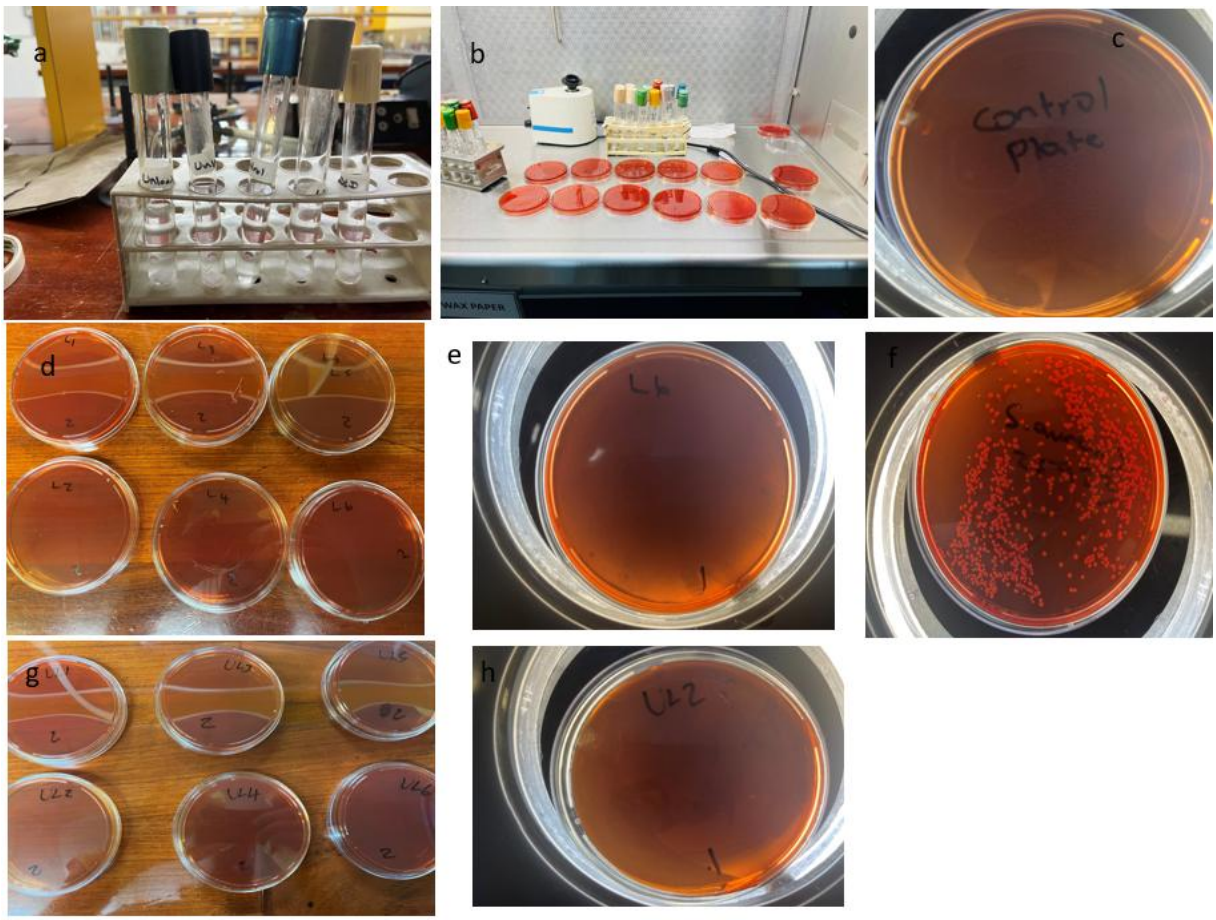


Figure S5 Representative images showing sterility testing of 3D-printed scaffolds. **(a)** Loaded and unloaded scaffolds incubated in sterile PBS prior to plating. **(b)** Tryptic Soy Agar (TSA) plates inoculated with supernatant and incubated at 37 °C for 48 hours. **(c)** Negative control plate with PBS only, showing no microbial growth. **(d, e)** Plates with drug-loaded scaffolds before and after incubation, confirming sterility after 48 hours. **(f)** Positive control with Staphylococcus aureus demonstrating robust bacterial growth, validating media suitability. **(g, h)** Plates with unloaded scaffolds before and after incubation, also showing no evidence of microbial contamination.

Appendix B: Animal Ethics Clearance Certificate

ANIMALS RESEARCH ETHICS COMMITTEE (AREC)

UNIVERSITY OF THE WITWATERSRAND JOHANNESBURG

STRICTLY CONFIDENTIAL

CLEARANCE CERTIFICATE NUMBER: AREC23-09-004C

APPLICANT: Mr M Mphaphuli
School: Therapeutic Sciences; Department: Pharmacy & Pharmacology; Location: WRAF

PROJECT TITLE: In vivo evaluation of 3D printed multi-component scaffolds incorperated with growth factor and bedaquiline nanoparticles for bone regeneration and drug distribution in young New Zealand rabbits.
Category: C; Species and Numbers involved: 48X, Male, 2.5-3.0 Kg, New Zealand White, Rabbits

Approval is hereby given for the use of animals for the research project named above and described in the application reviewed by a quorate meeting of the AREC held on 28 May 2024. This approval remains valid until 6 June 2026 and is conditional to the following (if blank there are no special conditions):

Condition 1	Condition 2	Condition 3	Condition 4

All material changes to the approved research must be reported to the AREC before they are implemented. Failure to do so will invalidate this clearance certificate.

An annual progress report must be provided to the AREC.

The use of these animals is subject to AREC guidelines on the use and care of laboratory animals, is limited to the procedures described in the application and is subject to additional conditions listed below:

I, the Chair of the AREC (or my designated representative) am satisfied that the proposed research is ethical as judged by local law, international standards and University policy.

Signed: _____ _____ Date: ____07/06/2024_____

(Chairperson of the AREC)

I am satisfied that the persons listed in this application are competent to perform the procedures described in the application, in the context of Section 23 (1) (c) of the veterinary and Para-veterinary Professions Act (19 of 1982).

Signed: __ _____ Date: _07 June 2024_____

(Registered Veterinarian)

CC: Student supervisor: Prof Y.E Choonara
Acting Director Wits Research Animal Facility (WRAF): Sr A Rammekwa

Appendix C: Publication

Journal of Drug Delivery Science and Technology 89 (2023) 105039

Contents lists available at ScienceDirect

Journal of Drug Delivery Science and Technology

journal homepage: www.elsevier.com/locate/jddst

Review article

Multi-purpose prototypes for extrapulmonary Mycobacterium tuberculosis targeting: A regenerative medicine perspective

Mashudu T. Mphaphuli [a], Mduduzi N. Sithole [a], Pradeep Kumar [a], Pierre P.D. Kondiah [a], Mostafa Mabrouk [b], Yahya E. Choonara [a,*]

[a] Wits Advanced Drug Delivery Platform Research Unit, Department of Pharmacy and Pharmacology, School of Therapeutic Science, Faculty of Health Sciences, University of the Witwatersrand, Johannesburg, South Africa, 7 York Road, Parktown, 2193, South Africa

[b] Refractories, Ceramics and Building Materials, National Research Centre, 33 El-Bohouth St. (former El-Tahrir St.), Dokki, Giza, P.O. 12622, Egypt

ARTICLE INFO

Keywords:
Extrapulmonary TB
Mycobacterium tuberculosis
Nanotechnology targeted therapy
Multi-purpose targeted therapy
Bioactive three-dimensional scaffolds
Biomaterials

ABSTRACT

Tuberculosis (TB) is a highly contagious infection caused by *Mycobacterium tuberculosis* that primarily affects the lungs but can spread to other organs. This is known as extrapulmonary tuberculosis (EPTB), which includes bone TB and central nervous system TB (CNS-TB). EPTB can alter the normal pathophysiological state of the affected tissue and affect drug absorption. Current treatment of bone TB and CNS-TB involves a combination of anti-TB drugs which can result in drug resistance; and also, the surgical intervention treatment, which has a slew of drawbacks such as, restricted donor sites and potential harvesting morbidity for autogenous bone grafts limitation. However, to mitigate drug resistance and surgical limitation of bone TB, a multi-purpose targeted therapy platform is necessary, capable of delivering drugs while promoting local bone regeneration. Although various nanotechnological-based drug delivery systems, such as polymeric nanoparticles, vesicular carriers, and metallic nanoparticles have been explored, they often lack mechanical properties and have yielded limited results in facilitating bone regrowth. This review article examines the current use of nanotechnology as a drug delivery system for anti-TB drugs, encompassing both pulmonary TB and EPTB treatment. Additionally, we explore the potential of integrating these nanoparticle systems into bioactive three-dimensional biomaterial scaffolds fabricated using the 3D-printing technology, with a specific focus on their ability to achieve concurrent bone regeneration and localised (targeted) drug delivery. This innovative approach has the potential to revolutionize the treatment of bone TB and CNS-TB.

Appendix D: Research Outputs

D1: Microphysiological Systems World Summit 2023 (Poster Presentation). JW Marriott Hotel, Berlin, Germany, June 26–30, 2023.

A NOVEL 3D PRINTED MULTI-COMPONENT SCAFFOLDS FOR TARGETED SPINAL TUBERCULOSIS THERAPY.

Mphaphuli M.T[a], Choonara YE[a], Kumar P[a], Sithole M[a], Kondiah P[a].

[a]Department of Pharmacy and Pharmacology, Faculty of Health Sciences, University of the Witwatersrand, Johannesburg, South Africa

[a]Corresponding author.

Email address: 1109238@students.wits.ac.za

Keywords: Scaffold, Biomaterials, 3d printing, *polymer, bioactive glass titanium.*

Introduction:

Spinal TB is the most prevalent type of skeletal TB accounting for over 50% of the cases. It disrupts the nervous system resulting in permanent spine distortion. Early detection and the use of combination chemotherapy are essential for the treatment and cure of spinal TB. However, due to low patient compliance and the emergence of drug-resistant strains, current therapies have been linked to unsatisfactory therapeutic outcomes. Additionally, the growth of bacteria in the spine damages the bone, necessitating repair through surgery which leads to bone defects (1). Currently, no effective strategies to achieve targeted-sustained anti-TB drug delivery and sufficient bone regeneration. Therefore, this research proposes the design and development of a dual-functional 3D-printed drug-loaded biomaterial scaffold, that addresses local chemotherapy delivery and critical-size bone defects. This approach has the potential to overcome challenges of bone regeneration and poor drug treatment of spinal TB in patients who have had surgery (2).

Aim: The study aimed to develop a novel multicomponent biomaterial scaffold conjugation using a 3D printing technique for the treatment of spinal TB.

Methods: Fabrication of the multicomponent scaffold consisted of a mixture of sodium alginate, polycaprolactone, polyvinyl alcohol, different concentrations of bioactive glass titanium, and bedaquiline as a model drug. The composition, structure, mechanical properties, and *in vitro* degradability of fabricated scaffolds were characterized. The cytocompatibility and osteogenic activity of the scaffolds were evaluated by *in vitro* cell culture.

Result: The results indicated that increasing the glass contents of the scaffold, decreased its porosity and degradation rate. However, the compressive strength was enhanced. Furthermore, the incorporation of bedaquiline microspheres improved the cell adhesion, proliferation, and osteogenic differentiation of MG63 cultured on the surface of the scaffolds.

Conclusion: This novel formulation has the potential to improve patients' healing time, therefore enhancing their quality of life.

References:

1. Ruparel S, et al. Surgical Management of Spinal Tuberculosis—The Past, Present, and Future. Diagnostics. 2022 Jun;12(6):1307.

2. Pei P, et al. 3D printed mesoporous bioactive glass/metal-organic framework scaffolds with antitubercular drug delivery. MMM. 2018 Dec 1; 272:24–30.

D2: 82nd FIP World Congress of Pharmacy and Pharmaceutical Sciences 2024 (Oral Presentation). Cape Town, South Africa, 1-4 September 2024.

A NOVEL 3D PRINTED MULTI-COMPONENT SCAFFOLD FOR TARGETED BONE TUBERCULOSIS THERAPY.

Mphaphuli M.T[a], Sithole M[a], Kumar P[a], Kondiah P[a], Choonara YE[a],

[a]Department of Pharmacy and Pharmacology, Faculty of Health Sciences, University of the Witwatersrand, Johannesburg, South Africa

Introduction: Bone tuberculosis (TB) is a common form of extrapulmonary TB and accounts for 1 to 3% of all TB cases. Effective management relies on a combination of chemotherapy and prompt detection. However, prolonged administration of anti-TB drugs often yields suboptimal results due to low adherence and drug resistance. Additionally, bacterial proliferation in bone leads to structural damage necessitating surgical intervention, resulting in bone loss and defects. Addressing these challenges necessitates innovative therapeutic strategies. Leveraging 3D-printing technology opens avenues for tailored scaffold design in biomedical engineering. Parameters such as mechanical strength, porosity, and biodegradability are crucial for scaffold success in bone TB therapy. While individual biomaterials have limitations, the multi-component approach offers distinct advantages over single-material scaffolds. The implementation of this pioneering approach holds transformative potential in bone TB treatment, promising improved patient outcomes, reduced surgical interventions, and enhanced quality of life.

Objective: The research explored the design, fabrication, and evaluation of the multi-component scaffold, focusing on its mechanical strength, porosity, and biodegradability.

Method: **The 4th generation 3D Bioplotter**™ (EnvisionTEC, Germany) was used to fabricate multi-component scaffolds. The scaffold was developed using four solutions containing polycaprolactone, sodium alginate, polyvinyl alcohol, and different concentrations of bioactive glass titanium. The solutions were mixed and homogenized to form a bio-ink suitable for 3D printing. The parameters for 3D printing were determined using a computer-aided design (CAD) and involved nozzle size, printing speed, temperature, waiting period, and printing pressure. The scaffolds were then printed into a solidifying solution of propanol.

Result: The composite's microstructural analysis and BET surface area measurement revealed that the majority of pores were in the micro-size range, ranging from 434 ± 4.58µm to 562 ± 10.87µm. Notably, pores larger than 50µm are conducive to cell infiltration and bone mineralization, indicating suitability for tissue regeneration. Initially, the scaffold experienced a 55% mass loss within 7 days due to bioactive glass-titanium, stabilizing thereafter until day 28. Incorporating bioactive glass-titanium into the PCL-PVA-Sodium Alginate scaffold enhanced compressive strength through robust bonding with the polymer matrix. Fourier transform infrared spectroscopy (FTIR) and X-ray powder diffraction (XRD) data suggested an interaction between the scaffold and simulated body fluid. Energy-dispersive X-ray spectroscopy (EDX) analysis revealed the scaffold's elemental composition, including Cl, Ca, Na, Si, and P peaks, essential for bone healing and regeneration.

Conclusion: This study utilized 3D printing to create multi-component biocomposite scaffolds with interconnected pores, improving mechanical strength and biodegradation. Adjusting the bioactive glass-titanium content allowed for control over the scaffold biodegradation rate and mechanical properties.